Dissertation
submitted to the
Combined Faculties for the Natural Sciences and for Mathematics
of the Ruperto-Carola University of Heidelberg, Germany
for the degree of
Doctor of Natural Sciences

presented by
Dipl. Phys. ROLAND ROCHOLZ
born in Lindlar

day of oral exam: 3^{rd} of December 2008

Spatio-Temporal Measurement of Short Wind-Driven Water Waves

Referees:
Prof. Dr. BERND JÄHNE
Prof. Dr. WERNER AESCHBACH-HERTIG

Abstract: Spatio-temporal measurements of wind-driven *short-gravity capillary waves* are reported for a wide range of experimental conditions, including wind, rain and surface slicks. The experiments were conducted in a linear wind wave flume and for the water surface elevation $\eta(x, y, t)$ both components of the slope field $\mathbf{s} = \nabla\eta$ were measured optically. For this the *color imaging slope gauge* (CISG) was realized, comprising a range of wavenumbers $k = \left(k_x^2 + k_y^2\right)^{1/2}$ from 60 to 4500 rad/m. The instrument was improved to achieve a sampling rate of 312.5 Hz, which now allows for the computation of 3D wavenumber-frequency spectra $S(k_x, k_y, \omega)$. Using a new calibration method it was possible to correct for the intrinsic nonlinearities of the instrument in the slope range up to ± 1. In addition, the *Modulation Transfer Function* (MTF) was measured and employed for the contrast restoration of the data. The results are generally consistent with former measurements. But, the shape of the saturation spectra in the vicinity of $k \sim 1000$ rad/m stands in contradiction to former investigations where a sharp spectral cutoff ($\propto k^{-2}$ or $\propto k^{-3}$) is commonly reported. The new MTF corrected spectra show just a gentle decrease (between $\propto k^{-0.5}$ and $\propto k^{-1}$) for $k > 1000$ rad/m, which has implications for the modeling of the energy fluxes in the wave field. Concerning the dispersion relation, a first approach for a quantitative evaluation of the wavenumber-frequency spectrum is shown. This includes estimates of the surface tension and the Doppler shift due to the surface shear flow and the wave-wave modulations. The wave measurements were accompanied by synchronized and spatially coinciding measurements of the surface temperature by means of infrared imagery. The temperature data is mapped onto an animated graphical model of the reconstructed surface elevation using a new interactive visualization tool. This allows for an investigation of intermittent small scale processes that are influencing the transfer of heat and gases at the air-water interface, such as microscale wave breaking, small scale Langmuir circulations, and the impact of rain drops.

Zusammenfassung: Ergebnisse zur raum-zeitlichen Messung von kleinskaligen windgetriebenen Wasserwellen werden für einen weiten Bereich experimenteller Bedingungen (Wind, Regen, Oberflächenfilme) präsentiert. Die Experimente wurden in einem linearen Wind-Wellen-Kanal durchgeführt und beide Komponenten des Gradienten der Wasseroberflächenauslenkung $\mathbf{s}(x, y, t) = \nabla\eta(x, y, t)$ wurden optisch gemessen. Dazu wurde eine bildgebende Technik (CISG) eingesetzt. Der Bereich der erfassten Wellenzahlen $k = \left(k_x^2 + k_y^2\right)^{1/2}$ reicht von 60 bis 4500 rad/m. Die CISG wurde verbessert, um eine Bildwiederholrate von 312.5 Hz zu erreichen, wodurch nun die Berechnung von 3D Wellenzahl-Frequenz-Spektren $S(k_x, k_y, \omega)$ möglich ist. Eine neue Methode zur Kalibrierung wurde entwickelt, die erstmals die Korrektur der intrinsischen Nichtlinearitäten des Instruments für einen Neigungsbereich bis zu ± 1 ermöglicht. Desweiteren wurde die Modulationsübertragungsfunktion (MTF) gemessen und zur Kontrast-Restauration eingesetzt. Im allgemeinen sind die Ergebnisse konsistent mit vorhergehenden Messungen. Allerdings steht die Wellenzahlabhängigkeit der Sättigungsspektren im Bereich von $k \sim 1000$ rad/m im Widerspruch zu frühreren Untersuchungen in denen ein scharfer spektraler Abfall berichtet wurde ($\propto k^{-2}$ oder $\propto k^{-3}$). Die neuen MTF-korrigierten Spektren zeigen hingegen nur einen sanften Abfall (zwischen $\propto k^{-0.5}$ und $\propto k^{-1}$) für $k > 1000$ rad/m, welches von Bedeutung für die Modellierung des Energietransfers im Wellenfeld ist. Bezüglich der Dispersionsrelation wird ein quantitativer Ansatz zur Auswertung der Wellenzahl-Frequenz-Spektrums vorgestellt. Dieser beinhaltet Abschätzungen der Oberflächenspannung sowie der Dopplerverschiebung aufgrund der Scherströmung und der Wellen-Wellen-Modulationen. Die Wellenmessungen wurden begleitet von synchonisierten und räumlich übereinstimmenden Aufnahmen der Oberflächentemperatur mittels einer Infrarotkamera. Mit einem neuen interaktiven Visualisierungswerkzeug werden die Temperaturdaten auf ein animiertes graphisches Modell der rekonstruierten Wasseroberfläche projiziert. Dies erlaubt die Untersuchung der lokalisierten und sporadischen Prozesse, die den Austausch von Wärme und Gasen an der Luft-Wasser-Phasengrenze kontrollieren, wie z.B. kleinskaliges Wellenbrechen, Micro-Langmuir-Zirkulationen und das Einschlagen von Regentropfen.

Contents

1. Introduction

The statistical description of wind-driven waves on the water surface is important in the chain that is leading from remote sensing of the ocean to reliable estimates for the exchange rates of heat, gas, and momentum between the atmosphere and the ocean [44, 49].

Approximately 30-40% of the fossile fuel-produced carbon dioxide is absorbed by the oceans [41]. This highlights the importance of air-sea transfer processes in the context of the *climate change* debate [14]. Nonetheless, the current constraints on the spatial and temporal variability of the oceanic uptake are rather poor, in large part because of the uncertainty in regional air-sea CO_2 fluxes [41]. Using semi empiric gas exchange parameterizations based on wind speed leads to estimates of the oceanic uptake ranging from 1 to $3 \cdot 10^{12}$ kg carbon per year [110, 169].

The gas transfer across the air-water interface is governed by the interplay of molecular diffusion and turbulent transport. At some distance from the interface, turbulent transport always exceeds diffusive transport. But as turbulent motions cannot penetrate the interface, the size of the turbulent eddies gradually decreases toward the surface, where they are attenuated by viscous forces [82][1]. Consequently, there exists a thin boundary layer in which the molecular diffusion dominates. The thickness of this boundary layer depends on the diffusion coefficient of the tracer and the intensity of the turbulent motions close to the surface. The main resistance for the transport of sparingly soluble gases[2] is therefore due to the water-sided mass boundary layer, which extends only over about $20 - 200\,\mu$m [79].

In the past decades, experiments in the laboratory and in the open ocean have provided evidence that transfer velocities[3] are particularly influenced by small scale surface waves in the decimeter to millimeter range [48, 72, 145]. This is attributed to instabilities of the waves, which induce near surface turbulence, i.e. thinning of the mass boundary layer. The most prominent effect is called *microscale wave breaking* [12], which depicts the breaking of steep wind-driven waves without air entrainment [175]. Another mechanism that is suspected to influence the air-water transfer is called *Langmuir Circulation*[4], which are due to nonlinear interaction between the waves and the shear flow [121, 158, 165].

Much progress has been made regarding the measurement techniques for the investigation of air-sea interaction processes. Especially the introduction of quantitative visualization techniques based on image processing has improved the non-intrusive access to the aqueous boundary layer [75]. For instance, by means of infrared imagery, it is possible to measure the local heat transfer across the wavy water surface (e.g. Garbe et al. [53], Schimpf et al. [148]). Also the imaging technique for the measurement of water waves has been continuously improved over the past two decades (e.g. Balschbach [9], Fuß [50], Jähne and Riemer [84], Klinke [93], Zhang and Cox [181]). These visualization techniques have gained much attention since they allow for an identification of the intermittent physical processes which control the air-sea interaction. An example is given in figure 1.1 which shows simultaneous measurements of the water surface slope and the temperature field for a microscale breaking wave, measured by Zappa et al. [176]. Based on the infrared

[1] Note, this is rather the depiction of the *small eddy model* than an incontrovertible fact. There are different conceptual models addressing the interplay of turbulent and diffusive transport, see for instance [37, 52, 147].

[2] e.g. carbon dioxide, methane, and fluorochlorocarbons [83].

[3] The transfer velocity is equal to the flux divided by the concentration difference.

[4] Langmuir Circulations are near-surface helix circulations in the water, with the axis almost parallel to the wind.

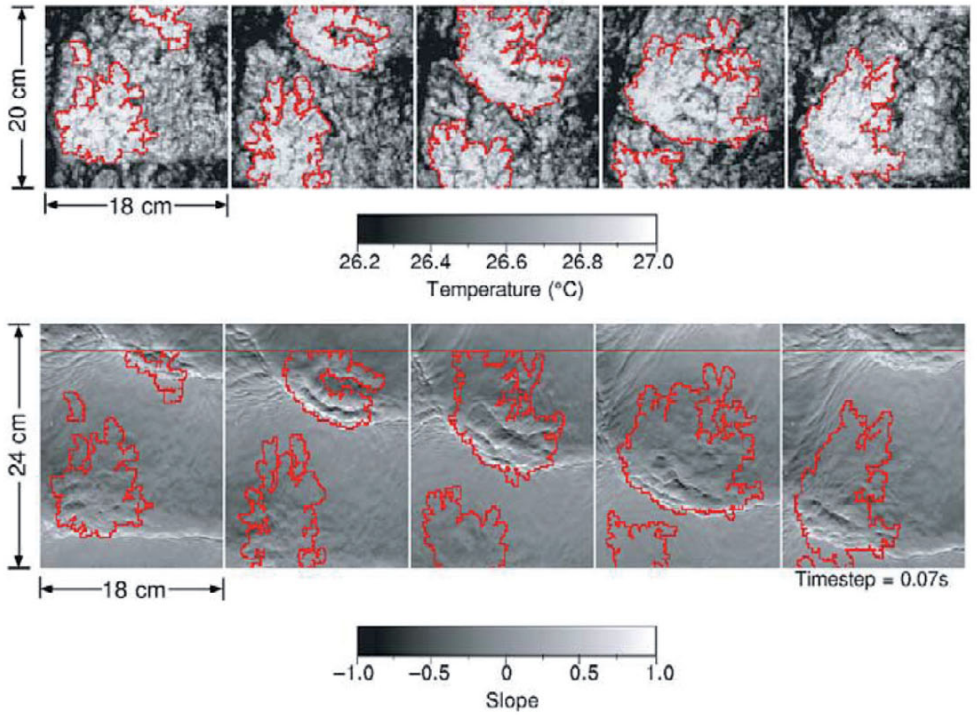

Figure 1.1.: Observation of a microscale breaking wave. The infrared images (top row) show the water surface temperature. In this experiment the water bulk is warm compared to the surface that is constantly cooled due to evaporation. The areas of significantly enhanced surface temperature (labeled with red borders) therefore indicate the disruption of the aqueous thermal boundary layer due to sub-surface turbulence. In the images of the water surface slope (bottom row) these areas are found to coincide with the turbulent wake of a microscale breaking wave (adopted from Zappa et al. [176]).

images, areas of enhanced subsurface turbulence were identified. These areas are found to coincide with the wake of a microscale breaking wave, see figure 1.1.

Moreover, the wave slope imaging enables a detailed statistical description of small scale wind-driven waves, i.e. two-dimensional wavenumber spectra. The publication of the first systematic measurements of such spectra by Jähne and Riemer [84, 1990] has strongly influenced the attempts to model the energy and momentum transfer from the turbulent wind field to waves (e.g. [8, 44, 58, 99]). Note that also the momentum is transferred through the viscous boundary layer[5] [166]. Therefore, the wave models provide a link between the spectral description of the wave field and the estimation of air-sea exchange of gases or heat. Admittedly, this link is not yet fully established and still an active research field (e.g. [30, 31, 115, 160]).

Despite the progress that has been made for the modeling and the measurement concerning the air-sea interaction, in both disciplines the knowledge is still rather fragmented. There are many variables influencing the wave field and the air-water gas transfer, e.g. wind forcing, cleanliness of the water surface, rain, sub-surface currents, salinity and stratification, convection, chemical enhancement, and marine biology. The global transfer rates are traditionally estimated from empirical correlations between the wind speed and mass transfer rates. Moreover, the global wind speed estimates are themselves based on empirical parameterizations by means of radar backscatter, which is measured by satellites. Consequently, there are efforts to introduce new transfer velocity parameterizations that are directly based on the surface roughness obtained by radar backscatter, e.g. Frew et al. [49]. This approach also accounts for the inhibition of the wave field by sur-

[5] Note, there are additional components of the stress carried by the waves and balanced by the wave growth.

face contaminations[6]. With respect to rain the transfer velocity estimates are unrealistically high [49, 66]. Thus, there is a need to further investigate the influence of rain on both, the wave field and the transfer velocity. The interpretation of radar backscatter from the ocean depends on a detailed understanding of the physics of electromagnetic scatter [8]. This also incorporates a statistical description of the hydrodynamic conditions in terms of the two-dimensional wavenumber spectrum [96, 126].

The observations of microscale breaking waves reveal that the exchange processes highly vary on time scales of a fraction of a second and horizontal spatial scales of several centimeters. In contrast, the relevant spatial scales for global modeling and remote sensing are several orders of magnitude larger. Thus, for the transfer estimates an adequate integration has to be performed, which takes the small scale intermittency into account [83].

Measurement of the small-scale variations in the open ocean are difficult. Infrared imagery was already deployed for field studies [64, 167], but for instance boundary layer visualizations and wave imaging techniques are not readily applicable in the open ocean. For the evaluation of infrared data the characteristics of the wave field need to be incorporated in order to establish a link to the surface roughness parameterizations for gas transfer. The investigation of the intermittent processes therefore manly relies on laboratory measurements.

1.1. Current Objectives of Laboratory Measurements

The context of the laboratory investigation of air-sea interaction was described in the preceding section. Based on this, some of the objectives of the laboratory measurements in the context of this study are outlined.

- There is a lack of new systematic measurements of the wavenumber spectra of wind-driven waves, i.e. since the mid 1990's only very few data was published. This is unsatisfactory with respect to the validation of wave modeling attempts. So far, the effects of rain and surface slicks on the wave spectra have not yet been systematically investigated. In addition, the capabilities of wave imaging techniques have been considerably improved.
  One objective of wave imaging in the laboratory is therefore to provide new wave data that is comprising a wide range of conditions (e.g. wind, rain, surface slicks). A long term goal is to collect wave spectra from different facilities in combination with gas transfer measurements in order to quantify the influence of the facility geometry (e.g. fetch[7], water channel width and depth, aerodynamic conditions, flow in the water bulk, linear vs. annular geometry).

- For the investigation of intermittent small-scale processes (e.g. *microscale breaking* and *micro Langmuir circulations*) spatially and temporally coinciding measurements of the heat transfer and the wave field are desired. Moreover, the aim is to study the temporal evolution of the surface flow structures, for that high frame rates are requested.

- The evaluation of gas transfer rates obtained from budget measurements in a linear wind wave flume are complicated by the fetch dependence of the wave field. One goal is therefore, to make an inter-comparison of simultaneous measurements of the local heat transfer and the spatially averaged gas transfer. This comparison is needed for the estimation of the bias in the gas transfer velocities that is introduced by the integration over inhomogeneous conditions.

[6] Surface contaminations are due to anthropogenic pollution (e.g. oil slicks) and marine biology (e.g. algae blooms).
[7] Fetch: distance over which wind acts on the water surface.

- Using multiple trace gases with different diffusion coefficients allows for the determination of the Schmidt-Number exponent n[8]. For the verification of the Schmidt-Number scaling between the transfer velocities of heat and gas the measurement of the gradual transition of n is required. Moreover, given the knowledge of the Schmidt-Number exponent, a physically based parameterization of the transfer velocity with the water surface roughness is expected to become available.
- Measurements under rain conditions are needed for the quantification of the rain effect on the transfer velocities and on the wave field. The long term goal is to extend the transfer velocity parameterization for the rain conditions.
- Due to the availability of higher frame rates of modern CCD cameras it is possible to resolve the wave frequencies by the wave imaging technique. This allows for the computation of wavenumber-frequency spectra. The evaluation of the wavenumber-frequency spectra of wind-driven water waves needs to be explored with respect to the dispersion relation.

1.2. Objectives of this Study

The scope of this study was the improvement of the *color imaging slope gauge* for the spatio-temporal wave measurement and the evaluation of the wave data with respect to the above listed wave-related objectives.

The aspired innovation of the wave imaging method comprises:

- Adaption of the *color imaging slope gauge* (CISG) for the setup in the rain tower section of the linear wind-wave tunnel in Hamburg, Germany. The CISG technique was chosen in order to measure both components of the water surface slope simultaneously.
- Development of a new calibration method that allows for a correction of the intrinsic non-linearities of the instrument. With former calibration methods only linear calibrations could be realized in practice.
- Development of a new method for the in-situ measurement of the *Modulation Transfer Function* (MTF). The MTF is desired for a correction of the wavenumber dependent loss in the image contrast, which directly influences the quality of the wavenumber spectra.
- Deployment of a new camera with a higher frame rate in order to measure the frequencies of the waves in addition to the 2D wavenumber vector.

For the investigation of the small-scale processes it is desired to combined the wave imaging with the infrared imagery by means of:

- Synchronization of the wave imaging (CISG) with the infrared imaging system (ACFT) (together with Dr. Schimpf).
- Geometrical registration of the obtained image sequences.
- Reconstruction of the water surface elevation from the slope image sequences. This facilitates a combined visualization of the wave field and the infrared data, which is desired for a direct comparison of the observations in space and time.

[8] Schmidt-Number exponent n depicts the scaling behavior between the transport of momentum and the transport of gas or heat. From theory follows $n = 2/3$ for a smooth surface, and $n = 1/2$ for a rough surface. Depending on the actual hydrodynamic conditions n varies between these two extremes [37].

- Investigation of the spatio-temporal characteristics of micro *Langmuir circulations* in reference to the waves.
- Investigation of *microscale wave breaking* in reference to the surface temperature field.
- Investigation of the evolution of rain drop impacts on the water surface and the resulting disturbances in the aqueous thermal boundary layer.

The acquisition of wave image sequences with high temporal resolution opens new perspectives for the spectral evaluation of the wave data. The computation of wavenumber-frequency spectra was not possible for the *CISG* method up to now. Therefore new computer scripts needed to be developed for the data evaluation. The evaluation of the spectral data comprises:

- Computation and interpretation of two-sided wavenumber spectra, including rain and surface slick conditions. Two-sided representations become available, since not only the orientation but also the direction of the 2D wavenumber vector can be determined when exploiting the frequency information. In former studies only the orientation of the wavenumber vector could be determined, leading to an 1π ambiguity.
- Evaluation of the 3D power spectra $S(\omega, \mathbf{k})$ with respect to the dispersion relation. In principle, the spectral volume contains information about the surface shear flow, the wave-wave interactions, and surface slick contaminations. The deviations between the measured dispersion relation and the theoretical dispersion relation were explored in order to infer these informations.
- Quantification of the rain effect on the surface roughness. The rain-induced ring waves are isotropic, whereas the wind-driven waves are directed. This can be exploited for quantification of the surface roughness contribution by rain.

The wave measurement, conducted in the period between Mai and July 2007 at the linear wind wave flume of the University of Hamburg, is part of the experimental campaign for the project *Impact of Wind, Rain, and Surface Slicks on Air-Sea CO2 Transfer Velocity - Tank Experiments*[9].

[9]The project is a collaboration of the research group of Prof. Dr. Detlef Stammer, University of Hamburg, and the research group of Prof. Dr. Bernd Jähne, University Heidelberg.

2. Theory

In this chapter we touch on two topics, namely fluid mechanic in the sections 2.1 through 2.4, and digital imaging in section 2.5. Both topics are equally important for this study.

2.1. Basic Physical Laws

A brief depiction of some fundamental laws of fluid mechanics is given in this section, covering the basic transport equations, the conservation laws and the equation of motion. Subsequently, the most important aspects of waves on the water surface will be introduced in section 2.2.

2.1.1. Diffusive Transport

The diffusive flux $\mathbf{j}$ of a concentration c is described by Fick's first law

$$\mathbf{j} = -\mathcal{D}\nabla c, \tag{2.1}$$

where $\mathcal{D}$ is a diffusion constant. In absence of concentration sinks or sources (such as chemical reactions) the only way to change the concentration with time is a divergence of the flux. This is expressed by the continuity equation in Lagrangian specification

$$\frac{Dc}{Dt} = -\nabla\mathbf{j}, \tag{2.2}$$

where $\frac{D}{Dt}$ is the *material derivative*, indicating that the observer moves with a fluid volume element. Inserting (2.1) in (2.2) yields Fick's second law of unsteady diffusion

$$\frac{Dc}{Dt} = \mathcal{D}\Delta c. \tag{2.3}$$

In contrast to the Lagrangian specification one can describe the same situation in the Eulerian specification, where the concentration and the velocity of the medium are taken as field variables within a fixed frame of reference. The material derivative is related to the field variables according to

$$\frac{D}{Dt} = \frac{\partial}{\partial t} + \mathbf{u}\nabla, \tag{2.4}$$

where $\mathbf{u}(\mathbf{x}, t)$ is the velocity field of the flow and the term $\mathbf{u}\nabla$ is called the advective derivation [102]. From (2.3) and (2.4) follows the transport equation in the fixed frame of reference

$$\frac{\partial c}{\partial t} = \mathcal{D}\Delta c - \mathbf{u}\nabla c. \tag{2.5}$$

So far it has not been stated what kind of concentration is actually transported. One usually thinks of some scalar concentration of gas or heat, so that the constant $\mathcal{D}$ is the molecular diffusivity or heat conductivity, respectively. It is also possible to consider the momentum of the fluid particles as a vectorial concentration. But in this case also additional forces have to be considered. The momentum transport is the subject of section 2.1.5.

	Meaning	Units
ρ	density	kg/m^3
μ	dynamic viscosity	Pa s
$\nu \equiv \mu/\rho$	kinematic viscosity	m^2/s
$\mathcal{D}$	diffusion constant	e.g. m^2/s
$\frac{D}{Dt}$	material derivative	1/s
c	concentration (section 2.1.1)	e.g. mol/m^3 or kg/m^3
$\mathbf{j}$	flux	e.g. (mol or kg) $\cdot$ 1/(m^2 s)
$\mathbf{u} = [u, v, w]^T$	flow velocity	m/s
Φ	velocity potential	m^2/s
η	surface elevation	m
σ	surface tension	N/m
H	water depth	m
g	acceleration due to gravity	m/s^2
c	phase velocity (section 2.2.1)	m/s
ω	angular frequency	rad/s
$\mathbf{k}$	wavenumber vector	rad/m
k	magnitude of the wavenumber vector	rad/m

Table 2.1.: Nomenclature for the sections 2.1.1 to 2.2.1

2.1.2. Turbulent Transport

Turbulent motions can be treated as statistical fluctuations superimposed on the mean flow. Therefore it is convenient to express the flow velocity as

$$\mathbf{u} = \mathbf{U} + \mathbf{u}', \tag{2.6}$$

with

$$\mathbf{u}'(t) = \mathbf{u}(t) - \overline{\mathbf{u}(t)}, \tag{2.7}$$

so that $\mathbf{u}'$ denotes the fluctuating part and $\mathbf{U} = \overline{\mathbf{u}(t)}$ depicts the mean flow. Similarly, for the concentration of a scalar tracer we write $c = C + c'$. Inserting into Fick's second law (2.3) and integrating over time yields

$$\frac{\partial C}{\partial t} + \mathbf{U}\nabla C = -\nabla \mathbf{J} = -\nabla \left(\overline{\mathbf{u}'c'} - \mathcal{D}\nabla C \right). \tag{2.8}$$

The averaged flux $\mathbf{J}$ is therefore consisting of the averaged flux due to molecular diffusion $\mathcal{D}\nabla C$ and some extra term $\overline{\mathbf{u}'c'}$ which is attributed to the turbulent transport of a scalar tracer.

2.1.3. Conservation of Mass

The law of conservation of mass states that the rate of change of mass in a fixed volume V must be equal to the flux across the boundaries A of the volume

$$\int_V \frac{\partial \rho}{\partial t} dV = -\int_A \rho\, \mathbf{u} \cdot d\mathbf{A}. \tag{2.9}$$

Using the divergence theorem of Gauss gives

$$\int_V \left[\frac{\partial \rho}{\partial t} + \nabla \cdot (\rho\, \mathbf{u}) \right] dV = 0. \tag{2.10}$$

This equation must hold for any fixed volume and thus requires that the integrand vanishes

$$\frac{\partial \rho}{\partial t} + \nabla(\rho\,\mathbf{u}) = 0. \tag{2.11}$$

Equation (2.11) is called the *continuity equation*. By expanding the $\nabla(\rho\mathbf{u})$ term and using the definition of the material derivative (2.4) we get the continuity equation in the Lagrangian specification

$$\frac{\partial \rho}{\partial t} + \rho\,\nabla\mathbf{u} + \mathbf{u}\,\nabla\rho = \frac{D\rho}{Dt} + \rho\,\nabla\mathbf{u} = 0. \tag{2.12}$$

Water in a wind wave flume is an incompressible fluid, therefore the continuity equation can be simplified in our case. Fluids are called incompressible if the magnitude of $\frac{1}{\rho}\frac{D\rho}{Dt}$ in (2.12) is small compared to each of the components $\frac{\partial u}{\partial x}$, $\frac{\partial v}{\partial y}$ and $\frac{\partial w}{\partial z}$. Neglecting $\frac{1}{\rho}\frac{D\rho}{Dt}$ gives the continuity equation for an incompressible fluid

$$\nabla\mathbf{u} = \frac{\partial u}{\partial x} + \frac{\partial v}{\partial y} + \frac{\partial w}{\partial z} = 0. \tag{2.13}$$

2.1.4. Conservation of Momentum

Newtons law demands, that the net force on an infinitesimal fluid element must be equal the mass times the acceleration

$$\rho\frac{Du_i}{Dt} = \rho g_i + \frac{\partial \tau_{ij}}{\partial x_j}, \tag{2.14}$$

where g_i is the i-component of the net body force, acting on the center of mass of the fluid element, and $\frac{\partial \tau_{ij}}{\partial x_j}$ is the i-component of the surface force per unit volume. Equation (2.14) is often referred as *Cauchy's equation of motion*. The stress tensor τ_{ij} is symmetric and for incompressible fluids it can be written as

$$\tau_{ij} = -p\delta_{ij} + 2\mu e_{ij}, \tag{2.15}$$

where p is the mean pressure, δ_{ij} is the Kronecker delta, and e_{ij} is the strain rate tensor

$$e_{ij} \equiv \frac{1}{2}\left(\frac{\partial u_i}{\partial x_j} + \frac{\partial u_j}{\partial x_i}\right), \tag{2.16}$$

see Kundu [102, chapter 10.10]. The relation (2.15) is called *constitutive equation* for an incompressible fluid.

2.1.5. Equation of Motion

The fundamental equation of motion for a fluid volume element is called the *Navier-Stokes equation*. It is similar to the transport equation (2.3), if we insert the momentum $\rho\mathbf{u}$ for the concentration and replace the diffusion constant by the kinematic viscosity μ. But in contrast to (2.3) we have to introduce additionally source terms that were explicitly excluded in the considerations of section 2.1.1. Here, we introduce these source terms from physical reasoning. More formally the Navier-Stokes equation can be found by substituting the constitutive equation (2.15) in Cauchy's equation of motion (2.14), see for instance Kundu [102]. For water in a wave flume we can write the Navier-Stokes equation as

$$\rho\frac{D\mathbf{u}}{Dt} = -\nabla p + \rho\mathbf{g} + \mu\nabla^2\mathbf{u}. \tag{2.17}$$

This states, that the acceleration $\rho\frac{D\mathbf{u}}{Dt}$ of the incompressible fluid volume element is due to a pressure gradient $-\nabla p$, the body force $\rho\mathbf{g}$, and molecular viscous friction $\mu\nabla^2\mathbf{u}$. The influence

of the centrifugal force or the Coriolis force, resulting from the earths rotation, can be neglected as long as the angular frequencies of the considered motions are large compared to the earths angular frequency [129]. For a wind wave flume this is always the case. The material derivative of the momentum $\frac{D\mathbf{u}}{Dt}$ in (2.17) indicates, that this equation holds in the Lagrangian description, following the fluid particle. In a fixed frame of reference the material derivative can be replaced using (2.4) to find the expression for the rate of change of momentum as a field variable

$$\rho\frac{D\mathbf{u}}{Dt} = \rho\frac{\partial\mathbf{u}}{\partial t} + \rho(\mathbf{u}\nabla)\mathbf{u}. \tag{2.18}$$

Inserting (2.18) into (2.17) leads to the Navier-Stokes equation in the Eulerian specification

$$\rho\frac{\partial\mathbf{u}}{\partial t} + \rho(\mathbf{u}\nabla)\mathbf{u} = -\nabla p + \rho\mathbf{g} + \mu\nabla^2\mathbf{u}. \tag{2.19}$$

This can be expanded, using the identity

$$(\mathbf{u}\nabla)\mathbf{u} = (\nabla\times\mathbf{u})\times\mathbf{u} + \frac{1}{2}\nabla u^2 \tag{2.20}$$

and the definition of the vorticity $\boldsymbol{\omega} \equiv \nabla\times\mathbf{u}$. It follows

$$\rho\frac{\partial\mathbf{u}}{\partial t} + \rho(\boldsymbol{\omega}\times\mathbf{u}) + \rho\frac{1}{2}(\nabla u^2) = -\nabla p + \rho\mathbf{g} + \mu\nabla^2\mathbf{u}. \tag{2.21}$$

The nonlinear term $(\mathbf{u}\nabla)\mathbf{u}$ in the Navier-Stokes equation prohibits general analytical solutions, unless further assumptions are made.

Common Approximations: Studying water wave phenomena, some common approximations are made to simplify the Navier-Stokes equation. First of all, the term describing the *viscous friction can be neglected* since

$$\rho\frac{\partial\mathbf{u}}{\partial t} \gg \mu\nabla^2\mathbf{u}, \tag{2.22}$$

which is generally found to be true far from the boundary of the flow field[1] [102]. Secondly, the fluid is assumed to be *irrotational*

$$\nabla\times\mathbf{u} = 0, \tag{2.23}$$

which can be seen as a consequence of equation (2.22) and Kelvin's circulation theorem if the motion is regarded to be generated from rest, see [102]. This simplifies the problem, since in the Navier-Stokes aquation the term $\rho(\boldsymbol{\omega}\times\mathbf{u}) = \rho(\nabla\times\mathbf{u})\times\mathbf{u}$ vanishes.

Due to the assumption of *irrotationality* the velocity vector can be written as the gradient of a scalar potential Φ

$$\mathbf{u} \equiv \nabla\Phi. \tag{2.24}$$

With this definition of the velocity potential Φ and the above approximations the *Bernoulli equation* for unsteady irrotational flow

$$\nabla\left[\frac{\partial\Phi}{\partial t} + \frac{1}{2}u_j^2 + \int\frac{\mathrm{d}\,p}{\rho} + g\,z\right] = 0, \tag{2.25}$$

can be derived from the Navier-Stokes equation (2.21) (see [102, p. 118–121] for details). The equations (2.24) and (2.25) are used in section 2.2.1 for the derivation of the dispersion relation of water waves.

[1] The water-sided viscous boundary layer typically extends over 0.6-2.0 mm [37].

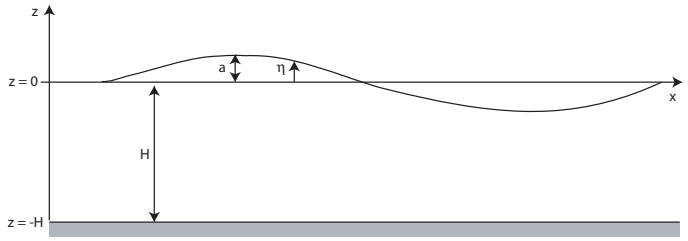

Figure 2.1.: Coordinate system and wave nomenclature

2.2. Waves on the Water Surface

Deep water surface waves are dispersive, i.e. the phase speed is a function of the wavelength. The dispersion relation is depicted in the following sections 2.2.1 and 2.2.2. Section 2.2.3 gives an explanation for the naming conventions of small scale waves, e.g. *short-gravity capillary waves*.

2.2.1. Dispersion Relation for Small Amplitude Waves

The theory for monochromatic linear and nonlinear wave propagation was already developed in the 19^{th} century by Airy [3], Stokes [153, 154], and Boussinesq [22]. Here we present a brief deduction of the dispersion relation for small amplitude water waves and irrotational flow, following Kundu [102]. The waves are called *small amplitude waves* if the amplitudes a are small compared to the water depth H and if they are small compared to the wavelengths λ. The first condition $a/H \ll 1$ allows us to neglect the difference between the undisturbed water depth and the instantaneous water depth, so that we can evaluate the velocity potential at $z = 0$ instead of $z = \eta$. The second condition $a/\lambda \ll 1$ implies that the slopes of the waves are small. This justifies to treat the free surface as a linear superposition of plane waves. Moreover, the small slope condition is used to approximate the curvature $1/r$ of the surface as $\frac{\partial^2 \eta}{\partial x^2}$ when dealing with the influence of the surface tension. This approximation is used in the formulation of the dynamic boundary condition (2.33).

The condition that the flow is irrotational allows for the definition of a velocity potential Φ such that

$$u = \frac{\partial \Phi}{\partial x} \qquad w = \frac{\partial \Phi}{\partial z}, \tag{2.26}$$

where u and w are the components of the fluid velocity $\mathbf{u}$ in x and z direction respectively. The waves are considered to propagate in the x-direction only, and the coordinate system is chosen as in figure 2.1. Using the incompressible form of the continuity equation (2.13)

$$\nabla \mathbf{u} = \frac{\partial u}{\partial x} + \frac{\partial w}{\partial z} = 0, \tag{2.27}$$

and substituting (2.26) into (2.27) yields the Laplace equation

$$\Delta \Phi = \frac{\partial^2 \Phi}{\partial x^2} + \frac{\partial^2 \Phi}{\partial z^2} = 0. \tag{2.28}$$

The crucial ingredients for the solution of the Laplace equation at the free surface are the boundary conditions. The velocity potential is subject to the *kinematic boundary conditions* that the vertical velocity component vanishes at the bottom (2.29) and that the fluid particles at the surface never leave the surface (2.30)

$$\frac{\partial \Phi}{\partial z} = 0 \qquad \text{at} \quad z = -H \tag{2.29}$$

$$\frac{\partial \Phi}{\partial z} = \frac{\partial \eta}{\partial t} \qquad \text{at} \quad z = \eta \approx 0. \tag{2.30}$$

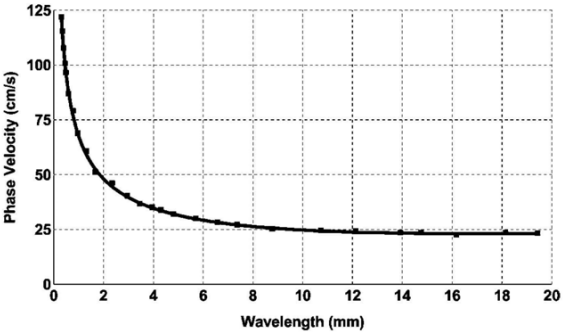

Figure 2.2.: Measured phase velocity in the capillary wave range from Behroozi and Perkins [13] for pure water at 20° C. The solid line is the theoretical phase velocity (2.35), using the surface tension value of $(72.8 \pm 0.1) \cdot 10^{-5}$ N/cm. The measurements were performed using laser interferometry on standing capillary waves that were generated in a small basin.

For the surface displacement we assume a single sinusoidal wave

$$\eta = a\cos(kx - \omega t). \tag{2.31}$$

This is motivated by the idea that we can decompose any small disturbance into sinusoidal components by Fourier analysis. The solution for the velocity potential is then

$$\Phi = \frac{a\omega}{k}\frac{\cosh k(z+H)}{\sinh kH}\sin(kx - \omega t), \tag{2.32}$$

which is derived in detail in most text books on fluid mechanics, e.g. [102, 129]. The relation between ω and k is now dictated by another boundary condition, the *dynamic boundary condition*. This is, that the pressure just below the free surface is always equal to the ambient pressure. Therefore the velocity potential must fulfill the Bernoulli equation (2.25). The Bernoulli equation can be linearized under the assumption off small amplitudes, small slopes and irrotational flow, which allows an evaluation at $z = 0$ instead of $z = \eta$. The dynamic boundary condition is then

$$\frac{\partial \Phi}{\partial t} = \frac{\sigma}{\rho}\frac{\partial^2 \eta}{\partial x^2} - g\eta \qquad \text{at} \quad z = 0, \tag{2.33}$$

where the first term on the right hand side reflects the pressure change due to the surface tension σ and the second term is due to the 'hydrostatic' pressure [102, chapter 7. 7]. The dispersion relation is to be found by inserting the respective derivatives of (2.31) and (2.32) in the dynamic boundary condition (2.33)

$$\omega = \sqrt{kg\left(1 + \frac{\sigma}{\rho g}k^2\right)\tanh kH}. \tag{2.34}$$

For the phase velocity $c = \frac{\omega}{k}$ follows

$$c = \sqrt{\left(\frac{g}{k} + \frac{\sigma}{\rho}k\right)\tanh kH}. \tag{2.35}$$

This result is in excellent agreement with measurements on monochromatic small amplitude waves, see figure 2.2. However, for a wind-wave field the situation is more complex and the validity of the linear dispersion relation is not guaranteed since finite amplitude effects and nonlinear interaction between waves may become important. Moreover, even if the phase velocity of a freely propagating wave is well described by equation (2.35), the phase speed, measured in a fixed frame of reference, may be influenced by Doppler shifts due to an underlying mean current or the

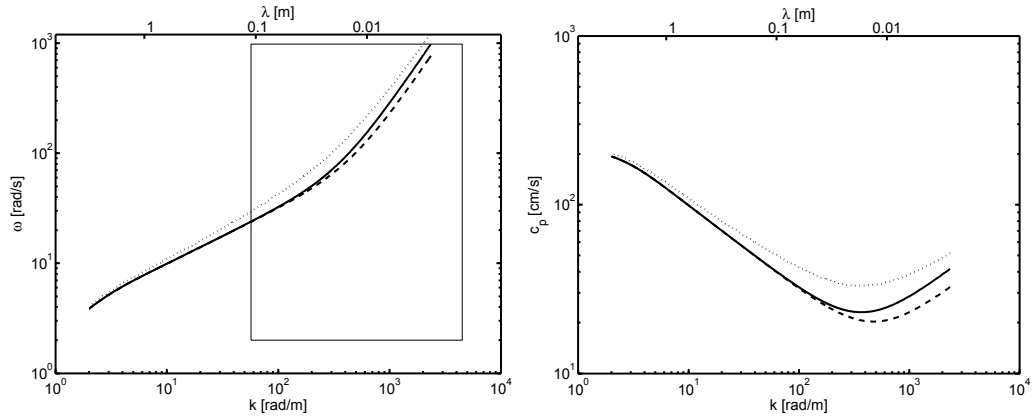

Figure 2.3.: Frequency $\omega(k)$ (left) and phase velocity $c(k)$ (right) of water waves.

orbital modulation of a longer wave [108, 155, 170]. Additionally, the surface tension can not always be treated as a known constant. This is because even slight contaminations of the water air interface with surface active materials can lead to rigorous changes in the surface tension, which consequently changes the dispersion of the capillary waves [4, 19, 159].

The dispersion relation (2.34) and the phase velocity (2.35) for waves on a clean water surface are shown in figure 2.3 as a solid line. The dashed line depicts a reduction of the surface tension to 60% of the value for the clean case, e.g. caused by a monolayer surface slick. The dotted line exemplifies the influence of a surface drift current of $U = 10\,\text{cm/s}$, leading to a Doppler shift $\omega_d = k \cdot U$, which adds to the linear dispersion relation[2]. The wavenumber and frequency range that is relevant for this study is marked by a rectangle in the left plot. We can see that in both cases the dispersion relation for the small scale waves is significantly altered. The minimum of the phase speed, that is observed for the clean surface at a wavenumber $k = 369\,\text{rad/m}$ ($\lambda = 1.7\,\text{cm}$), is shifted towards greater wavenumbers in the presence of a surface slick.

2.2.2. Dispersion Relation for Finite Amplitude Waves

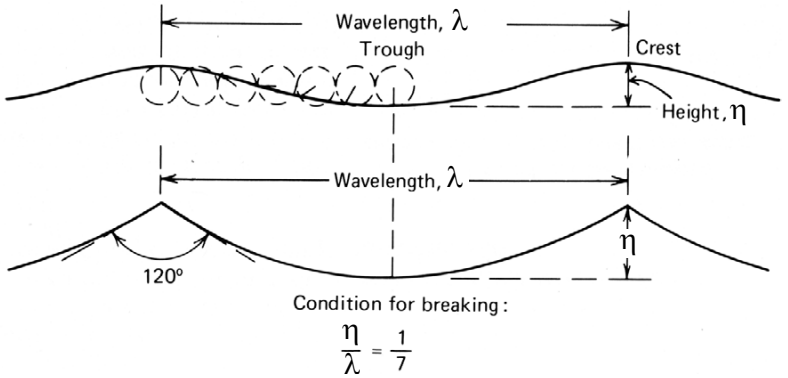

Figure 2.4.: Sketch of different wave forms. Top: sinusoidal small amplitude wave. Bottom: Stoke's limiting profile of an finite amplitude wave. (modified after Gross [57])

Since deep water waves are dispersive an accumulation of nonlinear effects is usually prevented, which limits the growth in amplitude. This is because the different Fourier components propagate at different speeds and become separated from each other. However, nonlinear steepening can

[2]Note, for this 1D example we have assumed that the surface drift current is in alignement with the wavenumber vector, whereas in general we have to consider the vector product $\mathbf{k} \cdot \mathbf{U}$ for the Doppler shift contribution.

cancel out the dispersive spreading, resulting in finite amplitude waves of unchanging form, as argued by Kundu [102]. There exist a few analytic solutions for the dispersion relation of finite amplitude waves. We will briefly mention two solutions: the *Stoke's waves*, which are pure gravity waves of unchanging form, and the *Crapper waves*, which represent a special solution for steep capillary waves. A comprehensive deduction can be found for instance in Kinsmann [90]. An instructive review about nonlinear gravity and capillary-gravity waves and interaction is given by Dias and Kharif [38].

Stoke's Waves: Stokes [153] showed that a solution for the surface elevation of pure gravity waves in deep water and irrotational flow can be given by a Fourier series

$$\eta = a\cos\left(k\left(x-ct\right)\right) + \frac{1}{2}ka^2\cos\left(2k\left(x-ct\right)\right) + \frac{3}{8}k^2a^3\cos\left(3k\left(x-ct\right)\right) + \ldots, \tag{2.36}$$

where the phase speed is given by

$$c = \sqrt{\frac{g}{k}\left(1+k^2a^2\right)}, \tag{2.37}$$

where a is the amplitude [90, 102]. These waves are no longer sinusoidal, i.e. they have a flattened trough and a peaked crest. The amplitude is limited with a maximum possible value of $a_{max} = 0.07\lambda$, for which the crest exhibits an angle of 120^o [102]. In this limiting case, the wave form can be approximated by the arc of a circle, see figure 2.4, and the orbital motion of particles at the surface can be approximated by a superposition of an uniform translation and the backward swing of a pendulum, see Longuet-Higgins [112].

Crapper Waves: Crapper [34] showed that for pure capillary waves of finite amplitude an analytic solution exists, which gives the phase speed as a function of the wave steepness $2\pi\delta = k\,a$,

$$c = \sqrt{\frac{\sigma k}{\rho}\left(1+\frac{\pi^2\delta^2}{4}\right)^{-1/2}}, \tag{2.38}$$

so that the effect of wave steepness is to slow down the capillary waves, in contrast to the situation of finite amplitude gravity waves [90]. Here, a is the maximum value of the surface elevation for the corresponding wave number k.

2.2.3. Short-Gravity Capillary Waves

The linear dispersion relation (2.34) was derived in the preceding section without explicitly distinguishing gravity waves from capillary waves. Generally speaking, *gravity waves* are big enough not to be significantly affected by the surface tension so that their restoring force is solely due to gravity. In contrast, the restoring force for *capillary wave*s is predominantly due to the surface tension [102].

Both restoring forces are equally important in the vicinity of $\lambda = 1.7$ cm, where the phase speed attains its minimum (see figure 2.3 (right)). For that we call waves in the range between a few decimeters down to several millimeters wavelength *short-gravity capillary waves*. Because of its importance for the air-sea interaction we are particularly interested in this regime.

Furthermore, one can distinguish *deep water waves* from *shallow water waves*. For deep water waves we have $kH \gg 1$ so that $\tanh(kH) \approx 1$ and it is convenient to restrict the following discussion to the deep water case, which is an appropriate approximation throughout this study.

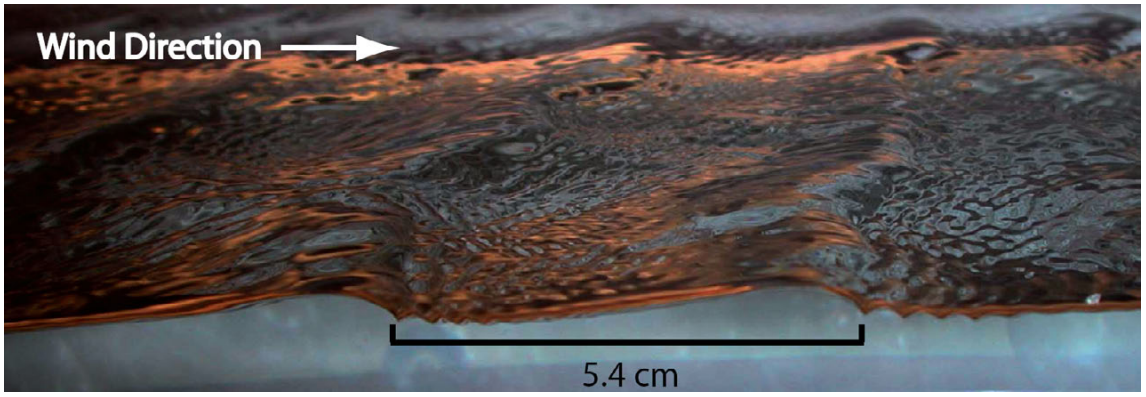

Figure 2.5.: Fetch 2.4 m; wind speed 6 m/s; modified after Huhn [70]

The dispersion relation for deep water gravity waves follows from the linear dispersion relation (2.34) as

$$\omega^2 = gk \qquad \text{for} \qquad \frac{\sigma}{\rho g}k^2 \ll 1 \qquad \text{and} \qquad kH \gg 1. \tag{2.39}$$

For deep water short gravity capillary waves we yield

$$\omega^2 = gk + \frac{\sigma}{\rho}k^3 \qquad \text{for} \qquad kH \gg 1, \tag{2.40}$$

and accordingly for pure capillaries we have

$$\omega^2 = \frac{\sigma}{\rho}k^3 \qquad \text{for} \qquad \frac{\sigma}{\rho g}k^2 \gg 1 \qquad \text{and} \qquad kH \gg 1, \tag{2.41}$$

Figure 2.5 shows a typical example for how wind driven short gravity capillary waves look like. In front of the short gravity wave ($\lambda \approx 5.4\,\text{cm}$) we can observe capillary waves that are bound to the longer wave and therefore called *parasitic capillary waves*. The denotation *parasitic* indicates that these waves extract energy from the short gravity wave, rather than being directly generated by the wind [99].

Since the parasitic capillaries (k, ω) are stationary with respect to the short gravity wave (K), their frequency - measured in a frame of reference moving with the phase speed $C = \omega(K)/K$ of the short gravity wave - is zero

$$\omega - k\,C = 0. \tag{2.42}$$

Using the dispersion relations (2.39) for the short gravity wave and (2.41) for the capillary waves, we obtain

$$k = \frac{\rho g}{\sigma K}, \tag{2.43}$$

which is the approximate relationship between the wavenumbers of the dominant wave (K) and its parasitic capillary waves (k) propagating at the same phase speed [99].

The photograph from figure 2.5 was taken at very short fetch[3]. Further characteristic examples for the wave field at somewhat longer fetch and higher wind speeds are given in figure 2.6. The most energetic waves, i.e. the short gravity waves with the largest wavelength, are called *dominant waves*. Figure 2.6 gives an impression of the evolution of the wave field and the dominant waves scales for different wind speeds. A systematic description of the three dimensional evolution of wind waves in the short-gravity capillary range can be found in Caulliez and Collard [28].

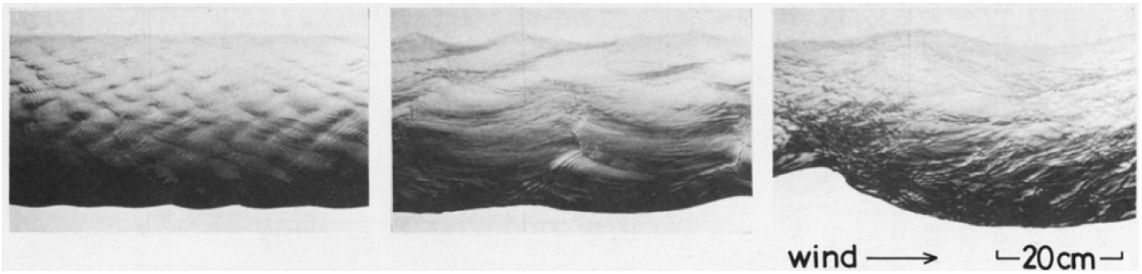

Figure 2.6.: Characteristic photographs of short gravity-capillary waves in a wind wave tank at a fetch of 10.65 m. left: $u_{ref} = 3.6$ m/s; middle: $u_{ref} = 7.6$ m/s; right: $u_{ref} = 13.6$ m/s; (adopted from Ebuchi et al. [43])

Symbol	Meaning	Physical Unit
$\mathbf{x}$	horizontal position vector (2d)	m
t	time	s
$\mathbf{k}$	wavenumber vector (2d)	rad/m
ω	angular frequency	rad/s
$\eta(\mathbf{x}, t)$	water surface elevation	m
$\hat{\eta}(\mathbf{k}, \omega)$	complex amplitude function for η	m^3 s
$R(\mathbf{r}, \tau)$	autocorrelation of η	m^2
$X(\mathbf{k}, \omega)$	energy density spectrum	m^4s
$\Psi(\mathbf{k})$	wavenumber energy density spectrum	m^4
$\Phi(\omega)$	frequency energy density spectrum	m^2s
$\mathbf{r}$	position shift (2d)	m
τ	time shift	s
$B(\mathbf{k})$	saturation spectrum	-

Table 2.2.: Nomenclature

2.3. Spectral Description of the Wave Field

To say it in the words of Phillips [132, Chapter 4.1, page 72]: "*The waves found on the surface of the sea are almost always random in the sense that the detailed configuration of the surface varies in an irregular manner in both space and time. Only the various statistical measures of the motion can be regarded as significant observationally or predictable theoretically*."

The conventions and concepts for the spectral and statistical description of the wavy water surface are based on definitions by Phillips [132], Pierson and Stacy [136], Longuet-Higgins [111], and Donelan et al. [39]. In section 2.3.1 we present the fundamental concepts and definitions, followed by a brief introduction of the *saturation spectrum*, in section section 2.3.2. Later, in section 6.7 we will elaborate on the link between the conventional continuous representations of the spectra and the discrete counterparts that are actually measured.

2.3.1. Basic Concepts

The water surface elevation $\eta(\mathbf{x}, t)$ is conventionally measured as the displacement from the mean free surface level, so that the expectation value is zero. For the specification of the wave field, higher moments are of central importance [111].

[3] fetch: distance over which wind acts on the water surface.

Consider the autocorrelation of the surface displacement

$$R(\mathbf{r},\tau) = \overline{\eta(\mathbf{x},t)\eta(\mathbf{x}+\mathbf{r},t+\tau)} \tag{2.44}$$

$$= \lim_{T\to\infty}\lim_{X\to\infty}\lim_{Y\to\infty}\frac{1}{TXY}\int_0^T\int_0^X\int_0^Y \eta(\mathbf{x},t)\eta(\mathbf{x}+\mathbf{r},t+\tau)d\mathbf{x}dt, \tag{2.45}$$

which is independent of the location and time for a *homogeneous* and *stationary* wave field. We call the wave field homogeneous, if the instantaneous covariance $R(\mathbf{r},\tau=0)$ is an even function of the position shift $\mathbf{r}$. The wave field is called stationary, if the covariance at a fixed point $R(\mathbf{r}=0,\tau)$ is an even function of the time shift τ.

The wave *energy density spectrum* is defined as the Fourier transform of the autocorrelation

$$X(\mathbf{k},\omega) \equiv \frac{1}{(2\pi)^3}\iiint R(\mathbf{r},\tau)e^{-\mathrm{i}(\mathbf{kr}-\omega\tau)}d\mathbf{r}d\tau. \tag{2.46}$$

Reversely we rewrite the autocorrelation by the inverse Fourier transform of the wave energy density spectrum

$$R(\mathbf{r},\tau) \equiv \iiint X(\mathbf{k},\omega)e^{\mathrm{i}(\mathbf{kr}-\omega\tau)}d\mathbf{k}d\omega. \tag{2.47}$$

The variance of the surface elevation is given by

$$\overline{\eta^2} = \iiint X(\mathbf{k},\omega)d\mathbf{k}d\omega, \tag{2.48}$$

which is easy to see by setting $\mathbf{r}$ and τ in (2.47) and (2.44) to zero. The energy of waves in the small wavenumber range is proportional to the variance of the surface elevation [102]. This explains why $X(\mathbf{k},\omega)$ is interpreted as the energy density contribution per unit volume in wavenumber frequency space. We can obtain reduced spectra from the energy density spectrum by integrating over wavenumbers or frequencies. The *wavenumber energy spectrum* and the *frequency energy spectrum* are

$$\Psi(\mathbf{k}) = \int X(\mathbf{k},\omega)d\omega, \tag{2.49}$$

and

$$\Phi(\omega) = \iint X(\mathbf{k},\omega)d\mathbf{k}, \tag{2.50}$$

respectively. For instance, frequency energy spectra are typically obtained, when capacitance wires are used to measure the surface elevation at a single point. Wavenumber energy spectra can be retrieved from surface imaging even if the temporal resolution is low and does not allow to resolve the frequencies. For the measurement of the frequency-wavenumber spectrum X higher temporal sampling rates are desired that were, until recently, not achievable with imaging techniques.

Using the new slope imaging technique we obtain discrete 3D slope spectra, presented in the sections 7.2 and 7.3. In section 6.7.1 we will explicitly show, how these discrete spectra are related to the conceptual definitions that were given here.

2.3.2. The Saturation Spectrum

The wavenumber spectrum is often presented in form of the dimensionless *saturation spectrum* $B(\mathbf{k})$, which is defined as

$$B(\mathbf{k}) = k^4\,\Psi(\mathbf{k}). \tag{2.51}$$

This quantity also called the *degree of saturation*[4] because in the pioneering work Phillips [131] assumed B to be only a function of the direction of waves relative to the wind, once that an equilibrium of the spectral energy fluxes for the wave-field is established. Based on purely dimensional grounds Phillips [131] argued that the wavenumber spectrum in the gravity-wave range must be of the form

$$\Psi(\mathbf{k}) \propto f(\Theta) k^{-4}, \tag{2.52}$$

where k is the norm of the wavenumber vector $\mathbf{k}$, $f(\Theta)$ is an angular spreading function and Θ is the angle between the wind and the wavenumber vector. The idea was that any excursion of the spectral density above $B(\mathbf{k})$ would be relieved immediately by wave breaking. Although the concept of the saturation spectrum as an upper limit asymptote to the spectrum, independent of wind stress, turned out not to be tenable, the representation of wind wave spectra in this form is very convenient. One practical aspect is that multiplication with k^4 leads to an considerable reduction of the dynamical range of the spectra.

Wavenumber Dependency: There exist several models for gravity waves predicting the shape of the saturation spectrum. Phillips [130] obtained

$$B(\mathbf{k}) = \frac{\beta}{\sqrt{g}} f(\theta)\, u_*\, k^{1/2}, \tag{2.53}$$

for *wavenumbers large compared with that of the dominant wave*[5] from a local balance of the spectral flux due to (i) exchange among different wave groups by nonlinear interactions, (ii) input from the turbulent wind field and (iii) dissipation by wave-breaking, assuming that these fluxes are of equal importance. In (2.53) β is an empirical scaling factor (see [130] for a discussion about the constraints on the empirical constants). The $k^{1/2}$ dependency is also found by Kitaigorodskii [91] using the hypothesis of a general similarity in the spatial statistical characteristics for the wavenumbers well below those associated with capillary ripples and those directly influenced by viscosity. His idea was that the energy of the wind input to the wave field primarily occurs at large scales and is then followed by a Kolmogoroff-type energy cascade to smaller scales where finally the energy is dissipated. The first systematic measurements of two dimensional saturation spectra in the short gravity-capillary range, performed in the Delft wind wave facility by Jähne and Riemer [84] using an *imaging slope gauge* (see section 3), revealed that the $k^{1/2}$ is approximately valid for high wind speeds even for wavenumbers up to $k = 200$ rad/m, see figure 2.7. For low wind speeds the degree of saturation showed a strong decrease from the small energy containing wavenumbers towards higher wavenumbers. In the wavenumber range of about 200-800 rad/m a plateau in the degree of saturation was reached. For wavenumbers $k > 800$ rad/m a strong decrease in the spectral energy was found by Jähne and Riemer [84] that is referred to as the *spectral cutoff*. The early appearance of this cutoff is in contrast to the assumption that the cutoff is determined by a balance between the wind input and viscous dissipation, which is expected to set in at 6283 rad/m by Apel [8]. Later measurements by Klinke [93] and Zhang [177] confirmed a spectral cutoff at a somewhat higher wavenumbers of about 1000-1200 rad/m. The cutoff was therefore adapted as a characteristic feature of the wind wave spectra for the attempts to construct a unified spectral model for the long and short waves by Apel [8] and Elfouhaily et al. [44] which are widely used for inverse modeling and interpretation of scatterometer and altimeter data (e.g. [49, 114]). From a comparison of modeled saturation spectra by Pierson and Moskowitz [135], Apel [8], Romeiser et al. [144], and Elfouhaily et al. [44] one can see that the models differ significantly while all

[4] Another name for the saturation spectrum is *curvature spectrum*, because $k^4\, \Psi(\mathbf{k})$ is related to the second derivative of the surface elevation.

[5] but still in the gravity wave range

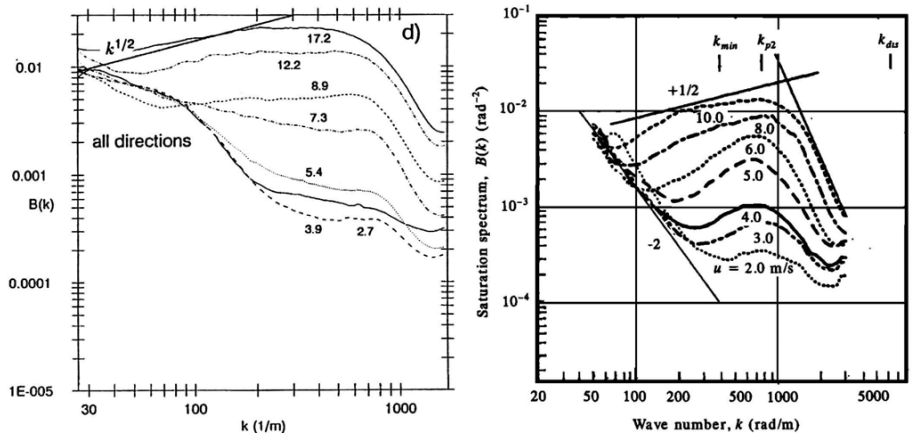

Figure 2.7.: Measured omnidirectional saturation spectrum integrated over all wave directions. wind speeds (u_{10} in m/s) as indicated; left: from Jähne and Riemer [84]; fetch 100 m. right: adopted from Apel [8], measurements performed in the Marseille facility by Klinke and Jaehne (1992), fetch 24 m.

models implement a spectral cutoff around 1000 rad/m, as shown in figure 2.8. However, the former measurements in the high wavenumber range are influenced by the Modulation Transfer Function (section 2.5.2) of the optical system which has been only vaguely accounted for [84]. A similar limitation also occurs for measurements with a laser slope gauge, where the diameter of the laser beam limits the spatial resolution, so that even from frequency spectra no definitive conclusion about the cutoff can be drawn [106, 159]. Note, that this statement is in contradiction to the discussion of the cutoff at high wavenumbers that is given in the book by Jones and Toba [88]. In chapter 7 we show experimental results that encourage a reexamination of this issue.

Angular Spreading: The directionality of the saturation spectra with respect to the wind direction, expressed by spreading function $f(\theta)$ in (2.52), strongly depends on the fetch and wave age (c/u_*). Klinke [93] found that in the short gravity capillary wave range at infinite fetch the spreading is multimodal at low wind speeds and unimodal at high wind speeds. In case of laboratory measurements the angular spreading also depends strongly on the geometry of the wind wave facility. Therefore Klinke [93] concludes: *"The significant variations of the angular spreading in different laboratory data indicates that the oceanic angular dispersion should not be modeled using wind wave tunnel data"*. There are very few reliable measurements of the spreading function for high wavenumbers from the open ocean. Most measurements were performed using an array of laser slope gauges or amplitude wires and are restricted to long waves due to the spatial separation of the probes (e.g. for Donelan et al. [39]: $k < 3.14$ rad/m). For their unified spreading function Elfouhaily et al. [44] assumed that long waves are aligned with the mean wind direction in steady conditions and that shorter waves are more dispersive. From radar observations they conclude that short-gravity waves lose their directionality while gravity-capillary waves become more directional, for details see [44]. Several alternative parametric forms of the spreading function have been proposed in the literature. Prominent examples are the $\cos^p(\Theta)$-form ($p \in \mathbb{N}$) [11, 27, 122, 137] or a sech^2-form proposed by Donelan et al. [39] and extended by Kukulka and Hara [101]. The angular distribution of the saturation spectrum in the gravity-capillary range is of special interest in the light of the resonant condition for wave-wave interaction. If the spread is narrow, the lowest order for wave-wave interaction is that of quartets [63, 130]. At high wind speeds, when the distribution of the short waves is broad also triad interaction can occur and become dominant over the quartet interaction [108, 177].

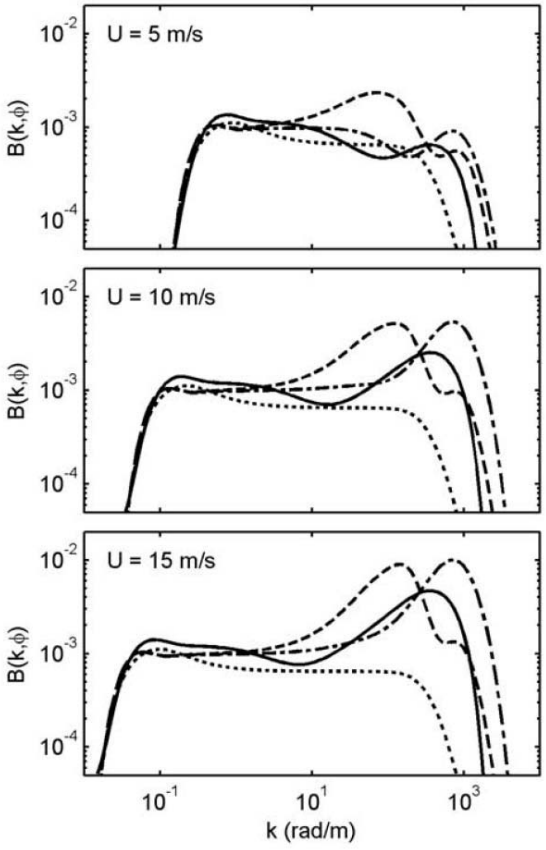

Figure 2.8.: Comparison of spectral models of Pierson and Moskowitz [135] (dotted line), Apel [8] (dash-dotted line), Romeiser et al. [144] (dashed line), and Elfouhaily et al. [44] (solid line) in wind direction, for wind speeds of 5, 10, and 15 m/s. The first three spectra have been symmetrized with respect to the wind direction for comparison with the Elfouhaily et al. spectrum, which is inherently symmetrical. (Adopted from Lyzenga [114])

2.4. Wind-Wave Interaction

The coupling between the wave field and the vertical momentum flux from the wind is (for instance) described by the *Wind-Over-Waves Coupling* model (WOWC) in terms of the saturation spectrum, the dispersion relation, and the wind profile. The WOWC model was developed by Makin et al. and Kuduryavtsev et al. [97–100, 117, 118] for the open sea. Recently this model was also applied to laboratory wave fields by Makin et al. [115] and Caulliez et al. [30]. In section 2.4.1 a concise description of the model is given which essentially follows Makin et al. [115].

The vertical momentum flux from the wind is commonly characterized by the friction velocity u_*, which is related to the mean total stress $\tau_0 = \rho\overline{u'_x\, u'_z}$ according to [102]

$$u_* = \sqrt{\frac{\tau_0}{\rho}}. \tag{2.54}$$

If u_* is measured far away from the surface then the wave-induced stress components can be neglected. In most situations the wind profile $U(z)$ is assumed to be logarithmic, and u_* can be calculated from the profile

$$U(z) = \frac{u_*}{\kappa} \ln \frac{z}{z_0}, \tag{2.55}$$

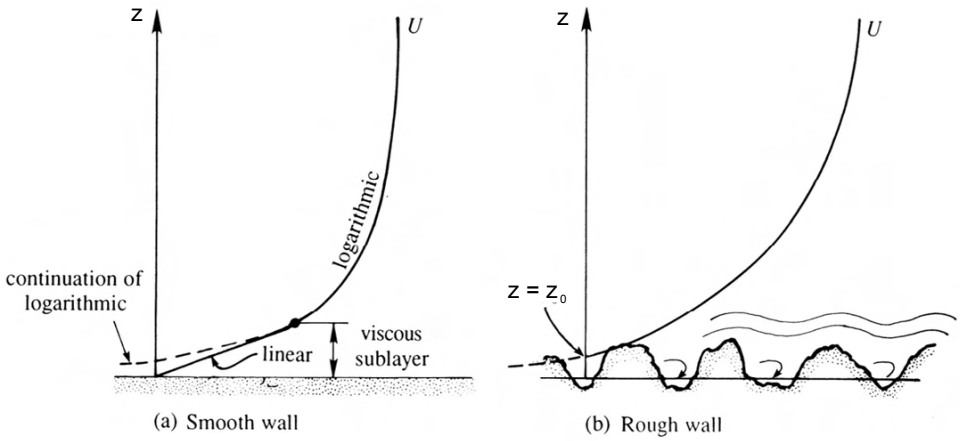

Figure 2.9.: Logarithmic velocity distributions near a smooth and a rough surface. (modified after [102])

where z_0 is the roughness length and $\kappa = 0.41$ is the Von Karman constant. The roughness length z_0 is the height where the logarithmic profile over a rough surfaces gives $U = 0$, see figure 2.9.

2.4.1. Wind-Over-Waves Coupling Model

The WOWC model is based on the conservation for the integral momentum

$$u_*^2 = \tau^\nu + \overline{p\frac{\partial \eta}{\partial x}}, \tag{2.56}$$

where τ^ν is the viscous surface stress, and $\tau^f = \overline{p\frac{\partial \eta}{\partial x}}$ is the form drag of the water surface. In this section the stress components are normalized by the density of air ρ_a. The form drag of the water surface is a correlation of the pressure field with the wave slope in the along wind direction which is here aligned to the x-direction

$$\tau^f = \overline{p\frac{\partial \eta}{\partial x}} = \overline{ps_x}. \tag{2.57}$$

This term is always dominant over the viscous stress, except for very low wind speeds [116]. In the WOWC model the water surface is described for stationary and spatial homogeneous conditions in terms of the saturation spectrum $B(\mathbf{k})$ which is introduced in section 2.3. The spectrum is assumed to be symmetric around the mean wind direction. The mean wind direction is again assumed to coincide with the mean direction of wave propagation. The form drag (2.57) can be related to geometrical properties of the surface and to the properties of the energy exchange between the waves and the wind. This means, that the stress at the water surface is directly coupled to the sea state which is described by the wave spectrum.

The wave-wind coupling is different if large-scale wave-breaking occurs or not. This is reflected in different contributions to the model for the form drag $\tau^f = \tau_w^f + \tau_s^f$ which are described in the following sections.

Non-Separated Sheltering Mechanism

In case of a regular wavy surface (no large-scale wave-breaking) the energy flux from the wind to the waves is described by the so called *non-separated sheltering mechanism* [32]. The corresponding wave-induced stress is denoted by τ_w^f. The stress supported by microscale breaking waves is also included in τ_w^f, as long as no airflow separation exists, i.e. the surface is streamlined. The

WOWC model expresses the wave-induced stress as

$$\tau_w^f = \int\int \beta(k,\Theta) c^2 B(k,\Theta) \cos\Theta \; d\ln k \; d\Theta, \tag{2.58}$$

were $B(k,\Theta)$ is log-polar representation of the saturation spectrum (section 2.3), and $c = c(k)$ is the phase speed of the wave component. The dimensionless energy flux to waves, denoted by β, can be parametrized by means of the wind profile and the roughness length of the surface [116, 122, 152]

$$\beta = C_\beta \left(\frac{u_*}{c}\right)^2 \cos^2\theta, \tag{2.59}$$

where θ is the angle enclosed by the mean wind direction and the direction of the wave vector. The proportionality coefficient C_β in (2.59) takes into account, that the growth rate for fast traveling waves reduces to zero. It can be expressed as [30]

$$C_\beta = \frac{c_\beta}{\kappa} \ln \frac{\pi}{k z_c}, \tag{2.60}$$

where $c_\beta \approx 1.5$ is an empirical constant [116] and z_c is the height of the critical layer, where $U(z_c) = c$ so that the relative velocity between the wind and the waves vanishes.

We can summarize (2.58) to (2.60): the wave-induced stress due to the non-separated sheltering mechanism τ_w^f can be computed with the knowledge of a) the saturation spectrum $B(k,\theta)$, b) the phase speed of the waves $c(\mathbf{k})$, and c) the wind profile above the water surface $U(z)$.

Air-Flow Separation Mechanism

In case of large-scale breaking waves a significant augmentation of the local stress occurs [10]. This is explained by the *airflow separation* (AFS) which emerges at the crest of the breaking waves. The WOWC model splits the contribution to the form drag by airflow separation τ_s^f in two parts,

$$\tau_s^f = \tau_{s_{eq}}^f + \tau_{s_d}^f, \tag{2.61}$$

where $\tau_{s_{eq}}^f$ is the stress supported by the AFS from the equilibrium range of short gravity waves, and $\tau_{s_d}^f$ is supported by the AFS according to dominant wind waves.

For the equilibrium range the form drag is modeled as

$$\tau_{s_{eq}}^f = \frac{\epsilon_b \gamma}{b} \int_\theta \int_{k<k_b} u_s^2 \beta(k,\theta) B(k,\theta) \cos\theta \; d\ln k \; d\Theta. \tag{2.62}$$

The empirical constants are the characteristic slope of the breaking wave $\epsilon_b = 0.5$ and $b = 0.01$, see Makin et al. [115]. Recently the empirical value for ϵ_b was refined as 0.62 in the study of Caulliez et al. [30]. The integration is only carried out over the low wavenumber range $k < k_b \approx \frac{2\pi}{0.3\,\mathrm{m}}$, because shorter waves rather generate parasitic capillaries than break [99]. The pressure drop which is induced by the air flow separation is represented by $\Delta p = \frac{1}{2}\gamma u_s^2$, where $\gamma \approx 1$ is an empirical constant [30]. The co-moving reference wind speed u_s is taken as the mean wind speed at the characteristic height of the breaking wave $z_b = 1/k$ in a reference frame that is attached to the breaking wave with the phase velocity c

$$u_s = U(z_b)\cos\theta - c. \tag{2.63}$$

The co-moving reference wind speed is additionally restricted with $\mathtt{min}(u_s) \geq 0$, so that there is no negative contribution by waves that are actually traveling faster than the wind.

The contribution to the form drag by dominant waves is modeled as

$$\tau_{s_d}^f = \frac{\epsilon_b \gamma}{2\pi} u_{sd}^2 \exp\left(-\frac{\epsilon_T^2}{\epsilon_d^2}\right), \tag{2.64}$$

with

$$u_s = U(z_d) - c(k_p), \tag{2.65}$$

where $z_d = \epsilon_b / k_p$ is the level just above the breaking dominant wave, which is defined as the wave corresponding to the spectral peak k_p. In (2.64) ϵ_d is the dominant wave steepness, and ϵ_T is a threshold steepness (tuning constant, see also Makin et al. [115] and Caulliez et al. [30]).

Viscous stress

Inside the viscous sublayer the wind profile is linear, see figure 2.9. The thickness of viscous sublayer δ is given by

$$\delta = d\frac{\nu}{u_*}, \tag{2.66}$$

where ν is the kinematic viscosity ($\nu \approx 18\,\text{Pa s}$, at sea level for air and T=291K) and $d = 20$ is a constant. E.g. for $u_* = 0.5\,\text{m/s}$ delta is about $0.3\,\text{mm}$. The viscous stress is obtained by matching the linear profile with the logarithmic profile above it, which yields

$$\tau^\nu = (\kappa d)^{-1} \frac{\delta}{z_0} u_*^2, \tag{2.67}$$

where z_0 is the roughness parameter from equation (2.55).

Total resistance of the water surface

Finally, the total resistance of the sea surface can be written as

$$u_*^2 = \tau^\nu + \tau_w^f + \tau_{s_{eq}}^f + \tau_{s_d}^f, \tag{2.68}$$

which relates the wind stress to the properties of the wave field.

2.5. Digital Imaging Background

Digital imaging has a huge impact on the techniques for the experimental investigation of small-scale air-sea interactions. Using digital cameras for measurements allows for quantitative and multidimensional investigations even at small scales at the wavy water surface, where conventional intrusive probes are no longer applicable.

In the following sections we will briefly introduce some issues of digital imaging that are essential in the context of this study. In section 2.5.1 we consider the spatiotemporal discrete sampling and its implications for the structure of the spectra, with emphasis on the understanding of the aliasing effect.

The section 2.5.2 deals with the contrast damping in the image formation and image processing steps, which is described by the Modulation Transfer Function.

Our method applies color imaging, i.e. the color in each pixel of the image delivers information about the water surface gradient. Even though nowadays almost everyone has a single chip digital camera that makes beautiful color images, in the context of this study it is not enough to regard the color imaging as a process in a black box. Therefore a typical concept of color interpolation is introduced in section 2.5.3, which is used with slight modifications also for the data processing in section 6.1.

Using standard digital image processing operations, we can reconstruct the surface elevation from the gradient field. One approach for the reconstruction is introduced in section 2.5.4 which provides the basis for section 7.5.

2.5.1. Spatiotemporal Sampling

An image sequence is basically a 3D array of numbers $g_{m,n,o}$ that are commonly called gray values. Let m and n denote the indices of the individual sensor elements or respectively the spatial coordinates, and let o be the frame index of the sequence which corresponds to the temporal scale. The sensor elements (or *pixel*) are typically arranged on a regular rectangular grid. For convenience we assume that the grid spacing δx is the same in both spatial directions[6]. If the sensor has M times N elements, and the reproduction scale of the optics is β [mm/pixel], then we get the field of view $X \cdot Y$ according to

$$\begin{aligned} X &= M\Delta x \\ Y &= N\Delta x, \end{aligned} \tag{2.69}$$

where we have used the abbreviation $\Delta x \equiv \beta \cdot \delta x$ for the real world length that corresponds to the edge length of one pixel. For the timespan of the sequence with O images we likewise have

$$T = O\Delta t, \tag{2.70}$$

where Δt is the time interval between two consecutive images. In general, the discrete spatial coordinates are given $\mathbf{r}_{m,n} = [m, n]^T \cdot \Delta x$ and the discrete time is $t_o = o \cdot \Delta t$.

Due to the limited field of view we loose information about variations that have bigger spatial scales than X and Y in the respective directions. The finite timespan causes a loss of information about temporal variations on longer time scales than T. Information loss means that the original form of the continuous signal can no longer be exactly reconstructed from the image sequence.

Conversely, the smallest spatial and temporal variations in the continuous signal that can be exactly reconstructed are given by the Sampling theorem. The Sampling theorem basically says

[6] Most modern CCDs are having square pixels ($\delta x = \delta y$), whereas in the past one occasionally had to deal with differing grid spacing ($\delta x \neq \delta y$).

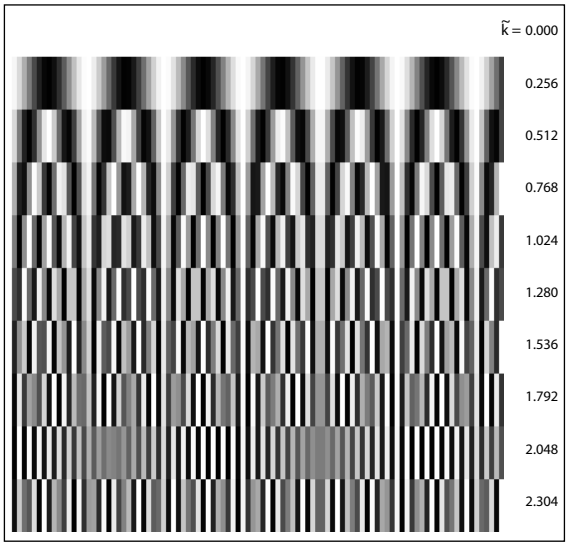

Figure 2.10.: Moirè effects occur if the wavelength of the structure λ is smaller than the minimal wavelength λ_{min} which is given by the Sampling Theorem. For the illustration $\tilde{k} = \frac{\lambda_{min}}{\lambda}$ is varied from top to bottom as indicated. For $\tilde{k} > 1$ the Sampling Theorem is no longer fulfilled, which leads to an incorrect reproduction of the structure in the discrete image.

that we need at least 2 discrete sampling points per wavelength of the continuous signal [77]

$$\lambda_{min} = 2\Delta x \tag{2.71}$$
$$\tau_{min} = 2\Delta t. \tag{2.72}$$

where λ stands for the wavelength of spatial variations and τ is the period of temporal variations.

If the observed scene contains structures that are smaller than λ_{min} then artifacts are introduced that are know as *Moiré effects*, see illustration in figure 2.10. The fine structures appear with incorrect wavelengths, and - in 2D - even under different directions [77]. The same kind of problem occurs if temporal changes a the scene exhibit a shorter time scale than τ_{min}. The corresponding artifacts are called *aliasing*, in order to be able to distinguish between the cause of the artifacts. The aliasing is discussed in more detail on page 27.

Wavenumber Frequency Domain

The image sequence can be transformed into a discrete 3D wavenumber frequency spectrum $\hat{g}_{u,v,w}$ according to

$$\hat{g}_{u,v,w} = \sum_{m=0}^{M-1} \sum_{n=0}^{N-1} \sum_{o=0}^{O-1} g_{m,n,o}\, \mathrm{w}_M^{-mu}\, \mathrm{w}_N^{-nv}\, \mathrm{w}_O^{ow}, \tag{2.73}$$

which is the Discrete Fourier Transform (DFT) of the sequence, where we have used an abbreviation for the discrete Fourier kernel $\mathrm{w}_Q \equiv \exp(2\pi\,\mathrm{i}\,/Q)$ [77]. Here, the indices u and v in the spectral domain are corresponding to the discrete wavenumber vector

$$k_{u,v} = \begin{bmatrix} u/M \\ v/N \end{bmatrix} \cdot \frac{2\pi}{\Delta x} = \begin{bmatrix} u/X \\ v/Y \end{bmatrix} \cdot 2\pi, \tag{2.74}$$

and w is corresponding to the angular frequency

$$\omega_w = w\frac{2\pi}{O\Delta t} = w\frac{2\pi}{T}, \tag{2.75}$$

with $u \in [0..M-1]$, $v \in [0..N-1]$, and $w \in [0..O-1]$, respectively. Note, in this study the physically motivated definitions $k = 2\pi/\lambda$ and $\omega = 2\pi/\tau$ are used, in contrast to common definitions in the image processing context, where the factor 2π is usually omitted. The **Sampling Theorem** can be reformulated here as follows: *If the spectrum of the continuous function is band limited, e.g. vanishing for $k > k_N$, then it can be reconstructed from samples with a distance $\Delta x = \pi/k_N$* [77]. Conversely, from a given spatial resolution Δx follows the so-called Nyquist wavenumber

$$k_N = \frac{\pi}{\Delta x} = \frac{2\pi}{\lambda_{min}} \tag{2.76}$$

which gives the limit in the Sampling Theorem. The same applies for the temporal sampling and thus the Nyquist frequency is given by

$$\omega_N = \frac{\pi}{\Delta t} = \frac{2\pi}{\tau_{min}}. \tag{2.77}$$

For the wavenumbers $k_{u,v}$ the Sampling Theorem is only fulfilled, if the indices are within the circle that is defined by

$$\sqrt{\left(\frac{u}{M}\right)^2 + \left(\frac{v}{N}\right)^2} = \frac{1}{2}, \tag{2.78}$$

e.g. $k_{M/2,0} = k_N$ or $k_{0,N/2} = k_N$.

Important Properties of the Discrete Fourier Transform: The Discrete Fourier Transform has a number of specific properties, all of which are comprehensively discussed in Jähne [77, Section 2.3.4]. Here, only some of these properties, which are important for the interpretation of the spectra, are outlined as follows:

- **Symmetry:**
  The spectrum of a real valued function is Hermitian:

  $$\hat{g}_{-u,-v,-w} = \hat{g}^*_{u,v,w}, \tag{2.79}$$

  where * denotes complex conjugation.

- **Periodicity:**
  The spectrum shows a periodicity:

  $$\hat{g}_{u,v,w} = \hat{g}_{u+iM,\,v+jN,\,w+kO}, \qquad \forall i,j,k \in \mathbb{Z} \tag{2.80}$$

- **Separability:**
  The kernel of the Fourier transform is separable.

Because of the symmetry property we know that the spectrum contains redundant information. Therefore we can restrict the spectral volume to half the size, compared to the spectral volume in equation (2.73). Moreover, combining the symmetry and periodicity, we can define the spectral volume to have the complete wavenumber plane (with positive and negative wavenumbers), whereas the frequency axis is restricted to positive values only[7]. The spectral components with negative wavenumbers are obtained using the periodicity and symmetry relations

$$\hat{g}_{-u,-v,w} = \hat{g}_{u-M,v-N,w} = \hat{g}^*_{u,v,-w} = \hat{g}^*_{u,v,O-w}. \tag{2.81}$$

[7] Note that the reduction of the size of the spectral volume needs to be compensated by a factor of two, when applying Parseval's Theorem as for instance in section 6.5

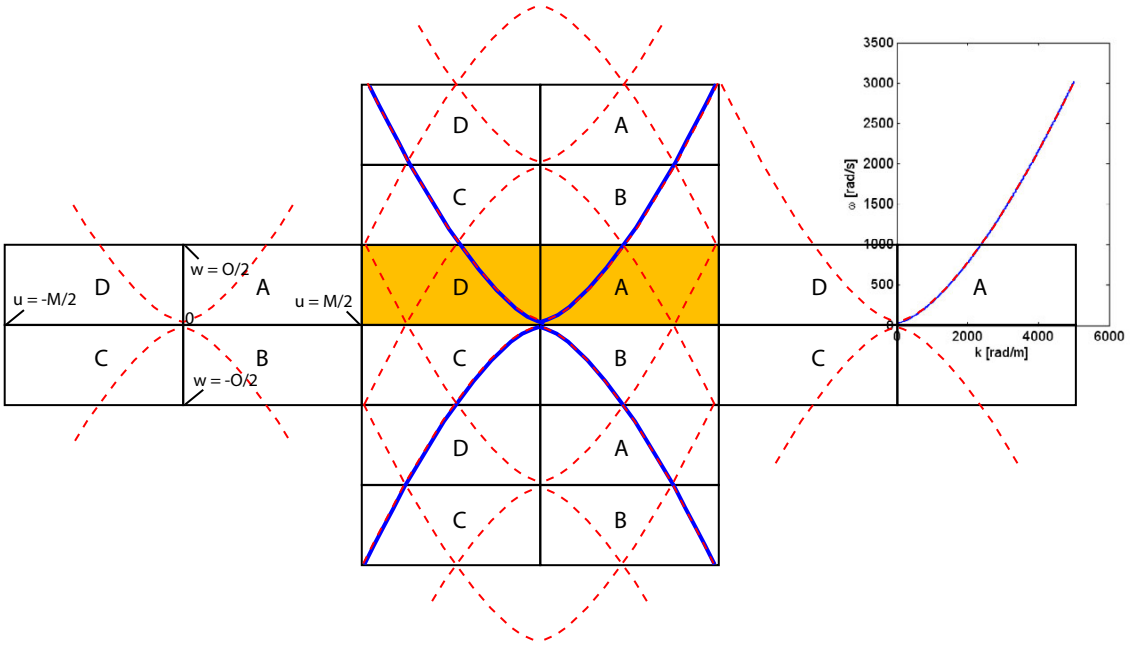

Figure 2.11.: Periodic reproduction of the dispersion curve in the discrete Fourier domain.

Therefore we can rewrite (2.73) as

$$\hat{g}_{u,v,w} = \sum_{m=-M/2}^{M/2} \sum_{n=-N/2}^{N/2} \sum_{o=0}^{O/2} g_{m,n,o}\, \mathrm{w}_M^{-mu}\, \mathrm{w}_N^{-nv}\, \mathrm{w}_O^{ow}. \tag{2.82}$$

The separability can be exploited for a splitting of the 3D transformation. For instance, at first a 1D temporal transformation from the real valued sequence into a complex valued spectrum can be performed, followed by a 2D spatial transformation from complex to complex for each slice of the spectrum in the orthogonal direction. This is an effective way to handle the huge amount of data with respect to memory availability.

The Aliasing Effect: The periodicity and symmetry properties of the spectrum enable a more specific discussion of the aliasing and Moire-effects. In figure 2.11 an illustration is shown that is referring to the actual limitations of our instrument and the dispersion relation of water waves which in this case provides a deterministic relationship $\omega(k)$. For convenience we assume, that the sampling in space is meeting the criterion of the Sampling Theorem, whereas the temporal sampling is too coarse. Thus, we are expecting aliasing but not Moire effects, which is physically motivated from the discussion of the results in section 7.3.

The sketch in figure 2.11 depicts one ω–k slice through the centerline of the 3D spectrum[8]. The actual spectrum that we describe with equation 2.82 is given by the segments A and D which are highlighted in yellow. In analogy to solid state physics we might associate the central segments A, B, C, and D with the first Brillouin zone. All other segments illustrate the periodic replication of the spectrum. The wavenumber and frequency indices corresponding to the boarders of the first Brillouin zone are given in the sketch of the replication to the left of the first zone.

The solid blue line is depicted to represent the continuous spectrum of the signal. For this illustration we have adopted the blue line to the dispersion shell $\omega(k)$ for small scale water waves, which is given by equation (2.34). The physical units are shown in the plot that is included to the right of figure 2.11.

[8]Without loss generality we might think of the slice for which $k_y = 0$ or respectively $k_{u,0}$.

Now, due to the discrete sampling, the discrete spectral volume is not large enough to contain the complete dispersion shell. We can see, for instance, that the blue curve leaves the yellow segment A and enters into a segment B of the periodic reproduction. Therefore the spectral energy is observed at a frequency index $w = -\frac{O}{2} + i$ rather than $w = +\frac{O}{2} + i$. Here $i \in 1..\frac{O}{2}$ represents the excess of the index w over the index $O/2$, which is corresponding to the frequency Nyquist limit. Note that, due to the symmetry, the spectral energy in segment B is transformed under a *point reflection at the origin* into segment D, which alternates the frequency index from $w = -\frac{O}{2} + i$ to $w = \frac{O}{2} - i$ and the wavenumber indices from u to $-u$ and from v to $-v$. It is important to notice that we are dealing with a point symmetry, even though the illustration could give the misleading impression of the existence of an axis symmetry[9]. Ultimately, we measure the spectral energy which is associated with ω and $\mathbf{k}$ at a frequency $\omega' = 2\omega_N - \omega$ and at a wavenumber $\mathbf{k}' = -\mathbf{k}$. From this we can see that we still get the right magnitude of the wavenumber vector, but it seems that the corresponding spectral energy belongs to a wave that is propagating in the opposite direction. In contrast, the frequency does no longer have the right magnitude, which is -in this case- even decreasing as the actual frequency increases. This discussion could be extended ad infinitum, taking even higher order aliasing into account, which for instance occurs when the blue line leaves segment B at the high frequency end and enters again at the low frequency end in segment A. Instead, we get an immediate impression of the location of the aliased spectral energy, if we regard the red dash-dot lines within the first Brillouin zone, which are stemming from the periodic reproductions of the blue curve in the neighboring Brillouin zones.

If the blue line in figure 2.11 would be extended for wavenumber values greater than the Nyquist wavenumber, we would of course observe Moirè effects which can be discussed in a analogy to the aliasing.

Spectral Leakage: There is one more peculiarity of the discrete spectra. From the continuum of possible frequencies and wavenumbers, only those which coincide with the basis of the Discrete Fourier Transform are projected onto a single basis vector[10]. All other frequencies and wavenumbers will exhibit non-zero projections on the entire basis set. This is commonly referred to as *spectral leakage* and is the result of processing finite-duration and finite-size sequences. Frequencies and wavenumbers other than those of the DFT basis are not periodic in the observation window, which leads to discontinuities in the periodic extension of the signal. These discontinuities are responsible for the leakage over the entire basis set. In order to reduce this effect, the sequence is usually multiplied by a weighting function which smoothly approach zero at the boarders of the observation window. There is a variety of windowing functions that are commonly used. A comprehensive review about spectral leakage and the properties of the most prominent windowing functions is given in the article by Harris [62], which also this paragraph is predicated on.

2.5.2. Modulation Transfer Function

Any imaging system shows certain contrast damping as a function of the structure size in the image. This contrast modulation can be measured by means of the *Modulation Transfer Function* (MTF), which is defined as the magnitude of the *Optical Transfer Function*. In this section we will give the context that is needed to understand the MTF measurement and MTF correction, which is described in section 6.2. With the MTF correction it is possible - at least to a certain extend - to restore the contrast. The MTF correction is essential if the magnitude of the spectral amplitudes

[9] The symmetry ambivalence in the illustration is due to the cylinder symmetry of the dispersion relation.
[10] See Jähne [77, chapter 2.3.2] for the depiction of the DFT as a projection.

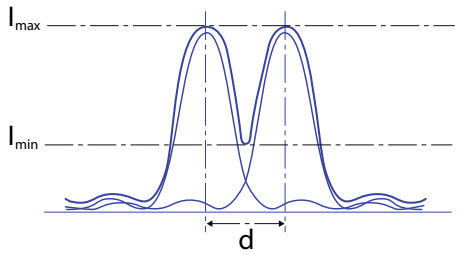

Figure 2.12.: The contrast is depending on the distance d of two structure elements in the image plane and on the width of the point spread function.

for different wavenumbers are to be quantitatively compared, e.g. in case of wind wave saturation spectra.

Contrast and the Point Spread Function: Consider a point light source in the object space that is imaged on a digital sensor. The image of that point will have a certain spatial extend with varying intensity. This is due to blurring effects and because the digital image of the point is discrete and therefore its extend is at least as big as one pixel of the sensor. The image of such a point (or delta peak) is called the *Point Spread Function* (PSF). In general the PSF is a function of all three spatial coordinates, but here we only consider the slice that is defined by the sensor plane and assume that the object is well focused on that plane. For most cases we can think of the PSF as a Gaussian shaped peak.

The link between the PSF and the contrast becomes clear, if we consider two point light sources in the object space that are separated by a varying distance. If their distance d on the image plane is in the order of the width of the PSF, then their intensity distributions will have a considerable overlap, see figure 2.12. Due to this overlap the difference between the peak intensity and the minimal intensity between the two peaks will decrease as a function of d. If we denote the intensity at the maximum of one of the Gauss peaks by I_{max} and the intensity in the middle between the two peaks by I_{min}, then we can define the contrast as

$$C = \frac{I_{max} - I_{min}}{I_{max} + I_{min}}, \tag{2.83}$$

which is therefore a measure of intensity[11] differences [124].

From this example we can see, that the width of the PSF leads to a decrease in contrast with decreasing size d of intensity patterns in the object space. The width of the PSF may stem from different sources, such as physical limitations of the optics, discrete sampling, or image processing filters. The above considerations are similar to those for the diffraction limit of optics which yield the Rayleigh criterion [77], but here we are interested in the gradual loss of contrast, not only in the limiting case. Moreover, the contrast damping that is stemming from the discrete sampling or from image processing filters may exceed the damping due to the limitations of the optics by orders of magnitudes.

In most cases we can assume that the optical system is a linear shift invariant system (LSI), so that the image of any complex object can be thought as a linear superposition of images of points on that object. This assumption holds, as long as the PSF is not dependent on position [77]. With this assumption we also exclude motion blur effects, because these effects may depend on time and position. With the LSI assumption we can regard the formation of the image $g'(\mathbf{x})$ as an ideal

[11] Strictly speaking we would need to say luminance instead of intensity, but we assume that intensity and luminance are proportional to each other.

projection $g(\mathbf{x})$ of the object on the image plane, which is then convolved with the PSF

$$g'(\mathbf{x}) = \mathrm{PSF} * g(\mathbf{x}). \tag{2.84}$$

Later, we refer to the ideal projection $g(\mathbf{x})$ on the image plane as the *a priori image*. Accordingly we call the acquired image $g'(\mathbf{x})$ the *a posteriori image*.

Point Spread Function and Modulation Transfer Function: Since convolution corresponds to a simple multiplication in Fourier space it is convenient to examine the contrast damping in this domain. The Fourier transform of the Point Spread Function is called the *Optical Transfer Function* (OTF),

$$\mathrm{PSF}(\mathbf{x}) \qquad \circ\!\!-\!\!\bullet \qquad \mathrm{OTF}(\mathbf{k}), \tag{2.85}$$

where the OTF is a complex valued function. For the spectra we can rewrite (2.84) as

$$\hat{g'}(\mathbf{k}) = \mathrm{OTF}(\mathbf{k}) \cdot \hat{g}(\mathbf{k}). \tag{2.86}$$

Regarding the contrast we are only concerned with the magnitude of the transfer function, which is called the *Modulation Transfer Function* (MTF)

$$\mathrm{MTF}(\mathbf{k}) \equiv \left|\mathrm{OTF}(\mathbf{k})\right|. \tag{2.87}$$

For an ideal imaging system, the MTF would be constant for all wavenumbers, which means that the PSF would be a delta peak, resulting in $g' = g$ according to (2.84). In contrast, real optical systems always have a PSF of finite width, which was explained above. The width of the MTF is reciprocal to the width of the PSF, which is a general property of the Fourier transform. Thus if the blurring effects are strong, then the MTF is narrow. For a digital sensor we know that the size of the sensor element defines the maximum wavenumber that is sampled correctly. This wavenumber is called the *Nyquist wavenumber* $\tilde{\mathbf{k}}$. To see the effect of the discrete sampling, we may regard the sampling step as a convolution of the ideal projection g with a rectangular box function. Then follows that the amplitude damping at the Nyquist wavenumber is $\mathrm{MTF}(\tilde{\mathbf{k}}) = 1/\sqrt{2}$, see Jähne [77, chapter 9.2.5].

Deconvolution: It is possible to reverse the amplitude damping effect, if the MTF is known. The restored spectral amplitudes $|\hat{g}|$ are gained by multiplying the spectral amplitudes of the *a posteriori image* $|\hat{g'}|$ by the inverse of the MTF

$$|\hat{g}| = \mathrm{MTF}^{-1} \cdot |\hat{g'}|, \tag{2.88}$$

which is of course only possible for wavenumbers where the MTF is non-zero. Note that the deconvolution in (2.88) does not improve the signal to noise ratio and that it does not allow for restoring spectral information that was completely lost in the acquisition of g' (see [77, chapter 17.5.3]). But still, the inverse filtering with the MTF restores the contrast, which is essential if the magnitude of the spectral amplitudes for different wavenumbers are to be quantitatively compared, i.e. in case of wind wave saturation spectra.

MTF Measurement from Spectra: The idea to measure the MTF is straight forward if the *a priori spectrum* $\hat{g}$ is known and if it is non-zero for all wavenumbers. Then we can use the prior knowledge about the *a priori spectrum* along with the *a posteriori spectrum* to compute the MTF using (2.88).

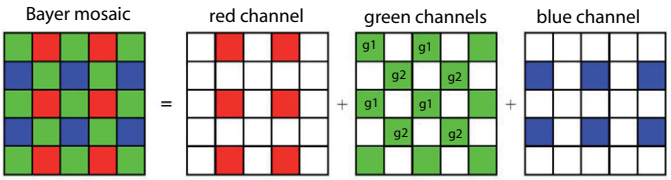

Figure 2.13.: Bayer mosaic layout of the color filter array. Modified after [109]

There exist several approaches to measure the MTF that use *a priori* knowledge about the spectrum [20, 35, 36, 120]. For instance one can try to realize a point light source and assume, that the *a priori spectrum* is constant. Though theoretically easy, this approach is barely useful, since a point light source is hard to realize in practice. A second example is the edge exposure method. Here, for instance, images of a knife blade are taken, with an homogeneous illumination from the back. Then the image is a step-like function of which the spectrum is also known. This approach has the disadvantage, that the orientation of the edge matters and one has to perform multiple measurements under different orientations. A third class of approaches try to use special noise characteristics [42], e.g. for white noise the spectrum should be flat. In practice this is realized using a so called *Imaged Random Test Pattern*.

For the MTF measurements in this work a method was desired that was applicable directly in the experimental setup. Therefore we designed a MTF target, see figure 4.25. This target is a thin metal stencil with circular holes of different diameters on a regular grid. An *a posteriori image* is taken with a homogeneous background illumination as in the edge exposure method. The circle diameters are chosen such that the *a priori spectrum* (which is an superposition of several Bessel functions) is non-zero everywhere [157]. Even in a single image of the MTF target we have edges with all possible orientations. Thus there is no need make more than one image for the measurement of the MTF in the full wavenumber plane. Unlike in the other methods, we compute the *a priori spectrum* via a model based reconstruction of the target. This is done using the geometrical properties in the *a posteriori image* to scale and rotate the *a priori image* with sub pixel accuracy, at higher resolution, and featuring sharp edges. The application of this new method is explained in detail in section 4.5.

2.5.3. Color Imaging

Modern digital color cameras are mostly having a single CCD sensor. The sensor material itself does not distinguish between the wavelengths of the incident light. Therefore the world looks gray for such a camera, even if we applied different color filters. In order to retrieve one colored image, we have to combine the gray value information of several images that are taken with different color filters.

A very elegant way to acquire images on a single chip sensor with different filters at the same time is to use a *color filter array* (CFA). The most prominent example for a CFA is the so called *Bayer mosaic layout*[12]. This Bayer mosaic was also employed for the camera that was used for the experiments in this study, so that we will restrict the discussion of color imaging to that example. With an Bayer mosaic, each individual pixel is equipped with a filter for one of the primary colors red, green and blue (R,G, and B). The filters are arranged on the chip in a certain pattern that is shown in figure 2.13. One can think of the CFA as four sub grids: two for green, one for red and one for blue. These sub grids are slightly shifted, relative to each other, and they only have half the spatial resolution of the original CCD.

Because of the CFA the actual acquired digital data constitutes a mosaic-like gray value image which is called the *raw image*. The task to convert the gray value information on the sub grids for

[12]US Patent3971065

the primary colors into a final image which contains full color information at each pixel is called *demosaicing*. The final color image is typically composed of three *color channels* R,G, and B. For most cameras the demosaicing can already be performed internally. However, this feature is not always useful, e.g. if high frame rates are desired as in this study. This is because the demosaicing consumes time and increases the data volume per image. Additionally, there are many different approaches to solve the demosaicing task, having different pros and cons. If the demosaicing is performed internally in real time, the build-in algorithm is predominantly chosen with respect to its computational efficiency which might not be the optimal processing solution. Surveys on state of the art demosaicing techniques are presented for instance by Li et al. [109] and Lukac [113]. In our case, only the so called *component-wise* approaches are suitable, since all other approaches already make inferences from the combination of the colors which is not allowed in case of the *CISG* data.

Using sub sampling of the raw image by a factor of two and with different offsets is the easiest way to retrieve the three color channels from the raw image. The sub sampling only delivers one of the four sub grids that are shown in figure 2.13. With this simple method, the color channels are not affected by any interpolation and not corrected for the spatial shift of the sub grids. While less interpolation and thus less smoothing might be desirable, the spatial shift is especially undesirable in our context because a spatial shift introduces a phase shift in the Fourier domain (shift theorem [77]).

To overcome the problem of shifted grids it is necessary to perform an interpolation of the data from the different sub grids onto a congruent sub grid. For example consider that the raw image g is convoluted by the following set of filter kernels

$$h_R \equiv \begin{array}{|c|c|c|}\hline \frac{1}{4} & 0 & \frac{1}{4} \\ \hline 0 & 0 & 0 \\ \hline \frac{1}{4} & 0 & \frac{1}{4} \\ \hline \end{array} \qquad h_G \equiv \begin{array}{|c|c|c|}\hline 0 & \frac{1}{4} & 0 \\ \hline \frac{1}{4} & 0 & \frac{1}{4} \\ \hline 0 & \frac{1}{4} & 0 \\ \hline \end{array} \qquad h_B \equiv \begin{array}{|c|c|c|}\hline 0 & 0 & 0 \\ \hline 0 & 1 & 0 \\ \hline 0 & 0 & 0 \\ \hline \end{array}.$$

The convolution masks are chosen such that the congruent grid is the blue subgrid of the raw image g. Therefore, after the convolution

$$\begin{aligned} g_R &= g * h_R \\ g_G &= g * h_G \\ g_B &= g * h_B, \end{aligned} \tag{2.89}$$

only the blue subgrid is extracted from the three resulting images

$$\begin{aligned} R &= \mathcal{S}_{\downarrow 2,b}(g_R) \\ G &= \mathcal{S}_{\downarrow 2,b}(g_G) \\ B &= \mathcal{S}_{\downarrow 2,b}(g_B), \end{aligned} \tag{2.90}$$

where $\mathcal{S}_{\downarrow 2,b}$ stands for the subsampling operator that retrieves the blue subgrid. Now R contains the average values of the surrounding red pixels on the blue subgrid. Correspondingly the same holds for G. In contrast, the image B has the unchanged content of the original blue subgrid. This kind of demosaicing was already used by Fuß [50] and it has the advantage of simplicity and computational efficiency, since the masks are separable. The disadvantage of this filter set is, that the transfer function show strong non-isotropy. Additionally the smoothing for the different color channels is not comparable, which means that the *PSF* is different.

For the evaluation of the *CISG* data the isotropy of the demosaicing is crucial. Moreover we desire that the color channels can be treated as equivalent with regard to the modulation transfer function, see section 2.5.2. Therefore we tested and actually used a set of filter kernels that were

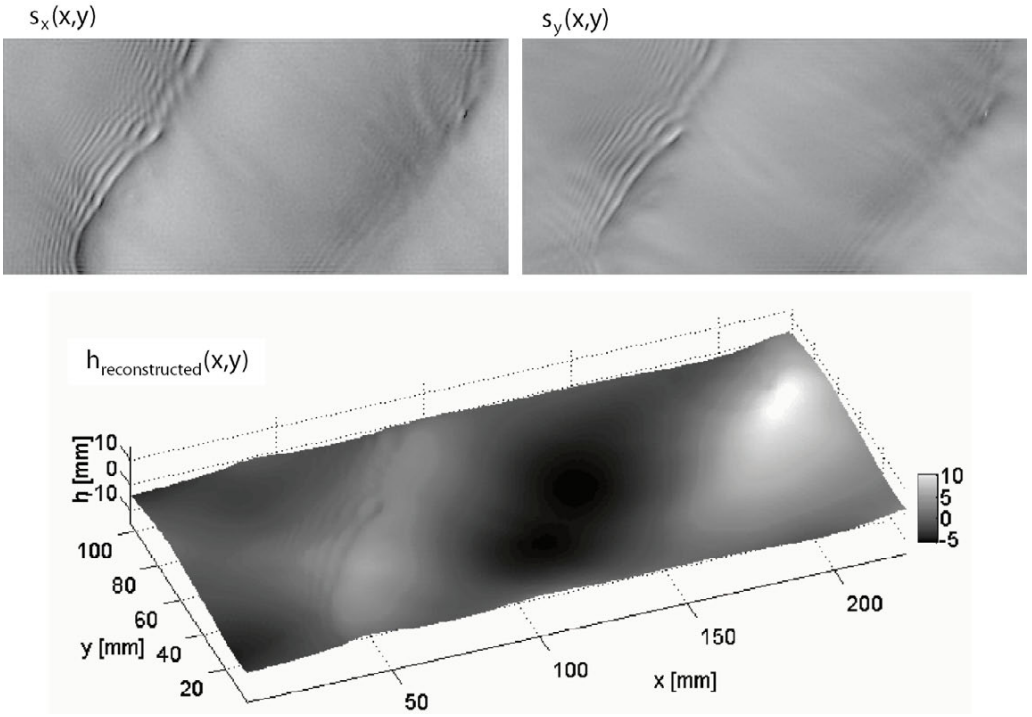

Figure 2.14.: Example for the height reconstruction from the measured gradient field $\mathbf{s} = [s_x, s_y]^T = \nabla h$ of small scale water waves. The measured data is shown in the top images. The reconstructed height (from equation (2.94)) is shown below as a 3D plot with equally scaled axes. [data: Run031, frame 294. The wind is blowing from the right to the left with 4 m/s.]

proposed by Scharr [146]. These filter kernels are optimized for isotropy and homogeneity. The demosaicing, based on these optimized filters, is conceptually the same as explained above. The properties and the application of these filters are the subject of section 6.1.

2.5.4. Height Reconstruction from a Gradient Field

The measurement technique of this study is related to the *shape from shading* paradigm of computer vision [77], i.e. the gray value of the image is related to the gradient of the object that is imaged. Some algorithms for the shape reconstruction based on the gradient information have been developed in the computer vision community (e.g. [1, 2, 67]). As a matter of fact, the 2D surface gradient $\mathbf{s}(\mathbf{x}) = [s_x, s_y]^T$ can be integrated to yield the surface elevation $h(\mathbf{x})$, except for an additive constant.

In this section we briefly introduce an elegant way to perform the integration in the Fourier domain. This approach was first presented by Frankot and Chellappa [47] and it was already successfully used by several investigators for the reconstruction of the wavy water surface [9, 50, 178]. Integration in the Fourier domain is very convenient, since it automatically enforces the integrability of the gradient field. With numerical schemes that work in the spatial domain some complications are experienced since the integrability of the gradient fields might be violated due to measurement errors, see Frankot and Chellappa [47] for details.

Height reconstruction means, that we are searching for the elevation function $h(\mathbf{x})$ that fulfills the requirements

$$\begin{aligned} \frac{\partial h(\mathbf{x})}{\partial x} &= s_x(\mathbf{x}) \qquad \circ\!\!-\!\!\bullet \qquad \mathrm{i}\, k_x \hat{h}(\mathbf{k}) = \hat{s_x}(\mathbf{k}) \\ \frac{\partial h(\mathbf{x})}{\partial y} &= s_y(\mathbf{x}) \qquad \circ\!\!-\!\!\bullet \qquad \mathrm{i}\, k_y \hat{h}(\mathbf{k}) = \hat{s_y}(\mathbf{k}). \end{aligned} \tag{2.91}$$

On the right hand side we have translated the relation into the Fourier domain, where the partial derivatives ∂_x and ∂_y correspond to a multiplication with $\mathrm{i}\,k_x$ and $\mathrm{i}\,k_y$ [77]. Combining the information of both slope components we can write

$$\mathrm{i}\,k_x \hat{s_x}(\mathbf{k}) + \mathrm{i}\,k_y \hat{s_y}(\mathbf{k}) = -\left(k_x^2 + k_y^2\right) \hat{h}(\mathbf{k}), \tag{2.92}$$

where we have added the right hand side equations (2.91) after a multiplication with $\mathrm{i}\,k_x$ and $\mathrm{i}\,k_y$, respectively. For $k^2 \equiv k_x^2 + k_y^2 \neq 0$ this can be transformed into

$$\hat{h}(\mathbf{k}) = \frac{-\mathrm{i}\,k_x \hat{s_x}(\mathbf{k}) - \mathrm{i}\,k_y \hat{s_y}(\mathbf{k})}{k^2}, \tag{2.93}$$

and for $k = 0$ we set $\hat{h}$ to zero in order to handle the division by zero. Note that we also loose the information that is contained in the spectral coefficients $\hat{s_x}(\mathbf{k} = 0)$ and $\hat{s_y}(\mathbf{k} = 0)$ which are corresponding to the mean gradients $\langle s_x \rangle$ and $\langle s_y \rangle$, respectively [77].

Hence, the surface elevation $h(\mathbf{x})$ can be obtained by the Inverse Fourier Transform

$$h(\mathbf{x}) = \mathrm{FT}^{-1}\left(\frac{k_x \hat{s_x}(\mathbf{k}) + k_y \hat{s_y}(\mathbf{k})}{\mathrm{i}\,k^2}\right), \tag{2.94}$$

except for the plain that is defined by the mean gradients and an integration constant.

This method is used - with only a minor modification - for the reconstruction of the water surface height in this study, exemplified in figure 2.14. Further examples are given in section 7.5.1 which deals with an interactive visualization of the wave field. In this section we also discuss some peculiarities of the implementation.

3. Method - Wave Slope Imaging

There exist a variety of methods for the measurement of waves at the water surface. Most prominent examples are the *wire gauge* [106], the *laser slope gauge* [69] and its extension the *scanning laser slope gauge* [16], the *reflective slope gauge* [107], which is similar to the *sun glitter method* by Cox and Munk [33], the *stereo imaging*, which was applied from the beginning of the 20^{th} century [103] until recently [50], the *radar altimeter* [49] and the *radar scatterometer* [24, 60], et cetera, and finally the *imaging slope gauge* [84, 181].

All these methods are non-intrusive, except for the *wire gauge*. For the family of *slope gauges* the gradient $\mathbf{s} = [\partial_x, \partial_y]^T \eta$ of the water surface is measured, which is advantageous because the dynamical range of the surface slope is much smaller than the dynamical range of the surface elevation. Therefore the *slope gauges* are also suitable to measure small scale waves in the presence of larger waves. For the slope measurement the refraction or the reflection of light is exploited in different manners. Reviews comprehending the pros and cons of the above listed methods can be found in Fuß [50], Balschbach [9], Klinke [93], Rocholz [142], Lange et al. [106], Jähne et al. [81, 85], to only name a few, so that we abstain from going into details.

Here, the most important statement is that all of these methods where either not fast enough to keep track with the rapidly moving waves or it was not possible to gain the spatial resolution that is needed to measure the tiny capillary waves.

It is a severe technical challenge to get a high spatial and temporal resolution at the same time. In this regard the greatest achievement could be made using the *scanning laser slope gauge*, which operated with 74.8 Hz sampling rate while resolving wavenumbers in the range of 25-1000 rad/m [17, 162]. The laser scanning systems do not reach the spatial resolution of imaging techniques (see table A.1), and conversely the imaging techniques were mostly limited to frame rates of 30-50 Hz. From the linear dispersion relation that was plotted in figure 2.3 it is obvious that this frame rate was not sufficient to seize the dispersion of the small scale waves. The spectral evaluation of *imaging slope gauge* data was therefore predominantly restricted to the 2D wavenumber domain.

For this study the *imaging slope gauge* technique was improved to achieve a sampling rate of 312.5 Hz, while resolving wavenumbers in the range of 60-4500 rad/m. Therefore we obtain image sequences that comprise the frequencies and the 2D wavenumber vector of the water waves at the same time and consequently can be used for a direct 3D Fourier transform. The resulting wavenumber-frequency spectra contain the same information as obtained by fast point probes such as the *laser slope gauge*, but in addition we have the possibility to distinguish the frequency spectrum for the wavenumber vector in its magnitude and direction.

The instrument is named *color imaging slope gauge* (CISG) because a color coding is used to measure the surface slope [9, 181]. In section 3.1 the fundamental ideas of the method are introduced. The technical realization of the CISG and its calibration is shown in chapter 4. Since the instrument and its calibration are closely connected, it should already be pointed out that a new calibration method was developed that allows for a compensation of intrinsic nonlinearities that are prevalent for this method for higher slopes, see section 4.4.

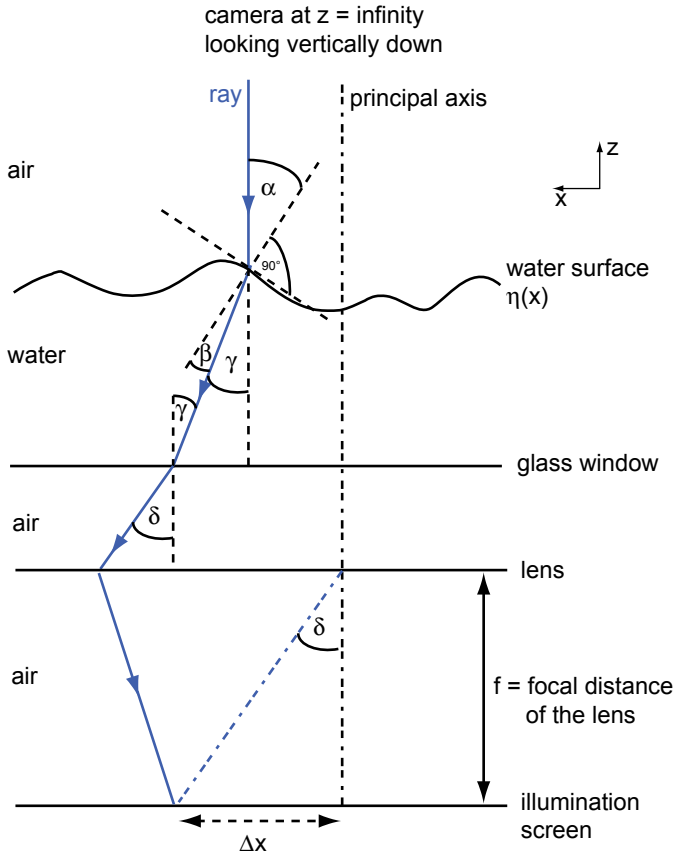

Figure 3.1.: Sketch of the ray geometry of the imaging slope gauge.

3.1. Basics of the CISG Method

The calculation of the water surface slope from the color of the *CISG*-images is based on light refraction and color coding. Here, the basic design of the CISG Method and principal relationships are explained. The implementation of the method is shown in section 4.1. The general expression, describing the trace of rays between the illumination and the digital camera is given in section 3.1.2. The CISG illumination implements a color coding for the origin of each light ray. The design of this color illumination is described in section 3.1.3.

3.1.1. Ray Geometry

The *Color Imaging Slope Gauge* consist of two main components, namely a digital color camera and a position coding light source. The camera is assumed to be at infinite distance and vertically looking down to the water surface. The light source is located below a glass window in the bottom of the wind wave flume. A sketch of the idealized ray geometry is shown in figure 3.1. Consider the trace of one light ray from the camera to the light source as indicated in the figure. At first the ray is parallel to the principal axis of the camera[1]. Then, at the wavy water surface it undergoes refraction. A second refraction occurs when the ray leaves the water body through the horizontal glass window in the bottom of the tank. The big Fresnel lens, which is part of the light source, images all rays with the same inclination angle δ onto the same spot of the illumination screen, (see figure 3.1). This is because the illumination screen is located at focal distance f to the lens

[1]This can be achieved by an object-space telecentric lens, see [142], or as an approximation by being far away from the water surface.

and the principal axis is parallel to the principal axis of the camera. We call this arrangement a *telecentric illumination* (see also figure 4.4 and [142]). Let Δx denote the distance between the spot where the light ray pierces the illumination screen and the piercing point of the principal axis. Now, because of the telecentric lens we can express Δx in terms of the the azimuthal inclination δ of the light ray at the entrance of the light source

$$\Delta x = \frac{\tan\delta}{f}.^{2} \tag{3.1}$$

The illumination screen is area extended and therefore the camera receives light for a range of angles δ. In one dimension the position on the screen can be coded by an intensity gradient. In two dimensions the position can be identified using color gradients. This is discussed in section 3.1.3. In 1D the relationship between the water surface slope $s \equiv \frac{\partial\eta}{\partial x} = \tan\alpha$ and the angle δ is given by

$$\tan\alpha = \frac{\tan\delta}{\sqrt{n_w^2 + \tan^2\delta(n_w^2 - 1)} - \sqrt{1 + \tan^2\delta}}, \tag{3.2}$$

where n_w is the refractive index of water. This one-dimensional relationship is derived and extended to 2D in the appendix A.10.

3.1.2. General Expression

A light ray that leaves the telecentric illumination with an azimuthal angle δ is refracted at the water surface in direction to the camera if and only if the following condition is fulfilled

$$\mathbf{s} = \begin{bmatrix} s_x \\ s_y \end{bmatrix} = \begin{bmatrix} \cos\Phi \\ \sin\Phi \end{bmatrix} \cdot \frac{|\tan\delta|}{\sqrt{n_w^2 + (n_w^2 - 1)\tan^2\delta} - \sqrt{1 + \tan^2\delta}}, \tag{3.3}$$

where $\mathbf{s}$ is the water surface slope, Φ is the polar angle of the light ray and n_w denotes the refractive index of water. The condition follows from Snell's law for the ideal setup[3] and is deduced in the appendix A.10. The azimuthal angle δ is again related to the position

$$\begin{bmatrix} X \\ Y \end{bmatrix} = r \begin{bmatrix} \cos\Phi \\ \sin\Phi \end{bmatrix} \tag{3.4}$$

on the illumination screen. We choose the principal axis of the fresnel lens to be the origin of the coordinate system on the illumination screen in which the positions X and Y are measured, so that the distance $r = \sqrt{X^2 + Y^2}$ corresponds to Δx in section 3.1.1 and figure 3.1. As in equation (3.1) we have

$$|\tan\delta| = \frac{r}{f} = \frac{\sqrt{X^2 + Y^2}}{f}, \tag{3.5}$$

with f being the focal length of the telecentric Fresnel lens. Consequently, we can write the water surface slope in terms of the ray origin on the illumination screen

$$\begin{bmatrix} s_x \\ s_y \end{bmatrix} = \frac{1}{f}\begin{bmatrix} X \\ Y \end{bmatrix} \cdot \frac{1}{\sqrt{n_w^2 + (n_w^2 - 1)\,(X^2 + Y^2)/f^2} - \sqrt{1 + (X^2 + Y^2)/f^2}} \tag{3.6}$$

$$= \begin{bmatrix} X \\ Y \end{bmatrix} \cdot \frac{1}{\sqrt{f^2\, n_w^2 + (n_w^2 - 1)\,(X^2 + Y^2)} - \sqrt{f^2 + (X^2 + Y^2)}}. \tag{3.7}$$

[2] please see page 167

[3] idealizations: a) the camera is at infinite distance and is looking vertically down to the water surface; b) the glass window at the flume bottom has zero horizontal inclination

Figure 3.2.: Position coding with a superposition of three linear color wedges in red, green and blue as in (3.9).

Linear Approximation: The general expression (3.6) can be simplified very much if the focal length f is large compared to the screen deflection $\sqrt{X^2+Y^2}$:

$$\begin{bmatrix} s_x \\ s_y \end{bmatrix} \approx \frac{1}{f\,(n_w-1)} \cdot \begin{bmatrix} X \\ Y \end{bmatrix}. \tag{3.8}$$

For instance, the relative error of this linearization is -6%, using the values for $|s_x| = 1$, $s_y = 0$ and the focal length $f = 39\,\mathrm{cm}$, which are adapted to the actual geometrical limitations of the instrument, see section 4.

3.1.3. Color Coded Illumination

Both slope components can be retrieved from color images at the same time, since the position $[X,Y]^T$ on the illumination screen is color coded. A very elegant design of the color coding was introduced by Balschbach [9] and also used by Fuß [50]. This design is a superposition of three linear wedges in red, green and blue

$$\begin{aligned} \text{red} &\propto -\frac{1}{2}X - \frac{1}{2}Y + \frac{1}{2} \\ \text{green} &\propto \quad X \qquad\quad + \frac{1}{2} \\ \text{blue} &\propto -\frac{1}{2}X + \frac{1}{2}Y + \frac{1}{2}, \end{aligned} \tag{3.9}$$

see also figure 3.2. The choice of the coefficients is such that the intensity (the sum of the three colors) is supposed to be independent of the position. However, deviations from the ideal configuration are hardly avoidable, due to the complex interplay of the light source spectrum, the actual spectral transmittance of the color coding screen, the spectral sensitivity of the camera, and the alignment of the light source. Therefore, the assumed transformation from color space to the positions is of the form

$$\begin{aligned} R &= I \cdot (r_x\,X + r_y\,Y + R_0/I_0) \\ G &= I \cdot (g_x\,X + g_y\,Y + G_0/I_0) \\ B &= I \cdot (b_x\,X + b_y\,Y + B_0/I_0), \end{aligned} \tag{3.10}$$

where

$$\begin{aligned} I_0 &= (R_0 + G_0 + B_0)/3 \\ I &= (R + G + B)/3. \end{aligned} \tag{3.11}$$

This transformation models a relative stretching and rotation of the coordinate systems, as well as individual offsets R_0, G_0, B_0, and allows spacial inhomogenity of the intensity $I(x,y)$. The subscripts 0 indicate that the constants are retrieved from images with zero surface slope. The zero-slope condition defines the origin of both coordinate systems.

4. Setup and Calibration

The *CISG* was set up during the WiSSCy campaign (see chapter 5) at the linear wind wave flume of the University of Hamburg, located at the Bundesanstalt für Wasserbau (BAW) in Hamburg, Germany. In section 4.1 we will describe the technical details concerning the facility and the wave imaging setup. The calibration comprises i) the geometrical calibration of the CISG camera in section 4.2, ii) the registration of the infrared camera and the CISG camera in section 4.3, iii) the determination of the color-slope relationship in section 4.4 , and iv) the measurement of the Modulation Transfer Function in section 4.5.

4.1. Experimental Setup

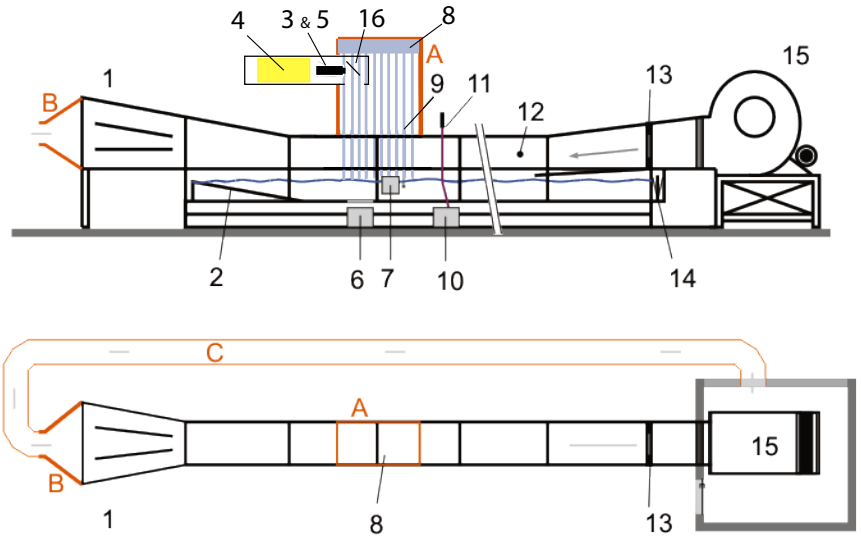

Figure 4.1.: Schematic of the modified wind-wave tank of the University of Hamburg. Upper Panel: side view. Lower Panel: top view. 1: diffuser, 2: beach, 3: IR camera, 4: CO_2-laser, 5: imaging slope gauge camera, 6: imaging slope gauge illumination, 7: CO_2 analyzer, 8: rain generator, 9: wire gauge, 10: laser optics, 11: laser slope gauge, 12: anemometer, 13: honeycomb, 14: wave flap, 15 blower, 16: mirrors for the imaging slope gauge camera and the IR camera, A: Plexiglas enclosure, B: sheet metal air tunnel adaptor, C: sheet metal tunnel. Note that the blower is located in a separate room. (Sketch modified after [23])

Figure 4.1 shows a schematic of the linear wind wave tank in Hamburg. The wave imaging camera was mounted 4.3 m above the water surface in a rain tower at a fetch of approximately 14.4 m. The total length of the water flume is 26 m. Figure 4.2 shows a true to scale drawing of the rain tower section. In this drawing the rain generator itself is not shown. The rain generator consists of water tubs with needles in the bottom. The rain rate could be controlled by adjusting the water level in the tubs. The camera system was just below these tubs and looking down via an adjustable mirror to a glass window in the tank bottom. Below this glass window the light source was set up with the principal axis pointing vertically through the center of the window. It was not possible to position the mirror for the camera exactly over the center of the glass window.

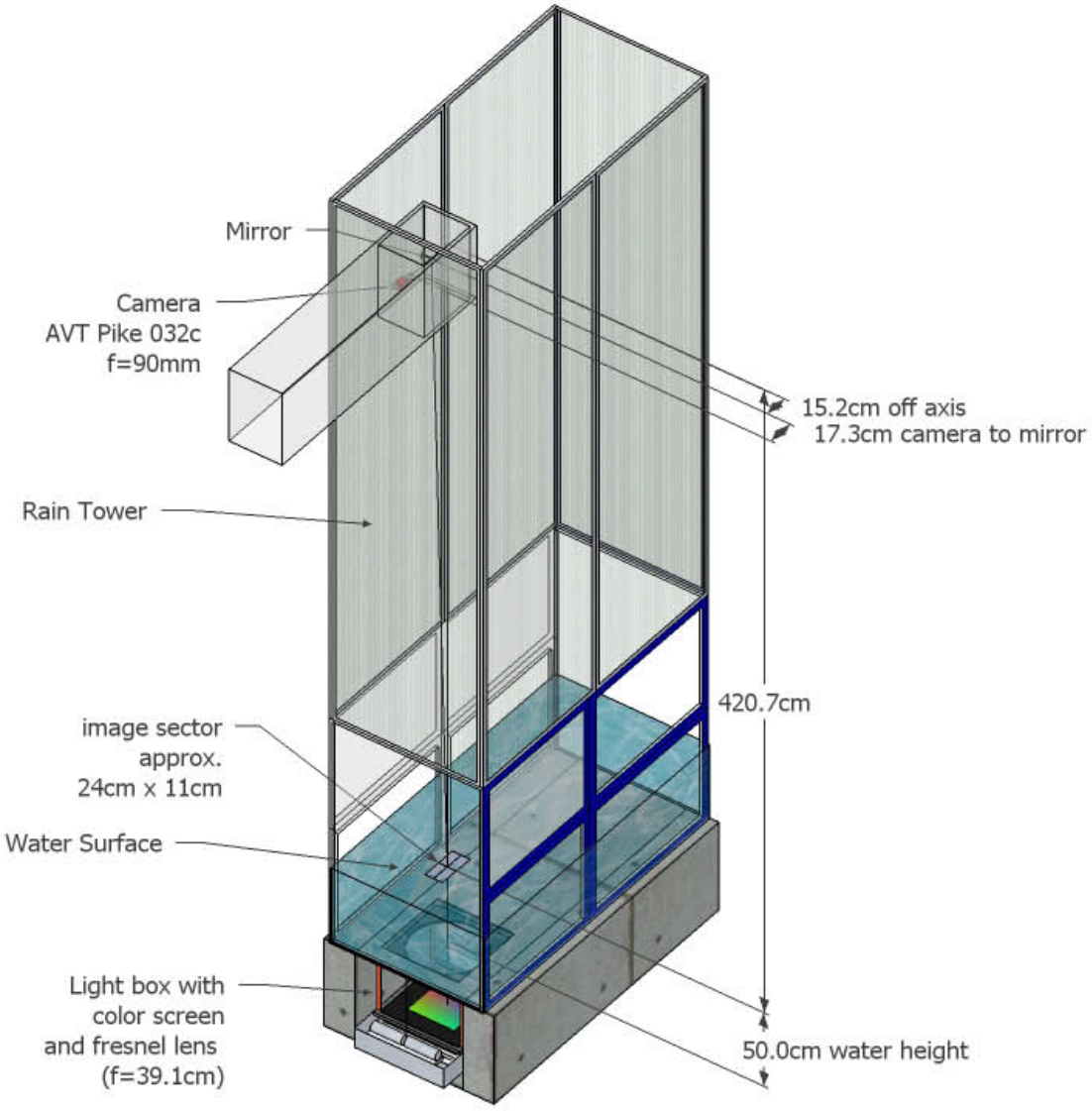

Figure 4.2.: *CISG*-Setup in the rain tower section of the linear wind wave flume. The section is located at a fetch of between 12.6 and 14.8 m.

Otherwise the camera system would have caused considerable shading of the rain area. As a compromise the azimuthal angle of the camera's principal axis was adjusted to be 2° in the along-wind direction.

For the camera a lens with 90 mm focal length was used. The size of the image footprint was 22.3 cm in the along-wind direction and 10.4 cm in the cross-wind direction. For the total deviation from the assumption of vertical rays in the object space the divergence of the rays at the border of the image has to be accounted for in addition to the inclination of the principal axis. From the given geometry the total deviation for the along-wind direction is $2.0^\circ - 1.5^\circ$ at the leeward boarder of the image and $2.0^\circ + 1.5^\circ$ at the windward boarder of the image. For the cross-wind direction we have $\pm 0.74^\circ$. The maximum relative deviation from the ideal ray geometry as expressed by (3.2) is therefore to be found at the windward border of the image. A detailed analysis of the influence of the inclined camera rays can be found in Fuß [50, chapter 4.2]. Following this analysis the maximum relative error for the slope measurement, based on a linear calibration, is smaller than 7%.

The f-number of the lens was set to 5. Therefore the depth of sharpness was $\pm 8.5\,\mathrm{cm}$ around the mean water level. This value is calculated assuming a circle of confusion corresponding to the size of one pixel. The mean water height during the experiments was $(51 \pm 3)\,\mathrm{cm}$. The greatest dominant waves at this fetch did not exceed amplitudes of $5\,\mathrm{cm}$ even for the highest wind speed.

The effective aperture of the illumination was 45 cm, due to the glass window at the tank bottom and the aperture of the fresnel lens. This aperture leads to a geometrical limitation for the maximum leeward slope that can be measured at the windward border of the image. The light source consists of 20 fluorescent tubes[1], a diffusion screen[2], a transparency [3], and a fresnel lens[4], see figure 4.3. In order to avoid fluctuations in the light intensity a 250V DC power supply[5] was used to power the high frequency power supply units[6] of the lamps.

The camera[7] operated with a reduced resolution of 640×298 pixel, so that a frame rate of 312.5 Hz could be achieved. The integration time was set to 1 ms. For the combined measurement of the active thermography system and the CISG it was possible to synchronize both cameras. The image footprint of the thermography system completely overlapped the footprint of the wave imaging camera and a registration was performed, see section 4.3. In the course of the measurement campaign we experienced a breakdown of the *CISG* camera because of the extraordinary humidity in the rain tower. Thus it was necessary to exchange the camera at the 14th of June 2007.

4.2. Geometrical Calibration

For a quantitative evaluation of the images we need to know the reproduction scale of the imaging system. A rough estimate of the magnification factor β of the optical system is

$$\beta = \frac{Z}{f} \approx \frac{4300\,\mathrm{mm}}{90\,\mathrm{mm}} = 47.7, \tag{4.1}$$

where we have used a pin hole camera model, the object distance $Z \approx 4300\,\mathrm{mm}$, and the focal length of the camera lens $f = 90\,\mathrm{mm}$. The edge length of one pixel is $7.4\,\mu\mathrm{m}$ and the pixels are quadratic. This estimate leads to a corresponding real world pixel edge length of $\Delta x = \Delta y \approx 0.353\,\mathrm{mm}$.

Estimating Δx by using (4.1) is prone to errors, mainly because a high accuracy measurement of the distance Z is difficult. Hence the scaling factor for the transformation from the pixel coordinates system to the world coordinate system was additionally determined from a geometrical calibration. For geometrical calibration we used images of the *MTF target*. An example of this target is shown in figure 4.5. The MTF target is a thin metal stencil with circular holes of different diameters that are arranged on a regular grid. The grid spacing is $10.0\,\mathrm{mm} \pm 10\,\mu\mathrm{m}$. The calibration images have been acquired in-situ as described in section 4.5. Form the calibration images the grid coordinates were extracted. This involves a segmentation step, followed by a computation of

[1] **fluorescent tubes:** Osram Dulux L 55W, light color 840

[2] **diffusion screen:** Plexiglas Satinice OD010DF, colorless, transmission 82%, throwing power 0.35, angle of half intensity 25°

[3] **transparency:** Duratrans, RGB-exposure technique; print shop: DiPixelprinter, Heidelberg, contact person: Jons Richter

[4] **fresnel lens:** Fresnel Optics GmbH, part number: SC2045; focal length 391.2mm; facet pacing 0.508mm; Fresnel conjugate 6096.0mm; plano conjugate 419.0mm; clear aperture 457.2mm

[5] **DC power supply:** manufacturer: Heiden Electronics; model: 1124-250

[6] **power supply units for the fluorescence tubes:** Quicktronic QT 2x55/230, Osram

[7] **camera:** manufacturer: Allied Vision Technologies; model: AVT-Pike032c; standard resolution of the color-filter array 640×480 pixel; frame rate at standard resolution: 200 Hz; chosen parameters for the measurements: integration time = 1ms, brightness = 120, gain=32, white balance = UB464 VR300

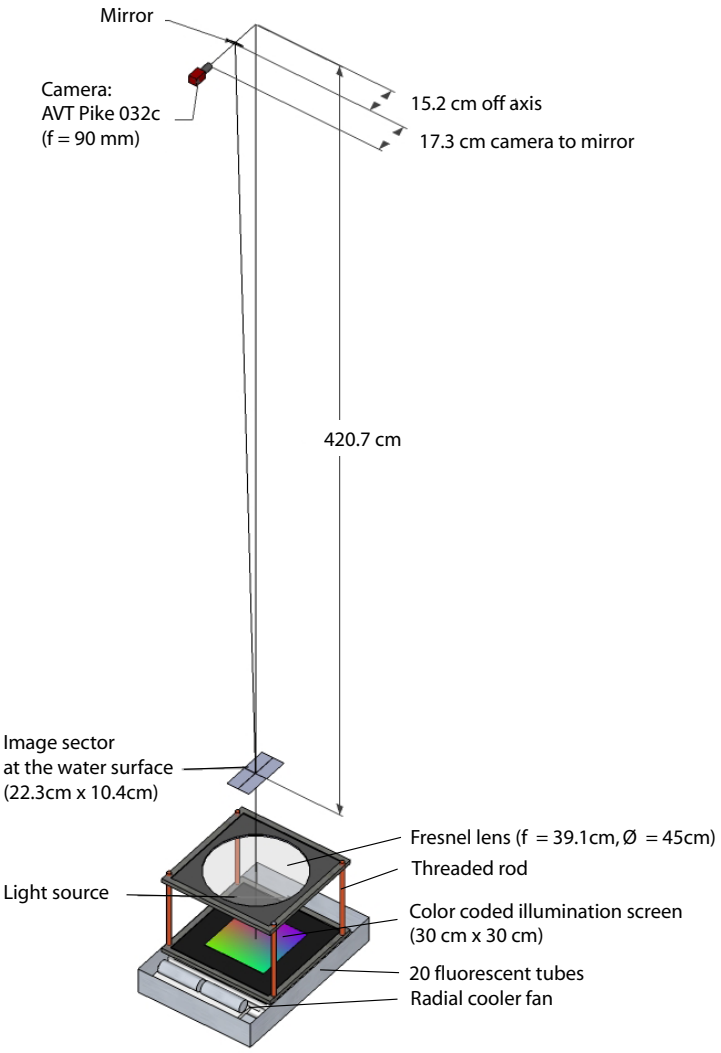

Figure 4.3.: Setup of the optical components.

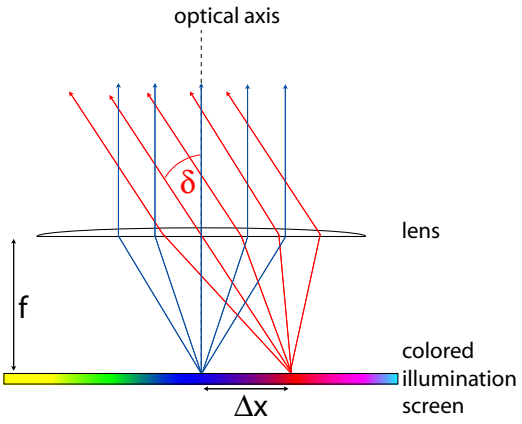

Figure 4.4.: Sketch of the telecentric color coded illumination. The ray inclination δ in the space above the lens is related to the ray deflection Δx from the origin on the illumination screen $\tan\delta = \frac{\Delta x}{f}$, where f is the focal distance of the lens. The illumination screen is color coded, so that Δx corresponds to a certain color.

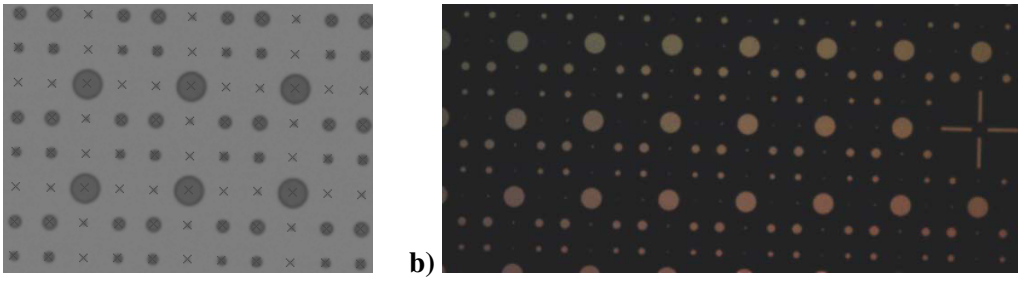

Figure 4.5.: a) Grid detection for the geometric calibration. The crosses indicate the detected centers of the circles of the MTF target. Only a subregion of the MTF target image is shown. The real-world grid spacing is 10.0 mm. **b)** Original image of the MTF target.

the center of gravity for each circle, using the gray values as weights. The world coordinates are given by a model function. Let the affine transformation between the image coordinates and the world coordinates be given by

$$\begin{bmatrix} x \\ -y \\ 1 \end{bmatrix}_{\text{world}} = \begin{bmatrix} c\cos\alpha & -c\sin\alpha & T_x \\ c\sin\alpha & c\cos\alpha & T_y \\ 0 & 0 & 1 \end{bmatrix} \begin{bmatrix} x \\ y \\ 1 \end{bmatrix}_{\text{image}} . \tag{4.2}$$

The only parameter that we are interested in is the scaling factor c, which determines the reproduction scale. The translation parameters T_x, T_y and the angle of rotation α can be arbitrary in this context. The 2x2 sub matrix

$$c \cdot \mathbf{R} = \begin{bmatrix} c\cos\alpha & -c\sin\alpha \\ c\sin\alpha & c\cos\alpha \end{bmatrix} \tag{4.3}$$

is a rotation matrix with, multiplied by a scaling factor c. The scaling factor can be computed from the square root of the determinant of the sub matrix

$$c = \sqrt{\det\left(c \cdot \mathbf{R}\right)}, \tag{4.4}$$

where we have used that $\det R \equiv 1$. The negative sign of the y-coordinate in equation (4.2) is due to the transition from a left handed image coordinate system to a right handed world coordinate system.

Results: Using the set of 88 image coordinate pairs from figure 4.5 a) the overdetermined system of equations was solved for the transformation matrix in a least squares sense. The result is

$$\begin{bmatrix} x \\ y \\ 1 \end{bmatrix}_{\text{world}} = \begin{bmatrix} 0.3491 & 0.0080 & 5.9742 \\ 0.0081 & -0.3489 & 83.4557 \\ 0 & 0 & 1.0000 \end{bmatrix} \begin{bmatrix} x \\ y \\ 1 \end{bmatrix}_{\text{image}} . \tag{4.5}$$

From (4.4) follows a scaling factor of $\Delta x = \Delta y = c = (0.3491 \pm 0.0030)$ mm/pixel which is in good agreement with the estimate from the magnification factor. For the wavy water surface we have to consider variations in the distance between the camera and the surface in the order of ± 5cm. This leads to fluctuations of Δx in the order of $\pm 1.2\%$ (where equation (4.1) has been used). A summary of the quantities that are affected by the geometric calibration is given in table 4.1.

	Quantity	Value	Unit
reproduction scale	$\Delta x = \Delta y$	(0.3491± 0.0030)	mm/pixel
image size	$X = 640 \cdot \Delta x$	(223.4 ± 1.9)	mm
	$Y = 298 \cdot \Delta x$	(104.0 ± 0.9)	mm
minimal wavenumber	$k_{x_{min}} = \frac{2\pi}{X}$	(28.12 ± 0.24)	rad/m
	$k_{y_{min}} = \frac{2\pi}{Y}$	(60.40 ± 0.52)	rad/m
Nyquist wavenumber	$k_{x_{nyq}} = k_{y_{nyq}} = 0.5 \cdot \frac{\pi}{\Delta x}$	(4500 ± 38)	rad/m

Table 4.1.: Results of the geometric calibration. Symbols x and y correspond to the along wind and cross wind direction, respectively. The factor 0.5 in the calculation for the Nyquist wavenumbers stems from the reduction of the resolution in the color interpolation, see section 6.1.

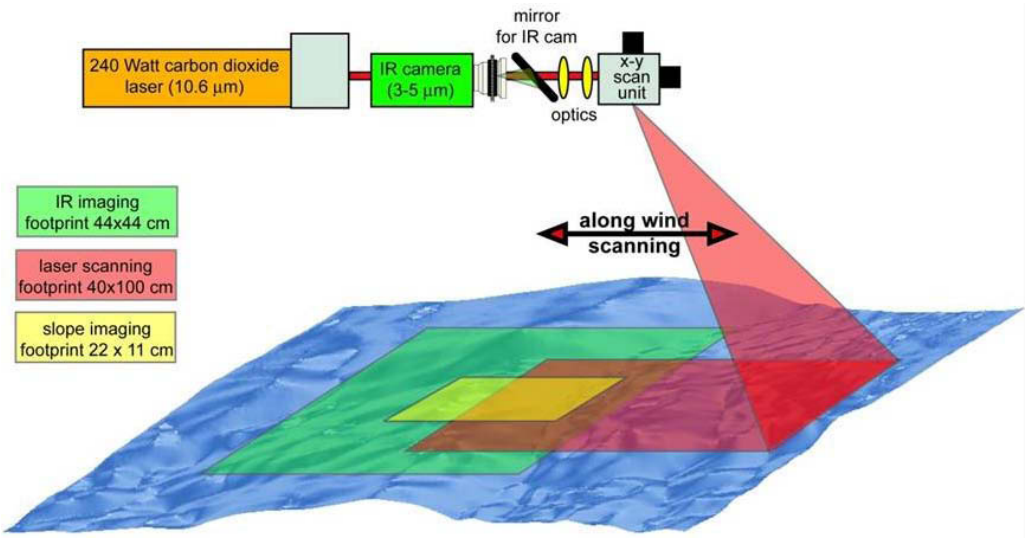

Figure 4.6.: Schematic drawing showing the overlapping footprints of the CISG camera (yellow) and the IR camera (green), as well as the scanning range of the infrared laser (red). (by Dr. Uwe Schimpf)

4.3. Registration of the IR-Images and the CISG-Images

During the WiSSCy measurement campaign the wave imaging was combined with the Active Controlled Flux System (ACFT) that was deployed by Dr. Uwe Schimpf for the measurement of the local heat flux. The ACFT system is basically consisting of i) a high power CO_2-laser, ii) a scanning mirror for the laser, and iii) an infrared camera (IR camera). The scanning laser is depositioning heat within the top 20 μm of the water surface and consequently enforces a local heat flux. The infrared camera measures the water surface temperature with a temperature resolution of about 0.020 K.

The CISG camera and the IR camera were (optionally) synchronized and had overlapping image footprints on the water surface, as shown in the schematic drawing in figure 4.6. The image footprint of the IR-camera was larger, so that the CISG image was completely enclosed. Both cameras were separated by a distance of approximately 30 cm in y-direction, i.e. perpendicular to the mean wind direction. In order to map the thermographic data on the wave images we need to compute the perspective projection of the IR-images on the CISG images. *Image registration* means to use the resulting mapping function, which leads - in our case - to fully synchronized and co-located image sequences of the wave slope and the Active Thermography.

For the computation of the perspective projection we used images of a checker-board pattern made of copper and plastic that is visible in the IR images as well as in the color images. This target was fixed at the mean water level for the acquisition of calibration images. In both calibration

images the grid points of the checker-board pattern were extracted with subpixel accuracy, using the geometric camera calibration toolbox by Jean-Yves Bouguet[21]. Then the grid point coordinates were used as controll points for the Matlab®function `cp2tform`, yielding the perspective transformation matrix. Using the transformation matrix we computed the corner coordinates of the color image in the IR image domain.

Since the CISG camera had to be exchanged during the course of the measurement campaign we had to perform these steps twice, yielding two sets of corner points

```
points[0] = {238.8748 , 85.0057};
points[1] = {106.4029 ,  89.9214};
points[2] = {109.5777 , 151.1468};
points[3] = {241.0080 , 146.3073};
```

valid before June the 14th 2007, and

```
points[0] = {168.6401 , 77.8098};
points[1] = {36.3000  , 83.8252};
points[2] = {39.5682  , 145.7987};
points[3] = {171.5244 , 138.7481};
```

valid after June the 14th 2007. Overlays of the two sets of calibration images and the location of the corner points are shown in figure 4.8. The actual registration of the image sequences was then performed by the Heurisko®build-in operator `TransformPerspectiveByPoints`. This operator extracts the data from the IR-image within the polygon defined by the corner points and performs an interpolation onto a regular grid that is the CISG image domain, see figure 4.7. The registration is not corrected for changes of the mean water level or for distance changes due to the waves amplitudes. These changes of the object distance are in the order of 1%. This leads to minor relative shifts of the images, because the perspective transformation assumes a constant object distance and a planar object. However, the registered image sequences now allow for a direct visual comparison of the moving wave field and the thermal signature of the infrared laser on the water surface, see section 7.5. Figure 4.9 shows two examples for the registration results. These images show impacts of rain drops that as blue dots in the false color temperature overlay. The images of raindrop impacts are chosen to give an impression of the accuracy of the images registration, see image caption for details.

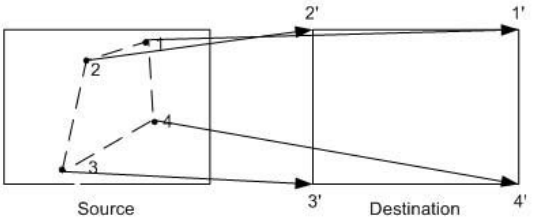

Figure 4.7.: Arrangement of the corner points for the Heurisko®operator `TransformPerspectiveByPoints`, Source: Heurisko®6.0 documentation

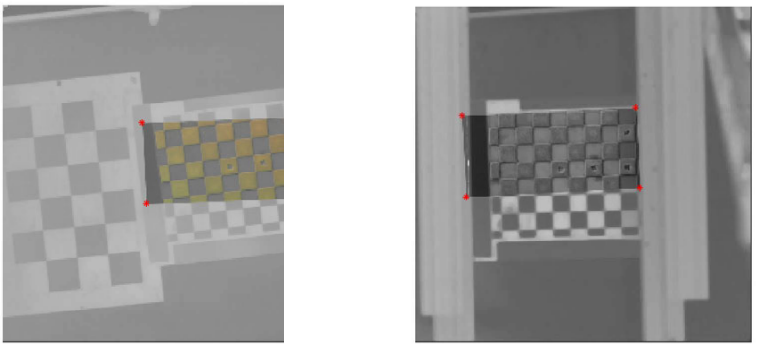

Figure 4.8.: Location of the CISG image (confined by the corner points, marked by the red stars) within the IR image domain. **a)** Overlay of the calibration images from Mai the 14^{th} 2007. **b)** Overlay of the calibration images from June the 14^{th} 2007 after the exchange of the CISG camera.

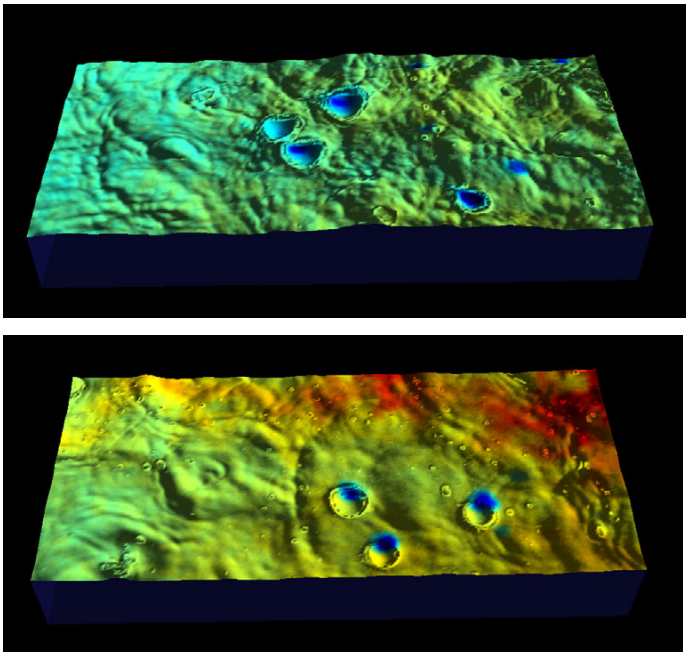

Figure 4.9.: Examples for the registered color overlay of the temperature images on the visualization [89] of the water surface. The water height is reconstructed from the slope measurement and rendered in a perspective view, see section 7.5. The colors of the overlay correspond to the temperature, where blue indicates cold and red means warm areas. In the top image several impacts of cold rain drops on the water surface are clearly collocated in the temperature overlay and the wave rendering, indicating that the registering was accurate. In contrast, the rain drops signatures show a slight residual shift in the bottom example.

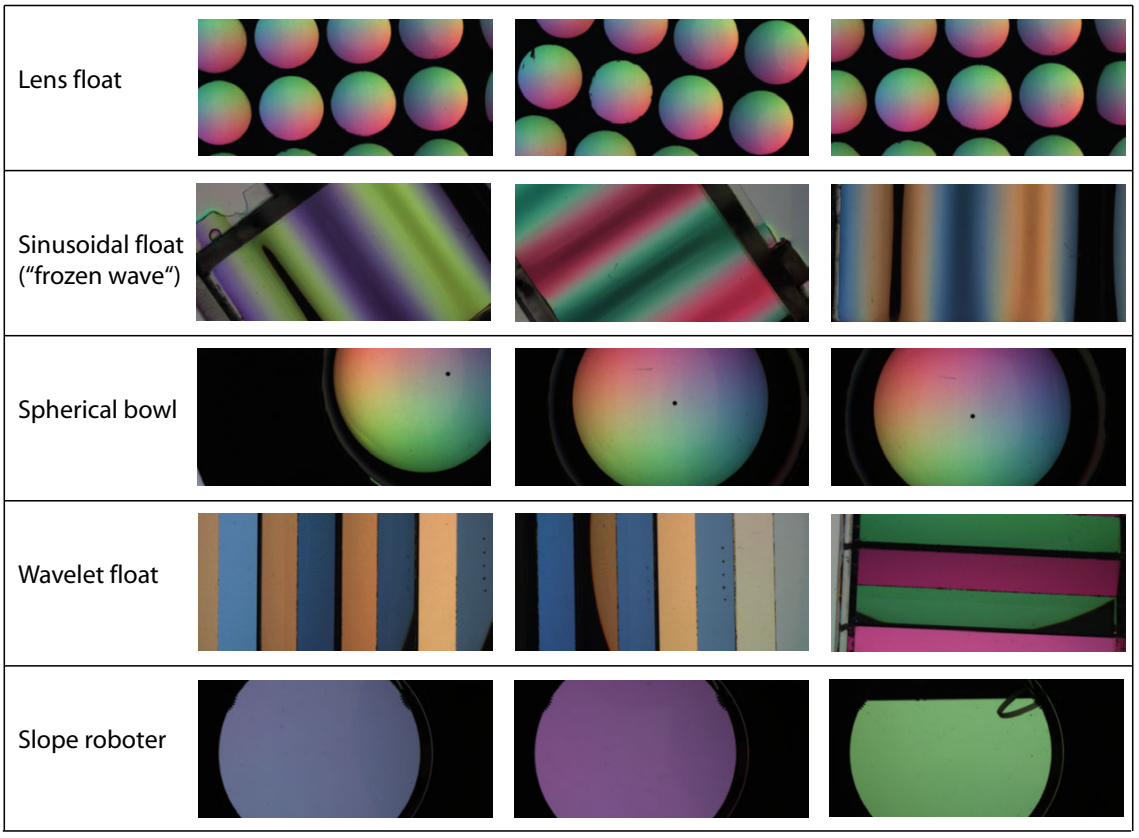

Figure 4.10.: CISG images of different calibration targets that have been deployed during the WiSSCy campaign.

4.4. Slope Calibration

The color in each pixel of the CISG images changes according to the slope of the water surface that is observed by the pixel. The principal relationship between the color and the slope is given by the combination of the ray tracing equation (3.7) and the color coding scheme of the illumination (3.10). However, for the real setup there are several reasons that prohibit the simple use of these equations for the slope calibration. The main reason is that the color coding scheme cannot be perfectly realized by a color transparency. Additionally, the ideal ray geometry is hardly met in reality and we have to consider a misalignment of the optical components (camera, mirror, water surface at rest, glass window, Fresnel lens, illumination screen). Thus we need to perform slope calibration measurements in order to determine the functional relationship f between the three color components $\mathbf{c} = [r, g, b]^T$ and the two components of the slope $\mathbf{s} = [s_x, s_y]^T$

$$\mathbf{c} \in \mathbb{R}^3 \xrightarrow{f} \mathbf{s} \in \mathbb{R}^2. \tag{4.6}$$

Of course, one can not perform a calibration at the free water surface. But using calibration targets we can force the interface to a known shape. For instance, Klinke [93] used a plexiglass float that defines a target function with eleven distinct slope values. This target, herein called the *wavelet target*, is shown in figure 4.11 a). For the calibration measurement the wavelet target is floating on the water surface, so that no air is enclosed under the float and no water is on top. The thickness of the plexiglass causes a minor displacement of the light rays, but does not change the rays inclination and can therefore be neglected. A similar calibration target, e.g. used by Jähne and Schultz [86], is the *frozen wave*, which is a sinusoidal float. The slope of the *frozen wave*

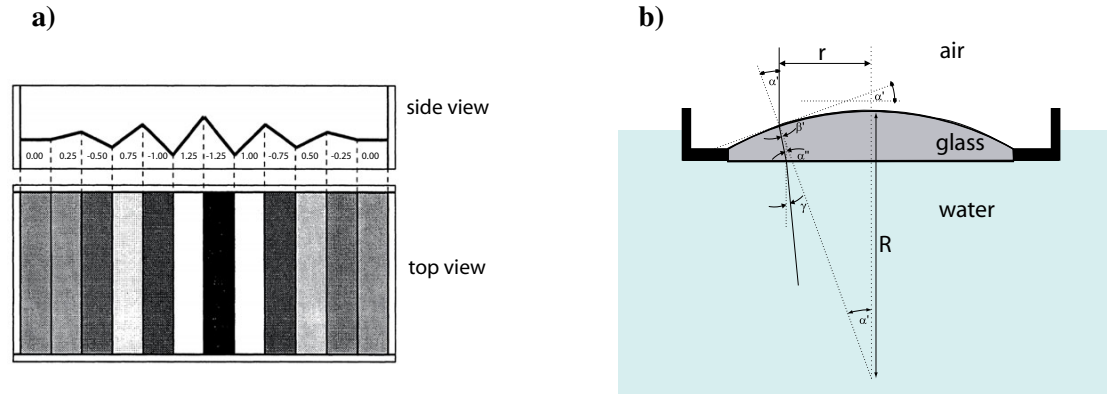

Figure 4.11.: Slope calibration targets. **a)** Sketch of the wavelet calibration target. The numbers indicate slope values for the different segments of the plexiglass float. (modified after [93]). **b)** Sketch of the lens float. The slope is a function of the position r on the lens, compare (4.7). (modified after [9])

and the *wavelet target* only changes in one direction. In order to comprise the 2D slope domain it is therefore necessary to make calibration images with different orientations of the targets. If the calibration function f is additionally dependent on the pixel position, then the calibration measurement and its evaluation become quite complex. The example images for the *frozen wave* and the *wavelet target* in figure 4.10 exemplify how the calibration images vary according to the orientation and position.

To overcome the difficulties arising from the orientation dependency, Balschbach [9] and later Fuß [50] used another type of calibration target which we call a *lens float*. This target consists of planoconvex lenses that are embedded into the bottom of a float as shown in figure 4.11 b). The lenses have the shape of a spherical segment with known radius R, so that the lens slope $\mathbf{s}_L$ can be computed as a function of the distance $\mathbf{r} = [\Delta x, \Delta y]^T$ from the lenses centers

$$\mathbf{s}_L = \frac{-\mathbf{r}}{\sqrt{R^2 - |\mathbf{r}|^2}}. \tag{4.7}$$

The index of refraction of the lens material is different from that of water. In order to translate lens surface slope (4.7) into water surface slope, also the second refraction at the flat lens bottom needs to be taken into account [9, 50, 76].

The lenses produce a continuous target function for both slope components. Therefore a single calibration image already delivers the information for the 2D slope domain and can be used to determine the calibration function f. This relies on the assumption that f can be considered as constant over the lens, i.e. the position dependency is weak within the spatial extend of one lens, which is true if a telecentric illumination is implemented. The position dependency can be checked by comparing the calibration for the lenses at the different positions in the image. Consequently, the employment of the *lens float* yields a considerable improvement of the calibration routine, compared to the *frozen wave* and the *wavelet target*. But still the calibration measurements with *lens floats* show some difficulties. First of all, it is not always possible to guarantee that the water body is completely at rest and that the float is perfectly balanced. Secondly, the use of equation (4.7) implies that the lens center can be accurately detected, which is not always true. For these reasons it is hard to automatize the evaluation of the calibration images. Example images made with different calibration targets acquired during the WiSSCy campaign are shown in figure 4.10. A systematic investigation of the calibration function with respect to height order position dependencies turns out to be very involved when using the floating targets (e.g. [50]).

This was the motivation to revive a method that was used for the calibration of a *laser slope gauge* (LSG) in the 70's and 80's. This method is based on mechanically adjustable slope of a

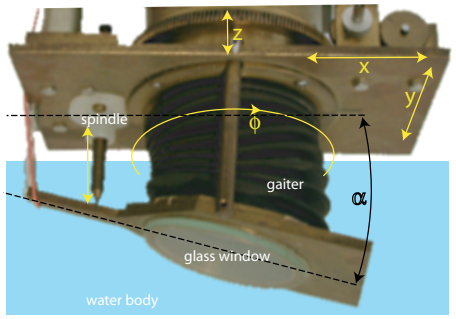

Figure 4.12.: LSG calibration apparatus

glass window rather than on a floating target. Figure 4.12 shows the apparatus that was build for the calibration of an LSG. Basically it consists of a glass window that is put in the water while a gaiter[8] prevents that water floods the glass from above. The inclination of the glass window can be adjusted by a spindle. Additionally, it was possible to alter the orientation of the apparatus so that the decomposition of the total inclination into the two slope components could be freely chosen. Thus the evaluation of the calibration data gathered by such a method is less susceptible to errors due to the determination of the target slope.

For the CISG calibration the window size of the apparatus in figure 4.12 was to small. Thus we build a bigger apparatus with an open aperture of 15 cm, see figure 4.13. We will refer to this slope calibration apparatus as the *slope robot*. The inclination of the glass window of the *slope robot* is dictated by the supporting points of three spindles that are driven by step motors. The vertical displacement of the spindles can be controlled via a computer interface and with an accuracy better than ± 0.1 mm. This gives an estimate of the maximum absolute error of the slope of the glass window that is $\Delta s_{max} = 0.0013$, where the trihedral geometry of the spindles has been incorporated. Apart from the slope it is also possible to adjust the mean height to investigate the height dependency without the need to change the mean water level. The glass window is surrounded by a baby swimming pool that serves as a gaiter and displaces the water, see figure 4.14. The contact between the spindles and the glass window is enforced by the buoyancy of the pool and some counter weights. For the WiSSCy slope calibration measurements a rubber band was fixing the position of one of the spindles, since fixation with a bearing was not possible. In principal the slope calibration was performed by a computer script that was commanding the settings of the *slope robot* and acquiring an image with the CISG camera for each slope configuration. The slope limit from the geometry of the *slope robot* is $|\mathbf{s}| < 1$. In practice it was necessary to manually control that the contact between the spindles and the glass window was always established and that the spindles did not stagnate because of too high forces and torsional moments. The actual slope limitation due to these issues was $|\mathbf{s}| < 0.56$. The occurrence of stagnation could be detected by the sound of the step motors and by controlling the zero point at the end of the measurement. The slope zero point was controlled by a surveyor's level at the beginning and at the end of each calibration measurement.

The benefit of the usage of the *slope robot* is an ideal data set for calibration, i.e. a set for the slope vector $\mathbf{s}_i$ and a corresponding color image sequence $\mathbf{c}_i$.

4.4.1. Measurements

During the course of the WiSSCy campaign the *slope robot* was set up several times to perform calibration measurements. The distinct dates and conditions are listed in table 4.4.1. Additionally, for each experiment, calibration images have been acquired, using the different kinds of floating targets that are shown in figure 4.10. With these measurements the quality of the calibration could

[8] german: Faltenbalg

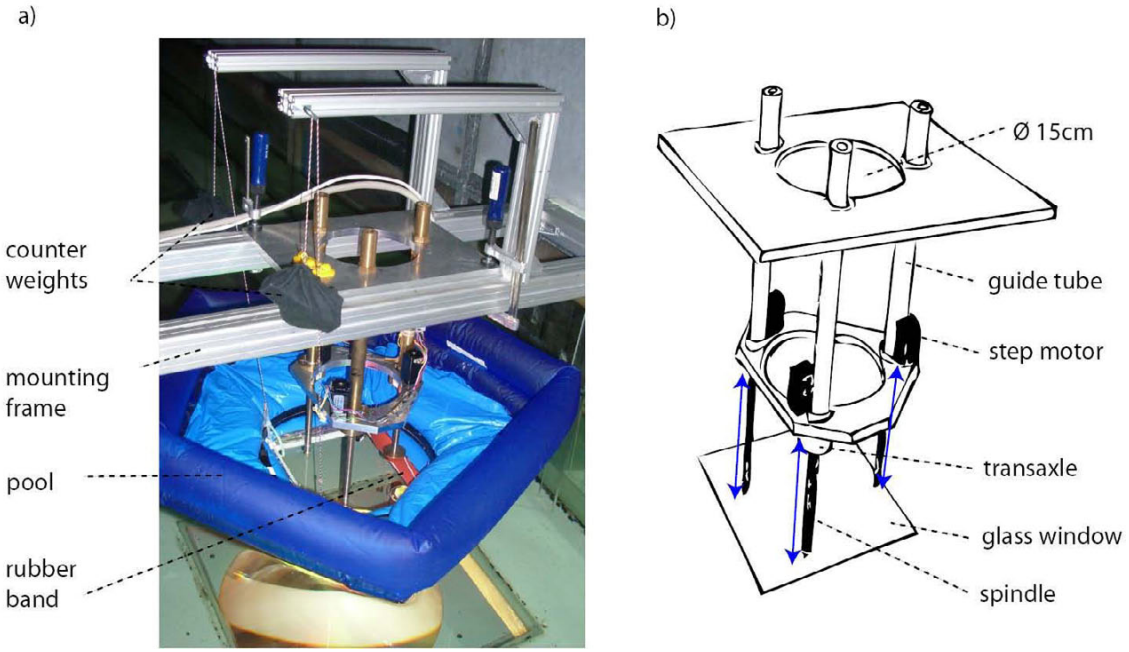

Figure 4.13.: The *slope robot*. **a)** The robot is mounted on a frame in the water filled wind wave flume. The swimming pool displaces the water from the top of the glass window. The inclination of the glass window is adjusted by three spindles. **b)** Sketch of the basic mechanical components of the apparatus.

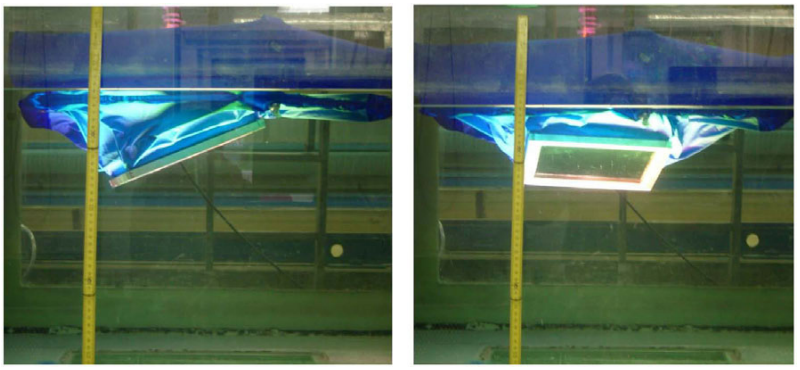

Figure 4.14.: Sideview of the *slope robot* in operation.

be monitored.

For the main calibration measurements (Run013 and Run157) the trajectory of the *slope robot* was programmed to be like a spiral on a regular grid, as shown in figure 4.15. The regular grid was chosen because this is very convenient for the evaluation of the calibration. With the spiral trajectory the traverse path of the spindles is reduced considerably, compared to a regular scanning of the slope domain. The spiral started at the origin of the s_x–s_y plane. The robot returned to the initial position after the outermost coordinate was reached. This is used for a quality control as explained in the preceding section.

In the main calibration measurements the mean water height (at the center of the open aperture) was kept constant. For the measurements Run384 through Run387 the height was also varied. The slope is varied along a line in the s_x–s_y plane. The orientation of the line was chosen to be 0, $\frac{\pi}{4}$, $\frac{\pi}{2}$ and $\frac{3\pi}{2}$ for the four consecutive measurements. For each slope configuration the height was varied in seven steps from -30 mm to 30 mm around the mean water level.

Run	Date	Time	Slope-Range	Grid s_x,s_y,h	Number of Images
009	07.05.07	17:58:26	0.05	3,3,1	14
010	07.05.07	18:19:27	0.05	3,3,1	14
011	07.05.07	18:25:43	0.4	7,7,1	58
012	08.05.07	11:36:33	0.4	3,3,1	14
013	08.05.07	12:21:24	0.4	15,15,1	242
014	08.05.07	17:31:33	0.5	7,7,1	58
104	13.06.07	18:25:00	0.1	7,7,1	58
105	13.06.07	18:52:00	0.1	7,7,1	58
106	13.06.07	19:27:00	0.4	7,7,1	58
156	18.06.07	09:17:05	0.5	7,7,1	58
157	18.06.07	09:37:52	0.4	11,11,1	133
384	03.07.07	09:26:12	0.4	17,1,7	121
385	03.07.07	10:09:36	0.4	17,1,7	121
386	03.07.07	10:48:54	0.4	17,1,7	121
387	03.07.07	11:23:04	0.4	17,1,7	121
388	03.07.07	11:50:20	0.3	7,7,1	58

Table 4.2.: Calibration measurements with the *slope robot*. For the measurements Run009 through Run157 and Run388 the slope components are set to values on a regular grid, while the mean height is kept constant. For Run384 through Run387 the slope components are chosen to lie on a line with certain orientation and for each slope setting the mean height is varied in seven steps.

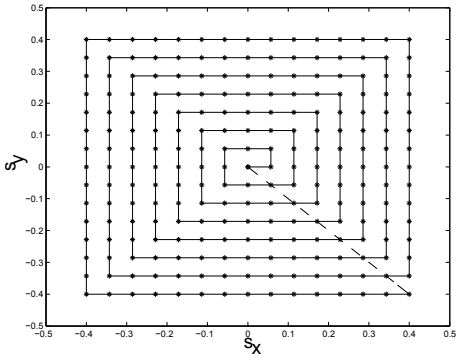

Figure 4.15.: Trajectory of the slope configuration of the robot for Run013.

4.4.2. Color Processing

The slope calibration is based on the images after some color processing steps. At first, the raw images are converted into color images via demosaicing, see section 6.1 and 2.5.3. As a second step the color channels are corrected for intensity fluctuations by normalization. The third step is a pixelwise correction for a constant offset. Let $\mathbf{C}$ denote the multi-channel images after the demosaicing[9]

$$\mathbf{C}_{i,j} \equiv \begin{bmatrix} R_{i,j} \\ G_{i,j} \\ B_{i,j} \end{bmatrix}, \tag{4.8}$$

where i, j are the pixel indices for the y and x direction respectively. As for the color coding scheme (3.11) we define the pixelwise intensity $I_{i,j}$ as the mean value of the three colors

$$I_{i,j} \equiv \frac{R_{i,j} + G_{i,j} + B_{i,j}}{3}. \tag{4.9}$$

[9]Here, the MTF correction is dispensable since a flat plane is being imaged.

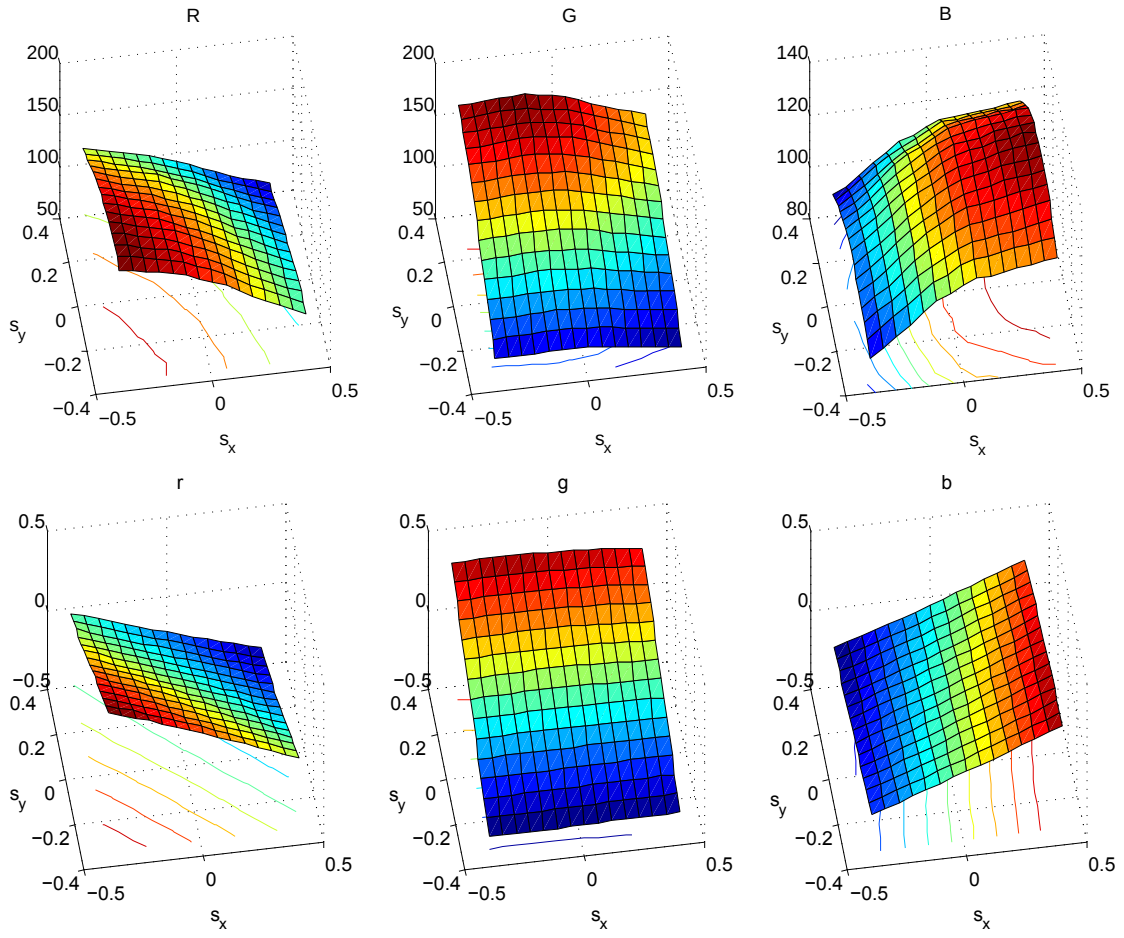

Figure 4.16.: Variation of the color components R, G, B with the slope s_x, s_y. Dataset: Run013. **Top row:** The colors have not yet been offset corrected or normalized. **Bottom row:** color channels after offset correction and intensity normalization showing much better linearity.

For convenience we skip the pixel indices i, j in the following and note that all operations are point operations if not mentioned explicitly elsewise. Now let $\mathbf{C}_o$ denote the offset image and let I_o be the corresponding intensity image. The resulting multi-channel image $\mathbf{c}$ after the color processing can then be formally written as

$$\begin{bmatrix} r \\ g \\ b \end{bmatrix} \equiv \mathbf{c} \equiv \frac{\mathbf{C}}{I} - \frac{\mathbf{C}_o}{I_o}, \tag{4.10}$$

compare Balschbach [9] and Fuß [50]. The effectiveness of the color preprocessing is evident from figure 4.16. This figure shows how the color components vary with the slope for the calibration Run013. The color components before the preprocessing steps are displayed in the top row. From the color coding design we would expect a linear relationship if the intensity and the offset were independent from the slope. One can see obvious deviations from this linearity, which is mainly due to variation in I. The bottom row shows the same data after the preprocessing according to (4.10). The nonlinearities are almost perfectly compensated for.

4.4.3. Parameter Estimation

The robot calibration data sets are used to estimate the parameters that allow to compute the slope components by a polynomial function of the colors. The linear behavior that is demonstrated in

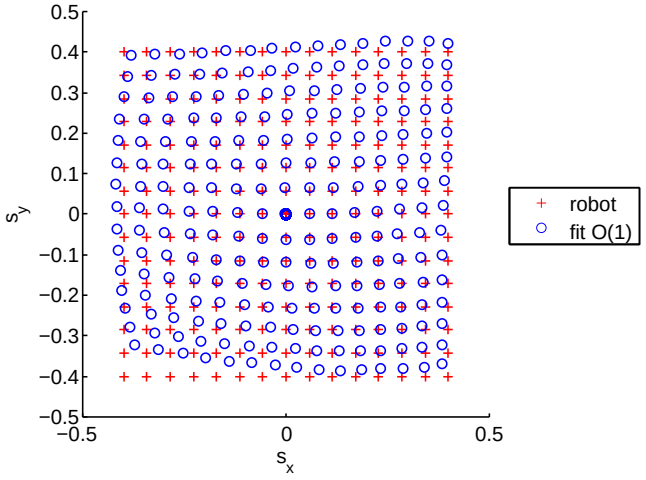

Figure 4.17.: Results for the robot slope calibration Run013. Fit-model: linear. Fit parameters are based on the same run.

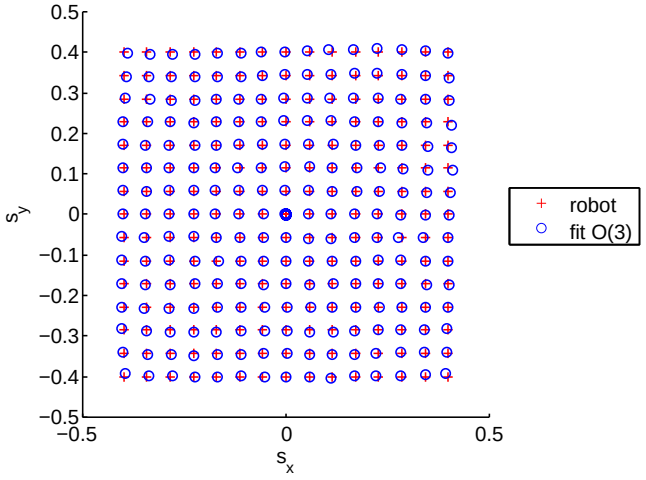

Figure 4.18.: Results for the robot slope calibration Run013. Fit-model: cubic. Fit parameters are based on the same run.

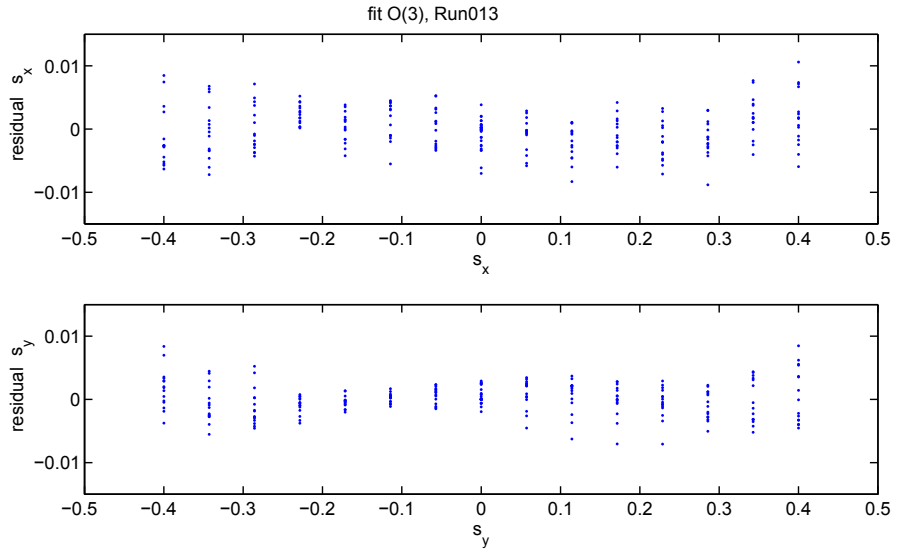

Figure 4.19.: Residuals of the higher order model fit for Run013.

figure 4.16 (bottom row) suggests a pure linear combination

$$\mathbf{s} = \mathbf{Q}\,\mathbf{c}, \tag{4.11}$$

where $\mathbf{Q}$ is the 2×3 parameter matrix. Indeed all former practical calibrations for the imaging slope gauges were somehow restricted to such a linear model (e.g. [9, 50, 93, 141]), except for the early works by Zhang and Cox [181] who used different color coding schemes.

Linear Model:

We want to compute the parameter matrix $\mathbf{Q}$ in (4.11) from the calibration measurements. At first we determine the pseudo inverse of the transpose of this matrix in the least squares sense. For this we can follow the formalism for solving an overdetermined discrete inverse problem as described in Jähne [77]. The robot slope settings s_x and s_y define the model matrix

$$\mathbf{S} \equiv \begin{bmatrix} s_{x_1} & s_{y_1} \\ s_{x_2} & s_{y_2} \\ \vdots & \vdots \\ s_{x_N} & s_{y_N} \end{bmatrix}, \tag{4.12}$$

where N is the number of data points in the calibration set which is given by the number of steps of the calibration multiplied by the number of pixels that are taken for the evaluation. The data matrix is given by the slope–corresponding color values after the color preprocessing

$$\mathbf{D} \equiv \begin{bmatrix} r_1 & g_1 & b_1 \\ r_2 & g_2 & b_2 \\ \vdots & \vdots & \\ r_N & g_N & b_N \end{bmatrix}. \tag{4.13}$$

The linear equation system can then be written as

$$\mathbf{S}\mathbf{P} = \mathbf{D}, \tag{4.14}$$

where $\mathbf{P}$ is a 2×3 parameter matrix which is the pseudo inverse of $\mathbf{Q}^T$. We can solve the system of equations for $\mathbf{P}$ by multiplying the equation by the *Moore-Penrose* pseudo inverse $\mathbf{S}^{-1}$ [95]. In Jähne [77] it is explicitly shown that this procedure yields an estimate for the parameter matrix that minimizes the norm of the residual in the least squares sense

$$\begin{aligned} ||\mathbf{e_r}||_2^2 &= ||\mathbf{D} - \mathbf{S}\mathbf{p_r}||_2^2 \rightarrow \text{minimum} \\ ||\mathbf{e_g}||_2^2 &= ||\mathbf{D} - \mathbf{S}\mathbf{p_g}||_2^2 \rightarrow \text{minimum} \\ ||\mathbf{e_b}||_2^2 &= ||\mathbf{D} - \mathbf{S}\mathbf{p_b}||_2^2 \rightarrow \text{minimum}. \end{aligned} \tag{4.15}$$

The vectors $\mathbf{p_r}$, $\mathbf{p_g}$ and $\mathbf{p_b}$ are the columns of the matrix $\mathbf{P}$. As a second step the matrix $\mathbf{Q}^T$ is determined by computing the pseudo inverse of $\mathbf{P}$, based on a singular value decomposition[10]. Then we can rewrite the problem as $\mathbf{S}^T = \mathbf{Q}\,\mathbf{D}^T$, corresponding to (4.11). As error measures we compute the residual of the slope components $||\mathbf{e_{s_x}}||_2^2$ and $||\mathbf{e_{s_y}}||_2^2$, which finally gives the unbiased variance between the ground truth and the measured slopes from

$$\begin{aligned} \sigma_x^2 &= \frac{1}{N-f}\,||\mathbf{e_{s_x}}||_2^2 \\ \sigma_y^2 &= \frac{1}{N-f}\,||\mathbf{e_{s_y}}||_2^2, \end{aligned} \tag{4.16}$$

[10] For this, the Matlab® function `pinv` was used.

where $N - f$ is the number of degrees of freedom (here $f = 3$) [77]. The resulting parameter matrices $\mathbf{Q} = \left(\mathbf{P}^{-1}\right)^T$ and error measures for different calibration measurements are listed in table 4.3. The quality of the fit can be assessed visually with s_x–s_y scatter diagrams as in figure 4.17. The diagram shows the result for the linear fit (blue circles) for Run013 along with the target slope values (red crosses) of the *slope robot*. We can see that the linear model fits well only for $|\mathbf{s}| < 0.2$. Deviations are obvious for higher slope values, especially in the first and third quadrant of the slope coordinate system. A better slope calibration is achieved using a higher order polynomial model, which is described in the following.

Higher order model:

The deviations from linearity that are visible in figure 4.17 can be effectively compensated using a higher order polynomial model for the fit. Extensive tests on the calibration data revealed that the simplest model which has a good performance is of the form

$$\mathbf{s} = \mathbf{Q} \left[\begin{array}{cccccccccc} r & g & b & r^2 & g^2 & b^2 & r^3 & g^3 & b^3 \end{array} \right]^T, \tag{4.17}$$

where $\mathbf{Q}$ is a 2×9 calibration parameter matrix. Let $\mathbf{D}$ be the extended N×9 data matrix defined by

$$\mathbf{D} \equiv \left[\begin{array}{ccccccccc} r_1 & g_1 & b_1 & r_1^2 & g_1^2 & b_1^2 & r_1^3 & g_1^3 & b_1^3 \\ r_2 & g_2 & b_2 & r_2^2 & g_2^2 & b_2^2 & r_2^3 & g_2^3 & b_2^3 \\ \vdots & \vdots & \vdots & \vdots & \vdots & \vdots & \vdots & \vdots & \vdots \\ r_N & g_N & b_N & r_N^2 & g_N^2 & b_N^2 & r_N^3 & g_N^3 & b_N^3 \end{array} \right], \tag{4.18}$$

then we can again write (4.17) as the matrix equation

$$\mathbf{S}^T = \mathbf{Q}\,\mathbf{D}^T, \tag{4.19}$$

where $\mathbf{S}$, defined in (4.12), holds the robot slope values as for the linear model.

The method of matrix inversion that we used for the linear model fails if we try to solve for the parameter matrix $\mathbf{Q}$ by extending the data matrix $\mathbf{D}$. Instead we use the Matlab®nonlinear optimization function `lsqnonlin` in order to minimize the cost function

$$\mathbf{E}(\mathbf{Q}) = \sum_{i=1}^{N} |\mathbf{e}_i(\mathbf{Q})|^2 = \sum_{i=1}^{N} \left|\mathbf{s}_i - \mathbf{Q}\,(\mathbf{D}_i)^T\right|^2, \tag{4.20}$$

where $\mathbf{E}$ contains the two components for the L_2 norm of the residuals, and i is the index of the calibration data points. The resulting parameter matrices $\mathbf{Q}$ and error measures for different calibration measurements are listed in table 4.3.

Applying this higher order model to the data of Run013 reduces the variances σ_x^2 and σ_y^2 by a factor of 6.4 and 26.9, respectively, in comparison to the linear model results. This is also apparent from figure 4.18 which shows the result for the same data as in figure 4.17. With the calibration based on equation (4.17) the target slope values are within the error bounds due to noise. The fit residuals are displayed in figure 4.19, showing that the deviations are within a ± 0.01 range for slopes within a range of ± 0.4 for both slope components. Concerning the slope magnitude[11] the deviation is consequently less than 2% for $|\mathbf{s}| = 0.56$.

[11] $|\mathbf{s}| = \sqrt{s_x^2 + s_y^2}$

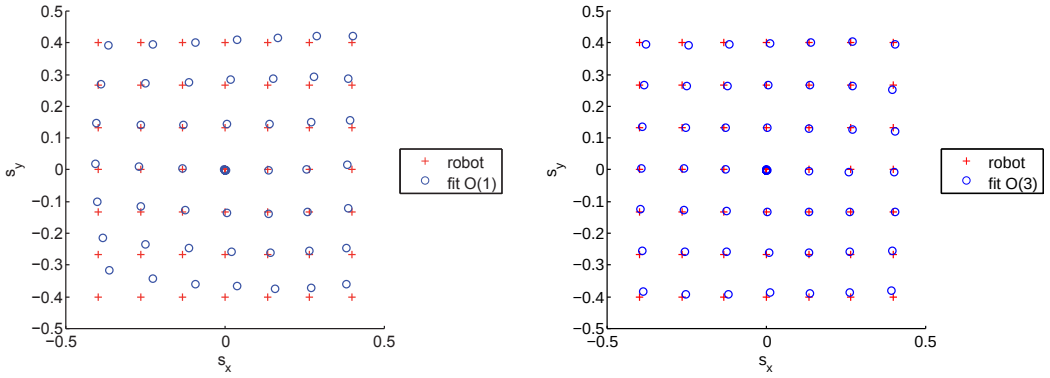

Figure 4.20.: Results for the robot slope calibration Run106. Fit coefficients are based on Run013. **Left:** linear calibration. **Right:** cubic calibration.

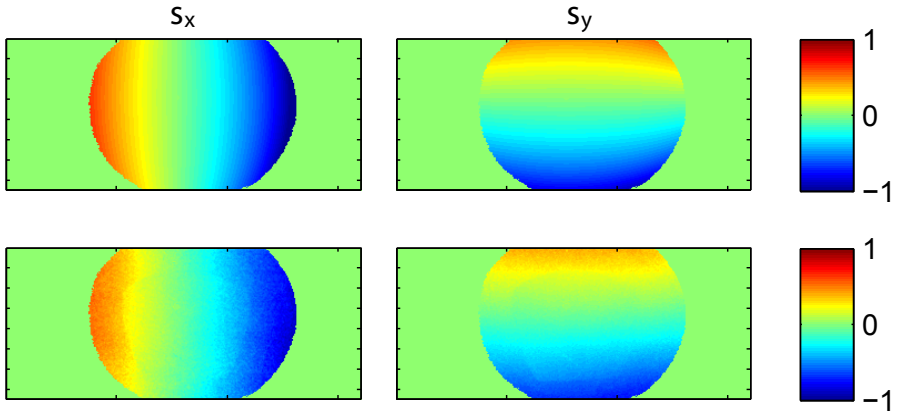

Figure 4.21.: The geometrically expected slope of the *spherical bowl* (top row) and the calibration result (bottom row) for the nonlinear calibration. (Data: Run144. Calibration parameters: Run157).

Extrapolation: The robot calibration data cover a slope range of at most $|\mathbf{s}| \leq 0.7$. See for instance figure 4.22. As pointed out in Jähne et al. [85] about 30% of the slopes of the wind wave field are found within the range between 0.4 and 1.0 for a high windspeed of 14 m/s, and only 0.44% of the slope values are higher than 1 for that wind condition. This estimate is based on measurements of the slope distribution performed with a laser slope gauge in the Marseille wind/wave flume [87]. Hence, we have to check how the calibration model performs for higher slopes. Especially overshooting must be prevented to avoid artifacts in the wave spectra, e.g. spectral leakage due to discontinuities. The extrapolation can be checked by an evaluation of the slope targets. Here we show the result for the sequences taken with the *spherical bowl* slope target. Images of this target are shown in the third row of figure 4.10. The bowl is made of thin transparent plastic and has a radius of $R = (10.15 \pm 0.15)$cm. The deepest point of the free floating sphere was marked simply by a little rolling marble. The position of the marble defines the coordinate system of the bowl ($\mathbf{r} = \mathbf{s} = 0$). From the reproduction scale and the sphere radius we get the slope for each pixel by using equation (4.7). For the bowl we do not need to consider a second refraction as for the *lens float*. The range of target slopes that are given by the *spherical bowl* images is about ± 1. With this we can qualitatively evaluate the extrapolation of the calibration for higher slopes. To exemplify this, in the top row of Figure 4.21 the geometrically expected slope components are displayed. The result of the calibration is shown in the bottom row for comparison. As we can see, the calibration performs well. A closer look at the data reveals that extrapolated slope values tend to be slightly underestimated within -8%. This is a very satisfactory result with respect to the high absolute slope range.

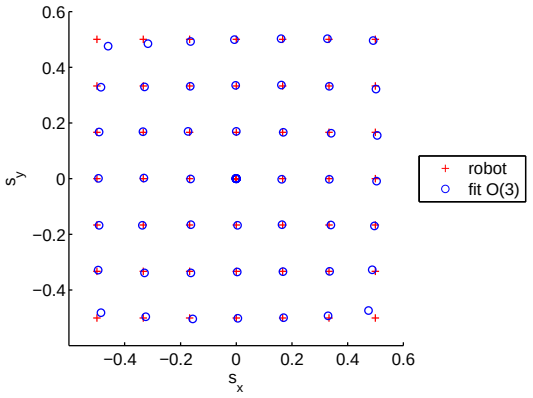

Figure 4.22.: Results for the cubic robot slope calibration Run156. Fit coefficients are based on Run157.

Inter–Variability: The variability of the calibration can be checked by an inter-comparison of the calibration result for the different measurements. Figure 4.20 exemplifies the accuracy of the slope computation for Run106, using the calibration parameters from Run013 which was performed more than one month earlier, see table 4.4.1. The comparison with figure 4.18 demonstrates the good repeatability of the calibration. No significant inter–variability is found. However, because of the camera exchange, the calibration parameters are different for the measurements Run001–Run107 and Run108–Run447. An example for the calibration result after the camera exchange is shown in figure 4.22 for the sake of completeness.

Position–Dependency: The parameter estimation already makes implicit use of the assumption that the calibration does not depend on the pixel position, because spatially averaged color values have been used for the entries in the data matrix. The color averages have been taken over the whole open aperture (diameter 15 cm) in the images of the slope robot. This is justified by the fact that the scatter[12] in the color values after the color processing steps is reasonable low, see for instance figure 4.23 where the standard error of the averaged color components is displayed. In addition to this, the position dependency has been checked qualitatively with the sequences of the *lens float*. In summary we can state that the calibration shows no significant position dependency, except for some systematic deviations at the windward boarder of the image. These deviations are attributed to reflections between the Fresnel lens and the glass window that cannot be corrected for.

Height–Dependency: In section 3.1.2 we have seen, that the ideal ray trace does not depend on the height of the water column. This is because the height influence is compensated by an implementation of the telecentric illumination. Anyhow, as pointed out by Fuß [50], the compensation is not always perfect, mainly because of aberration effects of the fresnel lens. For the WiSSCy campaign the wave amplitudes are small compared to measurements at the Heidelberg Aeolotron[13]. In our case, even for the highest wind speeds, the maximal wave amplitudes are well within $\pm 7\%$ of the mean water level. We can check the influence of height variations based on the evaluation of the measurements Run384–Run386. For these runs the mean water height was varied additionally in a manner that was already described in section 4.4.1. From figure 4.24 it is apparent that we have no height dependency of the slope calibration. For each slope configura-

[12] Note that any color variations, and thus variations in the calibrated slope, are due to position and height effects at the same time.

[13] The Hamburg facility is a linear flume with limited fetch whereas the Aeolotron is a circular facility with *infinite fetch* with much higher wave amplitudes for a given wind speed.

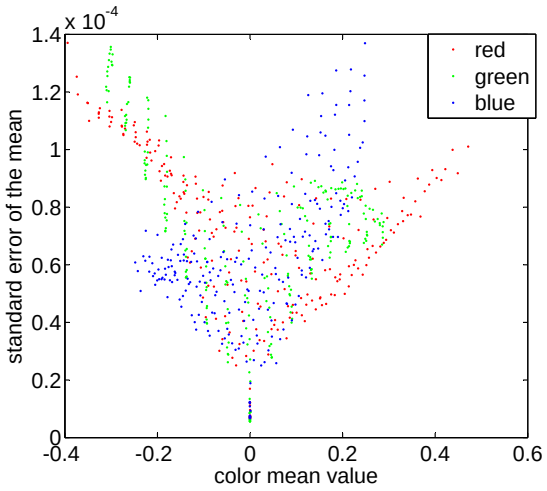

Figure 4.23.: Standard error of the color averages. (Data: Run013)

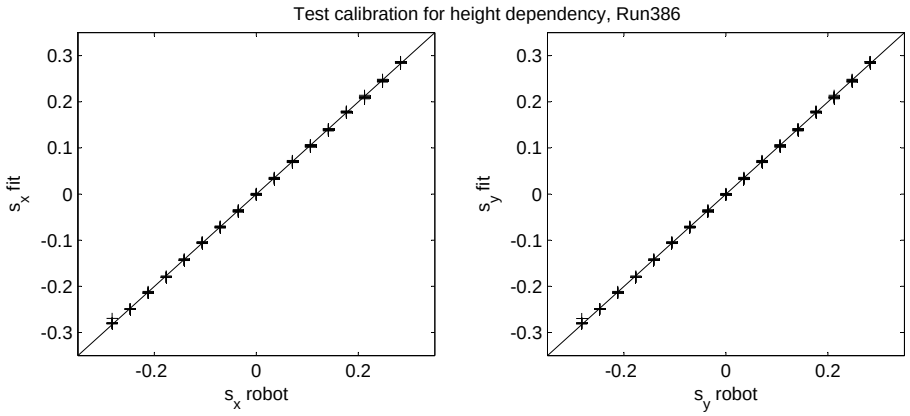

Figure 4.24.: Check for height dependency of the calibration. The mean height was varied in seven steps over a range of ± 35 mm for each robot slope setting (data: Run386). For each robot slope setting the seven corresponding slope values after the calibration almost collapse on single points. Thus, there appears no effect on the slope calibration due to the height variation.

tion the seven datapoints taken at different heights are reproducing calibrated slope values without significant deviations.

4.4.4. Summary

We have shown that the calibration of the CISG is improved by a nonlinear model that is used to fit the slope-color relationship. The absolute errors for small slopes ($|\mathbf{s}| < 0.4$) are smaller than ± 0.01, which is about the level of accuracy that can be achieved with respect to noise and the 8bit gray value discretization. For high slopes ($|\mathbf{s}| \sim 1$) the uncertainties are in the range of -10%, which is actually quite good in comparison with former studies. The recent implementation of the CISG shows no significant position dependency for the calibration. However, some symstematic errors can be observed at the windward boarder of the image. These errors are due to reflections between the fresnel lens and the glas window and therefore can not be corrected. No height dependency is observed within the range of the wave amplitudes. This comprehensive study of the calibration has become possible by the deployment of the *slope robot*. For future studies the robot needs to be improved such that the calibration measurement can indeed be performed without manual assistance.

		linear	cubic
Run013	Q	$\begin{bmatrix} 0.6647 & 0.3774 & -1.2104 \\ 0.4511 & -0.9069 & 0.4033] \end{bmatrix}$	$\begin{bmatrix} 0.6659 & 0.3867 & -1.1457 & -0.0405 & -0.2964 & 0.3996 & 0.3692 & 0.1483 & -1.2396 \\ 0.4367 & -0.8395 & 0.3946 & -0.3129 & -0.0133 & -0.1340 & 0.4715 & -1.0230 & 0.7609 \end{bmatrix}$
	σ_x^2	2.9560e-003	4.6121e-004
	σ_y^2	6.9264e-003	2.5757e-004
Run157	Q	$\begin{bmatrix} 0.6387 & 0.4064 & -1.2488 \\ 0.0615 & -1.3341 & -0.0193 \end{bmatrix}$	$\begin{bmatrix} 0.6491 & 0.4295 & -1.1948 & -0.0243 & -0.3177 & 0.4341 & 0.3179 & -0.0234 & -0.7739 \\ 0.4652 & -0.8735 & 0.3920 & -0.3414 & -0.0935 & -0.1932 & 0.4708 & -0.7824 & 0.6105 \end{bmatrix}$
	σ_x^2	2.3997e-003	8.5975e-004
	σ_y^2	9.0114e-003	4.8839e-004

Table 4.3.: Slope calibration parameters for the first and the second part (after camera exchange) of the WiSSCy campaign.

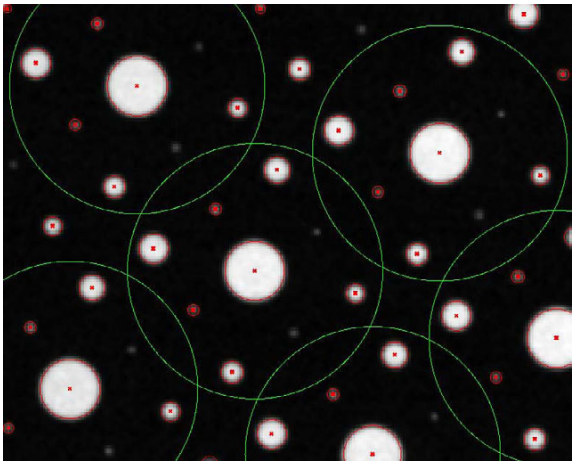

Figure 4.25.: This example shows a section of the acquired *a posteriori image* of the MTF target along with the result of an automatic feature detection, drawn as red and green overlays. The green overlays indicate unit cells of the stencil pattern. Each unit cell consist of 9 circular holes. In this particular image section only two unit cells are complete and could be used for an MTF measurement. The red overlays indicate the segementation of individual holes in the stencil of which only the biggest have to be identified correctly to estimate the reproductions scale and the rotation of the grid.

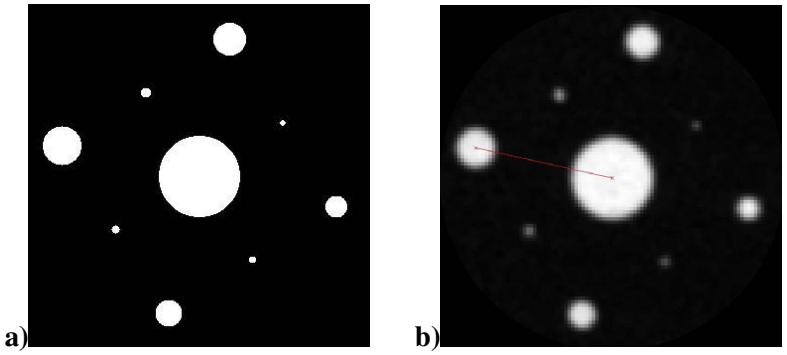

Figure 4.26.: a) Model based construction of the *a priori unit cell* with respect to the reproduction scale and the rotation of the grid. The *a priori unit cell* is constructed with seven times higher resolution compared to the original image resolution. **b)** One of the *a posteriori unit cells* in figure 4.25. The red line connects the biggest circle with the second biggest circle and allows for a determination of the grid rotation angle with respect to the model.

4.5. Measurement of the Modulation Transfer Function

The inverse filtering for the contrast correction was introduced in section 2.5.2. In order to perform the deconvolution we need to know the Modulation Transfer Function (MTF) for the CISG. Here we describe the measurement of the MTF based on the *a posteriori image* $g'(\mathbf{x})$ of the MTF target and a model based construction of the *a priori image* $g(\mathbf{x})$. According to equation (2.88) we get the MTF from the fraction of the magnitude of the *a posteriori image spectrum* $\hat{g}'(\mathbf{k})$ compared to the magnitude of the *a priori image spectrum* $\hat{g}(\mathbf{k})$

$$\mathrm{MTF} = \frac{|\hat{g}'(\mathbf{k})|}{|\hat{g}(\mathbf{k})|}, \tag{4.21}$$

see section 2.5.2. In our case (of a digital one chip CCD camera) the overall contrast damping is due to several reasons of different nature

- the physical limitations of the optics, such as aberration, finite depth of field, and the diffraction limit,

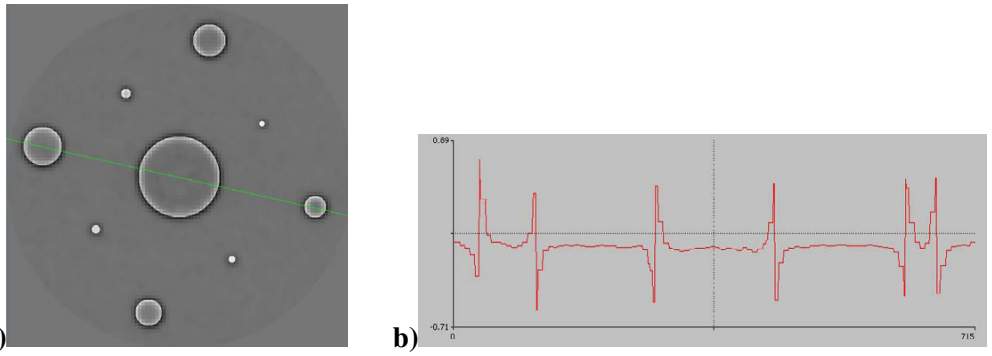

Figure 4.27.: **a)** Difference image between the *a priori unit cell* and the *a posteriori unit cell* from figure 4.26. The green line indicates the location for the line profile that is shown in **b)**.

- the spatial discretization on the sensor,
- the digital post processing steps, such as demosaicing,
- and motion blur.

The MTF measurement covers only effects that are compatible with the assumption of linear shift invariance and therefore the MTF does not account for motion blur in this particular case.

Acquisition of the *a posteriori image*: For the measurement a target was used, that was specially designed so that it was possible to perform the acquisition of the *a posteriori images* directly in the experimental setup of the CISG (section 4.1). The MTF target is a thin metal stencil with circular holes of different diameters on a regular grid, shown in figure 4.5 b). The *a posteriori image* is taken with a homogeneous background illumination. For this the target was lying on a diffusing screen in a plexiglass float that was floating on the water surface. The float is horizontally balanced by the water surface and illuminated by the CISG illumination from below. The diffusion screen was used to eliminate structures in the background, such as scratches in the float material. The *a posteriori image* is processed by the same demosaicing steps as described in section 6.1. Since the interpolation of the three color channels is performed with different filter kernels we need to investigate the MTF of each channel separately. In the following paragraphs the name *a posteriori image* stands for one of the color channels or for an average image.

Segmentation of the *a posteriori unit cells*: A section of the *a posteriori image* is shown in figure 4.25 along with the result of an automatic feature detection, drawn as red and green overlays. The green overlays indicate unit cells of the stencil pattern. Each unit cell consist of 9 circular holes. The red overlays indicate individual holes in the stencil, arranged on a $10.0\,\mathrm{mm}\pm10\,\mu\mathrm{m}$ grid. For the algorithm it is only important to find the biggest hole C_1 in the center and the second biggest hole C_2 at one corner of each unit cell. Once the unit cells in the image were detected, a stack of sections of these unit cells was build. The sections are taken as squares and all values outside the circumference of the green circle were set to the background gray value. This was done in order to exclude information from the neighboring unit cells. Each section of the unit cell was normalized to the maximum intensity within the section. After that, bad cells that contain only parts of a unit cell had to be removed from the stack. For the example in figure 4.25 only two unit cells are complete and could have been used for the following steps. In contrast, the results of the MTF measurements that are shown later are based on stacks that are containing at least 14 unit cells. Using the line that connects the centers of the holes C_1 and C_2 the rotation angle α and reproduction scale β of the unit cells were measured with subpixel accuracy. Since the MTF target

is a rigid body and the image distortion was very low an average of the values for α and β over the ensemble of unit cells was taken. In order to reduce noise, an averaging over the stack of unit cells was performed, yielding the *a posteriori unit cell* that we will from now on denote by $g'(\mathbf{x})$ (instead of the *a posteriori image*).

Model based construction of the *a priori unit cell*: The corresponding *a priori unit cell* $g(\mathbf{x})$ was then constructed, using the parameters α and β along with a model for the unit cell[14]. This was done with a seven times higher resolution, compared to the *a posteriori image*. Due to the higher resolution it was possible to model sharp edges and restrict the resulting discretization artefacts in the spectra to wavenumbers that are beyond the wavenumber range of the original image. Thus, the *a priori unit cell* can be regarded as quasi continuous with regard to the resolution of the *a posteriori unit cell*. Then also the *a posteriori unit cell* was sampled up by a factor of seven, using constant replication of the gray values and thus keeping the spectral information the same. The *a priori unit cell* and the *a posteriori unit cell* are shown in figure 4.26 for a direct comparison. The difference of both images is shown in figure 4.27, along with a line profile that gives an impression of the strength of the smoothing at the edges and the noise level. The smoothing of the edges results from the contrast damping that we want to comprise.

Retrieval of the MTF: Once we have $g(\mathbf{x})$ and $g'(\mathbf{x})$ at the same resolution we get $\hat{g}(\mathbf{k})$ and $\hat{g'}(\mathbf{k})$ from a 2D Fourier transform of each of them. The diameters of the nine circles in the unit cell were chosen such that the *a priori spectrum* $\hat{g}(\mathbf{k})$ (which is an superposition of several Bessel functions) is non-zero everywhere. Thus we can retrieve the MTF using (4.21) for the whole $\mathbf{k}$ plane. Because of the up sampling of $g(\mathbf{x})$ and $g'(\mathbf{x})$ during the construction of the *a priori unit cell* we are only interested in the part of the spectrum that covers the original wavenumber range. This part is extracted to yield the intrinsic MTF.

Results for the different color channels: The result for the MTF of the three individual color channels (R,G,B) and for the average gray image (R+G+B)/3 is shown in figure 4.28. Because of the fact that the PSF and thus the MTF show nearly a perfect polar symmetry it is convenient to transform the spectrum from the Cartesian coordinate system to a polar coordinate system. The MTF shows a decrease to about 60% for a wavenumber of 2000 rad/m, which is about the edge of the interesting range in the wave spectra. This implies that the power spectral density for $|k|$ = 2000 rad/m is reduced to 36%, which illustrates the importance of the MTF correction. In the polar representation we can easily see that the demosaicing filters introduce some minor deviations from the polar symmetry, but only for wavenumbers higher than 3000 rad/m. Since a deviation from the polar symmetry for lower wavenumbers is not observed we average over all polar angles to get omnidirectional representations of the MTFs which are plottet in figure 4.29. The errorbars represent the standard error with respect to the average over the angles. In this unidirectional representation we observe, that the contrast damping for the blue channel is stronger than for the red and green channel. This is no effect of the demosaicing filters, because the filters for red and blue are the same, except for the orientation. Apparently the lens focusing is a little better for red light than for the blue light. We chose the MTF curve for the gray image to represent the overall MTF for the correction of the spectra, minimizing the differences in the three color channels. The black line in figure 4.29 shows a 4^{th} degree polynomial fitted to the MTF curve for the gray image. This polynomial allows to compute the MTF for an arbitrary representation of the wave spectra.

[14]The rotation has to be accounted for because also the gaps between the holes in the stencil carry spectral information and no simplification based on symmetry can be applied at this point.

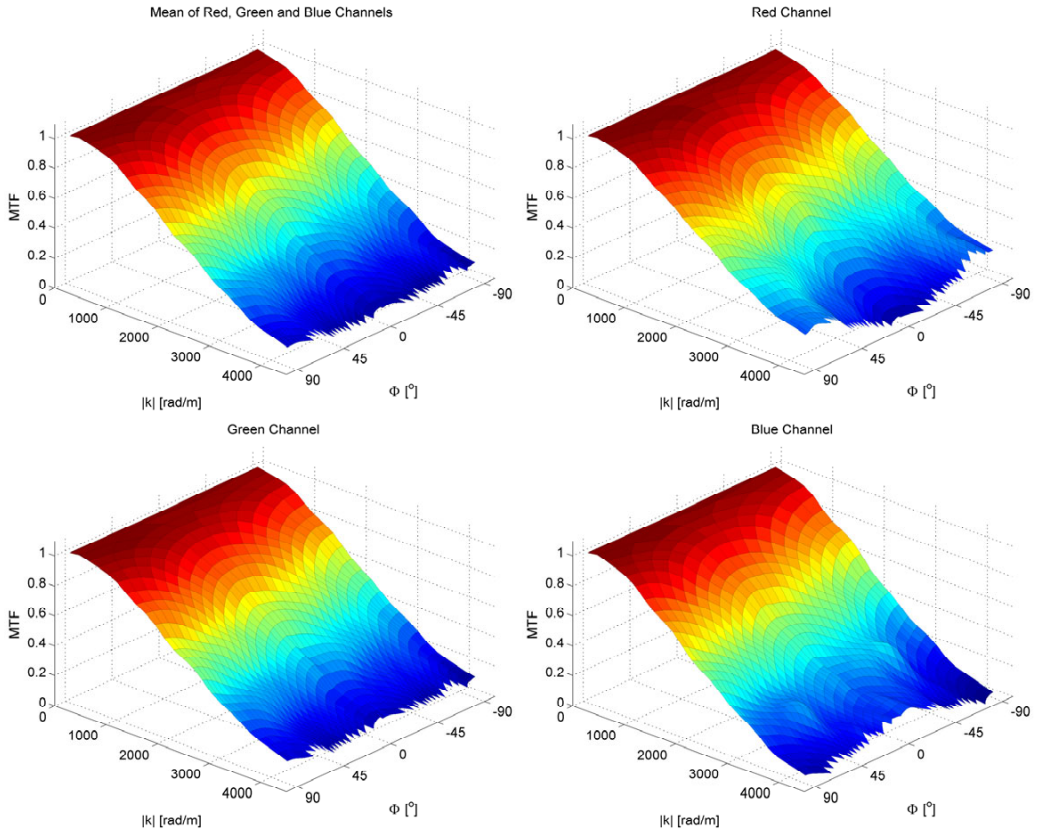

Figure 4.28.: Modulation Transfer Function after the demosaicing step. Top left: for the average image of the three color channels. Top right: red channel. Bottom left: green channel. Bottom right: blue channel. The MTF drops to about 60% for wavenumbers around 2000 rad/m. For the three color channels one can see slight deviations to the average MTF under certain orientations only for wavenumbers greater than 3000 rad/m.

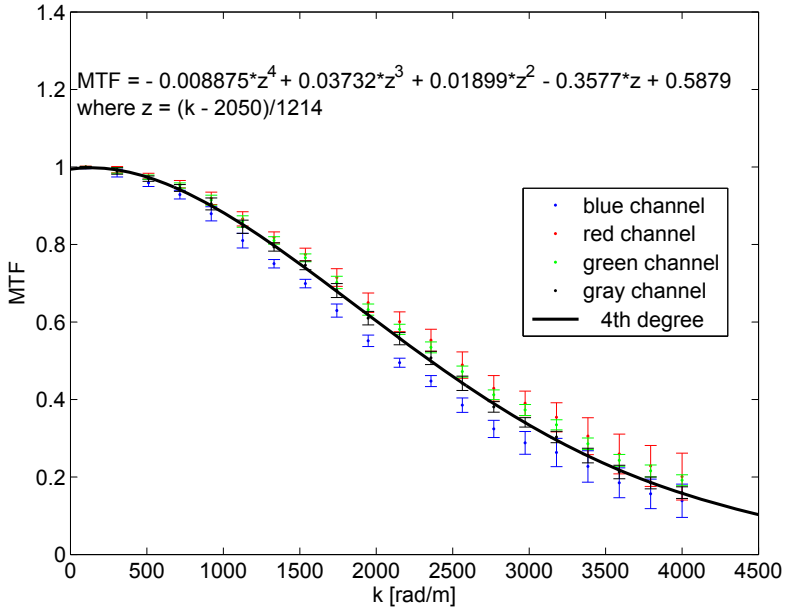

Figure 4.29.: Unidirectional MTF. Discussion see text.

5. Experiments

The measurements that are presented in this study have been conducted as part of the project *Impact of Wind, Rain, and Surface Slicks on Air-Sea CO2 Transfer Velocity - Tank Experiments*, which for convenience will be referred to as the *WiSSCy-Project*. The project is a collaboration of the research group of Prof. Dr. Detlef Stammer, University of Hamburg, and the research group of Prof. Dr. Bernd Jähne, University Heidelberg. The funding was provided by the German Research Foundation (DFG) under the contracts JA-395/13 and and STA-410/5-2.

Several aspects of air-sea interaction have been addressed with the experiments, especially the influence of *wind, rain, and surface slicks* as already apparent from the project title. The main focus of the project was the measurements of the gas transfer velocity aiming for a parameterization that is comprising a wide range of experimental conditions. In this context a statistical description of the properties of the wave field is desired, which has been compassed by means of the wave imaging technique that is described in section 3.1. In addition to the parameterization of transfer rates, we aim on a better understanding of the intermittent processes that controll the air-water exchange of gases and heat. For this we deployed infrared imagery[1] in combination with the wave imaging[2], both instruments being synchronized at a high frame rate (312.5 Hz) and observing the same patch of the water surface. The infrared imagery is used to measure the local heat transfer, which can now be observed in direct reference to the waves.

The experiments have been carried out using the linear wind-wave tank of the University of Hamburg, see section 4.1. The facility was upgraded with an air circulation and an improved rain tower. The air circulation now allows for invasion experiments, in addition to evasion experiments, so that it can be investigated if rain-induced gas transfer is symmetrical or asymmetrical. The rain section covered about 10% of the total water surface and the rain drops reached about 90% of their terminal velocity. The upgrade of the wind wave tank has been carried out by the Hamburg research team[3], who was also responsible for the measurements and simulations of the flow characteristics of the wind wave tank.

Bulk transfer rates for CO_2 have been measured using water samples that were taken at different positions along the tank and at different heights in the water column several times over the course for each experiment[4]. Further gas transfer measurements for the tracers H_2, He, CH_4, F12, N_2O, and volatile aromatic hydrocarbons have been made[5] using *IR spectroscopy*, *UV spectroscopy*, and *gas chromatography*. These measurements also allow for the estimation of the Schmidt-Number exponent and the rate of gas leakage.

The campaign was conducted in the period from the 9^{th} of May to the 4^{th} of July 2007. Table 5.1 shows the experimental conditions that were covered, with 3 to 24 hours of measurement per condition.

Wave Measurements: The acquisition of the wave image sequences was operated in two different modes. In the first mode, referred to as the *statistic measurements*, the time interval between

[1] infrared imagery: Dr. Uwe Schimpf
[2] wave imaging: Roland Rocholz
[3] Facility upgrade & flow characterization: Dr. M. Gade, A.-K. Anweiler, P. Rosendahl and Dr. P. Lange
[4] CO_2 measurement: A.-K. Anweiler
[5] Multi-tracer measurement: Kerstin Richter

wind speed [m/s]	2	3	4	5	6	8	10	12	14
date	11 May	14 May	09 May	18 June	15 May	10 May	29 June	21 June	18 June
condition	clean	clean	clean	clean	clean	clean	clean	clean	clean
date	29 June	14 June							
condition	clean	clean							
date	16 June		15 June		20 June	26 June	29 June		
condition	rain (3/3)		rain (6/3)		rain (3/3)	rain (3/3)	rain (3/3)		
date			04 July		02 July	03 July			
condition			mech. Wave rain & wave		OLA rain (3/3)	OLA rain (3/3)			
date			19 June		27 June	28 June			
condition			OLA		PME rain (3/3)	PME rain (3/3)			

Table 5.1.: Experimental conditions. To give one example how to read the items, "PME rain (3/3)" indicates: 3 hours of measurement with surface slick PME but without rain, followed by 3 hours of measurement with rain and surface slick PME.

two consecutive images was about 2 times larger than the longest period of the waves. Therefore the set of 5000 images per sequence can be assumed to be statistically independent. These image sequences are used for the computation of the long time wave field statistics, i.e. mean square slope (sections 6.6 and 7.4.1). In the second mode, referred to as the *continuous measurements*, the maximum frame rate with an inter frame interval of 0.0032 s was chosen. Moreover, for a set of 150 sequences in the continuous mode the wave imaging camera was synchronized with the infrared camera. The continuous measurements are the basis for the computation of the wavenumber-frequency spectra (used in section 7.2 through 7.4.2) and for the combined visualization of the water waves and temperature fields (section 7.5). A comprehensive table[6] for the WiSSCy wave measurements is included in the technical report [143].

Wind Profile Measurements: For a conclusive presentation of the results the knowledge of the friction velocity is desired. The friction velocity is usually extracted from measurements of the wind profiles. For a linear wind wave flume the shape of the wind profile varies with fetch due to a growth of the boundary layer thickness at the flume ceiling and at the same time because of the fetch dependent roughness height of the wave field, see figure 5.1. The concepts have been introduced in section 2.4.1. For the Hamburg wind wave flume the situations is even more complicated because of the influence of the rain tower which is a huge cavity in the ceiling at a fetch between 12.6 m and 14.8 m. In addition, for the conditions with surface slicks or rain the u_*-u_{ref} relationship is no longer unique.

The measurements of the wind profiles, exemplified in figure 5.3, have been conducted[7] one year after the actual WiSSCy campaign using a windmill anemometer [7]. The delayed measurement is justified for the pure wind conditions, which are reproducible. For the other conditions, we can only make estimates of the influences. Unfortunately, the u_* measurements have been accomplished just a few days before the deadline of this thesis. Therefore these values could not be incorporate into the results from the wave measurements which are always presented in terms of the reference wind speed u_{ref}. The u_*-u_{ref} relationship is presented in figure 5.2 as the basis for a supplementary analysis. Note that the wind profile measurements could only be performed closely before and after the rain tower section, so that the data from fetch 17.5 m and 11.5 m needs to be interpolated for the wave measurement site at a fetch of 14.4 m.

Heat/Gas Transfer Rates: A concluding analysis of the heat transfer and gas transfer measurements is still pending. Preliminary results are available from Richter [140] and Anweiler [7][6][5].

[6] 447 images sequences have been acquired for the CISG wave and calibration measurements.
[7] wind profile measurements: A.-K. Anweiler

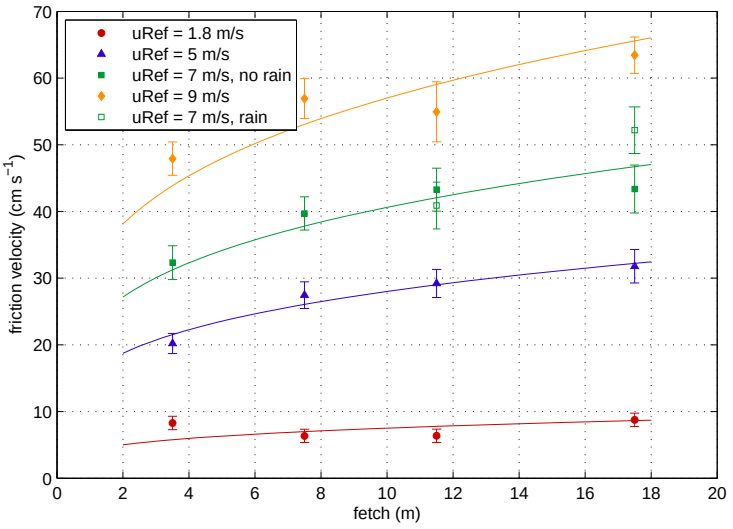

Figure 5.1.: Friction u_* velocity vs. fetch. (from Anweiler [7])

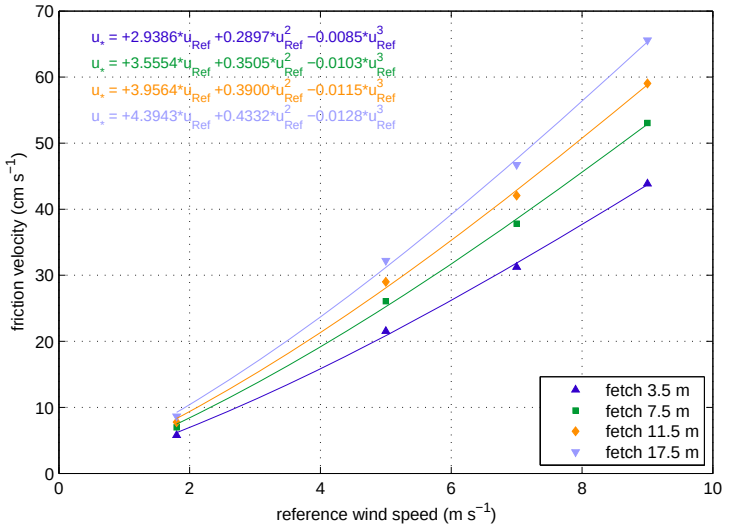

Figure 5.2.: Friction velocity u_* vs. reference wind speed u_{ref}. (from Anweiler [7])

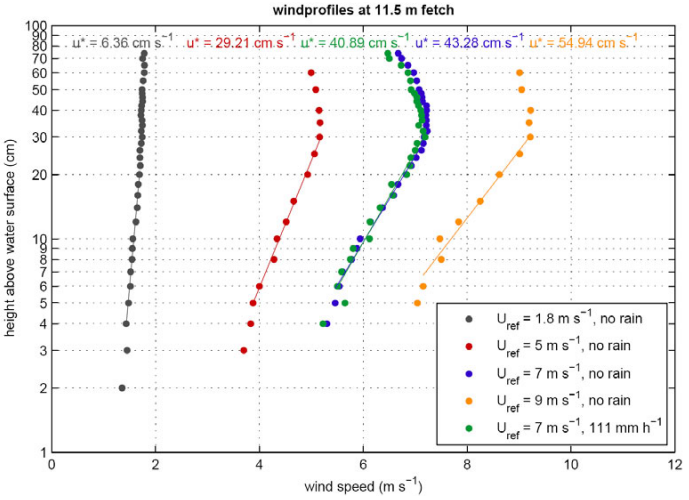

Figure 5.3.: Measured wind profiles. (from Anweiler [7])

6. Data Processing

Each image sequence is processed through a chain of operations, which is displayed in figure 6.1 in form of a flow chart. A single sequence typically contains 5000 images which are delivered by the camera as RAW images with 8 bit gray value resolution[1]. The RAW image size is 640 times 298 pixel. These images are decomposed into three color images with half the size of the RAW image. This step is called demosaicing, which was introduced in section 2.5.3. In section 6.1 we present the properties of the interpolation that was actually implemented for the color retrieval. After the demoisaicing follows the contrast restoration for the color channel images by means of an inverse filtering with the measured Modulation Transfer Function, see section 6.2. Before the color images enter the slope calibration an intensity normalization and an offset correction is performed. Formally these two color processing steps are equivalent to the steps in the slope calibration that was treated in section 4.4.2, equations (4.8) to (4.10). However, some additional aspects have to be considered for the processing of the actual wave image sequences. We discuss the issue of intensity normalization of the wave image sequences in section 6.3. In section 6.4 the offset correction is treated and it is shown how to retrieve an estimate for the color offset if no zero-measurements are available. All color processing steps are performed with 16bit floating point precision. The slope computation, see section 6.5, reduces the number of image sequences from three ($[R, G, B]$) to two ($[s_x, s_y]$). The slope sequences for both components, each 0.9Tbyte, are stored on hard drives.

Once the calibrated slope sequences have been computed, the further analysis follows different pathways. On the one hand we use the slope sequences in the space-time domain to compute the mean squared slope, section 6.6, and for a visualization of the wave field, section 7.5. On the other hand, we use the sequences as input for a 3D Fast Fourier Transform which yields the power spectral density of the surface slope, see section 6.7.

6.1. Demosaicing

The single chip sensor of the used camera is a so called color filter array (CFA). Each individual pixel is equipped with a filter for one of the primary colors red, green and blue (R,G, and B). The spectral sensitivity of the sensor-filter combination is shown in figure 6.2. The filters are arranged on the chip in a so called Bayer mosaic layout (US Patent3971065) as shown in figure 2.13. In order to retrieve the actual color images a demosaicing step needs to be performed, which was introduced in section 2.5.3.

The camera firmware already implements a demosaicing algorithm. However, for the WiSSCy experiments the images were captured in raw format with 8bit gray value resolution. The raw format was chosen in order to achieve the maximum possible frame rate. Moreover, since we use an off-line demosaicing procedure we have full control over the demosaicing quality, so that we do not rely on the camera producers choice.

For the demosaicing of the *CISG* image sequences we applied a component wise interpolation using an optimized set of filter kernels that were proposed by Scharr [146]. This filter set fulfills our requirements on isotropy and homogeneity, i.e. the transfer functions for the three different

[1] Internally the camera works with a higher dynamical range of 14 bit. Note that the camera exhibits a color filter array, see section 2.5.3.

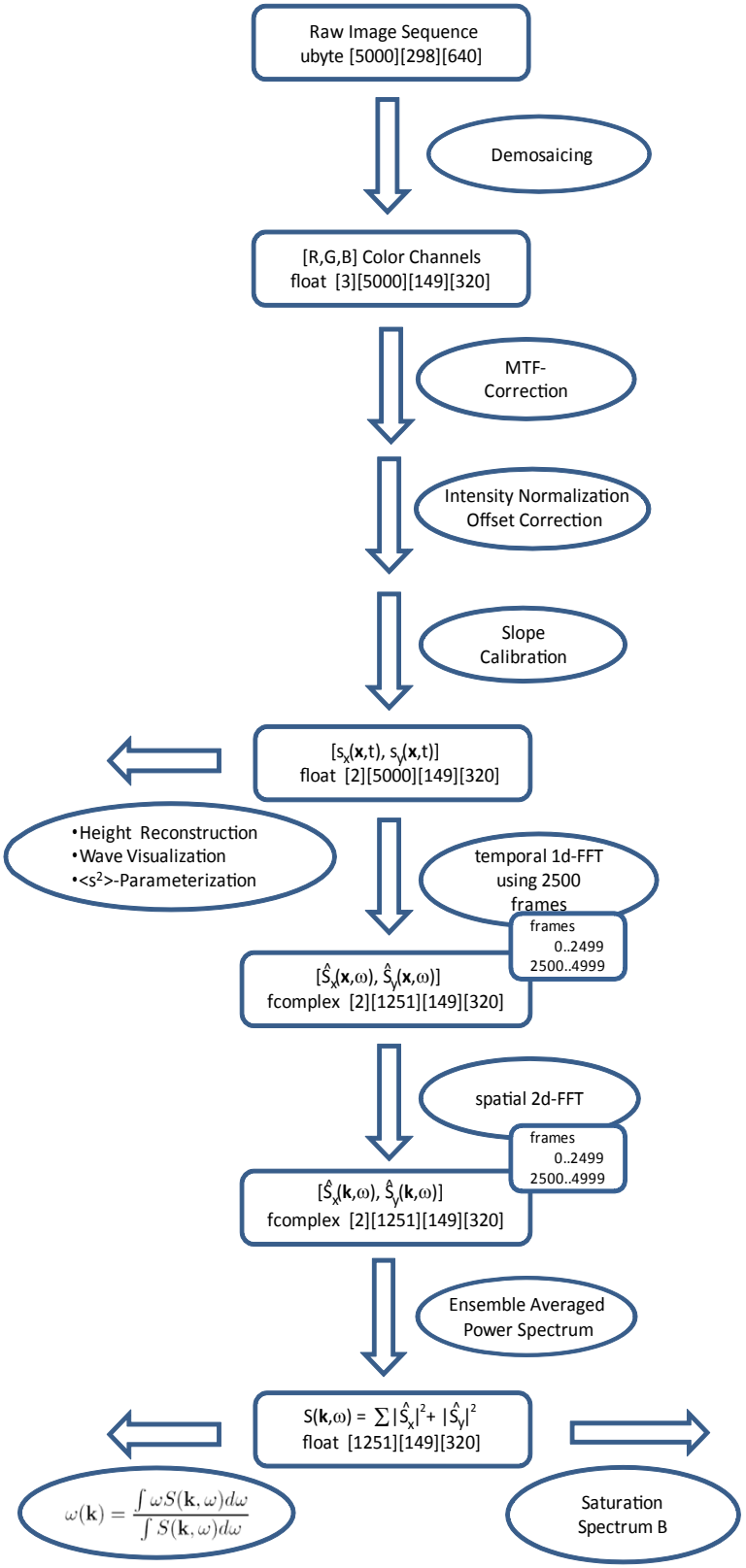

Figure 6.1.: Flow chart for the data processing.

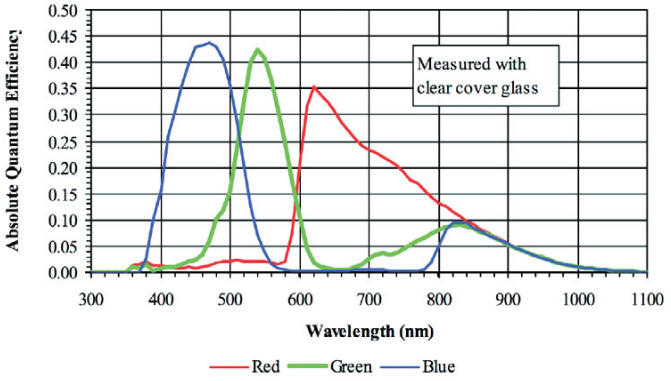

Figure 6.2.: Spectral sensitivity of the camera Pike F-032C. Source: AVT Pike Technical Manual, V2.0.0, 07 July 2006, Allied Vision Technologies GmbH, Germany

color channels are comparable with respect to the wavenumber dependence and they exhibit only minor directionality. The filter kernels are shown along with their transfer functions in figure 6.3. The filters are applied on the raw image, resulting in three color channel images aligned with respect to subgrid g_1, compare figure 2.13. On the other subgrids r, g_2, and b the color information is mixed. Thus, as a second step the resulting images are sub-sampled by a factor of two in order to retrieve only the color information on subgrid g_1 of the filter results. Due to this sub sampling step the resulting Nyqyist wavenumber is half that of the raw image (which is here set to one) , e.g. it is corresponding to the Nyquist wavenumber of the color subgrids. The optimized transfer functions therefore show a minimum for $k_N = 0.5$. All three filters show almost the same decline of the transfer function for wavenumbers smaller than k_N. The decline is approximately isotropic and can partially be corrected by the MTF correction, see section 4.5 and 6.2.

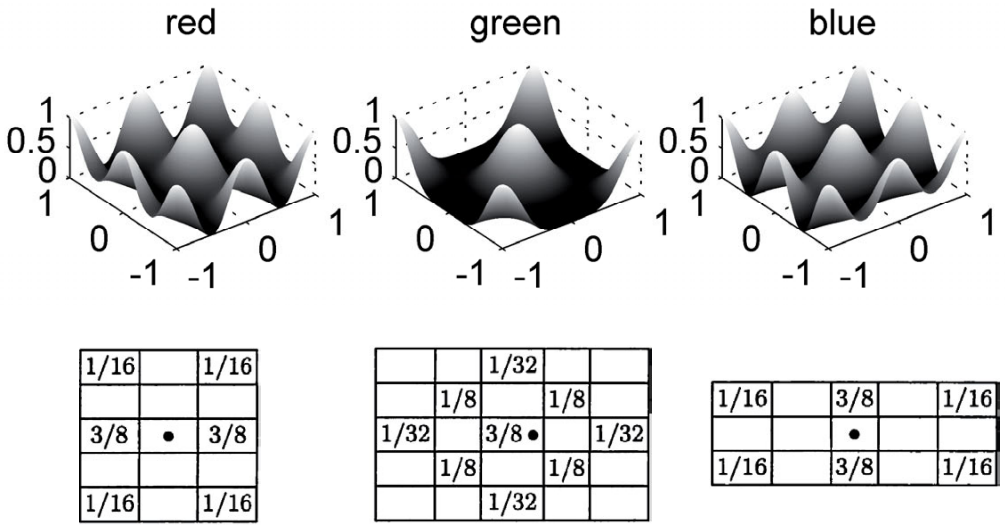

Figure 6.3.: Squared magnitude of the transfer functions for the optimized filter kernels by Scharr [146] for the color interpolation (upper row). Corresponding filter masks (lower row). The dots in the kernel matrices correspond to the g_1 subgrid from which the filter results are retrieved by the consecutive sub sampling step. The x and y axes in the plots for the transfer functions are representing the wavenumbers, normalized to the Nyquist wavenumber of the raw image. For the sub-sampled color channels the new Nyquist limit is half that of the raw image. The optimized filter kernels therefore go to zero for $k = 0.5$.

6.2. Contrast Restoration via MTF Correction

The measurement of the Modulation Transfer Function enables us to correct the color images for the contrast damping that results from the image acquisition as well from the demosaicing. The general procedure is explained in the sections 2.5.2 and 4.5. For the contrast correction in the data processing chain we use the polynomial fit on the omnidirectional measured MTF, which is displayed in figure 4.29. For each color channel image a 2D Fourier transform is performed just after the demosaicing step. The spectra are multiplied by the inverse of the MTF. In order to avoid the amplification of noise, the spectral amplitudes are left unchanged for wavenumbers where the MTF is less than 33%, which is the case for $|k| > 3019\,\mathrm{rad/m}$. The contrast corrected color channel images are then retrieved via the inverse Fourier transformation. This procedure is computationally quite expensive, because of the image-wise transformations. However, it was implemented this way because otherwise the memory management would have been unfavorable. Note that the MTF correction could be implemented much easier, if the data processing chain would comprise only linear operators. In this case we could have just divided the resulting spectra by an effective MTF correction function, using the linearity of the Fourier transformation. Since the CISG implementation is usually employing an intensity normalization, this more effective approach is not tenable. Moreover, the slope calibration in this study is using an polynomial model and therefore we have to perform the constrast restoration right at the beginning of the data processing, i.e. after the demosaicing step.

6.3. Intensity Normalization

Ideally the intensity image I as defined in equation (4.9) is independent of the image position (i, j) and also independent of the observed water surface slope. This idea is based on several assumptions:

1. The color transparency print is a perfect realization of the color coding design which dictates that I is independent of the screen position, see section 3.1.3.
2. The diffusion screen acts as a perfect Lambertian radiator, meaning that the radiant emmittance is independent of the ray inclination δ in equation (3.3).
3. The spectral emissivity of the fluorescence tubes is matching the spectral filter characteristics of the color transparency.
4. The screen is homogeneously illuminated from below.
5. There are no dirt particles in the water or scratches in the glass window.

In practice these assumptions are only approximately fulfilled. In particular the assumption of a Lambertian radiator can hardly be realized. The undesirable effects due to the angular characteristic of the light source is most pronounced in the *ISHG*-Method, where the intensity information is explicitly used for the height measurement, see Rocholz [142]. For the *CISG*-Method we can compensate for any intensity loss as long as the first assumption holds by normalizing each color component with I, see also Balschbach [9] and Fuß [50]. After the normalization the three color channels are no longer independent, which has to be considered in the slope calibration.

6.4. Offset Correction

In case of a flat water surface the ideal ray geometry implies that each pixel of the camera observes the center of the light source and therefore retrieves the same color information, see equation

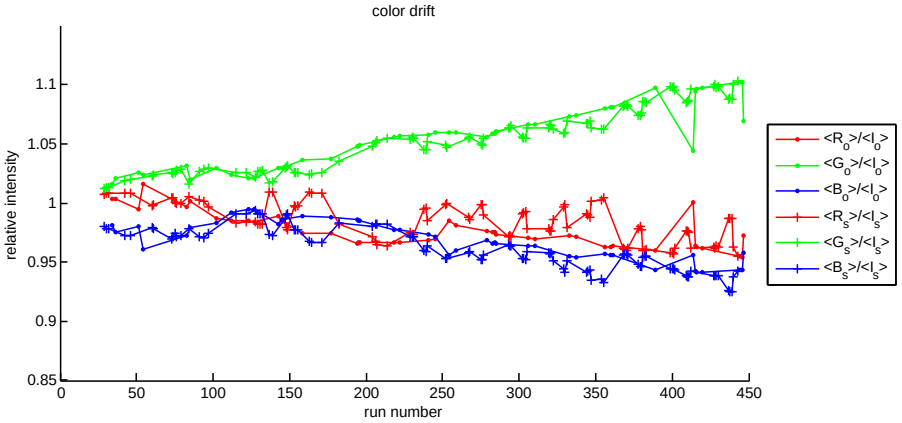

Figure 6.4.: Changes of the relative mean color contribution during the course of the experiment. Index o indicates mean values based on *zero measurements* for the flat water surface that could only be made at the beginning of each day. For these measurements the light source was switched on approximately 45 minutes in advance to avoid further changes due to the temperature drift of the lamps. Index s indicates mean values based on the *statistic measurements* at the wavy water surface that have been performed several times a day and therefore reflect diurnal variations. Note that the abscissa shows run numbers which is not a linear time measure, compare [143].

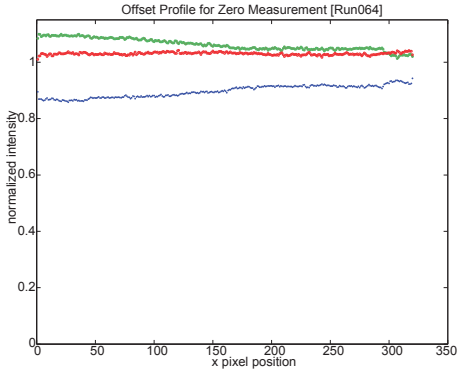

Figure 6.5.: Color offset for a zero measurement.

(3.7) and section 3.1.3. In other words, the color that is observed for a flat water surface (*zero measurements*) defines the origin of the coordinate system on the illumination screen. However, images of the flat water surface show a slight spatial trend in the colors with variations around the mean in the order of $\pm 5\%$, see figure 6.5. This observation can be explained by two facts. First and most important, the Fresnel lens deviates from a ideal lens and shows all kinds of optical aberration (see e.g. [50]). Secondly, the inclination of the principal axis and the ray divergence that is due to the geometry of the setup (see section 4.1) lead to an offset that depends on the image position. A first order correction of the spatial trend of the colors can be done by subtracting an appropriate offset image. The offset image defines the pixelwise color offset for zero slope of the water surface.

Despite of the spatial color trend there is another important reason to perform an offset correction. During the course of the experiments there were considerable changes in the mean color histograms. The color histograms were equalized using a so called *white balance* step during the setup of the experiment. After this initial histogram equalization the camera parameters were not changed again, because this would have affected the individual gain of the color channels. The color specific gain is not allowed to change since this would affect the slope calibration. The slope calibration can be interpreted as measuring distances in the color space. Changes in the white balance correspond to a non isotropic sheer operation in color space and therefore affect the distance

measures. We can explain the observed temporal changes in the mean color histograms by three main effects

- The spectrum of the fluorescence tubes changes in time because of temperature drifts and aging.
- The transmittance of the color transparency is changing in time because of aging.
- The color of the water is changing during the course of the experiment because of growth of algae.

Figure 6.4 shows the relative change of the mean color contribution over the course of the experiment. One can clearly see a global trend of the green channel that corresponds to the algae contamination of the water body. A comparison of the mean color histograms for the *zero measurements* and the *statistics measurements* (with respect to the time since the light source was switched on) revealed that the light source has a diurnal color drift [143]. Because of this diurnal variation is was not appropriate to follow the approach of Balschbach [9] and Fuß [50]. They used *zero measurements* at the flat water surface to compute an ensemble averaged offset image that defined $\mathbf{C}_o$ and I_o in equation (4.10). During the WiSSCy campaign it was only possible to make this kind of *zero measurements* before the start of each experiment, which then lasted the whole day. Therefore the offset correction for all image sequences was based on averages of the image sequences itself. This is based on the idea that the mean surface slope is zero. Since the color coding and the ray geometry is nearly linear (see equation (3.8)) the mean surface slope corresponds to the mean color image. Therefore we define the offset image as

$$\mathbf{C}_o \equiv \langle \mathbf{C} \rangle_N \,, \tag{6.1}$$

where $<>_N$ denotes an ensemble average of N frames[2]. Using the offset image definition (6.1) for the color processing, equation (4.10), in combination with a linear calibration automatically yields zero mean slope components.

6.5. Slope Computation

The image sequences for the two slope components $\mathbf{s} = [s_x(\mathbf{x}, t), s_y(\mathbf{x}, t)]^T$ of the water surface are obtained from the preprocessed color image sequence $[r, g, b]^T$ according to the higher-order model

$$\mathbf{s} = \mathbf{Q} \left[\begin{array}{cccccccccc} r & g & b & r^2 & g^2 & b^2 & r^3 & g^3 & b^3 \end{array} \right]^T ,$$

that was introduced in section 4.4.3. Depending on the date of the measurement, different calibration parameters matrices $\mathbf{Q}$ from table 4.3 are utilized.

6.6. Mean Square Slope Computation

The mean square slope mss is the sum of the variances of the slope components and therefore a measure for the roughness of the water surface

$$\begin{aligned} mss &= \sigma_{s_x}^2 + \sigma_{s_y}^2 && (6.2) \\ &= \overline{(s_x - \overline{s_x})^2} + \overline{(s_y - \overline{s_y})^2} \\ &= \overline{s_x^2} - \overline{s_x}^2 + \overline{s_y^2} - \overline{s_y}^2 \\ &\approx \overline{s_x^2} + \overline{s_y^2} && (6.3) \end{aligned}$$

[2] in most cases: $N = 5000$

The approximation (6.3) is valid as long as the measurements are unbiased, so that $\overline{s_x} = \overline{s_y} = 0$. In our case, the offset correction already ensures a zero mean of both slope components.

There are various ways to compute the variances according to the possibilities to combine spatial and temporal averaging. In order to have an estimate of the variance that characterizes the stationary and homogeneous wave field we need to ensure that either the individual slope measurements are statistically independent or that the mss value converges. Since we have a great number of data points[3] for each experimental condition, there is no need to be concerned about the convergence, as long as the experimental conditions are indeed stationary and homogeneous. A detailed analysis of this issue for the WiSSCy campaign is carried out in the technical report Rocholz [143]. In order to make a statement about the minimum number of frames for an appropriate ensemble average, we need to distinguish the modes for the acquisition of the image sequences. In the first mode, referred to as the *statistic measurements*, the time interval between two successive images was about 2 times larger than the longest period of the waves, so that we assume the set of 5000 images per sequence to be statistically independent. In the second mode, referred to as the *continuous measurements*, the maximum frame rate with an inter frame interval of 0.0032 s was chosen, so that from image to image only gradual changes are apparent. For the statistic measurements under stationary conditions, typically $N = 360$ images are sufficient for an ensemble average of the mean square slope. This was tested by a comparison of the subset ensemble average mss_N to the total ensemble average mss_{tot} with the requirement that the probability of a significant difference of more than 6% is less than 1%, using the t-statistics [143]. Hence, each statistic measurement can be processed by a central moving ensemble average of 360 images, yielding a time series of the mss for the timespan of the sequence (typically 45 minutes). From these time series it can be decided, whether or not the wave field is called stationary [143]. For the continuous measurement the timespan is only 16 s, and therefore the ensemble average is always computed over the whole sequence of 5000 images.

In addition to averaging in the space time domain, we can compute the mean square slope by means of a simple summation of the power spectral density

$$mss = \frac{1}{MNO} \sum_{m=0}^{M-1} \sum_{n=0}^{N-1} \sum_{o=0}^{O-1} (s_x^2 + s_y^2) = 2 \sum_{u=-M/2}^{M/2} \sum_{v=-N/2}^{N/2} \sum_{w=0}^{O/2} \left(\left| \hat{\mathsf{S}}_{\mathsf{x}} \right|^2 + \left| \hat{\mathsf{S}}_{\mathsf{y}} \right|^2 \right), \quad (6.4)$$

where Parseval's Theorem and the definition of the DFT have been used[4], see sections 2.5.1 and 6.7.1. Moreover, splitting the spectral volume into different segments for the summation yields the contribution of each segment to the mean square slope. For instance, for the continuous measurements we can distinguish between the contribution of leeward[5] and windward[6] propagating waves to the mean square slope according to

$$\begin{aligned} mss_{leeward} &= 2 \sum_{u=0}^{M/2} \sum_{v=-N/2}^{N/2} \sum_{w=0}^{O/2} \left(\left| \hat{\mathsf{S}}_{\mathsf{x}} \right|^2 + \left| \hat{\mathsf{S}}_{\mathsf{y}} \right|^2 \right) \\ mss_{windward} &= 2 \sum_{u=-M/2}^{-1} \sum_{v=-N/2}^{N/2} \sum_{w=0}^{O/2} \left(\left| \hat{\mathsf{S}}_{\mathsf{x}} \right|^2 + \left| \hat{\mathsf{S}}_{\mathsf{y}} \right|^2 \right), \end{aligned} \quad (6.5)$$

see section 7.4.2.

[3] Typically the number of data points per sequence is $2 \times 5000 \times 320 \times 149 = 4.768 \cdot 10^8$ and typically 6 sequences are acquired for each condition.

[4] Note that for the usage of equation (6.4) the windowing function that is applied before the DFT is required to be normalized so that the integral of its transfer function is one. Moreover, for (6.4) it is assumed that the spectral energy for $\omega = 0$ is zero (otherwise we need to discard the factor of two 2 for this slice of the spectrum).

[5] leeward means with the wind in the back, corresponding to $k_x > 0$

[6] windward means facing the wind, corresponding to $k_x < 0$

Symbol	Meaning	Equation	Physical Unit
$\eta(\mathbf{x}, t)$	water surface elevation	(6.6)	m
$\eta_{m,n,o}$	sampled water surface elevation	(6.18)	m
$\hat{\eta}(\mathbf{k}, \omega)$	complex amplitude function for η	(6.6)	m^3 s
$\hat{\eta}_{u,v,w}$	3d-DFT of the sampled water surface elevation	(6.21)	m
$\hat{\eta}\prime_{u,v,w}$	scaled 3d-DFT of the sampled water surface elevation	(6.23)	m^3 s
$X(\mathbf{k}, \omega)$	energy density spectrum	(2.46)	m^4s
$\Psi(\mathbf{k})$	wavenumber energy density spectrum	(2.49)	m^4
$\Psi_{u,v}$	discrete wavenumber energy density spectrum	(6.30)	m^4
$\Phi(\omega)$	frequency energy density spectrum	(2.50)	m^2s
Φ_w	discrete frequency energy density spectrum	(6.31)	m^2s
$S(\mathbf{k}, \omega)$	3d power spectrum of the slope	(6.11)	m^4s^2
$S'_{u,v,w}$	discrete 3d power spectrum	(6.25)	m^4s^2
$S_{u,v,w}$	discrete 3d power spectrum	(6.26)	-
$B(\mathbf{k})$	saturation spectrum	(2.51) (6.40)	-
$B_{u,v}$	discrete saturation spectrum	(6.32) (6.40)	-

Table 6.1.: Nomenclature

Another way to compute the mss is to perform a 2D Gauss-fit for the joint probability density function of the slope components to yield the variances $\sigma^2_{s_x}$ and $\sigma^2_{s_y}$, see for instance Balschbach [9].

Mean square slope values that are reported in this thesis are computed in different ways, depending on which approach was the most suitable. The actual method is specified along with the values. An inter-comparison of the results of the different approaches has been carried out in Rocholz [143], yielding an assignment of stationarity for each individual sequence and experiment. This assignment of stationarity is necessary in order to appropriately compute ensemble averages of the 3D power spectral density (section 6.7) and for the interpretation of peculiarities in the gas/heat transfer measurements with respect to changes of the wave field.

6.7. Computation of the Spectra

On the one hand, the computation of the spectra is straight forward. We only need to apply the DFT to the data. On the other hand, the quantitative presentation of the spectra requires a careful examination concerning the normalization. In the related literature different scaling factors are used without explicit reference. Sometimes the authors even abdicate any scaling to present the spectra in arbitrary units. This leads to the inconvenient fact that results that are presented in different publications are often only qualitatively comparable. In the following section 6.7.1 we will therefore address the scaling of the DFT so that the result is consistent with the basic concepts that reach back to the definitions by Phillips [132] which were presented in section 2.3.1. We make some basic considerations about the implications due to the symmetry and periodicity of the spectral volume in section 6.7.2. Followed by descriptions of the implementation in section 6.7.3, and the averaging of the power spectral density in section 6.7.4. Finally an alternative definition for the saturation spectrum $B(\mathbf{k})$ is proposed in section 6.7.5. The re-definition comprises only a minor difference to Phillips definition. It is proposed in order to preserve the information about the actual directionality of the wave field in the $B(\mathbf{k})$ representation.

6.7.1. Normalization Factors for the Discrete Spectra

The basic concept for the statistical description of the wave field has been introduced in section 2.3.1, where the standard continuous formulations of the spectra and the correlation function were used. However, we are neither measuring the surface elevation directly nor are we dealing with continuous data. Here, we are dealing with digital image sequences of the water surface slope which are processed by the Discrete Fourier Transform to yield the discrete counterparts of $X(\mathbf{k},\omega)$, $\Phi(\omega)$, $\Psi(\mathbf{k})$, and $B(\mathbf{k})$ (see table 6.1). It is not necessary to make a reconstruction of the surface elevation in order to evaluate the autocorrelation function, as it might be suggestive from equation (2.46). Instead we can use the basic relationship between the slope spectra $\hat{s_x}$, $\hat{s_y}$ and the elevation spectrum $\hat{\eta}$ (equations (6.9) and (6.10)).

While the general procedure is clear and can be found throughout the literature (e.g. [9, 74]), we are concerned about the correct normalization factors so that the results are really corresponding to the continuous definitions with the correct physical units. Unfortunately, it seems that in some cases different authors use different normalization factors to scale the DFT results. Since the saturation spectrum is dimensionless and often times only the spectral shape is of interest, this difference in not always important. However, in order to be able to compare data, for instance measured by a wire gauge and an imaging slope gauge, it is of course essential to take care about the physical units and dimensions. Usually the discrepancies in the different data sets can be compensated by scaling of the data or stretching of the coordinate system. But still, the situation is unsatisfactory since in this way an inter-comparison of measurements is always a bit tricky. From the authors point of view, we need to guarantee that the spectra are really just a discrete version of the continuous counterparts.

For this we explicitly show the link between the discrete and continuous descriptions. This eventually gives the answer on how to normalize the DFT results. At first we stick to the continuous Fourier transform to show the fundamental relationships. As a second step we investigate the modifications for the discrete case.

Assume that the water surface has a certain boundary in the horizontal extend so that outside of this boundary the surface elevation $\eta(\mathbf{x},t)$ is vanishing to zero. Further, assume some kind of temporal window so that η vanishes outside of this time window.[7] Then η becomes square integrable and we can represent it by a Fourier integral

$$\eta(\mathbf{x},t) = \iiint \hat{\eta}(\mathbf{k},\omega) e^{\mathrm{i}(\mathbf{xr}-\omega t)} d\mathbf{k} d\omega, \tag{6.6}$$

where $\hat{\eta}(\mathbf{k},\omega)$ is a complex valued amplitude function. Now $\mathbf{x}$ and t are restricted to the space-time volume defined by the extend of the boundary and the time window. For convenience we regard the space-time volume as a cuboid with the side lengths X, Y, and T. This is also the situation we have, using image sequences.

The partial derivative ∂_j in the spatial domain corresponds to a multiplication with $\mathrm{i}\cdot k_j$ in the Fourier domain [77]. Therefore the components of the surface slope $\mathbf{s} = \nabla\eta$ are represented by

$$s_x = \iiint \mathrm{i}\, k_x \hat{\eta}(\mathbf{k},\omega) e^{\mathrm{i}(\mathbf{kx}-\omega t)} d\mathbf{k} d\omega \tag{6.7}$$

$$s_y = \iiint \mathrm{i}\, k_y \hat{\eta}(\mathbf{k},\omega) e^{\mathrm{i}(\mathbf{kx}-\omega t)} d\mathbf{k} d\omega. \tag{6.8}$$

[7] Both assumptions are not that unnatural. E.g. imagine a storm over a lake.

Likewise we can write

$$\hat{s}_x(\mathbf{k},\omega) = \mathrm{i}\, k_x \hat{\eta}(\mathbf{k},\omega) \tag{6.9}$$
$$\hat{s}_y(\mathbf{k},\omega) = \mathrm{i}\, k_y \hat{\eta}(\mathbf{k},\omega). \tag{6.10}$$

Now we define the *power spectrum* S of the slope as the sum of the squared magnitude of the slope components

$$S(\mathbf{k},\omega) \equiv |\hat{s}_x|^2 + |\hat{s}_y|^2 = k^2 \,|\hat{\eta}|^2\,, \tag{6.11}$$

where $k^2 = k_x^2 + k_y^2$ is the squared magnitude of the wavenumber vector. The relation between S and X becomes clear if we rewrite (2.48) with the restriction to the above mentioned space-time volume TXY

$$\overline{\eta^2} = \frac{1}{TXY}\int_0^T\int_0^X\int_0^Y \eta^2(\mathbf{x},t)d\mathbf{x}dt = \iiint X(\mathbf{k},\omega)d\mathbf{k}d\omega. \tag{6.12}$$

Now, using Parseval's theorem

$$\iiint |\eta(\mathbf{x},t)|^2\, d\mathbf{x}dt = (2\pi)^3 \iiint |\hat{\eta}(\mathbf{k},\omega)|^2\, d\mathbf{k}d\omega \tag{6.13}$$

and the right hand side of (6.11) we get

$$\frac{(2\pi)^3}{TXY}\iiint \frac{1}{k^2} S(\mathbf{k},\omega)d\mathbf{k}d\omega = \iiint X(\mathbf{k},\omega)d\mathbf{k}d\omega. \tag{6.14}$$

The fact, that we have to divide by TXY explains why we call $k^{-2}S(\mathbf{k},\omega)$ and $S(\mathbf{k},\omega)$ the power spectral density of the surface elevation and power spectral density of the surface slope, respectively.

The extend of the space-time volume defines the minimal size of the wavenumber-frequency volume element which is needed for the discrete Fourier transform, see also section 2.5.1. The grid spacing in the discrete Fourier domain is given by

$$\Delta k_x = \frac{2\pi}{X}, \quad \Delta k_y = \frac{2\pi}{Y}, \quad \Delta\omega = \frac{2\pi}{T} \tag{6.15}$$

In this light the factor $\frac{(2\pi)^3}{TXY}$ can be interpreted as a discrete volume element in the Fourier domain. Up to this point we have written the spectra in terms of a continuous Fourier transform, so that the equations are more easy to read. Now, since we have restricted the spatial domain to a cubic volume in space and time, it is easy to switch to a discrete representation. Let M, N, O denote the number of sampling points in the cuboidal space-time volume, so that $X = M\Delta x$, $Y = N\Delta y$, and $T = O\Delta t$, where Δx, Δy, and Δt represent the grid spacing for the discrete sampling in the respective directions (compare section 2.5.1). With equation (6.15) we can also

$$M = \frac{2\pi}{\Delta k_x \Delta x} = \frac{X}{\Delta x}, \quad N = \frac{2\pi}{\Delta k_y \Delta y} = \frac{Y}{\Delta y}, \quad O = \frac{2\pi}{\Delta\omega\Delta t} = \frac{T}{\Delta t}. \tag{6.16}$$

Let $\eta_{m,n,o}$ be the sampled version of $\eta(\mathbf{x},t)$ on the space-time grid at the points $m\Delta x$, $n\Delta y$, and $o\Delta t$. Alike, let $\hat{\eta}_{u,v,w}$ be the sampled version of $\hat{\eta}(\mathbf{k},\omega)$ on the wavenumber-frequency grid at the points $u\Delta k_x$, $v\Delta k_y$, and $o\Delta\omega$. Then, the discretized version of the exponential function in the inverse Fourier transform is

$$\exp\left(\mathrm{i}(u\Delta k_x\, m\Delta x + v\Delta k_y\, n\Delta y - w\Delta\omega\, o\Delta t)\right) \equiv \mathrm{w}_M^{mu}\ \mathrm{w}_N^{nv}\ \mathrm{w}_O^{-ow}, \tag{6.17}$$

where we use abbreviations for the discrete Fourier kernel $\mathrm{w}_Q \equiv \exp(2\pi\,\mathrm{i}\,/Q)$ [77]. The discrete counterpart of the 3d Fourier transform in (6.6) can now be written as

$$\eta_{m,n,o} = \sum_{u=0}^{M-1}\sum_{v=0}^{N-1}\sum_{w=0}^{O-1} \hat{\eta}_{u,v,w}\,\mathrm{w}_M^{mu}\;\mathrm{w}_N^{nv}\;\mathrm{w}_O^{-ow}. \tag{6.18}$$

The forward 3d-DFT is equivalently

$$\hat{\eta}_{u,v,w} = \frac{1}{MNO}\sum_{m=0}^{M-1}\sum_{n=0}^{N-1}\sum_{o=0}^{O-1} \eta_{m,n,o}\,\mathrm{w}_M^{-mu}\;\mathrm{w}_N^{-nv}\;\mathrm{w}_O^{ow}. \tag{6.19}$$

So far, following the conventional definitions of the Discrete Fourier Fransform, we skipped the increments $d\mathbf{x}$, $d\mathbf{k}$, dt, and $d\omega$ in the discretization step. This leads to the inconvenient fact, that the physical units of the spectral components are no longer the same as in the continuous description. Anyhow, we can fix that problem by choosing a different normalization factor in the forward transform. We define a modified discrete spectrum $\hat{\eta\prime}_{u,v,w}$ which satisfies the modified inverse transform

$$\eta_{m,n,o} = \sum_{u=0}^{M-1}\sum_{v=0}^{N-1}\sum_{w=0}^{O-1} \hat{\eta\prime}_{u,v,w}\,\mathrm{w}_M^{mu}\;\mathrm{w}_N^{nv}\;\mathrm{w}_O^{-ow}\Delta k_x\Delta k_y\Delta\omega, \tag{6.20}$$

where only the discrete increments have been included in analogy to the continuous transformation. In other words, we defined the modified spectrum as

$$\hat{\eta\prime}_{u,v,w} \equiv \hat{\eta}_{u,v,w}/(\Delta k_x\Delta k_y\Delta\omega). \tag{6.21}$$

Then the modified forward transform is alike the continuous forward transform

$$\hat{\eta\prime}_{u,v,w} = \frac{1}{(2\pi)^3}\sum_{m=0}^{M-1}\sum_{n=0}^{N-1}\sum_{o=0}^{O-1} \eta_{m,n,o}\,\mathrm{w}_M^{-mu}\;\mathrm{w}_N^{-nv}\;\mathrm{w}_O^{ow}\Delta x\Delta y\Delta t. \tag{6.22}$$

The consistency concerning the normalization factor is explicitly shown in the appendix A.9. Note, that $\hat{\eta\prime}_{u,v,w}$ is the adequate discrete representation of the continuous function $\hat{\eta}(\mathbf{k},\omega)$, in contrast to $\hat{\eta}_{u,v,w}$ which has not the appropriate physical units

$$\hat{\eta\prime}_{u,v,w} \;\approx\; \hat{\eta}(\mathbf{k},\omega) \tag{6.23}$$

$$\hat{\eta}_{u,v,w} \;\not\approx\; \hat{\eta}(\mathbf{k},\omega). \tag{6.24}$$

Actually, $\hat{\mathsf{S}}_{\mathsf{x}u,v,w} \equiv \mathrm{i}\,u\Delta k_x\hat{\eta}_{u,v,w}$ and $\hat{\mathsf{S}}_{\mathsf{y}_{u,v,w}} \equiv \mathrm{i}\,v\Delta k_y\hat{\eta}_{u,v,w}$ are the spectra that we obtain, when applying the Discrete Fourier Transform on the surface slope image sequences $\mathsf{S}_{\mathsf{x}m,n,o}$ and $\mathsf{S}_{\mathsf{y}_{m,n,o}}$. Consequently, the power spectral density which is an appropriate approximation for the continuous representation of $S(\mathbf{k},\omega)$ in (6.11) is given by

$$S'_{u,v,w} \equiv \frac{1}{(\Delta k_x\Delta k_y\Delta\omega)^2}S_{u,v,w} \approx S(\mathbf{k},\omega), \tag{6.25}$$

where we have given the name $S_{u,v,w}$ to the power spectral density, as it is computed using the Discrete Fourier Transform (DFT)

$$S_{u,v,w} \equiv \left(\left|\hat{\mathsf{S}}_{\mathsf{x}u,v,w}\right|^2 + \left|\hat{\mathsf{S}}_{\mathsf{y}_{u,v,w}}\right|^2\right). \tag{6.26}$$

The energy spectral density $X(\mathbf{k},\omega)$ can now be approximated in terms of the computed power spectral density, using (6.14), (6.16), and (6.26)

$$X(\mathbf{k},\omega) \approx X_{u,v,w} = \frac{1}{(\Delta k_x \Delta k_y \Delta\omega)} \frac{S_{u,v,w}}{k_{u,v}^2}. \tag{6.27}$$

Here, it is convenient to express k^2 in the discretized form $k_{u,v}^2$. From (2.48) and (6.27) follows, that we get the variance of the surface displacement just by a summation over the slope power spectrum weighted with the inverse of the squared wavenumber magnitude

$$\overline{\eta^2} = \sum_{u=0}^{M-1} \sum_{v=0}^{N-1} \sum_{w=0}^{O-1} \frac{S_{u,v,w}}{k_{u,v}^2}. \tag{6.28}$$

Likewise, the mean squared slope $\left\langle s^2 \right\rangle$, also referred to as mss, is given by

$$\left\langle s^2 \right\rangle = \sum_{u=0}^{M-1} \sum_{v=0}^{N-1} \sum_{w=0}^{O-1} S_{u,v,w}. \tag{6.29}$$

For the wavenumber spectral energy density (2.49) and the frequency spectral energy density (2.50) we obtain

$$\Psi(\mathbf{k}) \approx \Psi_{u,v} = \frac{1}{(\Delta k_x \Delta k_y)} \frac{1}{k_{u,v}^2} \sum_{w=0}^{O-1} S_{u,v,w} \tag{6.30}$$

$$\Phi(\omega) \approx \Phi_w = \frac{1}{(\Delta\omega)} \sum_{u=0}^{M-1} \sum_{v=0}^{N-1} \frac{S_{u,v,w}}{k_{u,v}^2}. \tag{6.31}$$

The equations (6.27)-(6.31) are the basis for the computation of the spectral energies in the correct physical units. The spectral energies only have the right quantity if the appropriate scaling factors are applied. The scaling factors are dictated by the discretization grid.

According to the basic definition (2.51) and the discrete approximation of the wavenumber spectral density (6.30) we get

$$B(\mathbf{k}) \equiv k^4 \Psi(\mathbf{k}) \approx B_{u,v} = \frac{1}{(\Delta k_x \Delta k_y)} k_{u,v}^2 \sum_{w=0}^{O-1} S_{u,v,w}, \tag{6.32}$$

for the 2D saturation spectrum.

6.7.2. Symmetry and Periodicity Considerations

In calculations where summation or integration along the frequency axis are incorporated we have to pay attention to the symmetry and periodicity of the spectra[8] in order not to disguise valuable information. Here, we will only elaborate on the necessary considerations concerning the saturation spectrum.

The summation in (6.32) is carried out over the whole range of frequencies and thus even over frequencies that are beyond the Nyquist frequency, i.e. indices larger than $O/2$. This leads to the fact that the saturation spectrum is point symmetric around the origin of the wavenumber plane

$$B(\mathbf{k}) = B(-\mathbf{k}). \tag{6.33}$$

[8] see also section 2.5.1

However, this symmetry is not related to the actual physical properties of the wave field, e.g. if only a single wave train is propagating in the positive x direction we expect to find a spectral peak for some positive wavenumber, but not as well for the corresponding negative wavenumber[9]. This is because from the physical point of view negative frequencies are not desired, whereas in this example the negative wavenumber is associated with a negative frequency[10], since the direction of propagation is positive. As we can see, the actual directionality - and thus asymmetry - of the wave field is concealed due to the summation over the whole range of frequencies. To avoid this, we can split the summation into parts as follows

$$\begin{aligned} B_+(\mathbf{k}) &\equiv \frac{1}{(\Delta k_x \Delta k_y)} k_{u,v}^2 \sum_{w=1}^{O/2} S_{u,v,w} \\ B_0(\mathbf{k}) &\equiv \frac{1}{(\Delta k_x \Delta k_y)} k_{u,v}^2 S_{u,v,0} \\ B_-(\mathbf{k}) &\equiv \frac{1}{(\Delta k_x \Delta k_y)} k_{u,v}^2 \sum_{w=-O/2}^{-1} S_{u,v,w}, \end{aligned} \tag{6.34}$$

so that in total we still have $B(\mathbf{k}) = B_+(\mathbf{k}) + B_0(\mathbf{k}) + B_-(\mathbf{k})$. The part $B_0(\mathbf{k})$ corresponds to structures in the images that do not move at all ($\omega = 0$), so that it can be neglected in the following.

The negative frequency part $B_-(\mathbf{k})$ can be expressed in terms of the positive frequency part $B_+(\mathbf{k})$ because

$$\begin{aligned} B_-(\mathbf{k}) &= \frac{1}{(\Delta k_x \Delta k_y)} k_{u,v}^2 \sum_{w=-O/2}^{-1} S_{u,v,w} \\ &= \frac{1}{(\Delta k_x \Delta k_y)} k_{u,v}^2 \sum_{w=1}^{O/2} S_{u,v,-w} \\ &= \frac{1}{(\Delta k_x \Delta k_y)} k_{u,v}^2 \sum_{w=1}^{O/2} S_{-u,-v,w} \\ &= B_+(-\mathbf{k}), \end{aligned} \tag{6.35}$$

where we have used the symmetry of the power spectrum $S_{u,v,-w} = S_{-u,-v,w}$. Therefore the saturation spectrum is completely determined by B_+ according to

$$B(\mathbf{k}) = B_+(\mathbf{k}) + B_+(-\mathbf{k}), \tag{6.36}$$

which implies the symmetry relation that was given in equation (6.33) at the beginning of this discussion.

6.7.3. Implementation

As explained in section 2.5.1, we can exploit the separability of the DFT for a splitting of the 3D transformation. At first a 1D temporal transformation from the real valued sequence into a complex valued spectrum is performed, followed by a 2D spatial transformation from complex to complex for each slice of the spectrum in the orthogonal direction (see also figure 6.1). This is an effective way to handle the huge amount of data with respect to memory limitations on a

[9] but the DFT holds: $\cos(k_0 x) \quad \circ\!\!-\!\!\bullet \quad \frac{1}{2}\left(\delta(k-k_0)+\delta(k+k_0)\right)$ [77]

[10] Negative frequencies follow from the periodicity $\omega_N + \omega' \Leftrightarrow \omega' - \omega_N$, see section 2.5.1

32bit operating system[11]. In order to reduce the size of the resulting spectral volume, each image sequence was split in two parts (frame $1..2500$ and $2501..5000$). Using the periodicity and the symmetry property we retrieve the discrete spectra

$$\hat{\mathsf{S}}_{\mathsf{x}u,v,w} = \sum_{m=-M/2}^{M/2} \sum_{n=-N/2}^{N/2} \sum_{o=0}^{O/2} s_{x_{m,n,o}} \, \mathrm{w}_M^{-mu} \, \mathrm{w}_N^{-nv} \, \mathrm{w}_O^{ow} \tag{6.37}$$

and

$$\hat{\mathsf{S}}_{\mathsf{y}u,v,w} = \sum_{m=-M/2}^{M/2} \sum_{n=-N/2}^{N/2} \sum_{o=0}^{O/2} s_{y_{m,n,o}} \, \mathrm{w}_M^{-mu} \, \mathrm{w}_N^{-nv} \, \mathrm{w}_O^{ow}. \tag{6.38}$$

The computation was performed using the Heurisko®[12] fast Fourier transform operators in combination with cosine windowing function. The spectral volume is twosided with respect to the wavenumbers, whereas for the frequency only positive values are considered (this was explained in detail in the sections 2.5.1 and 6.7.2).

6.7.4. Ensemble Averages

Sequences that were acquired under the same experimental conditions are used to compute ensemble averaged power spectra. The typical number of image sequences for the average is 6. Due to the splitting of the sequences into halves and because we have two slope components, the number of 3D Discrete Fourier Transformations that are incorporated into the ensemble averaged power spectral density is typically 24 (corresponding to the DFT of 60000 images). Let A denote a set of N_A sequences that are incorporated into the ensemble average. Then we can specify the resulting power spectral volume as

$$S_{u,v,w} = \langle S_{u,v,w} \rangle_A = \frac{1}{N_A} \sum_{i \in A} \left(\left| \hat{\mathsf{S}}_{\mathsf{x}i,u,v,w} \right|^2 + \left| \hat{\mathsf{S}}_{\mathsf{y}i,u,v,w} \right|^2 \right), \tag{6.39}$$

where the index i denotes the serial number of the sequences and the complex valued spectral volumes are given by $\hat{\mathsf{S}}_{\mathsf{x}} = \mathrm{DFT}(s_x)$ and $\hat{\mathsf{S}}_{\mathsf{y}} = \mathrm{DFT}(s_y)$ (see preceding section).

6.7.5. Alternative Definition for $B(\mathbf{k})$

We will use a slightly different definition of the saturation spectrum

$$B(\mathbf{k}) \equiv 2 \cdot B_+(\mathbf{k}) = \frac{2}{(\Delta k_x \Delta k_y)} k_{u,v}^2 \sum_{w=1}^{O/2} S_{u,v,w} \quad , \tag{6.40}$$

instead of the definition in equation (6.32). From equation (6.36) we can see that, strictly speaking, this is not in agreement with the basic definitions of the saturation spectrum given by Phillips [130]. Phillips' saturation spectrum is symmetric by definition, whereas $2 \cdot B_+(\mathbf{k})$ is not symmetric. However, we are indeed interested in the asymmetry, because this gives information about the 2π-directionality of the wave field, see section 7.2. The factor of two is included in equation (6.40) because the values of $B_+(\mathbf{k})$ are to low by a factor of two[13] with respect to the total energy that is associated with the wavenumber $\mathbf{k}$. Note that, despite the symmetry, we are still consistent

[11] Actually the operating system was already 64bit. However, the software could not yet exploit the total amount of available memory of 8 Gbyte.

[12] Heurisko version 6.2.beta from the 9^{th} of July 2008

[13] for the DFT holds: $\cos(\omega_0 t) \quad \circ\!\!-\!\!\bullet \quad \frac{1}{2}\left(\delta(\omega - \omega_0) + \delta(\omega + \omega_0)\right)$

with Phillips' definitions in consideration of the normalization in equation (6.30), yielding $\Psi(\mathbf{k}) \approx \Psi_{u,v}$, which is of central importance for any quantitative inter-comparison of the spectra.

In former studies ensemble averages of onesided 2D slope spectra have often been used to compute the directional saturation spectrum

$$B(\mathbf{k}) \approx B_{u,v} \propto 2 \cdot \frac{1}{N} \sum_{i=1}^{N} S_{u,v} \qquad u > 0, \;\; k_x > 0, \tag{6.41}$$

e.g. Balschbach [9], Fuß [50], Jähne [74], Klinke [92]. Therefore in these cases the symmetry relation (6.33) is still valid, leading to an intermixture of the spectral energy from leeward and windward propagating waves (i.e. an 1π ambiguity). Also the one-sided spectra of the surface slope were multiplied by two, so that the total spectral energy is completely contained in the integral over the onesided representations [73].

The bottom line is: in order to preserve the directionality of the wave field and to be consistent with the energetic level from former publications we use the definition (6.40) for the saturation spectrum $B(\mathbf{k})$ in departure from Phillips [130] definition (6.32) with respect to the symmetry.

7. Results

In chapter 6 we have presented the whole chain of the operations that lead from the raw image sequences to the two component slope vector field $\mathbf{s}(\mathbf{x}, t)$ and further to the ensemble averaged 3D power spectral density of the surface slope $S(\mathbf{k}, \omega)$. Here we proceed with the physical evaluation of the data (i.e. at the outward directed arrows in the flowchart 6.1). Before we go into details, some typical slope image pairs are presented in section 7.1, which give an impression about the wave field under different experimental conditions. Then a comprehensive discussion about the saturation spectra is given in section 7.2 - divided in sub section for the different conditions. The saturation spectrum is a reduced form of the spectral density, obtained by an integration over all frequencies[1]. In contrast, the evaluation of the dispersion relation in section 7.3 predominantly deals with the spectral volume, which of course comprehends even more information about the wave field. In the context of transfer velocity parameterizations the spectral volume is commonly reduced to a scalar, namely the mean square slope, which is addressed in section 7.4. Last but not least we go back to the space-time domain in section 7.5, where observations are discussed that can be made with a new visualization for the combined measurements of the surface temperature and the wave field.

7.1. Surface Slope Images

Several examples of slope image pairs for different conditions are displayed in the following paragraphs. The slope components s_x and s_y are displayed to the left and right, respectively, and the gray scale is limited to the slope range $[-1 \ldots 1]^2$. In the images the wind is always blowing from the right to the left. The field of view is approximately $22.3 \times 10.4\,\mathrm{cm}^2$.

Microscale breaking waves can be observed for medium to high wind speeds. The microscale breaking does not produce foam, but it is apparent from the disordered structures behind the wave's crest. In front of the breaking short gravity wave, we can observe tiny parasitic capillary waves. This example corresponds to a reference wind speed of $u_{ref} = 8\,\mathrm{m/s}$.

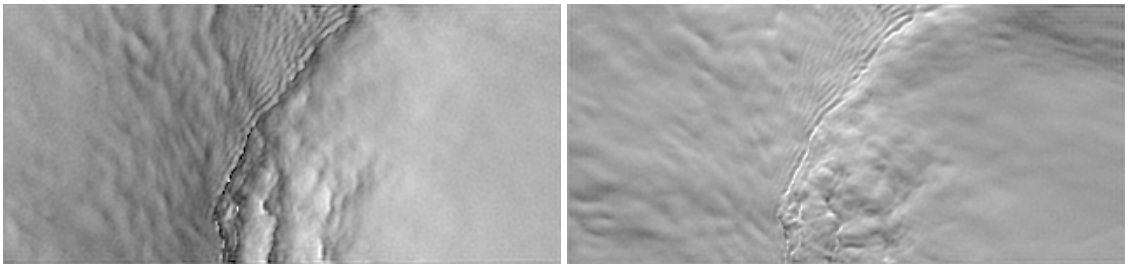

[1] ... and a scaling with k^2, to be complete.

[2] Occasionally the reproduction in printed versions is unsatisfactory, please refer to the electronic version.

The influence of surface slicks can be very pronounced. In the linear wind wave flume, with a limited fetch, the mono-molecular surface film OLA (see A.6 for details) prevents the growth of waves so that the water surface is flat, even though this example is taken at the same reference wind speed as in the preceding example ($u_{ref} = 8$ m/s).

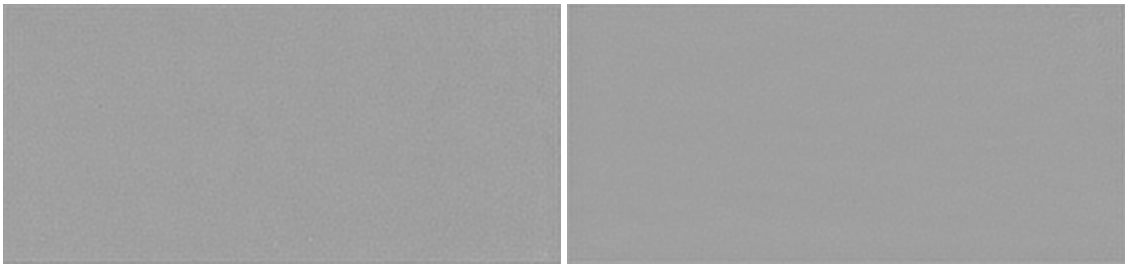

Parasitic capillary waves are propagating at the same speed in front of the crest of a short gravity wave ($u_{ref} = 4$ m/s).

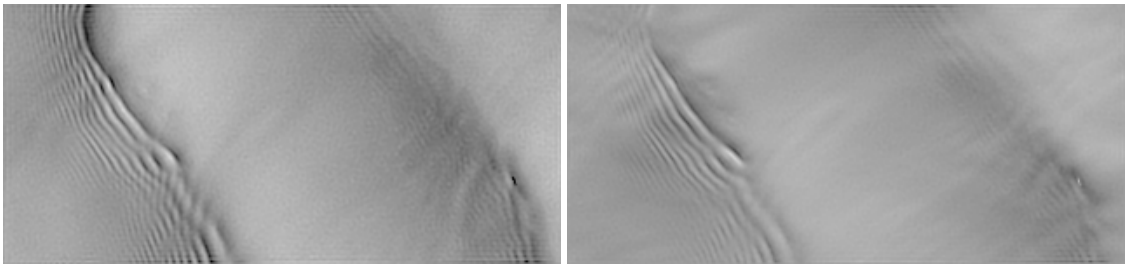

A very rough water surface resulting from strong wind forcing $u_{ref} = 14$ m/s. Note that, for a few pixels the surface slope exceeds the capabilities of the CISG (see section 4.1) which leads to missing data that is apparent as black or white dots.

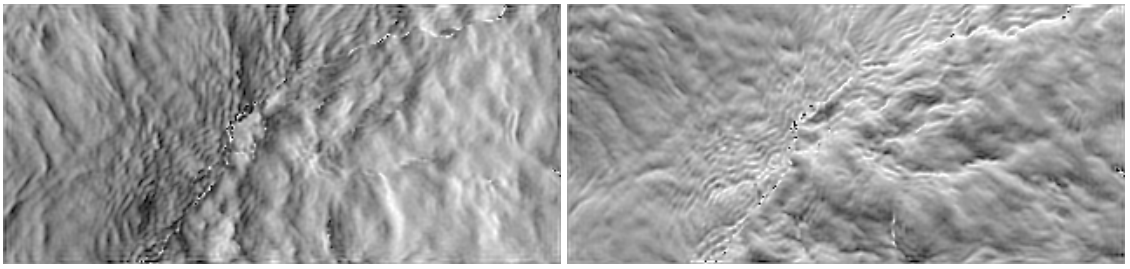

Rain drop impacts form craters and ring waves, which also leads to a very rough surface. (rain rate ≈ 57 mm/h; $u_{ref} = 4$ m/s).

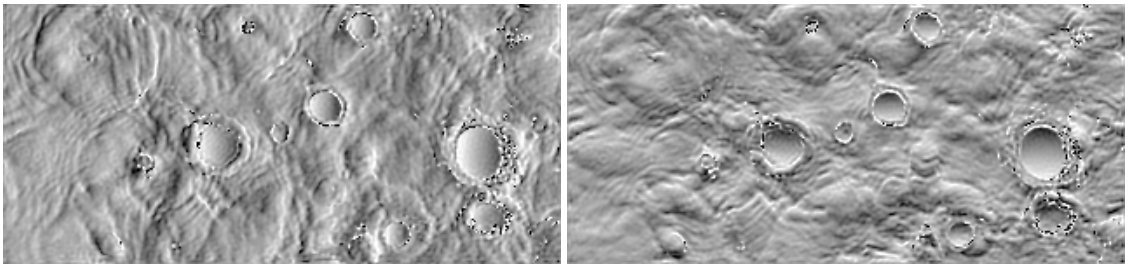

7.2. Saturation Spectra

The saturation spectra presented in this section are giving insights in the two-dimensional spatial structures of the wave field for the Hamburg linear wind wave tank (at a fetch of 14.4 m) under a wide range of experimental conditions, including surface slicks and rain. The wavenumber range includes short gravity waves with $k > 100$ rad/m ($\lambda \approx 6$ cm) and capillary waves up to $k < 2300$ rad/m ($\lambda \approx 2.7$ mm).

For the presentation the limit $|k|$<2300 is chosen well below the Nyquist wavenumber[3] because beyond 3000 rad/m artifacts stemming from the CCD sensor and noise are influencing the signal. Moreover, the color images are contrast corrected by inverse filtering with the MTF, see section 6.2. The recovery of the spectral energy works only reliably as long as the MTF is high enough, say 33% which is the case for $k > 3000$ rad/m. Additionally, from the Nyquist frequency of 982 rad/s and from the linear dispersion relation we expect aliasing effects for wavenumbers greater than 2300 rad/m.

Here, unlike former onesided directional wave spectra, we present twosided spectra. This is possible, because the spatiotemporal measurement allows for a determination of the direction in which the waves are propagating. Therefore the directional spectra cover a range of 2π for the wave direction, whereas most of the reported measurements only give the orientation rather than the direction of the wavenumber components, which leads to an 1π ambiguity (e.g. [68, 93]). The computation of the saturation spectra, based on the definitions from the sections 2.3 and 6.7.5, is performed according to

$$B(\mathbf{k}) \equiv 2 \cdot B_{+}(\mathbf{k}) \approx B_{u,v} = \frac{1}{(\Delta k_x \Delta k_y)} k_{u,v}^2 \cdot 2 \cdot \sum_{w=1}^{O/2} S_{u,v,w} \quad , \tag{7.1}$$

where

$$S_{u,v,w} \equiv \left(\left| \hat{\mathsf{S}}_{\mathsf{x}u,v,w} \right|^2 + \left| \hat{\mathsf{S}}_{\mathsf{y}u,v,w} \right|^2 \right) . \tag{7.2}$$

is the power spectral density of the surface slope. The indices u and v are the grid points in the wavenumber plane, ranging from $-M/2$ to $+M/2$ and $-N/2$ to $+N/2$ respectively, where M and N correspond to the sensor size in the x and y direction. The index w ranges from 1 to $O/2$ and represents the positive frequency axis, where $O = 2500$ is the number of images that were used for the 3D Fourier transform, see also section 6.7.3. The spectra are based on ensemble averages of the power spectral density computed over 4-24 sets of 2500 images, acquired at constant experimental conditions, see also section 6.7.4.

The saturation spectra are presented in groups, according to the experimental condition, see figures 7.1 through 7.13. Each individual plot is accompanied by a title that can be read in terms of the experimental conditions, e.g. `u062` stands for a reference windspeed of 6.2 m/s; `r057` stands for a rain rate of 57 mm/h; `s2` stands for slick type 2 (see table A.6 for the slick type coding); `w1` stands for a superimposed mechanical wave with a frequency of 1 Hz.

It is well established to display the 2D saturation spectra after a transformation of the wavenumber space from the cartesian coordinate system to a polar coordinate system (e.g. [9, 84, 92, 93]). This enables to compare the degree of saturation for a given wavenumber magnitude $k = (k_x^2 + k_y^2)^{1/2}$ and for its polar angle $\Phi = \mathrm{atan}(k_y/k_x)$, which gives the direction of the wavenumber vector relative to the wind direction. Based on this representation two descendant diagrams are commonly used for the discussion and modeling. These are the omnidirectional spectra $B(k)$ which follow from an integration over the polar angles

$$B(k) = \int_{-\pi}^{\pi} B(k, \Phi) d\Phi \tag{7.3}$$

[3] Nqyuist wavenumber $k_N = 4488$ rad/m

and the angular spreading function which follows from an average over the wavenumber magnitudes.

In the following sections the characteristics of the spectral distributions are discussed, starting with the pure wind condition in section 7.2.1. The influence of rain is shown in section 7.2.2. Section 7.2.3 deals with the results for surface slick conditions. The saturation spectra for the combination of rain and surface slicks are shown in section 7.2.4. Finally, section 7.2.5 displays the results for a condition where a 1 Hz mechanically generated was superimposed on the wind wave field.

7.2.1. Pure Wind Conditions

The 2D saturation spectra for wind speeds in the range of 3 m/s to 14 m/s are displayed in figure 7.1. The overall picture is very consistent with previous measurements at limited fetch and pure wind conditions. Thanks to the advances in the measurement technique and the data evaluation there are some new aspects that need to be adressed. Especially concerning the wavenumber dependence a new look at the cutoff at high wavenumbers is recommended.

The spectra are presented on a polar–logarithmic wavenumber grid, where Φ gives the direction of the wave propagation relative to the mean wind direction. The spectral components for $\Phi = \pm 180^\circ$ correspond to structures that are traveling against the wind. In case of rain conditions we expect a significant isotropic spectral contribution due to ring waves from rain drops, which is discussed in section 7.2.2 and shown in figure 7.8. However, under conditions without rain the waves are expected to travel in the leeward direction (along with the wind) as long as no significant wave breaking is observed. Behind breaking crests a turbulent wake is frequently observed (e.g. see examples in section 7.1). The turbulent wake is visible in the slope images as disordered structures that are linked to the subsurface turbulence. Therefore an enhancement of the windward spectral energy can be a hint of wave breaking. Anyhow, most of the spectral energy found in the windward direction is due to aliasing, which leads to a point reflection around the origin in the k_x–k_y plane, see also section 2.5.1. Aliasing does not occur for very low wind speeds ($u < 3$ m/s) under normal conditions (top left in figure 7.1). But we can already observe characteristic humps in the windward direction for the saturation spectra in figure 7.1 for all wind speeds greater or equal 4 m/s. The spectral energy contained in these humps is consequently missing in the leeward direction, which might give the misleading impression of a spectral cutoff beyond 1000 rad/m. This artifact is not to be confused with the cutoff at high wavenumbers that had been observed for instance by Zhang [177] or Klinke [93]. In fact, the typical k^{-3} behavior in the cufoff range seems to be compensated for if we apply the MTF correction, which can be assessed best regarding the direct comparison of the omnidirectional saturation spectra with and without MTF correction presented in figure 7.2. This observation will be discussed in more detail at the end of the next paragraph.

Wavenumber Dependence

For a low wind speed ($u_{ref} = 3$ m/s) the degree of saturation shows a $k^{-2.5}$ decrease in the range between spectral peak of the dominant wave at $k_p = 111$ rad/m and $k \approx 400$ rad/m where $B(k)$ fades into a local minimum, see figures 7.1 and 7.2[4]. For higher wind speeds the scales of the dominant waves ($k < 100$ rad/m) cannot be resolved in the saturation spectra due to the finite image size. Using the dispersion relation, the wavenumbers of the dominant waves can be inferred from the peak frequency ω_p of the frequency spectra, presented in section A.3.2. However, the spectral energy in the short gravity range is affected by the energy of the dominant wave so

[4]Figure 7.2 displays the the omnidirectional saturation spectra, i.e. $B(k, \Phi)$ integrated over $\Phi = -\pi \ldots \pi$.

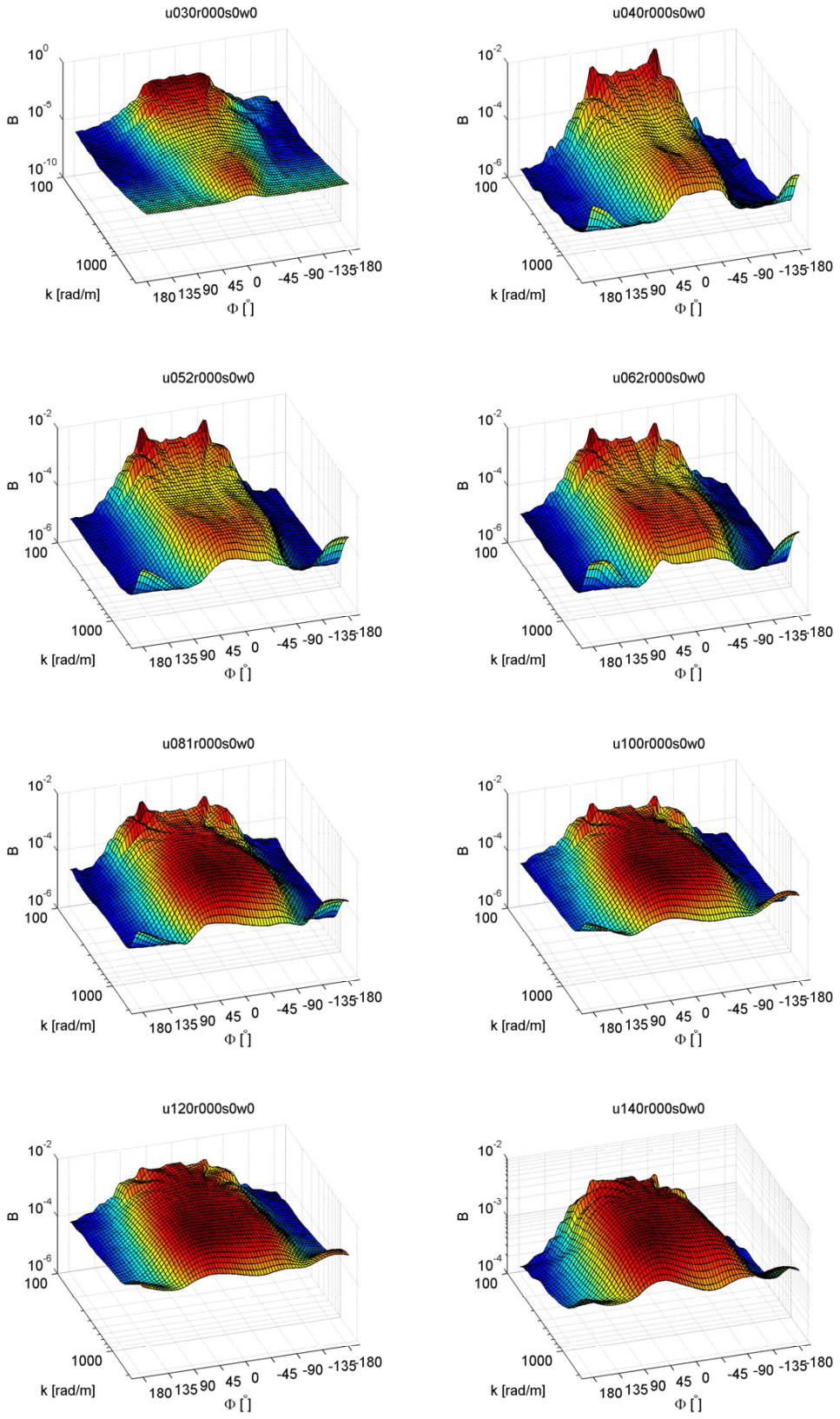

Figure 7.1.: Twosided and MTF corrected saturation spectra for windspeeds 3.0,4.0,5.2,6.2,8.1,10.0,12.0, and 14.0 m/s at fetch 14.4 m.

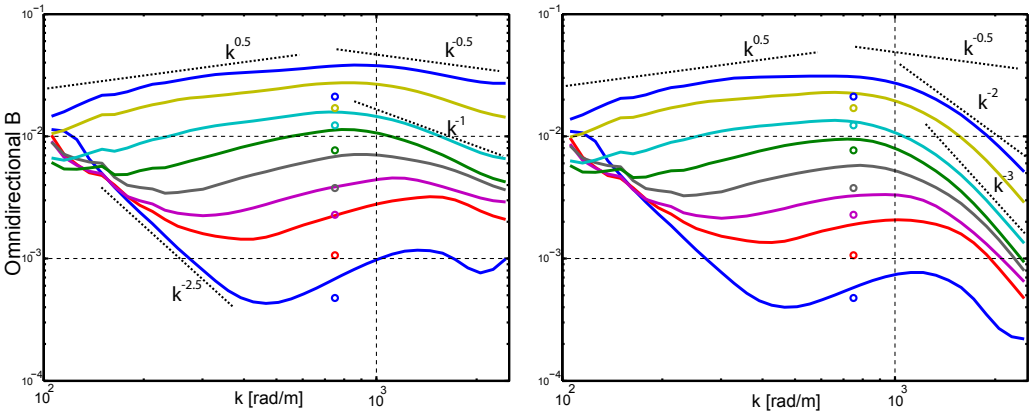

Figure 7.2.: Omnidirectional saturation spectra. Wind speeds are 3.0, 4.0, 5.2, 6.2, 8.1, 10.0, 12.0, and 14.0 m/s (according to low to high degree of saturation). The additional circles correspond to the empirical formula (7.4) for the degree of saturation at $k = 750$ rad/m given by Apel [8]. left: with MTF correction; right: without MTF correction.

that a local minimum of the degree of saturation is observed in this range. For medium wind speeds of 4 m/s through 6 m/s the local minimum is gradually filled up and shifted toward smaller wavenumbers while the decrease toward the minimum is less steep. This is because the wavelength of the energy containing dominant waves increases, so that their spectral energy has less influence on the captured wavenumber range, despite the fact that the short gravity waves produce parasitic capillary waves. The dip in the capillary-gravity range is a common feature for medium wind speeds and small fetch. Zhang [177] showed that this can be attributed to the effect of capillary blockage of both capillary-gravity wind waves and parasitic capillary waves (see also Phillips [133]).

In the range of gravity-capillary and capillary waves, to the right of the local minimum of each spectrum, the degree of saturation gently rises, following approximately a $k^{0.5}$ trend. This is consistent with measurements by Jähne and Riemer [84], Klinke [93], Klinke and Jähne [94] and Balschbach [9] performed in a variety of wind-wave tanks (Delft, Marseille, Urbana, Heidelberg). An increase of B with $k^{0.5}$ is characteristic for an equilibrium range, which was originally modeled by Phillips [130] and Kitaigorodskii [91] for short gravity waves, see section 2.3.2. But strictly speaking, these models are not readily expected to be valid in that wavenumber range since capillary effects have been excluded and the dispersion relation for deep water gravity waves ($\omega^2 = g \cdot k$) was used for the derivation of the 0.5 power law. For the given wavenumber range the capillary effects can no longer be neglected since the ratio of the gravitational force to the surface tension force is already smaller than one for wavenumbers greater than $k = 364$ rad/m, where the phase velocity attains its minimum.

The degree of saturation for the capillary waves reaches a maximum at wavenumbers between 700 rad/m and 1500 rad/m. For the lowest wind speed the wavenumber at the peak of this maximum is approximately described by equation (2.43), indicating that parasitic capillary waves strongly contribute to the degree of saturation [99]. For higher wind speed, the expected wavenumber of the parasitic capillaries would already be greater than 2700 rad/m, which is not covered by our analysis due to the limited resolution.

The MTF corrected omnidirectional spectra in figure 7.2 (left) show that the degree of saturation for medium to high wind speeds decreases according to a $k^{-0.5}$ to $k^{-1.0}$ power law for wavenumbers greater $\sim$1000 rad/m. The incidence of a change in the wavenumber dependence beyond 1000 rad/m is in correspondence with former observations. But, the strength of the decrease is considerably less and stands in contradiction to what has apparently become part of the general knowledge in our community. I.e. former measurements by e.g. Jähne and Riemer [84], Klinke

[93], and Zhang [177] showed a sharp spectral cutoff with a wavenumber dependence according to k^{-2} to k^{-3} power laws (see for instance figure 2.7). The appearance of this cutoff in the former measurements was interpreted as a characteristic feature of the fully developed wave field [92]. Since then, the cutoff feature has guided the modeling approaches for the energy fluxes in the capillary range, e.g. Kudryavtsev et al. [99], Apel [8], Elfouhaily et al. [44], Lyzenga [114], see also figure 2.8. Klinke [92] found the cutoff wavenumber[5] to be independent of the wind forcing. Based on this finding it was argued in Jones and Toba [88, chapter 4.3.6] that the spectral energy could not be solely modeled by a balance between the wind input and viscous dissipation, as postulated by the Donelan and Pierson [40] model. In the model by Kudryavtsev et al. [99] a spectral cutoff $B(k) \propto k^{-2}$ is obtained for the parasitic capillaries from an energy balance assuming that the nonlinear dissipation of the dominant waves is equal to the energy losses of the capillaries due to molecular viscosity. These examples are given to illustrate the impact of the cutoff observation for the wave modeling.

As described above, the MTF corrected spectra only gently decrease in the vicinity of 1000-2300 rad/m. Presumably this behavior might even be observable for higher wavenumbers up to 6300 rad/m where the viscous dissipation ($\propto k^2$ [104]) is believed to be predominant [8] and finally leading to a viscous cutoff.

Spectral cutoff in the vicinity of 1000 rad/m: Feature or Artifact? Now, even for the recent measurement we would diagnose a cutoff for wavenumbers greater 1000 rad/m if we omitted the MTF correction, see figure 7.2 (right). In this case we would testify a wavenumber dependence following k^{-2} to k^{-3}, in compliance to former measurements. Therefore we can attribute the discrepancies to the MTF correction which was not incorporated into former evaluations. For digital images, the MTF is mainly determined by the spatial discretization, see sections 2.5.2 and 4.5. Since the resolution for most measurements was in the same order of magnitude (see table A.1) it is plausible that the cutoff wavenumbers from different experiments was found to be consistent. Moreover, also the wind speed independence of the cutoff wavenumbers could be explained by the influence of the MTF. Therefore, in the light of the new measurements, it is likely that the spectral cutoff in the vicinity of 1000 rad/m is an artifact, but not a feature of the wave field. This implies the need for a reexamination of the whole issue.

However, also the MTF corrected spectra presented in this work may have some undetermined biases so that this question cannot be finally answered here. There are two sources that artificially enhance the high wavenumber spectral energy:

1. The MTF correction also amplifies the spectral energy of noise.
2. Extremely high slopes ($|s| > 1$) cannot be measured due to the finite size of the illumination (see section 4.1), this occasionally leads to missing data (discontinuities) which in turn affect the spectral energy at all scales.

Here the influence of noise is not crucial since its contribution to the spectral energy is only noticeable for measurements where the surface is essentially flat - this is the case for very low wind speeds $u \leq 2$ m/s or with strong surface slicks as shown in section 7.2.3. For the clean surface condition and wind speeds greater 3 m/s the noise level is at max -35 dB. In contrast, the second issue may have a significant influence for high wind speeds as the incidence of steep waves and wave breaking increases. But still, since former instruments also suffer from this problem, the actual discrepancy cannot be explained by this.

[5] The cutoff wavenumber was obtained from the intersections of two straight lines in the log-log representation. While one line was describing the spectral increase in the equilibrium range, the other line was describing the spectral cutoff beyond 1000 rad/m.

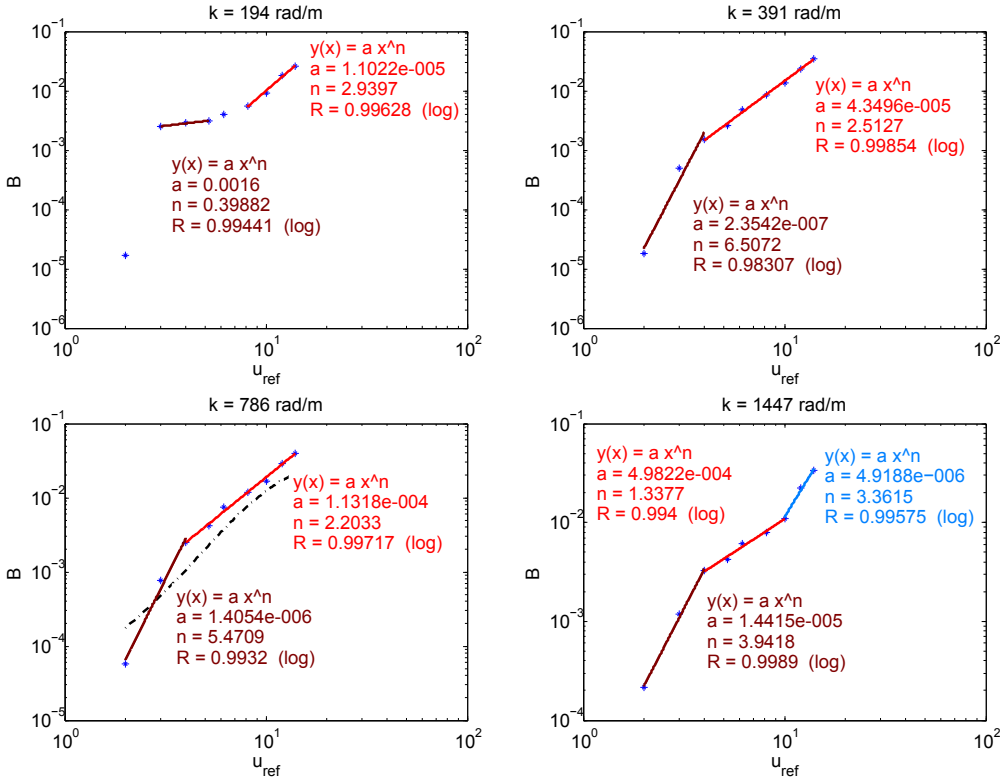

Figure 7.3.: Wind speed dependence of the degree of saturation for selected wavenumbers as indicated. The additional dash dot curve in the lower left plot corresponds to the empirical formula (7.4) for the degree of saturation at $k = 750$ rad/m given by Apel [8].

The contrast damping unavoidably occurs in the acquisition and post-processing of the slope images as long as the spatial resolution is in the same order of magnitude as the smallest wavelengths occurring within the wind wave field. As mentioned earlier, the MTF correction can compensate for the contrast modulation, but only to a certain extend since the MTF measurement for high wavenumbers is also affected by uncertainties. Therefore, new measurements with higher spatial resolution are requested in order to answer the questions that arise from the analysis in this work.

Wind Speed Dependence

The wind speed dependence of the degree of saturation at certain wavenumbers is shown in figure 7.3. Note, the degree of saturation is displayed as a function of reference wind speed instead of u_* because at the time of this analysis the u_*-u_{ref} relationship was not yet available. Therefore we assumed, as a first order approximation, that u_* and u_{ref} are proportional[6]. Under this assumption the power law relations remain unchanged and can be compared with results by Klinke [93], Balschbach [9] and Hwang [71]. For capillary waves with wavelengths in the range of 1.7-0.8 cm (391-780 rad/m) the degree of saturation follows approximately an u_{ref}^2 power law for medium to high wind speeds. For the shorter capillary waves with $\lambda = 0.43$ cm (1447 rad/m) there is a steep increase in the degree of saturation for low wind speeds ($\propto u_{ref}^4$) and also for high wind speeds ($\propto u_{ref}^{3.4}$) while for medium wind speeds the increase is less steep ($\propto u_{ref}^{1.3}$). In the short gravity range $\lambda = 3.2$ cm (194 rad/m) there is only a very weak wind speed dependency ($\propto u_{ref}^{0.4}$)

[6]The u_*-u_{ref} relationship, shown in section 5 became available just a few days before the deadline of this thesis. From figure 5.1 one can see, that the approximation $u_* \propto u_{ref}$ leads an overestimation of u_* for $u_{ref} < 5$ m/s and an underestimation for $u_{ref} > 5$ m/s.

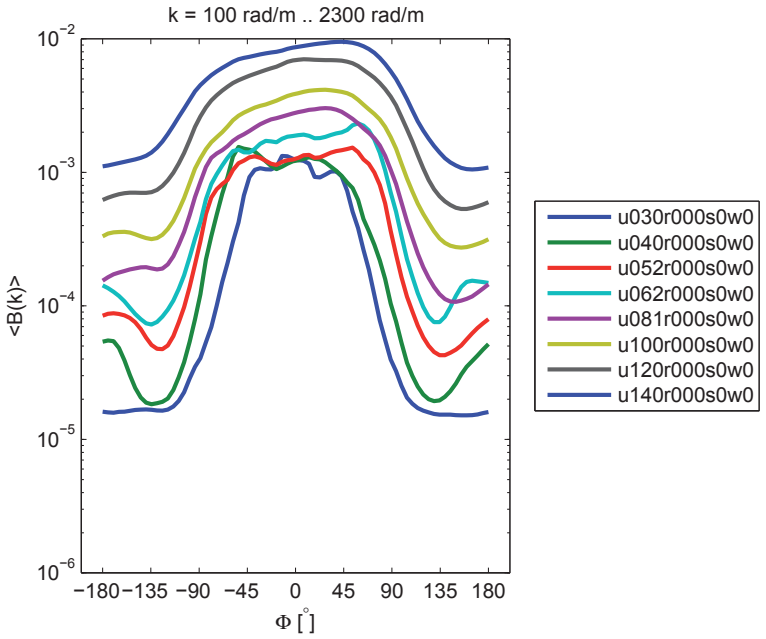

Figure 7.4.: Angular Spreading averaged over the whole wavenumber range.

for medium wind speeds, followed by an u_{ref}^3 power law for wind speeds greater than 8 m/s. In comparison with data by Klinke [93] and Balschbach [9] no clear conclusion about the wind speed dependence can be drawn. The dependency is sensitive to the choice of the wavenumbers relative to the position of the capillary peak. This can be partially explained by the fact that the laboratory wave fields have not yet fully established an equilibrium range, so that waves in the capillary range strongly depend on the fetch limited upgrowth of the dominant waves. Moreover, as pointed out by Hwang [71], the wind speed dependence of the degree of saturation from laboratory measurements are not directly comparable to the available measurements from the open ocean.

Based on data by Klinke [92] the model by Apel [8] gives a formula for the degree of saturation for k=750 rad/m

$$B_A(u) = \exp\left(\left[-4.95 + 3.45\left(1 - e^{\frac{-u}{4.7m/s}}\right)\right]\ln 10\right), \tag{7.4}$$

where u is a reference wind speed. As a qualitative check for the order of magnitude $B_A(u)$ was computed using (7.4) along with the reference wind speed of our measurement. These values are plotted as additional circles in figure 7.2 and as a dash-dot line in the bottom left plot in figure 7.3. The levels of the degree of saturation are surprisingly consistent, taking into account that neither the fetch nor the wind speed are strictly comparable.

Angular Spreading

As stated in section 2.3.2, the angular distribution of the saturation spectrum in the gravity-capillary range is of special interest in the light of the resonant condition for wave-wave interaction. If the spread is narrow, the lowest order for wave-wave interaction is that of quartets [63, 130]. At high wind speeds, when the distribution of the short waves is broad also triad interaction can occur and become dominant over the quartet interaction [177].

Angular profiles are obtained by averaging the 2D saturation spectra over all wavenumbers, see figure 7.4. Additionally, in order to make a qualitative distinction between the short gravity wavenumber and the capillary wavenumber ranges, the average was compute over selected

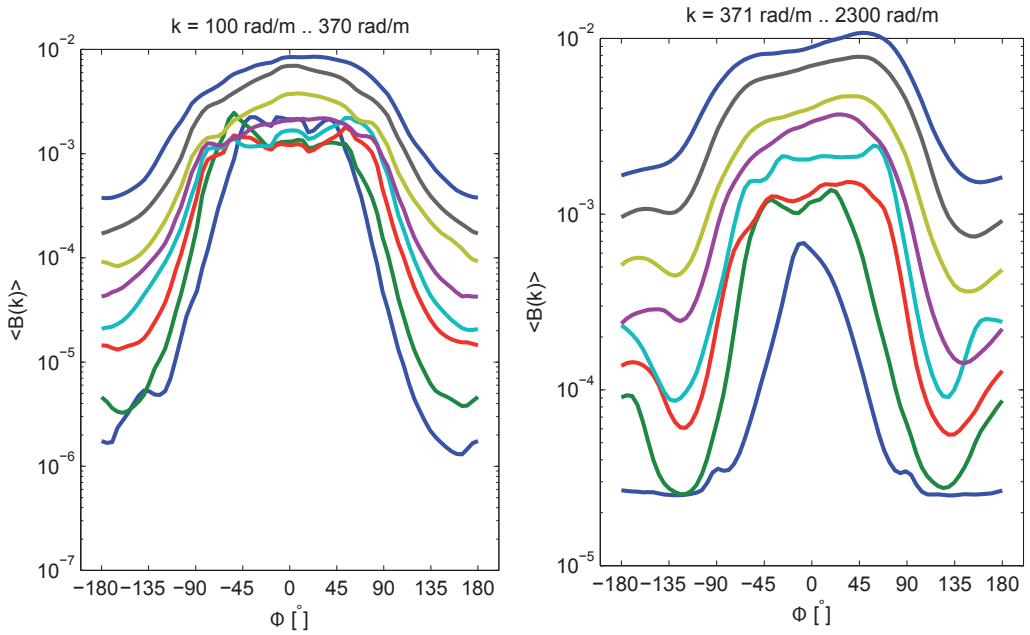

Figure 7.5.: Angular Spreading. Left: short-gravity range; Right: capillary range. (legend, same as figure 7.4)

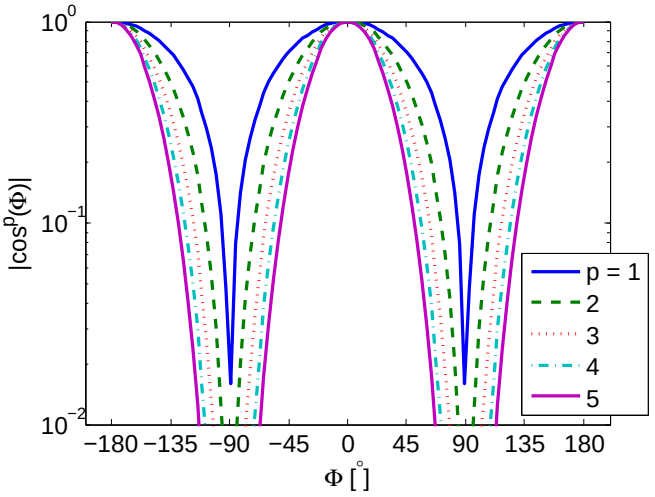

Figure 7.6.: Angular Spreading. Model curves $|cos^p(\Phi)|$ for different values of p as indicated.

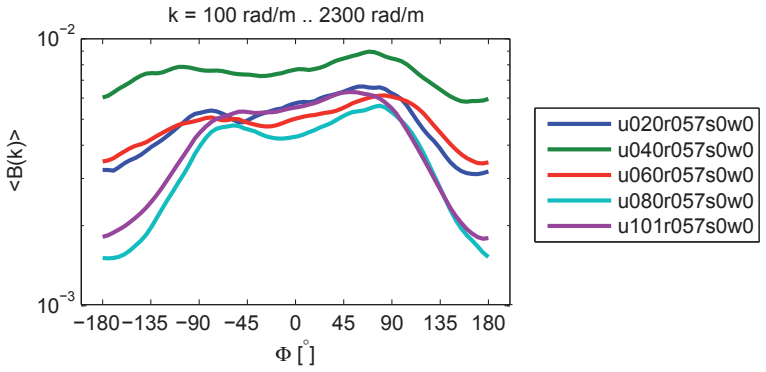

Figure 7.7.: Angular spreading for the wind and rain conditions. (Note, the relative enhancement of spectral level for the condition `u040r057` is presumably due to an anomalous high rain rate.)

wavenumber ranges, see figure 7.5. For low to medium wind speeds the spectral energy is confined within an $\pm 45°$ cone which gradually increases with wind speed. The directional distribution in the short gravity range is always broader than the spread in the capillary range. (Note that the angular resolution for the long waves is rather poor. This can be seen directly in the 2D spectra, figure 7.1, that show step-like behavior for small wavenumbers according to limitations in the angular resolution.) In the capillary range a slight asymmetry can be observed which might be due to the geometry of the tank and the location of the image section. For high wind speed ($u \geq 10$ m/s) the angular spreading even extends over $\pm 90°$ which can be an indicator for wave breaking. Additionally, the modulation of short wind waves by the orbital motion of the long waves may contribute to the signal beyond $|90°|$. Due to the $180°$ ambiguity of former measurements both effects could not be quantified from spectral analysis even though it is already apparent from the visual inspection of the image sequences. As a matter of fact, the angular distribution is also affected by aliasing which is discussed right in the beginning of section 7.2.1. The aliasing primarily leads to the humps in the capillary distribution close to $|180°|$. To overcome this artifact a higher camera frame rate is necessary.

Model curves of $|cos^p(\Phi)|$-type[7], as introduced in section 2.3.2, are shown in a semi-logarithmic plot in figure 7.6. In comparison with the data from the Hamburg wind wave tank we see that in the capillary regime for low wind speeds p must have a value of at least 5, while for higher wind speed and longer waves p must gradually go down to 1.

7.2.2. Wind & Rain Conditions

Rain strongly contributes to the degree of saturation in the capillary wave range. For low to medium wind speeds the saturation spectra are clearly dominated by the isotropic rain signal, see figure 7.8. Only for wind speeds greater 8 m/s the angular distribution recovers its directionality from the wind driven components of the wave field as apparent from figure 7.7. The spectral energy of the long waves is less, compared to pure wind conditions, which can be explained by wave damping due to the sub surface turbulence that is induced by the rain. This observations is consistent with measurements by Yang et al. [172] who performed measurement with a scanning laser slope gauge 31 cm away from the downwind edge of their rain module. To the authors knowledge no two-dimensional saturation spectra for rain conditions are available by now. For our experiments only a single rain rate with a fixed drop size could be realized. Thus, only first impressions of the rain influence on the wave spectra can be given here. In the context of gas-exchange investigations it was found that the drop size distribution has significant influence on the

[7] usually the range is only $\pm\pi$.

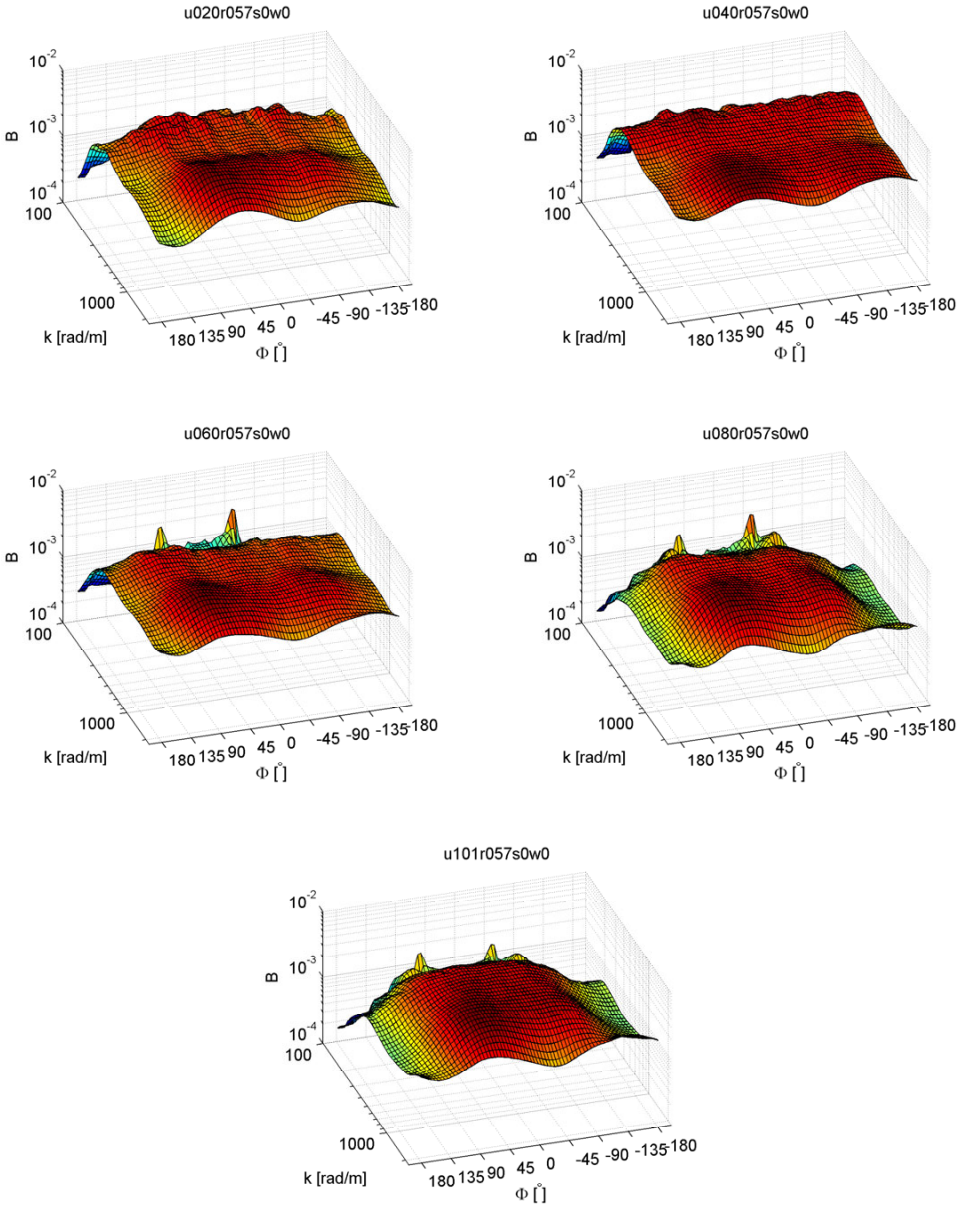

Figure 7.8.: Twosided and MTF corrected saturation spectra for windspeeds 2.0, 4.0,6.0,8.0, and 10.1 m/s at fetch 15 m with a rainrate of 57 mm/h.

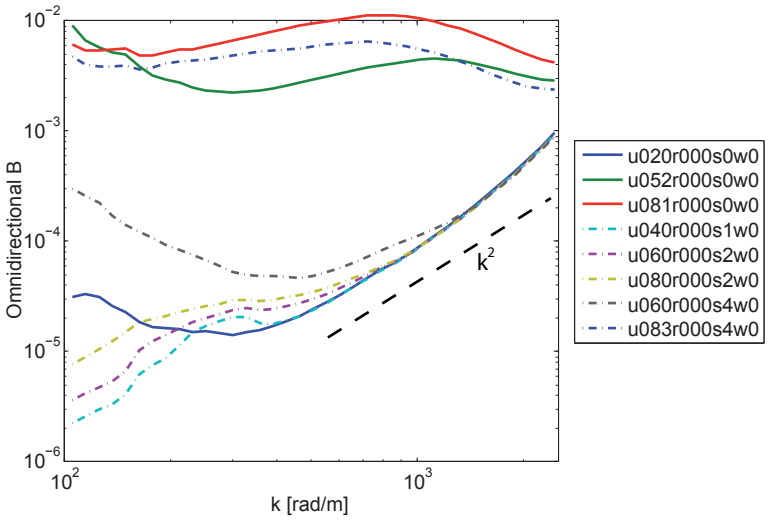

Figure 7.9.: Omnidirectional saturation spectra for slick conditions (dash dot lines) and selected pure wind conditions (solid lines).

correlation between the transfer velocity and the measured surface roughness [65]. The shape of the spectra is of great interest for the interpretation of radar backscatter as pointed out by Braun et al. [25]. For that, future investigations combining the slope imaging with radar measurements are desired.

The omnidirectional saturation spectra, corresponding to figure 7.8, are shown in the comparison of the wind&rain and the wind&rain&slick conditions in figure 7.11. The enhancement factor for the degree of saturation that is due to rain is exemplified in figure 7.12, see also the discussion section 7.2.4.

7.2.3. Wind & Slick Conditions

For the experiments with the mono-layer surface slicks[8] PME and OLA the water surface is essentially flat. The saturation spectra for the slick conditions are thus comparable to the spectrum from a very low wind speed 2 m/s, except for the small wavenumber range, see figure 7.10. Only for a wind speed of 8.3 m/s the PME slick broke up and waves could develop. The general shape of the spectra from the flat water surface is dominated by the noise signal. Since the saturation spectra are proportional to k^2 times the slope spectra, also the contribution of noise appears as an increase in the degree of saturation, following a k^2-power law. Due to the MTF correction, which also amplifies the spectral energy of noise, the actual increase in the high wavenumber range of the saturation spectra shows an $k^{2.7}$ behavior. From a comparison to the pure wind case (see figure 7.9 and section 7.2.1) we can see that the energy level of the noise is still orders of magnitude lower than the energy of the wind waves, e.g. for 1580 rad/m the degree of saturation for a wind speed of 5 m/s is 15 times higher than the noise level that can be inferred from the 2 m/s saturation spectrum.

Despite the general trend that is due to noise we can observe enhanced spectral energy around $\Phi = \pm 90$ that might be due to waves that are produced by vibration and reflections in the tank, see figure 7.10. However, crosswind traveling waves are not observed by visual inspection of the image sequences and therefore we cannot rule out the possibility that this is an artifact.

[8] Further informations about the surface slicks are to be found in the appendix A.6

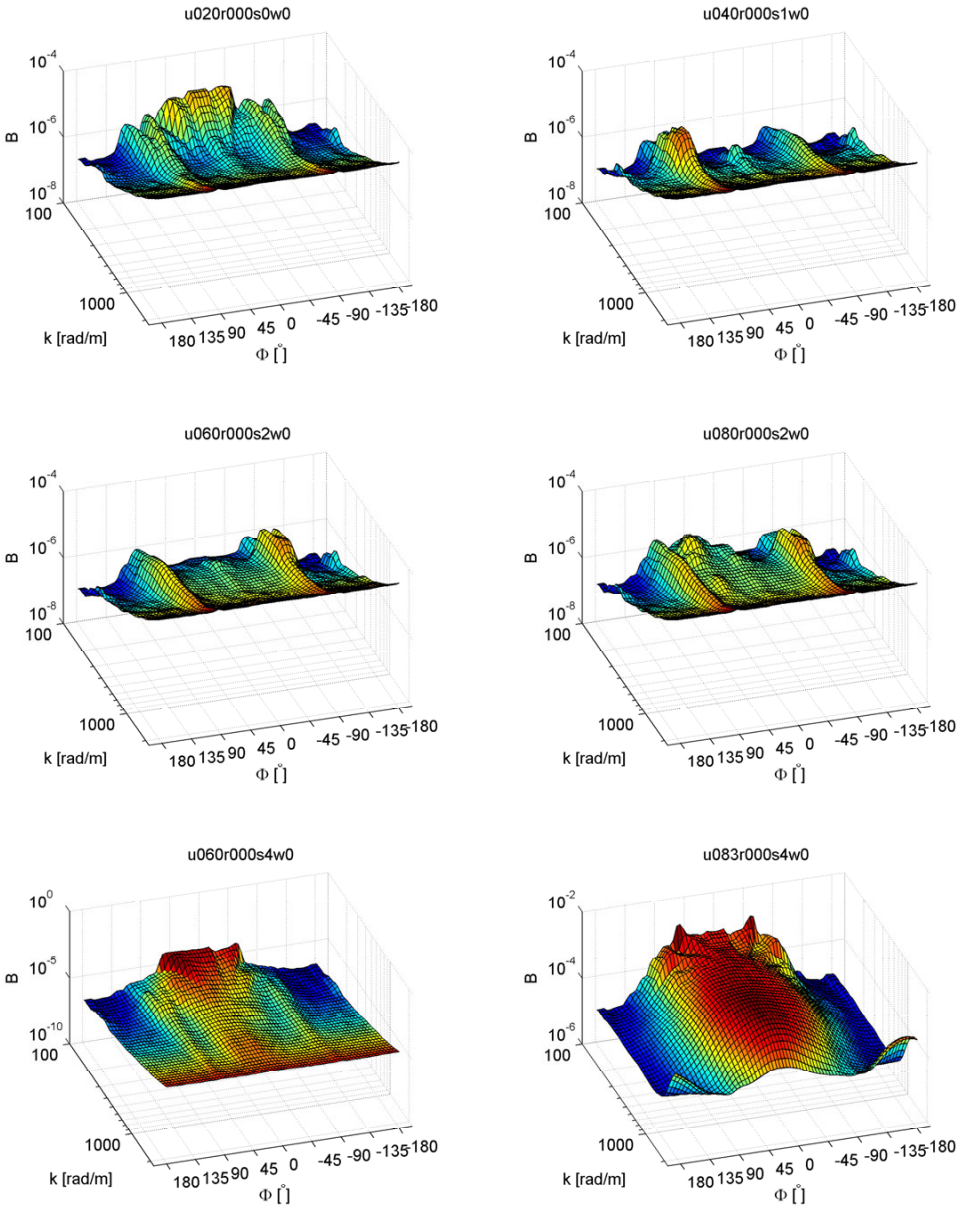

Figure 7.10.: Twosided and MTF corrected saturation spectra for a very low windspeed (2 m/s top left) and with surface slicks (4, 6, 8 m/s). Slick type as coded in table A.6.

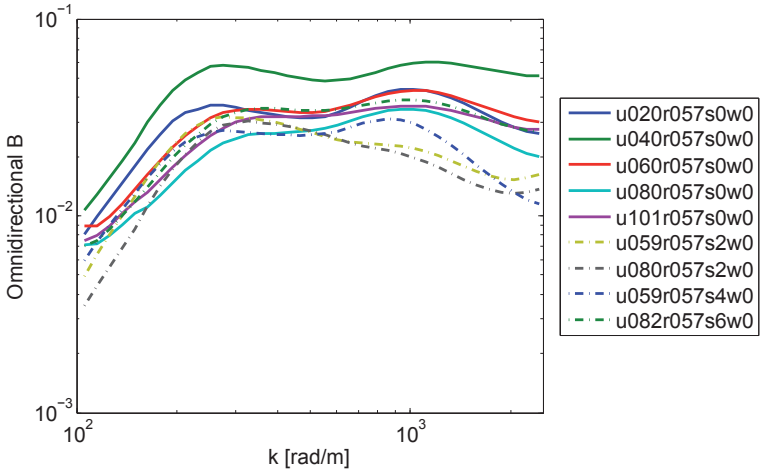

Figure 7.11.: Omnidirectional saturation spectra for rain conditions, with and without surface slicks.

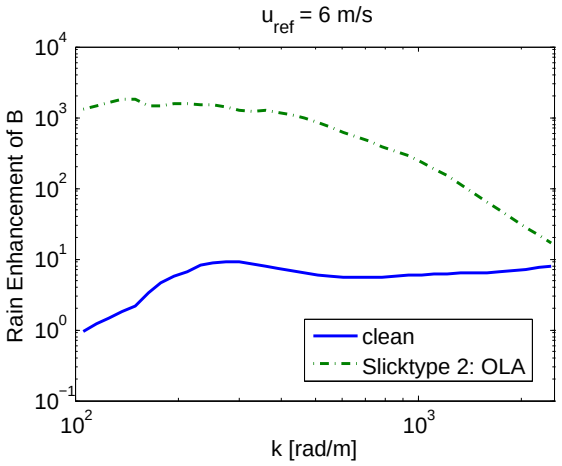

Figure 7.12.: The enhancement of the degree of saturation due to rain for clean and slick conditions.

7.2.4. Wind & Rain & Slick Conditions

The combination of wind, rain and surface slicks leads to saturation spectra that look very much like those for wind and rain conditions alone. The 2D saturation spectra are displayed in the appendix, figure A.1. Regarding the omnidirectional spectra 7.11 we can see that the degree of saturation for the slick conditions, compared to clean conditions, is diminished for k>500 rad/m. This is consistent with our expectation, based on former investigations of wave damping with the same surface slicks by Gade et al. [51]. The enhancement of the degree of saturation due to rain is shown in figure 7.12 for a clean surface and a surface slick condition. The enhancement curves correspond to $\frac{B_{u060r000s2w0}}{B_{u059r057s2w0}}$ (dash-dot line) and $\frac{B_{u062r000s0w0}}{B_{u060r057s0w0}}$ (solid line). From this example we can see that especially for the combination of rain and surface slicks the rain effect is very pronounced. The rain enhancement factor for the clean surface condition is in the range of 1 to 10, while for the surface slick condition it goes up to a factor of 1800. For the surface slick conditions in the absence of rain we observed an increase of $B(k)$ for higher wavenumbers corresponding to noise, compare figure 7.9. This explains the decline of the rain enhancement factor for the slick condition at higher wavenumbers.

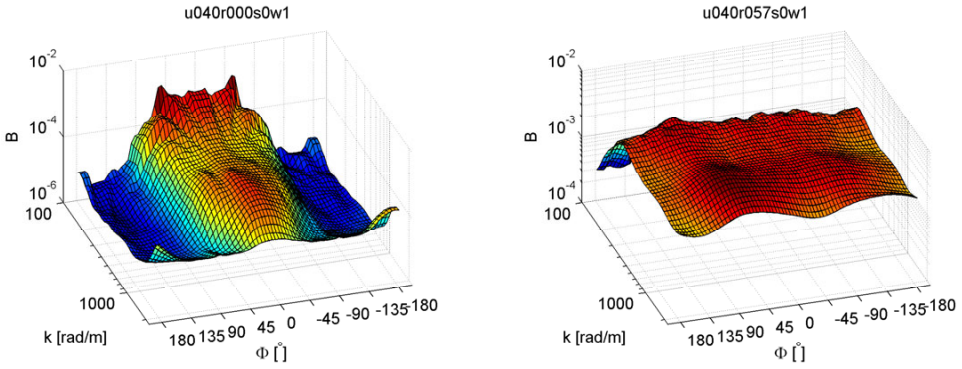

Figure 7.13.: Twosided and MTF corrected saturation spectra with additional 1Hz mechanical wave.

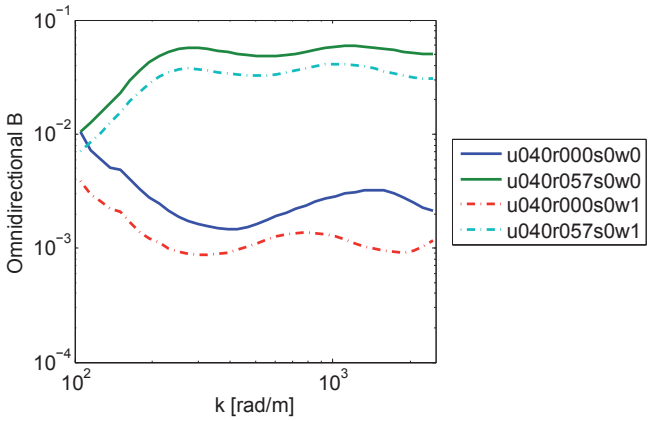

Figure 7.14.: Omnidirectional saturation spectra with superimposed mechanical wave (dash-dot line) in comparison to similar conditions without the mechanical wave.

7.2.5. Mechanical Wave Conditions

The wind wave fields measured in the laboratory differ from open ocean measurements[93]. One important difference is the lack of gravity waves in the laboratory wind wave fields due to the limited fetch. This has implications for the gravity-capillary regime for several reasons: (i) short and steep gravity waves may generate parasitic capillaries [132]; (ii) straining may be imposed on the capillaries as they propagate through the orbital velocity field of the gravity waves [125, 155, 177]; (iii) the momentum input to smaller waves by the wind field may be altered, e.g. through the non-separated sheltering mechanism [116]; (iv) capillary blockage may occur for gravity waves with $k > 12\,\mathrm{rad/m}$ [177]; (v) breaking of the gravity waves.

In order to come closer to field conditions in the wind wave tank, mechanically generated waves with a frequency of 1 Hz ($k \approx 4.16\,\mathrm{rad/m}$) have been superimposed to the wind wave field for a selected wind speed of 4 m/s. The wavelength of the mechanical wave is too big and its amplitude to low, so that the above mentioned influences (i), (iv) and (v) are still not expected to be relevant. However, at least a qualitative check whether or not (ii) and (iii) are significantly influencing the saturation spectra in the short-gravity capillary range can be made. Concerning the mechanical wave it should be noted that: the wave form was not perfectly sinusoidal (easily to be seen from harmonics in the frequency spectra in figure A.6); the amplitude was within $\pm 4\,\mathrm{cm}$; the wavelength ($\lambda = 1.5\,\mathrm{m}$) is not within the wavenumber range of the instrument.

The saturation spectrum for the mechanical wave and a wind speed of 4 m/s is shown in figure 7.13 on the left. The result with additional rain is displayed on the right in the same figure.

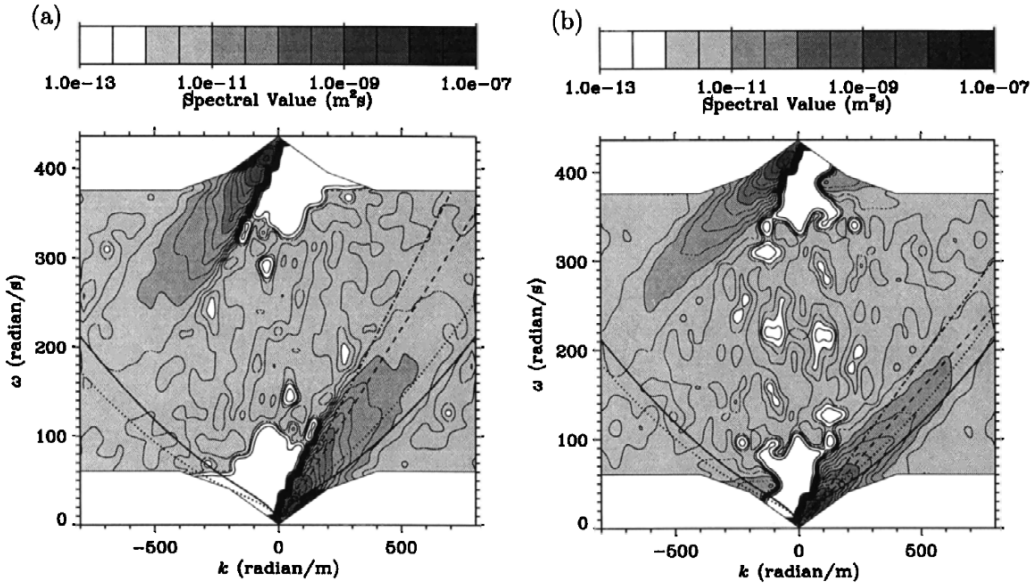

Figure 7.15.: Examples of the frequency wavenumber spectra, measured by Hara et al. [59]. (a) along wind direction 0^o. (b) oblique direction 45^o.

The superposition of the mechanical wave results in an overall decrease of the degree of saturation in the short-gravity capillary wave range, which is in qualitative agreement with measurements of frequency spectra under similar experimental conditions by Makin et al. [115]. From the omnidirectional spectra in figure 7.14 we can see that the maximum in the capillary range is significantly shifted towards smaller wavenumbers. For the pure wind condition the maximum degree of saturation in the capillary regime was around 1500 rad/m whereas with the mechanical wave a maximum is observed for 785 rad/m. A definitive attribution of this observation to the above mentioned influences due to the long waves is behind the scope of this analysis.

Comparing the omnidirectional spectra obtained with and without mechanical wave in combination with rain (figure 7.14) we see that the spectral shape is almost the same. The degree of saturation without the mechanical wave is a factor of 1.6 lower, which is possibly due to variations in the rain rate over the course of the experimental campaign.

For the condition without rain we observe a change of the degree of saturation in the short-gravity capillary wave range, whereas the influence of rain appears to be dominant over the influence of the swell.

7.3. Dispersion of Wind Driven Short-Gravity Capillary Waves

The dispersion relation $\omega(\mathbf{k})$ of water waves is a key property for the interpretation of many kinds of measurements of the wave field. For instance, it is necessary for a conversion of frequency spectra (e.g. measured using point probes such as wire gauges or laser slope gauges) into wavenumber spectra[30]. Also for the modeling of the energy fluxes between different wavenumbers requires the knowledge of the dispersion relation because most approaches are based on conservative equations for the action spectrum[9]. In many cases it is simply assumed that the short waves satisfy the theoretical dispersion relation.

Measurements using laser interferometry on monochromatic small amplitude standing capillary waves in a small basin showed that the linear dispersion relation, that was introduced in section 2.2.1, is in excellent agreement with the experimental data [13].

[9]The action spectrum is defined as $N(\mathbf{k}) \equiv \frac{g}{\omega}\Psi(\mathbf{k})$, see Phillips [130] for details.

However, in the case of a wind driven wave field the simple usage of the theoretical dispersion relation is not always appropriate since the short wind waves are subject to strong Doppler shifts due to near-surface drift currents and the modulation by longer gravity waves [60]. Moreover, the surface tension, that mainly determines the phase velocity of the capillary waves, can not be treated as an a priori constant. This is because in any natural environment, as well as in tank experiments, the water is hardly ever free of contamination from surface active material. It has been shown that the surface contamination strongly influences the exchange between ocean and atmosphere [48]. If we aim at a physical relationship that links the exchange processes to the wave field, we cannot ignore changes of the surface tension.

Comprehensive data for the dispersion of gravity waves is available since the 1970's. Gotwols and Irani [56, 1980] published frequency wavenumber spectra for wavenumbers smaller than 3 rad/m and frequencies up to 19 rad/m, acquired with a video based technique. Another method makes use of microwave Doppler spectrometry, e.g. Plant and Wright [138] and Wright and Keller [171]. Nowadays conventional marine radar instruments can be used to compute the surface drift currents from the Doppler shift of the spectra [149, 150, 174]. However, the spatial resolution of these techniques does not allow for a precise measurement of the dispersion for wavelengths in the cm to mm range.

In order to measure the dispersion relation of small scale wind driven waves one needs an instrument that provides the combined spatio-temporal information at high resolution. This is an exigent experimental challenge and therefore the amount of available data is very poor. Basically, there exist three main approaches. One is based on a cross-correlation method, which delivers the mean phase shift as a function of the wavenumber between two consecutive measurements of the surface topography [80, 164, 179]. The phase shift of one single wave component is simply the product of the frequency and the time interval between the two measurements. This method suffers from one severe problem: computing the mean phase shift leads to a mutual cancellation of the symmetric parts of the wavenumber spectrum. A second approach is based on scale decompositions of the wave field in combination with image velocimetry algorithms [26, 46, 141, 179]. For the decomposition the images are processed by filters that are similar to bandpass filters, which does not ensure that the spectral energy that is corresponding to a specific physical wave component is really completely contained in the corresponding wavenumber band. Another complication is the spatial averaging of the resulting velocity vectors with respect to the directions of the wavenumber vectors on the different scales[10]. However, using this technique Zhang et al. [182] concluded: *"Solid evidence is found that short wind waves in the wave facilities are predominately dispersive rather than bounded to the dominant wave components. The capillaries are closely resonant with the longer wave components. They can extract energy directly from the long waves and may be important dissipation sources of longer wave components especially at low wind speeds."*

Until now, direct measurements of the frequency wavenumber spectrum could only be acquired with the scanning laser slope gauge technique [17]. Hara et al. [59, 1997] published the most comprehensive data for the short-gravity capillary regime measured in a wind wave tank. Examples are shown in figure 7.15. Their effective range of wavenumber was between 20 and 800 rad/m and the Nyquist frequency was 218 rad/s. The results revealed that for their experiments a significant portion of the short wind wave energy was contained in wave modes that propagate with the dominant waves rather than at their phase speed predicted by the dispersion relation. These wave modes were called *generalized bound waves* which spanned a much wider range of wavenumbers than those typically associated with parasitic capillary waves [59]. Until now the scanning laser slope gauges is state of the art for the measurement of frequency wavenumber spectra [18, 161, 163]. Moreover, this technique has already been successfully deployed in the open ocean [15]

[10]For this a physical decomposition of the superimposed motion is desired [Personal communication with Martin Schmidt, HCI, Uni Heidelberg].

In the following sections we show the first measurement of the frequency wavenumber spectrum obtained by an imaging slope gauge. Before we give a qualitative interpretation of the spectral energy distribution we have to discuss how the dispersion relation is expected to deviate from the linear theory in the case of wind driven water waves. Then the qualitative interpretation already allows to discuss the physical aspects and the features that are due to artifacts, separately. As a second step we show a first approach to treat the data for an quantitative analysis, which yields estimates of the surface drift velocity, the modulation of short waves by long waves, and the surface tension.

7.3.1. Modifications to the Linear Dispersion Relation

As mentioned before, the dispersion relation of freely propagating short-gravity capillary waves is well described by the linear theory which gives

$$\omega_T(k,\sigma) = \sqrt{kg\left(1+\frac{\sigma}{\rho g}k^2\right)\tanh kH}, \tag{7.5}$$

where g, ρ, and H are treated as constants, see section 2.2.1. The surface tension σ is treated as a variable, which is explained below. In our situation we have to account for several aspects that can alter the $\omega(k)$ relationship.

First of all we have to include the Doppler shift ω_d that results from the mean shear flow at the water surface

$$\omega_d(\mathbf{k},\mathbf{U}) = \mathbf{k}\cdot\mathbf{U}(k) = k\,U(k)\,\cos(\Phi), \tag{7.6}$$

where $\mathbf{U}(k)$ is the velocity vector of the mean shear flow. The explicit wavenumber dependence is depicted here to indicate that the flow velocity (as *seen* by the wave) is given by an weighted average over the penetration depth of the wave (see Young et al. [174] for details). The cosine dependency of the Doppler shift leads to an increase of the phase velocity for waves that are traveling in direction of the flow ($\Phi = 0$) and to a decrease for waves traveling in the opposite direction. For measurements in the centerline of a linear wind wave tank the direction of the mean surface current is assumed to coincide with the direction of the wind.

Secondly, the small scale waves are modulated by the orbital motion of longer waves. To a first order approximation we may assume that the relative phases of the long and the short waves are randomly distributed and that the long waves are sinusoidal. Under this assumption the long wave modulation only leads to a broadening of the dispersion shell but leaves the mean value $\langle\omega(k)\rangle$ unchanged. However, dominant waves are usually having a Stokes wave profile, so that the orbital velocity is higher at the crests and lower at the trough, compared to the linear theory [59]. In addition, in many cases a significant portion of the small scale waves is made up of parasitic capillary waves which are coupled to the forward front of the dominant wave crest. This asymmetry can cause an upward Doppler shift ω_w in addition to the Doppler shift due to the surface drift. Due to the directionality of the short gravity waves (see page 93) no equivalent to the relationship (7.6) can be given for ω_w.

Thirdly, the value of the surface tension varies, especially if artificial surface slicks are applied. The monolayer surface slicks PME and OLA that have been used in this study can reduce the surface tension down to about 10% of the value for pure water [105]. As a matter of fact, even for the conditions without surface slicks the surface tension is expected to vary because of residual contaminations of any surface active material that can hardly be avoided. Moreover, the surface tension is a function of the temperature, which might have a significant local effect if cold rain is impinging on a warm surface. Any reduction of the surface tension leads to a decrease in $\omega_T(k,\sigma)$. In this case the effect is not depending on the waves direction.

For the discussion of the wavenumber-frequency spectra the different influences are taken into account, formally summarized as

$$\langle \omega(\mathbf{k}) \rangle = \langle \omega_T(k,\sigma) + \omega_d(\mathbf{k},\mathbf{U}) + \omega_w(\mathbf{k}) \rangle \,. \tag{7.7}$$

7.3.2. Interpretation of the 3D Spectral Energy Density

In this section we will discuss the structure of the 3D spectral energy density for one example that is shown in figure 7.16. The experimental condition (wind speed 8 m/s, rain rate 57 mm/h, surface slick type 2 (OLA)) is chosen such that all contributions to the effective dispersion relation can be discussed. For convenience we use the term *dispersion shell* for the center of mass of the measured spectral distribution. In other words: the dispersion shell is the expectation value of ω using the 3D power spectral density $S(\mathbf{k},\omega)$ in terms of a probability density function

$$\langle \omega(\mathbf{k}) \rangle = \frac{\int \omega S(\mathbf{k},\omega) d\omega}{\int S(\mathbf{k},\omega) d\omega}, \tag{7.8}$$

which is of course only valid as long as the relation between k and ω is unambiguous. On basis of the measurements we approximate (7.8) by

$$\omega_{u,v} = \frac{\sum_{w=0}^{w=O/2} \omega_w \, S_{u,v,w}}{\sum_{w=0}^{O/2} S_{u,v,w}}, \tag{7.9}$$

where O is the number of frames that were used for the computation of the spectrum. In addition to the matter of ambiguity, for unbiased estimate $\omega_{u,v}$ we would require that $S(\mathbf{k},\omega)$ vanishes for $w \to O/2$ and $w \to 0$. Unfortunately this is not true due to the limited frame rate and the limited timespan of the measurement. But still we can detect the occurrence of a bias by checking the requirements. The first step, before computing the dispersion shell, is therefore a visual inspection of the spectral volume.

What is displayed: In figure 7.16 several slices through the 3D spectrum are shown. These slices display the specral energy density in false colors with a logarithmic color map. The range of the color map is adapted to the dynamical range of each slice separately, so that the *dispersion shell* is visible in each slice. Therefore the colors from different slices are not directly comparable to each other. Each slice corresponds to a specific polar angle Φ in the wavenumber domain, where $\Phi = 0$ is aligned to the direction of the wind. The wavenumber and frequency axis are the same for all plots. The diagram in the middle shows the scaling of the axis and the dispersion relation from the linear theory for pure water, which is also included in each slice for reference. Even according to the linear theory the frequency is beyond the Nyquist frequency ω_N[11] for $k > 2300\,\text{rad/m}$. The corresponding spectral energy re-enters the spectrum under a point reflection at the origin of the 2D wavenumber plain (or accordingly at polar angles in the range between 90^o and 270^o) and at frequencies that obey $\omega' = 2\omega_N - \omega$. The expected location of the aliased spectral energy is indicated as a dash-dot line. The aliasing is explained in more detail in section 2.5.1.

What can be observed: Please regard the different slices in figure 7.16.

- Because in this example a rain condition was selected we can see significant features in the spectral energy for all directions of wave propagation Φ.

[11] $\omega_N = 981.7\,\text{rad/s}$

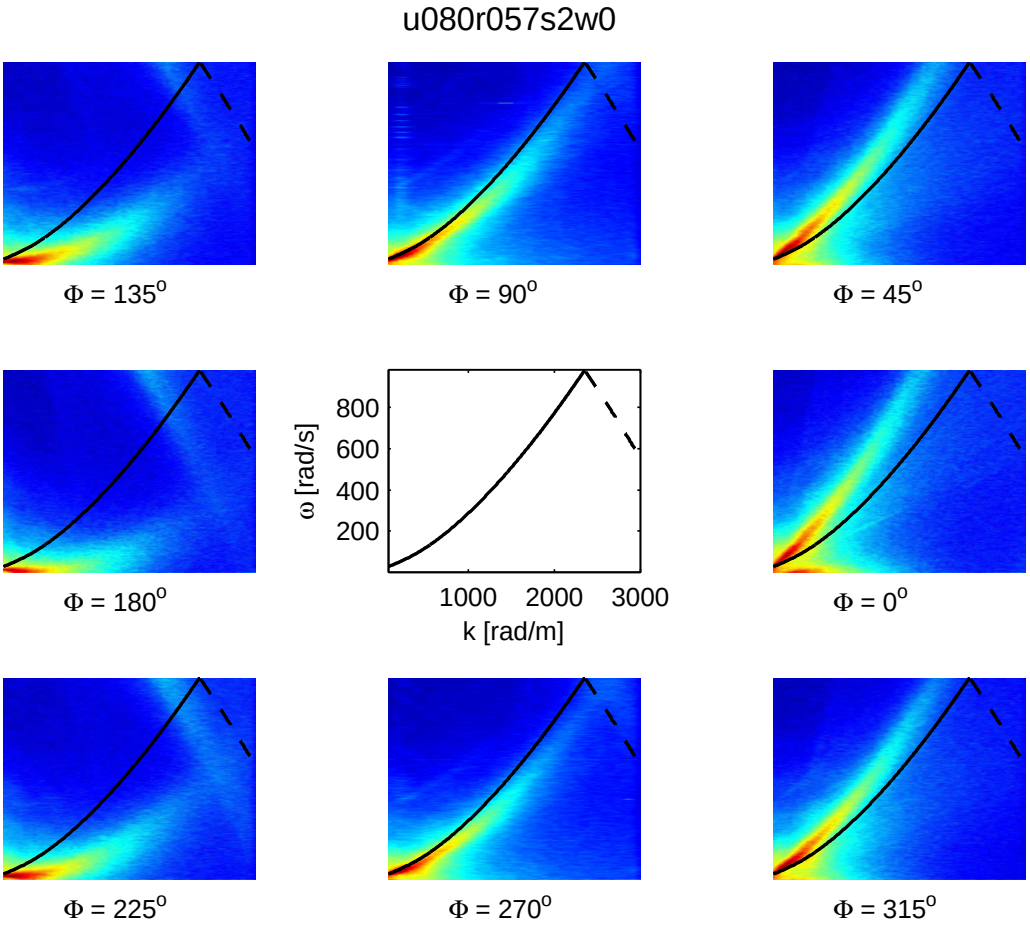

Figure 7.16.: ω-k slices through the 3D power spectrum with different directions relative to the wind, as indicated. Explanation, see text.

- Looking at the cross wind directions 90^o and 180^o we observe that the dispersion shell is very close to the linear theory. In the capillary range we can see that $\langle\omega(\mathbf{k})\rangle$ is actually below the reference curve, which is due to the reduction of the surface tension by the monolayer surface slick. The spread of the dispersion shell can be interpreted in terms of modulation due to wave-wave interaction. In these directions, perpendicular to the wind and the surface current, no Doppler shifts can be identified, which is in agreement with our expectation.

- For the along wind direction 0^o the dispersion shell is fiercely shifted toward higher frequencies, which is due to the Doppler shifts stemming from either the shear flow or wave-wave interaction. Note that the Doppler shift and the influence of the surface tension partially annihilate each other. At the very low frequency end we can see that the spectrum is contaminated by spectral leakage from the dominant waves that are not well resolved by the instrument and which can not completely be removed by the windowing function that was used for the Fourier transformation.

- Below the reference curve in the 0^o-slice another tiny feature can be seen that looks like a straight line. A straight line corresponds to a constant phase speed, which is in this case approximately 0.20 m/s and therefore less than the minimum phase speed 0.23 m/s for clean water. According to the linear theory the surface tension needs to be reduced to about 0.04 N/m (compared to $\sigma_{clean} = 0.07197$ N/m for T = 25^{o}C) to yield a minimum phase speed of 0.20 m/s, but only for $k = 491$ rad/m ($\lambda = 1.28$ cm). Waves with such a small wave-

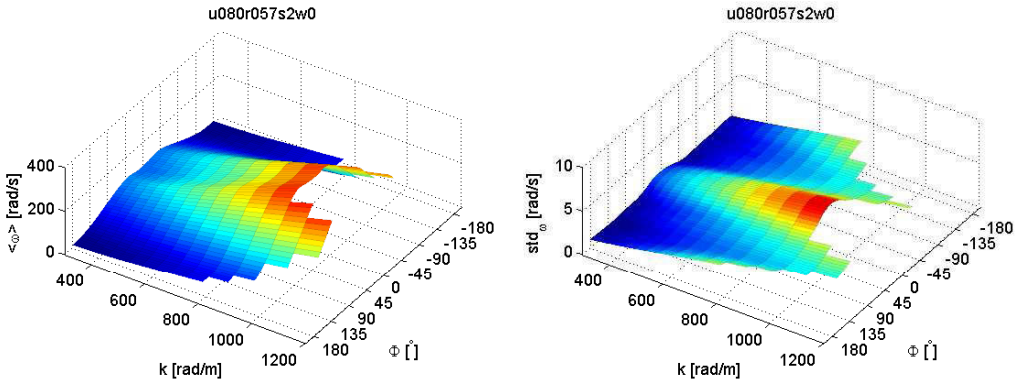

Figure 7.17.: left: Expectation value for ω (equation (7.9)). right: Standard deviation for ω (equation 7.12).

length are not expected to have bound waves. Since the feature extents to about 1500 rad/m it is presumably linked to higher harmonics, e.g. produced by slope discontinuities from the craters of the rain drop impacts. This also means that the above estimate of the surface tension might have no physical meaning.

- In the directions 45^o and 315^o the dispersion shell looks alike in the along wind direction, but obviously the Doppler shift is reduced, corresponding to the $cos(\Phi)$ proportionality in equation (7.6). No severe spectral leakage is observed at the low frequency end. Comparing the two slices at the high frequency end it seems that the spectral energy in the 45^o direction is more pronounced than in the 315^o direction.

- Regarding the slices for wavenumbers in the windward directions 135^o, 180^o, and 225^o we notice some ambiguity in the spectral distribution for wavenumbers greater than 1500 rad/m. The features in the high frequency range are due to the aliasing, which would be expected to coincide with the dashed reference curve if the theoretical dispersion relation for pure water would be tenable. The actual dispersion shell is drastically shifted to lower frequencies because in the upstream direction the surface current Doppler shift contribution is negative and adds to the reduction of ω caused by the surface slick.

- With respect to the wavenumber range, the frequency range, as well as the resolution within the spectral volume we have achieved considerable advances in comparison to existing data. For a direct comparison of the abundance of the spectra, take for instance the quadrant to the bottom right in figure 7.15 (a), which corresponds to the $\Phi = 0^o$ slice in figure 7.16 - despite the differences in the experimental conditions.

7.3.3. Quantitative Evaluation

In the preceding discussion we have gained a qualitative understanding of the structure of the 3D spectral energy density and how it is related to physical aspects that modify the dispersion shell of the wind driven wave field. For the quantitative analysis, based on the expectation value $\langle\omega(\mathbf{k})\rangle$, we need to remove the ambiguities due to the aliasing and spectral leakage that was discussed in the foregoing section. Here, we implement this in a rather crude way. A binary image $M(\mathbf{k})$ is constructed that is used to mask out biased values after we computed the dispersion shell according to equation (7.9). We define the mask M in the following way

$$M(\mathbf{k}) = \begin{cases} 0 & \text{if} \quad S_{974}^{\omega_N}/S_0^{\omega_N} > 0.1\% \\ 0 & \text{if} \quad S_0^{39}/S_0^{\omega_N} > 1\% \\ 1 & \text{else} \end{cases}, \tag{7.10}$$

where S_a^b is an abbreviation for a summation of the spectral energy density over the frequency range $[a, b]$ rad/s.

$$S_a^b \equiv \sum_{w=a}^{b} S_{u,v,w}. \tag{7.11}$$

The first condition in (7.10) discards wavenumbers that are suspected to be biased due to aliasing. Wavenumbers affected by severe spectral leakage are masked out by the second condition.

For the same experimental condition as in figure 7.16 the dispersion shell is displayed on the left in figure 7.17. The expectation value is computed according to (7.9) and multiplied with the mask M. The result is shown as a function of the polar coordinates, which makes it easy to see the differences due to the angular dependency of the Doppler shift. In general, this representation shows the Doppler shift by the surface drift as a cosine shaped envelope. For this special case we observe that the Doppler shift in the direction $\Phi = 0$ is less pronounced than for $\Phi = \pm 45^o$. This anomaly is presumably due to the asymmetry in the width of the dispersion shell in the windward direction for small wavenumbers, compare figure 7.16. Another reason could be the Doppler shift contribution from the wave-wave interaction, if this contribution is stronger for the $\pm 45^o$ directions. The width of the dispersion shell is displayed in terms of the standard deviation std_ω in figure 7.17 to the right, which in correspondence to (7.9) is computed according to

$$\mathrm{std}_{u,v} = \sqrt{\frac{S_o^{\omega_N}}{\left(S_o^{\omega_N}\right)^2 - S_o^{\omega_N}} \sum_{w=0}^{\omega_N} S_{u,v,w} \left(\omega_{u,v,w} - \langle \omega_{u,v} \rangle\right)^2}. \tag{7.12}$$

The standard deviation of ω is expected to be related to all kinds of modulations, stemming from nonlinear wave-wave interaction as well as from the modulation due to the orbital motions on different scales. However, as a matter of fact, std_ω is also influenced by noise and artifacts, which makes a strict assignment precarious. Note that the distribution of the spectral energy for a given wavenumber is not always shaped like a Gauss function. Especially for low wavenumbers the distribution is asymmetric and the expectation value for omega is shifted to lower frequencies, compared to the peak of the distribution for a given wavenumber and direction.

Model Fit: Based on the modified dispersion relation (7.7) we can perform a fit to the dispersion shell according to the model function

$$\langle \omega(k, \Phi) \rangle = a(k) + k \cdot b(k) \cos(\Phi - c(k)), \tag{7.13}$$

where the parameter a can be identified with the linear dispersion relation $\omega_T(k, \sigma)$, the parameter b gives the amplitudes of the cosine modulation due to the Doppler shift, and c accounts for little deviations of the direction of the surface current from the wind direction. The wavenumber dependency is depicted here, because we perform this fit for each wavenumber separately. The fit is illustrated for one selected wavenumber in figure 7.18.

It is not possible to distinguish the Doppler shift contributions from gravity waves and from the shear flow. Therefore b and c only account for the mean Doppler shift, assuming that the directionality of both contributions is the same. However, we can already infer from figure 7.17 that this assumption is only a first order approximation.

The model fit for the dataset u080r057s2w0 yields the parameters a, b, and c as a function of wavenumber which are displayed in figure 7.19. The fit result, based on this set of parameters, is shown in figure 7.20 along with a plot of the relative deviation between data and fit. In this case the model represents the data only within -10 to $+30$ %, which is not surprising with respect to the anomaly of the dispersion shell that we have already discussed above. Therefore the fit parameter b gives only an estimate of the order of magnitude of the Doppler velocity, which is

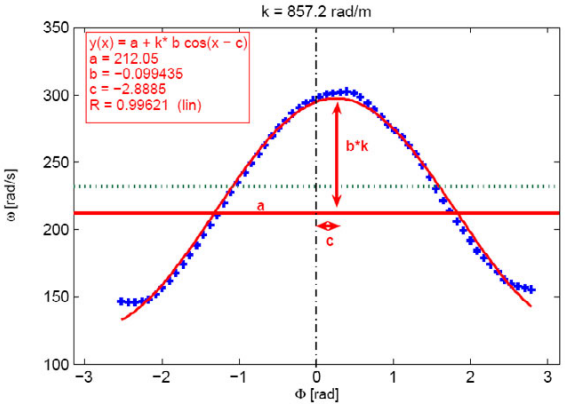

Figure 7.18.: Illustration of the model fit according to (7.13) for a selected wavenumber as indicated. (+ symbol : data u080r057s0w0; dotted line: $\omega(k)$ from linear theory for pure water.)

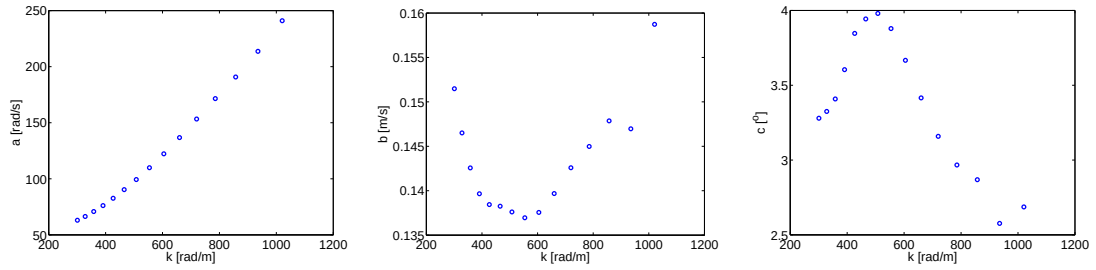

Figure 7.19.: Fit parameter, data: u080r057s2w0

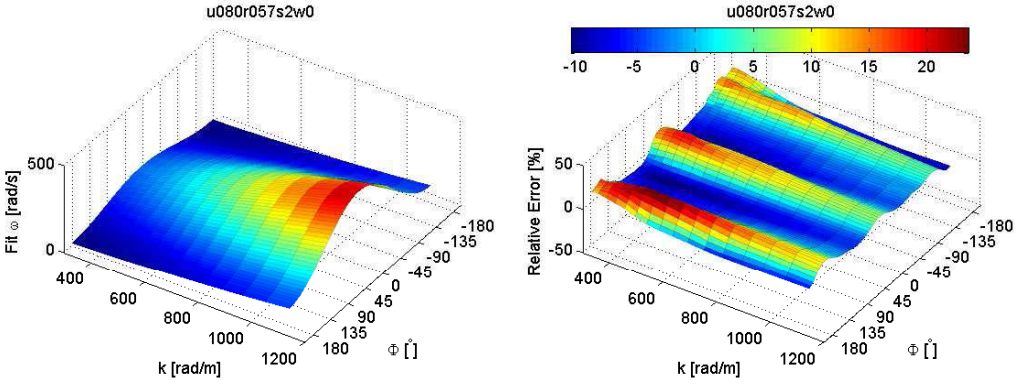

Figure 7.20.: Left: Fit by the model function 7.13 with parameters as shown in figure 7.19. Right: Deviation of the fit result from the measured expectation value.

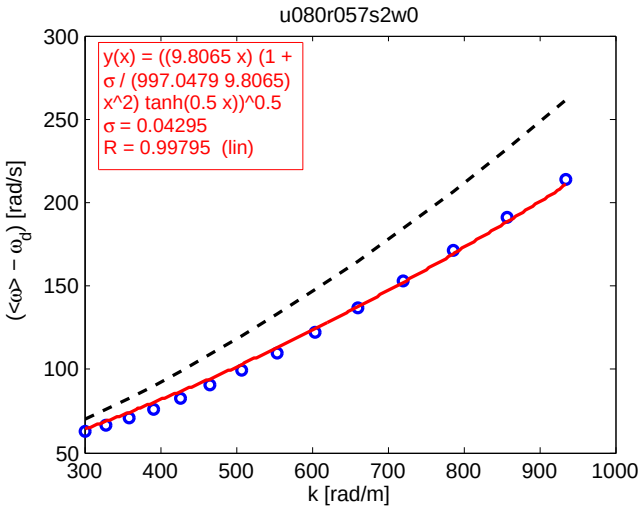

Figure 7.21.: Fit for the surface tension on parameter a in figure 7.19.

around 14.5 cm/s. For wavenumbers between 600 and 900 rad/m the Doppler velocity rises linearly, which might be directly linked to the velocity gradient in the surface shear flow. This is an interesting aspect that should be adressed by future investigations where also direct measuerements of the shear flow should be incorporated. The mean direction in the Doppler term, given by the parameter c, varies slightly around 3^o in correspondance to the assumption that wind direction and mean Doppler velocity are in alignement. The frequency a can be intepreted as the theoretical dispersion minus the Doppler shift. Therefore it can be used for an attempt to yield the surface tension by fitting the theoretical curve with σ as a free parameter. This is shown in figure 7.21, where also the pure water relationship is shown as a dashed line for reference. In this case we get $\sigma = 0.043$ N/m, with an coefficient of determination of $R^2 = 0.996$. Note that a monolayer surface slick was applied in combination of rain.

7.3.4. Summary & Future Perspectives

The condition that was selected for this case study allowed to demonstrate a first approach to evaluate the physical aspects that alter the dispersion relation. It was shown, that we can - at least in principle - extract valuable information about the shear flow, the wave-wave interaction, and the influences of surface slicks from the new spatio-temporal measurements. However, the temporal resolution is still not high enough, which leads to severe difficulties that arise from the aliasing. Masking out the biased values of the dispersion shell works well as a first approach, but it conversely discards to much valuable information. Moreover, the case study showed that we need to improve the model approach in order to distinguish the Doppler shift contribution of the shear flow from the contribution due to wave-wave interaction. For this a model for the wave-wave interaction that directly incorporates the measured angular spreading at different scales (section 7.2.1) might presumably be helpful. The interaction between short surface waves and surface shear is modeled in some detail by Zhang [180].

A systematic analysis of the complete data set from the WiSSCy campaign is beyond the scope of this study. It should be noted, that in some cases the model fit performs significantly better than for the show case, whereas in some other cases the approach fails. The frequency wavenumber slices for all 26 conditions are included in the appendix A.4 for the sake of completeness. This comprehensive overview should give an impression about the variety of features in the 3D spectra and in turn it should serve as a guidance for future investigations.

It would be desirable to combine the slope imaging with direct measurements of the shear flow

as well as of the surface tension in order to validate the results. One approach that could be applicable even for the recent data set could be the shear flow estimation from active thermography, which was introduced by Garbe et al. [54]. It would be a milestone for the experimental investigations of air-sea interaction if the velocity gradient in the shear flow can be correctly inferred from the measurement of the dispersion relation, because with conventional techniques the measurement of the flow velocities near the wavy surface is very challenging [29].

Another promising application of the new technique can be seen in the context of the Wind Over Waves Coupling Model, which was introduced in section 2.4.1. In the recent publication by Caulliez et al. [30, (2008)] they write: "*..., in this range wave kinematics strongly depends on direction of wave propagation, as well as upon drift current and longer wave modulations. Therefore to model the wave dispersion for the different wind and fetch conditions to derive the wavenumber spectrum in the small scale wave equilibrium region from the observed frequency spectrum, still looks out of reach....*". The bottom line is that the linear dispersion relation is used for the model. Therefore the incorporation of direct measurements of the dispersion relation can be expected to lead to a considerable improvement concerning the description of the interaction between wind and waves.

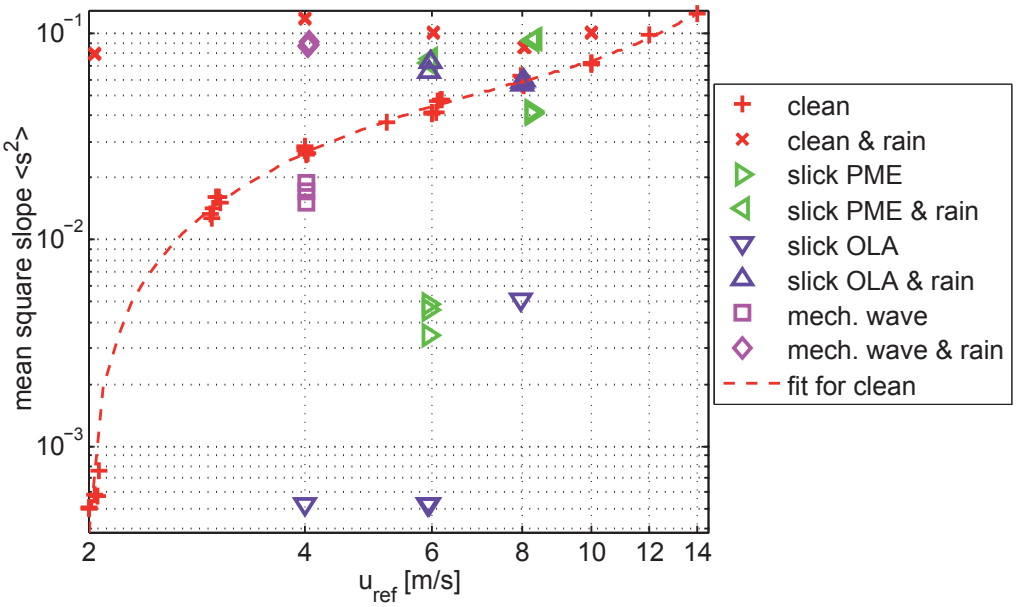

Figure 7.22.: Surface roughness $\langle s^2 \rangle$ as a function of the reference wind speed for different conditions of the WiSSCy 2007 campaign.

7.4. Roughness of the Water Surface

The mean square slope $\langle s^2 \rangle$, also referred to as mss, is a measure for the roughness of the water surface. It was shown that mss is a better parameter for the description of air-water transfer rates than the conventional wind speed parameterizations [48, 82]. This is the case because the transfer of heat or gas is mainly controlled by the water sided diffusive boundary layer, which is in turn influenced by the amount of turbulence that is induced by instabilities of the surface waves. Even though wind is the main mechanism for the generation of waves it is not the only criterion which defines the state sea surface. Most prominent is the influence of even very little contaminations with surface active material[12], referred to as surface slicks, which effectively inhibit the generation of capillary waves. Therefore the actual sea state and consequently air-sea exchange can be very different although the wind speed is the same.

Another reason for the interest in mss is its accessibility by means of remote sensing from satellites. This is important in the context of global climate modeling. Frew et al. [49] introduces a new approach to estimation of global air-sea gas transfer velocity fields using dual-frequency altimeter backscatter[13]. This represents a potential alternative to commonly used parameterizations based on wind speed (e.g. [110, 168, 169]).

From remote sensing it is only possible to retrieve information that is averaged over the mesoscale[14]. But the processes involved in air-sea interaction act on the centimeter to millimeter scales - as can be seen in section 7.5.3 - so that from remote sensing alone it is not possible to really understand what is happening on the surface.

In section 7.4.1 we show the diversification of the mss-u_{ref} relationship in cases of rainfall and slick contamination. Since the mss parameterization of transfer rates seems to overestimate the transfer velocity in cases of rain [65], we provide a first approach to separate the mss contribution by rain from the mss contribution by the wind driven waves in section 7.4.2.

[12] e.g. from algae blooms or pollution.
[13] ... which in this case is related to the mean square slope in the wavenumber band 40-100 rad/m.
[14] mesoscale: medium spatial scale 5-100 km.

7.4.1. Influence of Surface Slicks and Rain

Figure 7.22 shows a plot of mss versus the reference wind speed in order to given an impression of how the surface roughness is changed by intense rainfall or monomolecular surface slicks. A polynomial fit to the data for the clean surface condition (symbol +) is included as a red dashed line. This fit has no strict physical meaning and is shown to easily compare the other experimental conditions to the clean surface case.

For instance we can see that the rain[15] (symbol $\times$) constitutes as much surface roughness as typically observed for high wind speeds in the range of 10-12 m/s. The fact that the scatter for the rain condition is higher than for all other conditions might be explained by variations in the rain rate over the course of the campaign.

In contrast to rain, surface slicks lead to an immense reduction of mss for low wind speeds and small fetches[16]. In our laboratory measurements at 17 m fetch the monolayer slicks OLA and PME (see appendix A.6 for details) prevented any waves for wind speeds smaller than 8 m/s. Above that wind speed that the slicks occasionally broke up and waves developed. In the field the situation might be more complicated, since the fetch is typically longer and one can frequently observe smooth patches next to rough patches of the water surface. This is one one of the reasons why the uncertainties of transfer estimates based on any integral measurement of wind speed or surface roughness over the mesoscale are typically in the order of 20-30% [49, 127].

In section 6.6 we have introduced several ways to compute the mean square slope from the images of the water surface slope. The data points shown in figure 7.22 are stemming from ensemble averages over 5000 statistically independent images, see section 6.6. Only stationary conditions have been selected for this plot, so that we omitted the errorbars. For a more detailed description please refer to Rocholz [143]. A detailed analysis of the gas and heat transfer rates of the WiSSCy-campaign with respect to a mean square slope parameterization is still pending, while preliminary results are available from Richter [140] and Anweiler [7][6][5]

7.4.2. Contribution of Windward Propagating Waves

Ho et al. [65] showed that the transfer rate k_{600} in a rain-driven system is no longer in distinct correlation with $\langle s^2 \rangle$. While for a particular drop size the data was well correlated, different drop sizes produced separate linear relationships. They conclude that the ring waves from the rain are not directly coupled to the near surface turbulence that is controlling the gas exchange and therefore direct measurements of the enhanced turbulence are needed.

However, with the new measurement technique we are able to distinguish between waves that propagate leeward[17] and waves that propagate windward[18]. Generally speaking, the wind driven waves travel with the air flow so that they only contribute to the leeward part of the energy spectrum. In contrast, the ring waves from rain drops contribute equally to the leeward and windward spectral energy. Therefore we might be able to separate the mean square slope contribution from the ring waves and the wind driven waves by a comparison of the leeward and windward parts of the spectra according to equation (6.5) in section 6.6. This information could be useful for future applications of transfer models that incorporate the intermittent nature of the air-see exchange, such as the *composite model* [78] which is described in detail by Degreif [37, chapter 2.6].

The roughness contribution from waves that are propagating against the wind (i.e. windward) can be assessed from figure 7.23, where the contribution $mss_{windward}$ and $mss_{leeward}$ are displayed in red and blue symbols as a function of the total mss. We can see that the leeward con-

[15] rainrate 57 mm/h, drop diameter 2.9 mm
[16] fetch: distance over which wind acts on the water surface.
[17] leeward: having the wind in the back.
[18] windward: having the wind in the face.

tribution to the total mean square slope is always greater than the windward contribution, which is again due to the fact that wind driven water waves hardly travel against the mean wind direction.

Moreover, we can see that the leeward contribution is about 80% to 90% for moderate wind-speeds (3 m/s $< u_{ref} <$ 8 m/s, $0.02 < mss < 0.06$) and no-rain conditions. For the same condition but higher wind speeds the leeward contribution drops to about 80%. This can be explained by two reasons a) there is the undesirable effect of aliasing (see sections 2.5.1, 7.3, and 7.2.1) and b) there are some *real* structures propagating against the wind. What could these *real* windward traveling structures be? When a dominant wave breaks, it leaves behind irregular and undirected surface structures which can be attributed to the turbulent wake that is found behind the breaking crest in the water body. This is demonstrated in section 7.5.3. Since these structures are undirected, about half of their contribution to the surface roughness is found in the windward partition. Following this idea the enhancement of the windward contribution could be interpreted as an indicator for enhanced turbulence production by the waves. Another reason for windward traveling structures under no-rain conditions could be the occurrence of strong modulation of capillary waves by the orbital motion due to longer gravity waves.

The situation in presence of surface slicks and without rain is similar to the situation for moderate wind speeds and the clean surface condition. For the slick conditions we can distinguish whether or not the wind forcing is strong enough to break up the slick to generate wind waves. If wind waves are present, then the leeward contribution is 90%. In absence of waves we find a greater scatter which is explained by the poor signal to noise ratio.

Drastic changes in the partition are expected under the influence of raindrops. This is because the resulting ring-wave patterns are intrinsically isotropic. From the measurements under rain and slick conditions, when the wind is not strong enough to produce significant wind waves, we find that the windward contribution rises to about 45%. The fact that the leeward contribution is still 55% and therefore higher than the windward contribution can be explained by two reasons. Firstly the wind can drive the small scale waves once they exist, and secondly because the downwind part of the imaging section was not as much exposed to the rain as the upwind part. This was due to technical reasons (see section 4.1) and leads to some asymmetry: the leeward traveling ring waves can be followed longer within the images because they are not that much disturbed by neighbouring raindrop impacts (e.g. see figure 7.30). Moreover, the windward traveling ring waves disappear from the imaging section in a shorter time. For the measurements with the PME slick at $u_{ref} = 8$ m/s the windward partition was only about 35%, because the wavefield was comparable to the clean surface and rain conditions.

For the clean surface condition with rain we can observe that the windward contribution to the mss is in the range of 30% to 45%. From this we can estimate the portion due to wind driven waves to be in the range of 40% to 10% - according to $mss - 2 \cdot mms_{windward}$ - if we assume that the windward contribution is completely determined by the isotropic ring waves. This kind of estimate could be incorporated in some *composite model* in order to improve the mean square slope parameterization of transfer rates as explained at the outset.

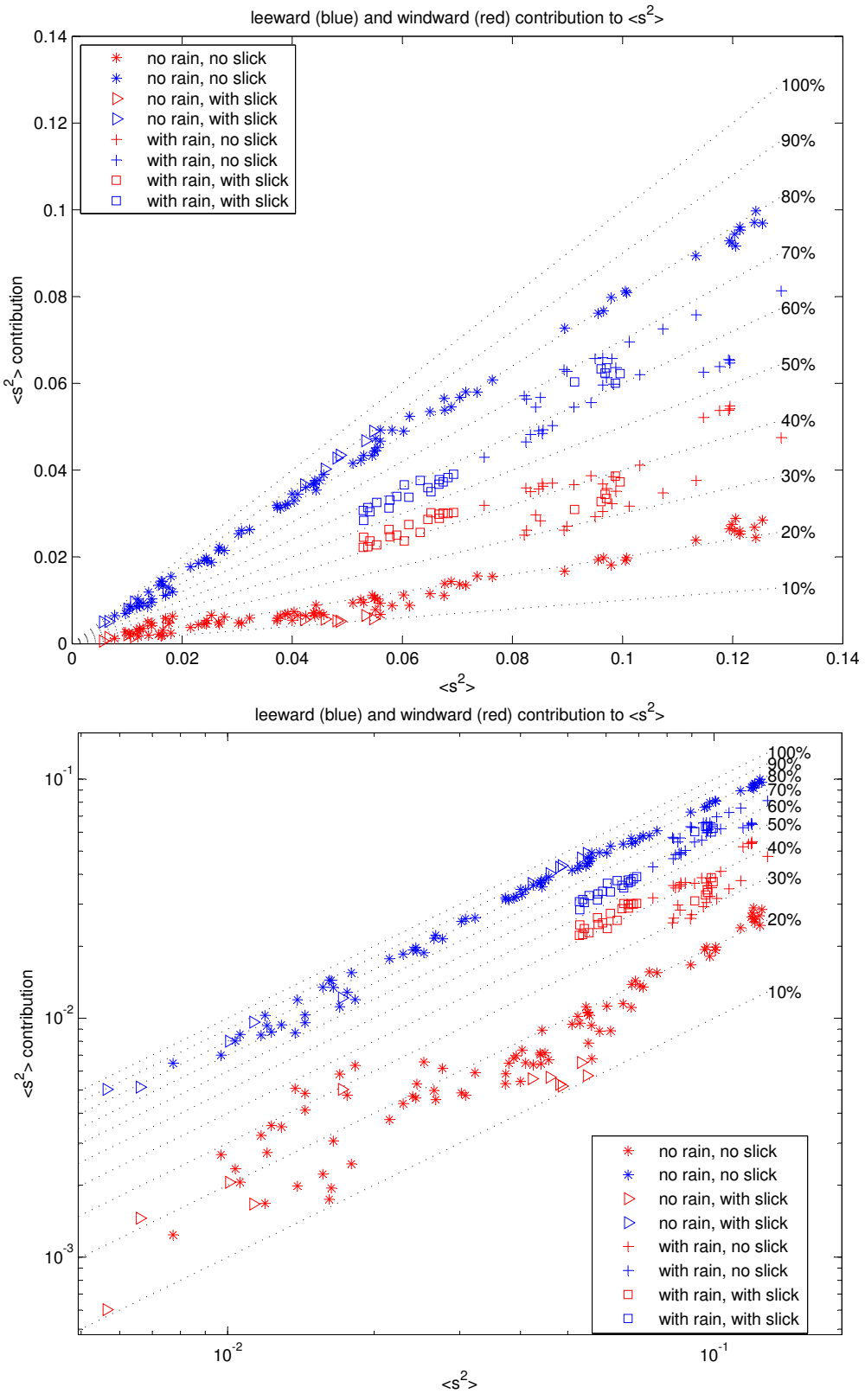

Figure 7.23.: Contribution to the mean square slope from windward traveling waves (red) and leeward traveling waves (blue). Both plots display the same data just in different representations.

7.5. Wave Visualization

The co-located and synchronized 2D measurements of the surface slope and active thermography provide insights into the influence by the passing waves on the near surface turbulence.

Over the course of the WiSSCy campaign we have acquired 150 synchronized image sequences, encompassing the variety of experimental conditions, see section 5. Each sequence comprises 5000 frames, acquired with a frame rate of 312.5 Hz, i.e. a time span of 16 s.

Concerning this huge amount of data a visualization is desired that allows for a direct comparison of the features in the images. In many cases, a visual inspection of image sequences is performed using color overlays or side by side displays. Displaying the images in different colors on top of each other can be misleading for the human perception. A side by side display of corresponding images makes a direct comparison difficult, especially when the image content is changing as for a movie display of an image sequence. Therefore, a visualization tool was developed by Jung [89] which maps the thermal images onto a 3D graphical model of the surface elevation. This tool is based on OpenGL and receives three image sequences

- the reconstructed water surface height $h(\mathbf{x}, t)$ (in units of pixel/mm)
- and both slope components $s_x(\mathbf{x}, t)$ and $s_x(\mathbf{x}, t)$

as primary input[19]. The primary input is used for a 3D rendering of the water surface with interactive control for the projection. The surface slopes are incorporated for the shading model, in order to make even the small scale waves visible. As secondary input

- the registered thermographic images

can be provided[20]. This additional data is mapped onto the virtual water surface using false color that is defined by a programmable color map.

7.5.1. Height Reconstruction from the Gradient Field

In section 2.5.4 the method of Frankot and Chellappa [47] for the height reconstruction was introduced. The discrete version of equation (2.93) can be written as

$$\hat{h}_{u,v} = \begin{cases} \left(\mathrm{i}\, 2\pi k_{u,v}^2\right)^{-1} \left(k_{x_{u,v}} \hat{s_x}_{u,v} + k_{y_{u,v}} \hat{s_y}_{u,v}\right) & \text{for} \quad [u,v] \neq [0,0] \\ 0 & \text{for} \quad [u,v] = [0,0] \end{cases}, \tag{7.14}$$

where the wavenumber grids are defined by

$$\begin{aligned} k_{x_{u,v}} &= k_{u,0} \qquad \forall \quad v \\ k_{y_{u,v}} &= k_{0,v} \qquad \forall \quad u \\ k_{u,v}^2 &= (k_{x_{u,v}})^2 + (k_{y_{u,v}})^2. \end{aligned} \tag{7.15}$$

The surface elevation $h_{m,n}$ follows from the inverse DFT. Not only the information about the mean surface height is lost by setting $\hat{h}_{0,0} \equiv 0$ to handle the devision by zero. Also the mean surface gradient is lost at the same instance, because the spectral components $\hat{s_x}_{0,0}$ and $\hat{s_y}_{0,0}$ are excluded from the reconstruction. However, it is easy to add the plane that corresponds to the mean gradient to the result of the Fourier reconstruction

$$h(\mathbf{x}) = \mathrm{FT}^{-1}\left(\hat{h}(\mathbf{k})\right) + \langle s_x(\mathbf{x})\rangle\, x(\mathbf{x}) + \langle s_y(\mathbf{x})\rangle\, y(\mathbf{x}), \tag{7.16}$$

[19] Required format for the input: 32 bit float

[20] Note, the secondary input is not restricted to thermographic images. Any sequence which corresponds to the primary input can be used.

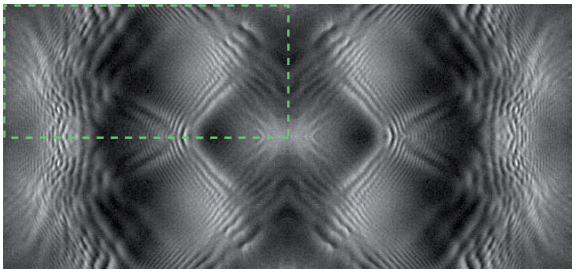

Figure 7.24.: Example for the periodic reproduction of the slope image by mirroring. The original image is highlighted by the surrounding dash-dot rectangle. The gray values are now continuous at the image boarders. However, the directions of the gradient vectors are still dis-continuous at the axis of reflection.

where we choose the coordinate system such that the origin is at the center of the field of view. This automatically yields

$$\langle \langle s_x \rangle \, x + \langle s_y \rangle \, y \rangle = 0, \tag{7.17}$$

so that also the mean of the elevation function h is always zero.

The accuracy of the height reconstruction has been investigated using artificial data, since for the water surface itself no ground truth is available. The reconstruction performs reasonably well, even if we add an realistic amount of white noise. The pixel wise absolute errors are within three times the standard deviation of the noise, if we discard unavoidable artifacts that arise in the boarder regions of the images, typically within the outer 10 pixels. Note that for the height reconstruction we omit the windowing function, since this would cause even more artificats in the boarder regions when inverting the windowing at the end. The effects of the boundary and noise have also been explored by Zhang [178], coming to similar conclusions. Here, we only have extended the method in consideration of the mean gradient.

Concerning the real data, we can compare the gradient fields before and after the reconstruction, which yields reasonable results, though we cannot really quantify the accuracy from this, since it is partially limited by the applied derivative filters. However, from these test we can state that in our case the Fourier integration is the method of choice, whereas in other situations - especially in cases where the accuracy of the gradient field is not homogeneous in space - one might need to use a regularized reconstruction as proposed by O'Sullivan et al. [128].

Balschbach [9] and Fuß [50] have proposed a periodic reproduction of the slope images before the computation of the spectra, in order to avoid the discontinuities of the gray values at the image boarders. This is achieved by a specific mirroring of the data, which is exemplified in figure 7.24. From this example we can see that the discontinuities in the magnitude of the gradient can be intercepted by this method. However, the polar orientation of the gradient vector now shows systematic discontinuities at the axis of reflection, leading to the same kind of artifacts as without enforcing the periodicity of the gradient magnitudes. Therefore, we omitted this approach from the height reconstruction in this study.

In the examples that will follow (section 7.5.3) we can see that the addition of the mean gradient plane in equation (7.16) leads to much more realistic wave profiles, compared to former reconstructions where the long wave contribution was discarded (e.g. [9]). Of course, the reconstruction can only reproduce the long wave amplitudes to some extend. It is limited by the finite size of the field of view for which the mean gradient is determined. This is reflected by the fact, that the integration constant corresponding to the mean surface elevation within the field of view (which might be a function of time) is still unknown.

7.5.2. Registration of the Thermographic Images:

In section 4.3 we have described the registration procedure of the thermographic images with respect to the slope images.

The registration of the calibrated IR images is performed for all synchronized measurements. For that we obtain image sequences of the surface temperature that are in correspondence to the height sequences and therefore can be used as secondary input for the visualization tool. Ultimately, the surface temperature evolution can be inspected in direct reference to the waves.

7.5.3. Observation of Small Scale Processes

In this section we display several examples of the wave visualization, with emphasis on the dynamical aspects, such as microscale wave breaking and micro Langmuir circulation. All examples have some common features

- the wind is blowing from the right to the left in the images,
- the field of view is $22.3\,\text{cm} \times 10.4\,\text{cm}$,
- the time interval in-between two consecutive frames is 0.0032 s for the actual sequence, but in the figures we will adjust the time increment as indicated by the frame numbers,
- the false colors represent the temperature at the water surface,
- the water surface elevation is displayed in perspective and true to scale, with an offset of 3 cm to indicate the water body, which is 52 cm deep in reality.

Microscale Wave Breaking

Figure 7.25 shows a typical microscale breaking event. The experimental conditions are: clean surface and a wind speed of 6 m/s. The time interval between the displayed images[21] is $0.032\,\text{s}$. The CO_2 laser scans over a small region at the upstream boarder of the images and deposits heat within the top 20 μm of the water surface. The laser was switched on just before the first frame was acquired, so that the water surface is hot in the scanning region, but cool elsewhere. For the whole time, the laser continuously heats the surface in the scan region, which is apparent as the red line at the right edge of each frame. In frame 10 we see that a steep short-gravity wave enters the field of view. As the wave propagates to the left we can observe that heated parcels of the surface water are trapped just behind the crest of the wave. The temperature in this trapped region decreases in time because of the heat exchange with surrounding water and air parcels, as well as because of shearing and turbulent deformation of the parcels itself. Starting with frame 40 we can see that the wave breaks and relieves the warm water as pale streaks in its wake. In the frames 60-80 the microscale wave breaking is visible due to the disordered surface structures behind the crest. Zappa et al. [176] showed that the surface area which is disrupted by micro-breaking is strongly correlated with enhanced air-water transfer. This is also apparent from the visualization of other micro-breaking events, where we can frequently observe that the induced sub-surface turbulence influences the thermal signature for up to about three periods[22] of the dominant waves. This has to be taken into account when comparing the frequency of micro scale breaking events with the surface renewal rate [55]. The intermittent nature of microscale breaking leads to variations of the transfer processes on time scales of a fraction of a second and the horizontal spatial scales of several centimeters. This has severe implications on large scale averaging of transfer velocities

[21] corresponding to 10 frames of the original sequence

[22] e.g. for 8 m/s windspeed the period of the dominant wave in our experiments was about 0.42 s

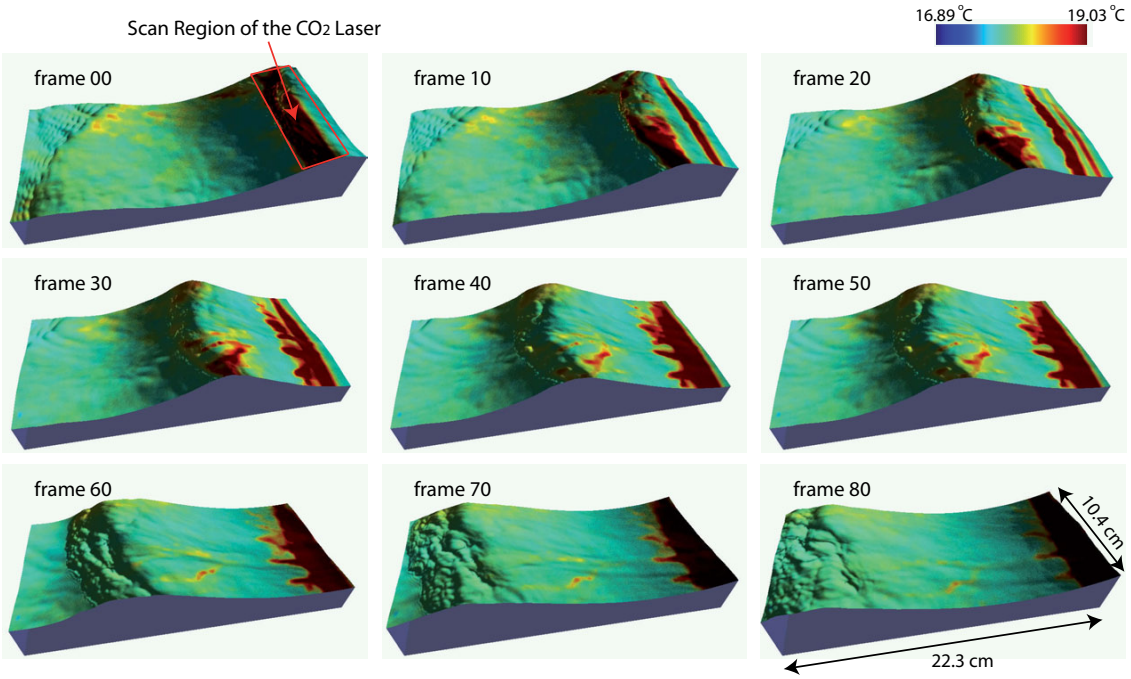

Figure 7.25.: Microscale breaking wave at 6 m/s wind speed.

as pointed out in detail by Jähne et al. [83]. From frame 30 through frame 80 we can see that in the region where the laser heats the surface, some elongated structures develop. These streaks are oriented in direction of the wind, i.e. the mean shear flow. This is an indication to the formation of coherent flow structures which are explained in the following paragraph.

Micro Langmuir Circulation

For the same condition as in the preceding paragraph, just 50 frames (0.16 s) later, we can observe the formation of elongated streaks in figure 7.26. The short gravity wave that is visible in frame 150 is the dominant wave which is subsequent to the micro breaker from frame 80 in figure 7.25. This subsequent wave is apparently not steep enough to break, but we can see that it leads to a significant horizontal transport of the heated water surface parcels. Moreover, the thermal signature exhibits streaks that might be attributed to upwelling and downwelling zones of (micro) Langmuir

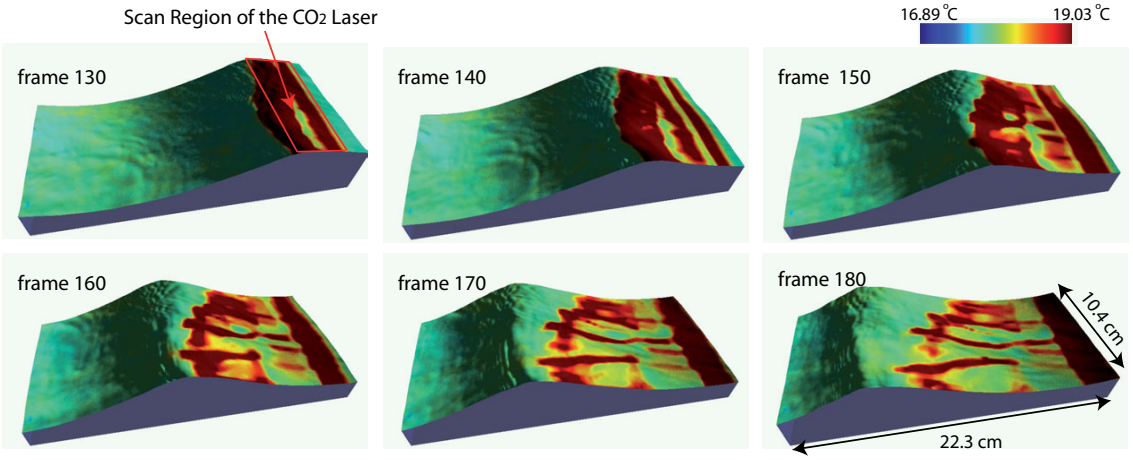

Figure 7.26.: Micro Langmuir Circulation at 6 m/s wind speed.

circulations, as depicted by the sketch in figure 7.27. The Langmuir circulations are vortices that are parallel to the water surface and oriented in direction of the shear flow. The shear flow is mainly responsible for the generation of these circulations [134] but there also exists interaction of the turbulence with passing waves, which is sketched in figure 7.28 (see [158] for details).

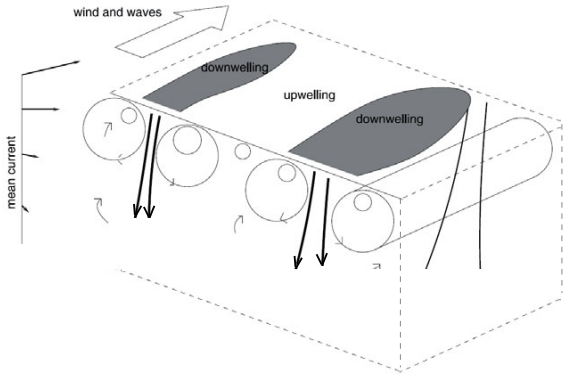

Figure 7.27.: Upwelling and downwelling zones due to Langmuir Circulations (modified after Polton and Belcher [139]).

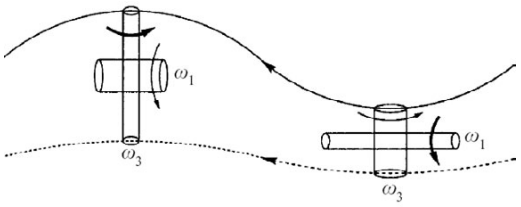

Figure 7.28.: Schematic diagram showing the vorticity strechting and compression induced by the orbital motion at the crest and at the trough of a surface wave, in a frame of reference travelling with the wave (adopted from Teixeira and Belcher [158]).

Veron and Melville [165] and Melville et al. [123] have experimentally investigated the coupling between such-small scale Langmuir circulations and the wind-driven water waves. They studied the generation and evolution of Langmuir circulations in laboratory experiments for incipient winds. The streaks that we observe in figure 7.26 look similar to the observations of Veron and Melville [165] after about 20 s of wind forcing[23], while in general the experimental conditions are not readily comparable. However, the interpretation of these structures may be guided by the former findings.

We assume that the structures are not due to thermal instability, i.e. convection. Then, Langmuir circulations can be seen as an additional mechanism that enhances the vertical mixing in the subsurface flow under natural conditions[24]. Concerning the air-water transfer the question is always, whether or not the vortices can penetrate into the diffusive boundary layer for gases or heat[25]. Recently Hara et al. [61] introduced an *eddy renewal model* that incorporates the influence of coherent vortices into the estimation of gas and heat fluxes from the infrared imagery. This model may also be used to yield the distribution of eddy sized and eddy intensities. Since the apparent Langmuir circulation originates from an instability of the surface shear flow [123] it is suspected to effectively constitute mixing between the water surface and the water bulk, i.e. thinning of the effective viscous boundary layer thickness.

[23] with 5 m/s wind speed

[24] i.e.: without active heating of the surface

[25] The diffusive boundary layer at the top of the ocean for carbon dioxide and methane has a thickness of about 20-200 μm [83]. For heat the boundary layer thickness is in the range of 0.1-1 mm [148].

Moreover, the streak signatures can be observed under a wide range of wind speed conditions. This includes low to moderate wind speeds, see figure 7.29, where no micro-scale wave breaking takes place. Therefore, we hypothesize that the small-scale Langmuir circulation - in addition to microscale breaking [151, 176] - plays a significant role for the air-sea exchange [Personal communication with B. Jähne] [166, 167]. The presented visualization is giving insights of how persistent the flow structures are. These observations encourage a more detailed study concerning our hypothesis. In addition, by virtue of the high frame rate of 312.5 Hz we are able to directly study the evolution and interaction of Langmuir cells and wind driven waves. Future investigations should incorporate measurements of the 3D subsurface turbulence in combination to the wave imaging and infrared imagery. This would allow for a more detailed analysis of the streak features and a verification of the predictions from the *eddy renewal model* concerning the eddy sizes and intensities [61].

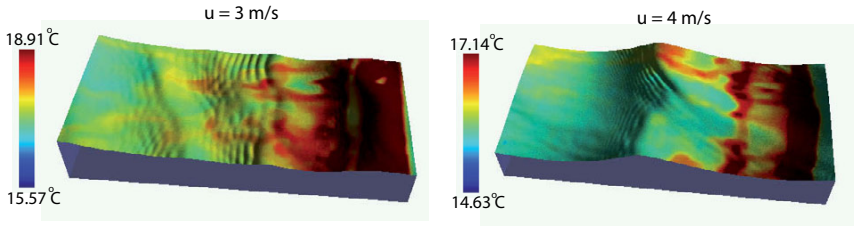

Figure 7.29.: Streaks appear also for low wind speeds.

Rain Drop Impacts

Figure 7.30 displays consecutive frames for a rain condition. Before we go into detail it is worth mentioning - even though not surprising - that the surface roughness is drastically different compared to the no-rain condition with the same wind speed (e.g. compare with figure 7.29 to the right). Additionally, we observe that short gravity waves are hardly existent for the rain condition at this moderate wind speed, although the rain tower section only covers a small range of the flume, see section 4.1.

The rain drops are cold compared to the water surface and can therefore easily be identified as blue dots in the temperature overlays in figure 7.30. Note, in the IR image a rain drop is actually already visible before it hits the surface, but due to the focusing of the camera one can see only drops that are close to the water surface.

For the first frame (1405) two markers have been included. Marker A is next to the spot where the next rain drop hits the surface. Marker B is located next to rain drop craters from two impacts that occurred approximately 7-10 frames (0.022-0.032 s) earlier.

Though with these still images it is a bit tricky to see, one can study the rain drop impacts to some detail and follow their evolution in time. The rain drop impinging at position A forms a crater, which develops in size for about 7 frames (0.022 s) before it begins to collapse. At position B we can observe how the crater is collapsing and at the same time it is disturbed by the wind wave field. Using the visualization tool (i.e.: the animation instead of still images), one can distinguish the isotropically propagation ring waves from the directional wind driven waves. To the authors knowledge these are the first measurements of the combined effect of rain and wind on the water waves at this high spatial an temporal resolution. A review of common features and visualization techniques for drop impacts on a quiescent water surface can be found in Fedorchenko and Wang [45] and Yarin [173]. Braun [23] and Yang et al. [172] investigated the influence of rain on the wind driven water surface using point measurements of the slope and height and radar backscatter. Ho et al. [65], Ho et al. [66], and Takagaki and Komori [156] studied the mechanisms and the net-effect of rain-induced air-water gas exchange. They found that rainfall enhances the turbulent

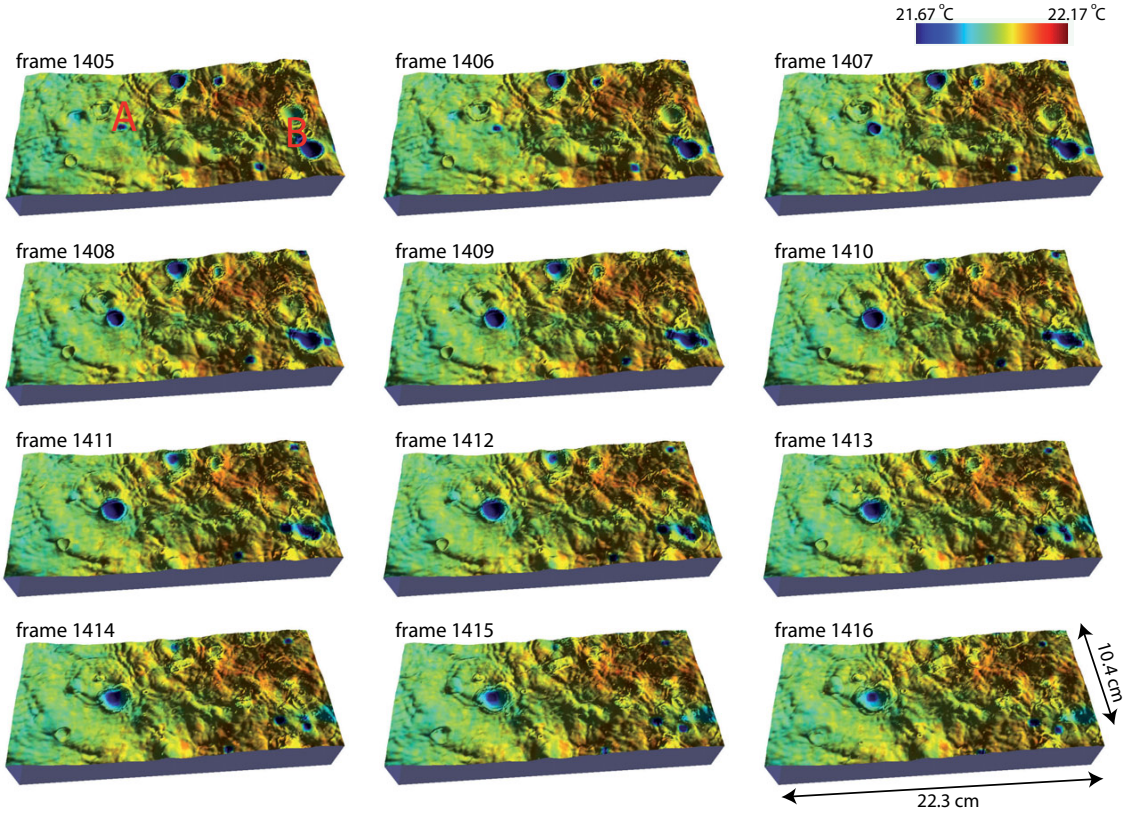

Figure 7.30.: Impacts of cold rain drops on a warmer water surface. Wind speed 4 m/s.

mixing near the free surface on the liquid side, and the enhancement results in an increase of the gas transfer across the air-water interface. Ho et al. [66] concludes: "*The mechanisms behind rain-induced gas exchange, and the interaction of rain- and wind-generated waves and turbulence, should be examined in greater depth*". This is especially important for the mean square slope parameterization of gas transfer rates, since Ho et al. [65] found, that the gas transfer velocities in case of rain do not fall on the same line as for the ordinary conditions. This issue is also addressed in section 7.4.2.

From the observations in figure 7.30 and the visualization of other sequences we get the impression, that the rain drops hit through the water surface without much influence on the surface temperature next to the crater. Therefore it seems that the turbulence that is generated by the impact is not reaching into the skin layer of the water surface that controlls the heat exchange. Our measurements only comprise one distinct drop size (⌀ 2.9 mm) and one rain rate (57 mm/h), so we can not make a general statement about this by now. Moreover, an analysis incorporating the results of the measurements of the turbulent kinetic energy is still pending.

8. Conclusion and Outlook

Due to the improvement that was achieved for the *color imaging slope gauge* (CISG) we are able to investigate the wavenumber-frequency spectrum of short wind-driven water waves at higher spatio-temporal resolution and accuracy than ever possible.

8.1. Conclusion

no spectral cut-off

One of the most surprising insights is that the spectral energy exhibits no cut-off for wavenumbers higher than 1000 rad/m (section 7.2.1, page 91), which is contradictory to former findings. This discrepancy is attributed to the fact that the wavenumber dependent contrast damping, which is inherent to the data acquisition and processing, was not corrected for in the former studies. In this study the contrast damping was corrected for by means of a deconvolution using the measured *Modulation Transfer Function* (MTF). For the measurement of the MTF a new method was developed that can be applied in-situ, i.e. within the experimental setup (section 4.5).

MTF correction

MTF measurement

3D spectral density

dispersion relation

aliasing

The high temporal resolution ($\Delta t = 0.0032\,\mathrm{s}$) of the wave imaging now allows for the computation of the *dispersion shell*, which includes valuable information about the hydrodynamic conditions (section 7.3). A detailed physical interpretation of the 3D power spectral density $S(k_x, k_y, \omega)$ is given by means of one case study (section 7.3.2). In addition, a quantitative approach is introduced to evaluate the dispersion of the capillary waves. This yields estimates for the reduction of the surface tension due to surface slicks and for the Doppler shifts, which are caused by the surface shear flow and the wave-wave interaction (section 7.3.3). The results are encouraging, while at the same time it becomes clear that the temporal sampling rate is still not sufficient to avoid aliasing. Already for wavenumbers larger 1500 rad/m the wave frequency occasionally exceeds the Nyquist frequency of 982 rad/s, e.g. due to the Doppler shift caused by long wave orbital motion. This introduces aliasing in the discrete spectral volume, which in turn leads to difficulties in the evaluation, i.e. ambiguity in the frequency that is associated with a certain wavenumber component.

campaign

synchronized infrared imagery

wave visualization

The wave measurements were conducted in a linear wind wave tank as part of the *WiSSCy* project (section 5), covering a wide range of experimental conditions: wind, rain, surface slicks, and a mechanically generated long wave. An active infrared imaging system (ACFT) was deployed by a co-worker for the measurement of the local heat transfer. The infrared camera of the ACFT system and the CISG camera were synchronized at a frame rate of 312.5 Hz and observed the same patch on the water surface. The registration of the image sequences was performed (sections 4.3 and 7.5.2) and the water surface elevation was reconstructed from the gradient field (section 7.5.1) for a set of 150 combined measurements of the waves and the water surface temperature. An interactive visualization tool (section 7.5)

maps the surface temperature field in false color onto an animated 3D graphical model of the surface elevation. This new visualization provides insights into the wave related small scale processes that are controlling the local air-water transfer of heat and gases, i.e.: microscale wave breaking and (mirco) Langmuir circulation (section 7.5.3). The thermal streaks that are interpreted as an indication for Langmuir circulation were observed for a wide range of wind speeds. Therefore it is hypothesized that small scale Langmuir circulation plays a significant role for the air-sea exchange.

microscale breaking & Langmuir circulation

Moreover, the impact of raindrops on the wind-driven wave field can be studied in great detail. Apparently, the raindrops hit through the surface without much influence on the water sided thermal boundary layer at the interface next to the crater (section 7.5.3, page 120). This indicates that rain induced sub surface turbulence might not necessarily lead to significantly enhanced air-water transfer rates.

raindrop impacts

From the spatio-temporal measurements it is possible to distinguish wave components that are propagating along with the wind or against the wind. This enables a decomposition of the spectral energy, e.g. separating the wind driven waves from ring wave patterns caused by rain drop impacts (section 7.4.2).

mss decomposition

The CISG measurements always rely on a calibration of the color-slope relationship. Commonly the calibration is performed with a linear model, disregarding the inherent non-linearities which are due to the ray geometry and the color coding transparent sheet. In this study, higher accuracy was obtained by the implementation of a third order polynomial calibration model (section 4.4.3). This could be achieved by the development of a new in-situ calibration method utilizing a *slope robot* (section 4.4.1).

higher accuracy

slope robot

8.2. Outlook

New methods for the analysis of wind-driven small scale waves are now at hand. With this, the understanding of the complex interaction between wind and waves will presumably be pushed forward, e.g. via a direct validation of the *Wind Over Waves Coupling* model (WOWC) predictions.

WOWC

The spectral cut-off issue needs to be clarified because of its importance for the modeling of energy fluxes in the wave field. This can be achieved simply by using a new camera with higher spatial resolution, for that the MTF is still high enough to allow for a contrast correction up to high wavenumbers (at least 6000 rad/m). Additionally, higher frame rates (> 1000 Hz) are desired to avoid the aliasing dilemma, which hinders the quantitative evaluation of the dispersion relation. Already now cameras are forthcoming, which are approaching our requirements.

new camera

Basically two tracks exists, which will be followed in order to support the analysis of the observations that are made by the combined ACFT and CISG visualization. On the one hand, direct numerical simulations (DNS) will be carried out in order to validate the conceptual models that are used. On the other hand, new multidimensional visualization techniques - based on laser induced fluorescence (LIF) - are being developed to gain insight for the enhancement of near-surface turbulence due to waves.

DNS

LIF

Bibliography

[1] A. Agrawal, R. Chellappa, and R. Raskar. An algebraic approach to surface reconstruction from gradient fields. In *International conference on computer vision (ICCV)*, 2005.

[2] A. Agrawal, R. Raskar, and R. Chellappa. What is the range of surface reconstructions from a gradient field. In *European conference on Computer Vision (ECCV)*, 2006.

[3] G. B. Airy. On tides and waves. In *Encyclopaedia Metropolitana*, pages 241–396. B. Fellowes, London, 1845.

[4] W. Alpers. The damping of ocean waves by surface films: A new look at an old problem. *Journal of Geophysical Research*, 94(C5):6251–6265, May 1989.

[5] A. Anweiler and M. Gade. Tank Experiments on the Influence of Rain on Air-Sea CO2-Exchange. *AGU Fall Meeting Abstracts*, pages A914+, Dec. 2007.

[6] A.-K. Anweiler. Ergebnisse der CO2-Austauschmessungen am Wind-Wellen-Kanal der Universität Hamburg im Rahmen des Projekts WiSSCy. Technical report, Institut für Meeresforschung, Universität Hamburg, Germany, 2008.

[7] A.-K. Anweiler. *Tank experiments on the influence of rain-induced turbulence on air-water CO_2 exchange*. PhD thesis, University of Hamburg, 2008. in preperation.

[8] J. R. Apel. An improved model of the ocean surface wave vector spectrum and its effects on radar backscatter. *Journal of Geophysical Research*, 99:16269–16292, Aug. 1994.

[9] G. Balschbach. *Untersuchungen statistischer und geometrischer Eigenschaften von Windwellen und ihrer Wechselwirkung mit der wasserseitigen Grenzschicht*. PhD thesis, Institut für Umweltphysik, Universität Heidelberg, February 2000.

[10] M. L. Banner. The influence of wave breaking on the surface pressure distribution in wind-wave interactions. *J.Fluid Mech.*, 211:463–495, 1990.

[11] M. L. Banner, I. S. F. Jones, and J. C. Trinder. Wavenumber spectra of short gravity waves. *Journal of Fluid Mechanics*, 198:321–344, 1989.

[12] M. L. Banner and O. M. Phillips. On the incipient breaking of small-scale waves. *J.Fluid Mech.*, 65:647–656, 1974.

[13] F. Behroozi and A. Perkins. Direct measurement of the dispersion relation of capillary waves by laser interferometry. *American Journal of Physics*, 74(11):957–961, 2006.

[14] N. Bindoff, J. Willebrand, V. Artale, A. Cazenave, J. Gregory, S. Gulev, K. Hanawa, C. Le Quéré, S. Levitus, Y. Nojiri, C. Shum, L. Talley, and A. Unnikrishnan. Observations: Oceanic climate change and sea level. In S. Solomon, D. Qin, M. Manning, Z. Chen, M. Marquis, K. Averyt, M. Tignor, and H. Miller, editors, *Climate Change 2007: The Physical Science Basis. Contribution of Working Group I to the Fourth Assessment Report of the Intergovernmental Panel on Climate Change*. Cambridge University Press, Cambridge, United Kingdom and New York, NY, USA., 2007.

[15] E. J. Bock, J. B. Edson, and F. N. M. et. al. Overview of the CoOP experiments: Physical and chemical measurements parameterizing air-sea gas exchange. In M. A. Donelan, W. M. Drennan, E. S. Saltzman, and R. Wanninkhof, editors, *Gas Transfer at Water Surfaces*, volume 127 of *Geophysical Monograph*, pages pp. 39–44. American Geophysical Union, 2002.

[16] E. J. Bock and T. Hara. Optical measurements of ripples using a scanning laser slope gauge. In *Optics of the Air-Sea Interface*, volume 1749, page 272ff, 1992. Part II: Data analysis and interpretation from a laboratory.

[17] E. J. Bock and T. Hara. Optical measurements of capillary-gravity wave spectra using a scanning laser slope gauge. *Journal of Atmospheric and Oceanic Technology*, 12(2):395–403, April 1995.

[18] E. J. Bock, T. Hara, N. M. Frew, and W. R. McGillis. Relationship between air-sea gas transfer and short wind waves. *Journal of Geophysical Research-Oceans*, 104(C11):25821–25831, 1999. J NOV 15.

[19] E. J. Bock and J. A. Mann. On ripple dynamics II. a corrected dispersion relation for surface waves in the presence of surface elasticity. *Journal of Colloid And Interfacial Science*, 129, 2:1989, 1989.

[20] G. D. Boreman and E. Dereniak. Method for measuring transfer function of changed-coupled devices using laser speckle. *Opt. Eng.*, 24:148–150, 1986.

[21] J.-Y. Bouguet. Camera calibration toolbox for matlab, `http://www.vision.caltech.edu/bouguetj/calib_doc/`. 2008.

[22] J. Boussinesq. Théorie des ondes et des remous qui se propagent le long d'un canal rectangulaire horizontal, en communiquant au liquide contenu dans ce canal des vitesses sensiblement pareilles de la surface au fond. *J. Math. Pures Appl.*, 17 (2):55–108, 1872.

[23] N. Braun. *Laboruntersuchungen zum Einfluss von künstlichem Regen auf eine Wasseroberfläche mit Hilfe von Wellendraht-, Laser- und Radarsonden*. PhD thesis, Universität Hamburg, 1998.

[24] N. Braun and M. Gade. Multifrequency scatterometer measurements on water surfaces agitated by artificial and natural rain. *Int. J. Remote Sens.*, 27:27–39, 2006.

[25] N. Braun, M. Gade, and P. Lange. The effect of artificial rain on wave spectra and multi-polarisation x band radar backscatter. *Int. J. Remote Sens.*, 23(20):4305–4322, 2002.

[26] H. Carstens. Ein Skalenraumverfahren zur Orts/Wellenzahl-Raum-Analyse winderzeugter Wasserwellen. Master's thesis, University of Heidelberg, 1998.

[27] G. Caudal. A physical model for the narrowing of the directional sea wave spectra in the short gravity to gravity-capillary range. *Journal of Geophysical Research (Oceans)*, 107: 3148 – 12; 1–9, Oct. 2002.

[28] G. Caulliez and F. Collard. Three-dimensional evolution of wind waves from gravity-capillary to short gravity range. *Eur. J. Mech. B/Fluids*, 18:3,389–402, 1999.

[29] G. Caulliez, R. Dupont, and V. Shrira. Turbulence generation in the wind-driven subsurface water flow. In C. S. Garbe, R. A. Handler, and B. Jähne, editors, *Transport at the Air Sea Interface*, pages 103–117. Springer-Verlag, 2007.

[30] G. Caulliez, V. Makin, and V. Kudrayavtsev. Drag of the water surface at very short fetches: observations and modelling. *Journal of Physical Oceanography*, 2008. In Press.

[31] L. Cavaleri, J. Alves, F. Ardhuin, A. Babanin, M. Banner, K. Belibassakis, M. Benoit, M. Donelan, J. Groeneweg, T. Herbers, and P. Hwang. Wave modelling - the state of the art. *Progress in Oceanography*, 75:603–674, 2007.

[32] J. Cohen and S. Belcher. Turbulent shear flow over fast moving waves. *J. Fluid Mech.*, 386: 345–371, 1999.

[33] C. Cox and W. Munk. Statistics of the sea surface derived from sun glitter. *Journal of Marine Research*, 13(2):198–227, 1954.

[34] G. D. Crapper. An exact solution for progressive capillary waves of arbitrary amplitude. *Journal of Fluid Mechanics*, 2:532–540, 1957.

[35] A. Daniels, G. D. Boreman, A. D. Ducharme, and E. Sapir. Random targets for modulation transfer function testing. In G. C. Holst, editor, *Proc. SPIE Vol. 1969, p. 184-192, Infrared Imaging Systems: Design, Analysis, Modeling, and Testing IV, Gerald C. Holst; Ed.*, volume 1969 of *Presented at the Society of Photo-Optical Instrumentation Engineers (SPIE) Conference*, pages 184–192, Aug. 1993.

[36] A. Daniels, G. D. Boreman, A. D. Ducharme, and E. Sapir. Random transparency targets for modulation transfer function measurement in the visible and infrared regions. *Optical Engineering*, 34:860–868, Mar. 1995.

[37] K. Degreif. *Untersuchungen zum Gasaustausch - Entwicklung und Applikation eines zeitlich aufgelösten Massenbilanzverfahrens*. PhD thesis, Institut für Umweltphysik, University of Heidelberg, 2006.

[38] F. Dias and C. Kharif. Nonlinear gravity and capillary-gravity waves. *Annual Review of Fluid Mechanics*, 31(1):301–346, 1999.

[39] M. A. Donelan, J. Hamilton, and W. H. Hui. Directional spectra of wind-generated waves. *Royal Society of London Philosophical Transactions Series A*, 315:509–562, Sept. 1985.

[40] M. A. Donelan and W. J. Pierson. Radar scattering and equilibrium ranges in wind-generated waves with application to scatterometry. *Journal of Geophysical Research*, 92: 4971–5030, May 1987.

[41] M. A. Donelan and R. Wanninkhof. Gas transfer at water surfaces - conepts and issues. American Geophysical Union, 2002.

[42] A. D. Ducharme and G. D. Boreman. Holographic elements for the modulation transfer function testing of detector arrays. *Opt. Eng.*, 34(8):2455–2458, 1995.

[43] N. Ebuchi, H. Kawamura, and Y. Toba. Fine structure of laboratory wind-wave surfaces using an optical method. *Boundary-Layer Meteorol.*, 39:133, 1987.

[44] T. Elfouhaily, B. Chapron, K. Katsaros, and D. Vandemark. A unified directional spectrum for long and short wind-driven waves. *Journal of Geophysical Research*, 102(C7):15781–15796, July 15 1997.

[45] A. I. Fedorchenko and A.-B. Wang. On some common features of drop impact on liquid surfaces. *Physics of Fluids*, 16(5):1349–1365, May 2004.

[46] R. Fitzenberger. Lokale Transformationsmethoden zur Auswertung von Wellenneigungsbildern der Wasseroberfläche im Bereich kleinskaliger Oberflächenwellen. Diplomarbeit, Institut für Umweltphysik, Fakultät für Physik und Astronomie, Univ. Heidelberg, 1997.

[47] R. T. Frankot and R. Chellappa. A method for enforcing integrability in shape from shading algorithms. *IEEE Trans. Pattern Anal. Mach. Intell.*, 10(4):439–451, 1988.

[48] N. M. Frew, E. J. Bock, U. Schimpf, T. Hara, H. Haußecker, J. B. Edson, W. R. McGillis, R. K. Nelson, B. M. McKeanna, B. M. Uz, and B. Jähne. Air-sea gas transfer: Its dependence on wind stress, small-scale roughness, and surface films. *Journal of Geophysical Research*, 109(C8):C08S17, 2004.

[49] N. M. Frew, D. M. Glover, E. J. Bock, and S. J. McCue. A new approach to estimation of global air-sea gas transfer velocity fields using dual-frequency altimeter backscatter. *J. Geophys. Res.*, 112:C11003, 2007.

[50] D. Fuß. *Kombinierte Höhen- und Neigungsmessung von winderzeugten Wasserwellen am Heidelberger Aeolotron*. Dissertation, University of Heidelberg, Heidelberg, Germany, 2004.

[51] M. Gade, W. Alpers, H. Hühnerfuss, and P. A. Lange. Wind wave tank measurements of wave damping and radar cross sections in the presence of monomolecular surface films. *Jounral of Geophysical Research*, 103(C2):3167–3178, Feb 1998.

[52] C. S. Garbe. *Measuring Heat Exchange Processes at the Air–Water Interface from Thermographic Image Sequence Analysis*. PhD thesis, University of Heidelberg, Heidelberg, Germany, December 2001.

[53] C. S. Garbe, D. Banerjee, U. Schimpf, and B. Jähne. Aktive Thermografie für die Untersuchung von Transportprozessen. In *Thermografie-Kolloquium*, pages 1–8. Deutsche Gesellschaft für Zerstörungsfreie Prüfung e.V., 2007.

[54] C. S. Garbe, K. Degreif, and B. Jähne. Estimating the viscous shear stress at the water surface from active thermography. In C. S. Garbe, R. A. Handler, and B. Jähne, editors, *Transport at the Air Sea Interface - Measurements, Models and Parameterizations*, pages 223–239. Springer-Verlag, Berlin, Heidelberg, 2007.

[55] C. S. Garbe, H. Haußecker, and B. Jähne. Measuring the sea surface heat flux and probability distribution of surface renewal events. In E. Saltzman, M. Donelan, W. Drennan, and R. Wanninkhof, editors, *Gas Transfer at Water Surfaces*, volume 127 of *Geophysical Monograph*, pages 109–114. American Geophysical Union, 2002.

[56] B. L. Gotwols and G. B. Irani. Optical determination of the phase velocity of short gravity waves. *Journal of Geophysical Research*, 85:3964–3970, 1980.

[57] M. G. Gross. *Oceanopgraphy, a view of the earth.* Prentice-Hall, Inc., 1982.

[58] T. Hara and S. E. Belcher. Wind forcing in the equilibrium range of wind-wave spectra. *J. Fluid Mech.*, 470:223–245, 2002.

[59] T. Hara, E. J. Bock, and M. Donelan. Frequency-wavenumber spectrum of wind-generated gravity-capillary waves. *Journal of Geophysical Research*, 102(C1):1061–1072, January 15 1997.

[60] T. Hara, E. J. Bock, and D. Lyzenga. In situ measurements of capillary-gravity wave spectra using a scanning laser slope gauge and microwave radars. *Journal of Geophysical Research*, 99(C6):12593–12602, June 15 1994.

[61] T. Hara, E. VanInwegen, J. Wendelbo, C. S. Garbe, U. Schimpf, B. Jähne, and N. Frew. Estimation of air-sea gas and heat fluxes from infrared imagery based on near surface turbulence models. In C. S. Garbe, R. A. Handler, and B. Jähne, editors, *Transport at the Air Sea Interface - Measurements, Models and Parametrizations*. Springer-Verlag, 2007.

[62] F. J. Harris. On the use of windows for harmonic analysis with the discrete fourier transform. In *Proceedings of the IEEE*, volume 66-1, January 1978.

[63] K. Hasselmann. On the nonlinear energy transfer in a gravity wave-spectrum. part 1: General theory. *J. Fluid Mech.*, 12:481, 1962.

[64] H. Haußecker, U. Schimpf, and B. Jahne. Measurements of the air-sea gas transfer and its mechanisms by active and passive thermography. In U. Schimpf, editor, *Proc. IEEE International Geoscience and Remote Sensing Symposium IGARSS '98*, volume 1, pages 484–486 vol.1, 1998.

[65] D. T. Ho, W. E. Asher, L. F. Bliven, P. Schlosser, and E. L. Gordan. On mechanisms of rain-induced air-water gas exchange. *Journal of Geophysical Research*, 105(C10):24,045–24,057, October 2000.

[66] D. T. Ho, C. J. Zappa, and W. R. e. a. McGillis. Influence of rain on air-sea gas exchange: Lessons from a model ocean. *Journal of Geophysical Research*, 109:C08S18, 2004.

[67] B. K. P. Horn. *Robot Vision*. MIT Press, Cambridge, MA, 1986.

[68] N. E. Huang, Y. Toba, Z. Shen, J. Klinke, B. Jähne, and M. L. Banner. Ocean wave spectra and integral properties. In I. S. F. Jones and Y. T. a, editors, *Wind Stress over the Ocean*, pages 82–123. Cambridge University Press, Cambridge, UK, 2001.

[69] B. A. Hughes, R. W. Grant, and R. W. Chappell. A fast response surface-wave slope meter and measured wind-wave moments. *Deep-Sea Res.*, 24:1211–1223, 1977.

[70] F. Huhn. A simple instrument for the measurement of the slope and height distributions of small scale wind-driven water waves. Master's thesis, Institute for Environmental Physics, University of Heidelberg, 2008.

[71] P. A. Hwang. Spatial measurements of small-scale ocean waves. In B. J. Monahan, editor, *Air-Water Gas Transfer - Selected papers from the Third International Symposium on Air-Water Gas Transfer*, pages 153–164, 1995.

[72] B. Jähne. *On the transfer processes at a free air-water interface*. Habilitation, Institut für Umweltphysik, Fakultät für Physik und Astronomie, Univ. Heidelberg, 1985. IUP D-200.

[73] B. Jähne. Protokollbuch Wellen II. Seite 146, Vermerk bezüglich des Faktors 2 in der Auswertungen der Spektren von Delft 1988, August 1989.

[74] B. Jähne. Motion determination in space-time images. In O. Faugeras, editor, *Proc. Computer Vision – ECCV 90, Lecture Notes in Computer Science 427*, pages 161–173, New York, 1990.

[75] B. Jähne. Impact of quantitative visualization and image processing on the study of small-scale air-sea interaction. In B. Jähne and E. Monahan, editors, *Air-Water Gas Transfer, Selected Papers, 3rd Intern. Symp. on Air-Water Gas Transfer*, pages 3–12, Hanau, 1995. AEON.

[76] B. Jähne. Analytische Beschreibung der Bildgebung bei der kombinierten Neigungs- und Höhenmessung von Windwellen. Technical report, Institut für Wissenschaftliches Rechnen, Universität Heidelberg, Germany, 2004.

[77] B. Jähne. *Digitale Bildverarbeitung, 6. Auflage*. Springer, 2005.

[78] B. Jähne and E. J. Bock. Physically-based modelling of air-sea gas transfer. In E. Saltzman, M. Donelan, W. Drennan, and R. Wanninkhof, editors, *Gas Transfer at Water Surfaces*, volume 127 of *Geophysical Monograph*. American Geophysical Union, 2002. Interdisziplinäres Zentrum für Wissenschaftliches Rechnen und Institut für Umweltphysik, Universität Heidelberg.

[79] B. Jähne and H. Haußecker. Air-water gas exchange. *Annual Reviews of Fluid Mechanics*, 30:443–468, 1998.

[80] B. Jähne, J. Klinke, P. Geißler, and F. Hering. Image sequence analysis of ocean wind waves. In S. Sideman and K. Hijikata, editors, *Imaging in Transport Processes*, pages 257–268, New York, 1993. Begell House Publishers.

[81] B. Jähne, J. Klinke, and S. Waas. Imaging of short ocean wind waves: a critical theoretical review. *J.Opt.Soc.Am.*, 11(8):2197–2209, 1994.

[82] B. Jähne, K. O. Münnich, R. Bösinger, A. Dutzi, W. Huber, and P. Libner. On the parameters influencing air–water gas exchange. *Journal of Geophysical Research*, 92(C2):1937–1949, February 1987.

[83] B. Jähne, C. Popp, U. Schimpf, and C. Garbe. The influence of intermittency on air/water gas transfer measurements. In C. S. Garbe, R. A. Handler, and B. Jähne, editors, *Transport at the Air Sea Interface*. Springer-Verlag, 2007.

[84] B. Jähne and K. Riemer. Two-dimensional wave number spectra of small-scale water surface waves. *J.Geophys.Res.*, 95(C7):11531–11646, 1990.

[85] B. Jähne, M. Schmidt, and R. Rocholz. Combined optical slope/height measurements of short wind waves: principles and calibration. *Measurement Science & Technology*, 16(10): 1937–1944, 2005.

[86] B. Jähne and H. Schultz. Calibration and accuracy of optical slope measurements for short wind waves. In L. Estep, editor, *Optics of the Air-Sea Interface: Theory and Measurements*, volume 1749 of *SPIE Proceedings*, pages 222–233, 1992.

[87] B. Jähne, T. Wais, L. Memery, G. Gaulliez, L. Merlivat, K. O. Münnich, and M. Coantic. He and Rn gas exchange experiments in the large wind-wave facility of IMST. *J. Geophys. Res.*, 90:11,989–11,998, 1985.

[88] I. S. F. Jones and Y. Toba. *Wind Stress over the Ocean*. Cambridge University Press, Cambridge,UK, 2001.

[89] M. Jung. Miniforschungsbericht - Entwicklung einer Visualisierung von Messdaten mittels OpenGL. Technical report, Institut für Wissenschaftliches Rechnen, Universität Heidelberg, 2008.

[90] B. Kinsmann. *Wind Waves*. Prentice-Hall, Englewood Cliffs, 1965.

[91] S. A. Kitaigorodskii. On the theory of the equilibrium range in the spectrum of wind-generated gravity waves. *JPHO*, 13:816–827, 1983.

[92] J. Klinke. 2D wave number spectra of short wind waves – results from wind wave facilities and extrapolation to the ocean. *Optics of the Air-Sea Interface: Theory and Measurement, Proc. SPIE - Int. Soc. Opt. Eng.*, 1749:1–13, July 1992.

[93] J. Klinke. *Optical Measurements of Small-Scale Wind Generated Water Surface Waves in the Laboratory and the Field*. PhD thesis, University of Heidelberg, Heideleberg, Germany, 1996.

[94] J. Klinke and B. Jähne. Two-dimensional wave number spectra of short wind waves: results from wind-wave facilities and extrapolation to the ocean. In L. Estep, editor, *Optics of the Air-Sea Interface: Theory and Measurement*, volume 1749 of *Presented at the Society of Photo-Optical Instrumentation Engineers (SPIE) Conference*, pages 245–257, Dec. 1992.

[95] K. R. Koch. *Parameter Estimation and Hypothesis Testing in Linear Models*. Springer-Verlag, Heidelberg, Germany, 1988.

[96] V. Kudryavtsev, D. Akimov, J. Johannessen, and B. Chapron. On radar imaging of current features: 1. Model and comparison with observations. *Journal of Geophysical Research (Oceans)*, 110:7016–+, July 2005.

[97] V. Kudryavtsev and V. Makin. On the impact of short waves on the wind growth rate of long surface waves. *EGS XXVII General Assembly, Nice, 21-26 April 2002*, 27:3500–+, 2002.

[98] V. N. Kudryavtsev and V. K. Makin. Aerodynamic roughness of the sea surface at high winds. *Boundary-Layer Meteorology*, 125:289–303, Nov 2007.

[99] V. N. Kudryavtsev, V. K. Makin, and B. Chapron. Coupled sea surface atmosphere model. 2. spectrum of short wind waves. *J. Geophys. Res.*, 104:7625–7640, 1999.

[100] V. N. Kudryavtsev, C. Mastenbroek, and V. K. Makin. Modulation of wind ripples by long surface waves via the air flow: a feedback mechanism. *Boundary-Layer Meteorology*, 83: 99–116, 1997.

[101] T. Kukulka and T. Hara. Momentum flux budget analysis of wind-driven air-water interfaces. *Journal of Geophysical Research*, 110:C12020, 2005.

[102] P. K. Kundu. *Fluid Mechanics*. Academic Press, San Diego, CA, 4th edition, 2007.

[103] W. Laas. Photographische Messung der Meereswellen. *Zeitschr. d. Vereins Dtsch. Ingenieure*, 49:S.1889 ff. S.1937 ff. und S.1976 ff., 1905.

[104] H. Lamb. *Hydrodynamics*. Cambridge University Press, 1932.

[105] P. A. Lange and H. Hühnerfuss. Horizontal surface tension gradients induced in monolayers by gravity water wave action. *Journal of Physical Oceanography*, 14:1620–1628, 1984.

[106] P. A. Lange, B. Jähne, J. Tschiersch, and I. Ilmberger. Comparison between an amplitude-measuring wire and a slope-measuring laser water wave gauge. *Rev. Sci. Instrum.*, 53(5): 651–655, May 1982.

[107] H. Lauer. *Untersuchung der Neigungsstatistik von Wasseroberflächenwellen mittels eines schnellen, bildaufnehmenden Verfahrens*. Dissertation, Universität Heidelberg, 05 1998.

[108] P. LeBlond and L. A. Mysak. *Wave in the Ocean*. Elsevier Science Publishing Company, 1978.

[109] X. Li, B. Gunturk, and L. Zhang. Image demosaicing: a systematic survey. In *Visual Communications and Image Processing 2008. Edited by Pearlman, William A.; Woods, John W.; Lu, Ligang. Proceedings of the SPIE, Volume 6822, pp. 68221J-68221J-15 (2008).*, volume 6822 of *Presented at the Society of Photo-Optical Instrumentation Engineers (SPIE) Conference*, Jan. 2008.

[110] P. S. Liss and L. Merlivat. Air-sea gas exchange rates: Introduction and synthesis. In P. Buat-Menard, editor, *The role of air-sea exchange in geochemical cycling*, pages 113–129. Reidel, Boston,MA, 1986.

[111] M. S. Longuet-Higgins. The statistical analysis of a random, moving surface. *Journal of Marine Research*, 249:321–387, February 1957. A. 966.

[112] M. S. Longuet-Higgins. Why is a water wave like a grandfather clock? *Physics of Fluids*, 22:1828–1829, Sept. 1979.

[113] R. Lukac. Single-sensor imaging in consumer digital cameras: a survey of recent advances and future directions. *Journal of Real-Time Image Processing*, 1(1):45–52, 2006.

[114] D. R. Lyzenga. Ocean wave spectrum and dissipation rate derived from cmod4 model function. *Journal of Geophysical Research (Oceans)*, 109:C07019; 1–11, July 2004.

[115] V. K. Makin, H. Branger, W. L. Peirson, and J. P. Giovanangeli. Stress above wind-plus-paddle waves: Modeling of a laboratory experiment. *Journal of Physical Oceanography*, 37(12):2824–2837, 2007.

[116] V. K. Makin and V. Kudrayavtsev. Coupled sea surface-atmosphere model - 1. wind over waves coupling. *Journal of Geophysical Research*, 104(C4):7613–7623, 1999.

[117] V. K. Makin and V. N. Kudryavtsev. Impact of dominant waves on sea drag. *Boundary-Layer Meteorology*, 103:83–99, 2002.

[118] V. K. Makin, V. N. Kudryavtsev, and C. Mastenbroek. Drag of the sea surface. *Boundary-Layer Meteorology*, 73:159–182, 1995.

[119] J. A. Mann. Dynamic surface tension and capillary waves. *Surface and Colloid Science*, 13:145–212, 1984.

[120] W. C. Martin. Determination of optical transfer functions by direct measurement. *Photogrammetria*, 33(4):133–144, 1977.

[121] J. C. McWilliams, P. P. Sulliivan, and C.-H. Moeng. Langmuir turbulrnce in the ocean. *Journal of Fluid Mechanics*, 334:1–30, 1997.

[122] J. F. Meirink, V. K. Makin, and V. N. Kudryavtsev. Note on the growth rate of water waves propagating at an arbitrary angle to the wind. *Boundary-Layer Meteorology*, 106(1):171–183, 2003.

[123] W. K. Melville, R. Shear, and F. Veron. Laboratory measurements of the generation and evolution of langmuir circulations. *Journal of Fluid Mechanics*, 364:31–58, 1998.

[124] A. Michelson. *Studies in Optics*. University of Chicago Press, 1927.

[125] S. J. Miller, O. H. Shemdin, and M. S. Longuet-Higgins. Laboratory measurements of modulation of short-wave slopes by long surface waves. *Journal of Fluid Mechanics*, 233: 389–404, 1991.

[126] F. W. Millet, K. F. Warnick, J. R. Nagel, and D. V. Arnold. Physical Optics-Based Electromagnetic Bias Theory With Surface Height Slope Cross-Correlation and Hydrodynamic Modulation. *IEEE Transactions on Geoscience and Remote Sensing*, 44:1470–1483, June 2006.

[127] T. Naegler, P. Ciais, K. Rodgers, and I. Levin. Excess radiocarbon constraints on air-sea gas exchange and the uptake of CO_2 by the oceans. *Geophysical Research Letters*, 33(11): L11802, 2006.

[128] F. O'Sullivan, J. Huang, K. R. Choudhury, G. Caulliez, and V. Shrira. Regularized reconstruction of water surfaces from noisy gradient information via plane-wave superposition. *Inverse Problems*, 24(3):034016 (21pp), 2008.

[129] J. Pedolsky. *Waves in the Ocean and Atmosphere*. Springer, 2003.

[130] O. Phillips. Spectral and statistical properties of the equilibrium range in wind-generated gravity waves. *Journal of Fluid Mechanics*, 4:426–434, 1985.

[131] O. M. Phillips. The equilibrium range in the spectrum of wind-generated waves. *Journal of Fluid Mechanics*, 156:505–531, 1958.

[132] O. M. Phillips. *The dynamics of the upper ocean*. Cambridge University Press, 1969.

[133] O. M. Phillips. The dispersion of short wavelets in the presence of a dominant long wave. *Journal of Fluid Mechanics*, 107:465–485, 1981.

[134] W. R. C. Phillips. Langmuir circulations beneath growing or decaying surface waves. *Journal of Fluid Mechanics*, 469:317–342, 2002.

[135] W. J. Pierson and L. Moskowitz. A proposed spectral form for fully developed wind seas based on the similarity theory of S. A. Kitaigorodskii. *Journal of Geophysical Research*, 69:5181, Dec. 1964.

[136] W. J. J. Pierson and R. A. Stacy. The elevation, slope, and curvature spectra of a wind roughened sea surface. Technical report, School of Engineering and Science New York University University Heights, 1973.

[137] W. J. Plant. A relationship between wind stress and wave slope. *Journal of Geophysical Research*, 87(C3):1961–1967, March 20 1982.

[138] W. J. Plant and J. W. Wright. Phase speeds of upwind and downwind traveling short gravity waves. *Journal of Geophysical Research*, 85:3304–3310, 1980.

[139] J. A. Polton and S. E. Belcher. Langmuir turbulence and deeply penetrating jets in an unstratified mixed layer. *Journal of Geophysical Research (Oceans)*, 112:C09020 – 1–11, Sept. 2007.

[140] K. Richter. Bestimmung des Schmidtzahlexponenten und Transferraten für die WiSSCy-2007 Multi-Tracer Experimente. Technical report, Institut für Umweltphysik, Universität Heidelberg, 2008. in preparation.

[141] K. Riemer. *Analyse von Wasseroberflächenwellen im Orts-Wellenzahl-Raum*. Doktorarbeit, Univ. Heidelberg, 1991.

[142] R. Rocholz. Bildgebendes System zur simultanen Neigungs- und Höhenmessung an kleinskaligen Wind-Wasserwellen. Diploma thesis, University of Heidelberg, 2005.

[143] R. Rocholz. WiSSCy Messkampagne in Hamburg, Mai bis Juli 2007 - Kalibrierung der Color Imaging Slope Gauge & Auswertung der Wellenmessungen. Technical report, Institut für Umweltphysik, Universität Heidelberg, 2007.

[144] R. Romeiser, W. Alpers, and V. Wismann. An improved composite surface model for the radar backscattering cross section of the ocean surface. 1. theory of the model and optimization/validation by scatterometer data. *Journal of Geophysical Research*, 102(25): 25237–25250, 1997.

[145] J. Saylor. The role of capillary waves in oceanic air/water gas exchange. *Tellus B*, 51(3): 616–628, 1999.

[146] H. Scharr. Optimale Interpolation von Farbbildern mit Bayer-Muster. Technical report, Interdisziplinäres Zentrum für Wissenschaftliches Rechnen, Ruprecht-Karls-Universität Heidelberg, Germany, 2000.

[147] U. Schimpf. *Untersuchung des Gasaustausches und der Mikroturbulenz an der Meeresoberfläche mittels Thermographie*. PhD thesis, University of Heidelberg, Heidelberg, Germany, 2000.

[148] U. Schimpf, C. Garbe, and B. Jähne. Investigation of transport processes across the sea surface microlayer by infrared imagery. *Journal of Geophysical Research-Oceans*, 109 (C8):C08S13, 2004.

[149] J. Seemann. *Interpretation der Struktur des Wellenzahl-Frequenzspektrums von Radar-Bildsequenzen des Seegangs*. PhD thesis, Universität Hamburg, 1997.

[150] C. M. Senet, J. Seemann, and F. Ziemer. The near-surface current velocity determined from image sequences of the sea surface. *IEEE Transactions On Geoscience And Remote Sensing*, 39, 3:492 – 505, 2001.

[151] M. H. K. Siddiqui, M. R. Loewen, C. Richardson, W. Asher, and A. T. Jessup. Turbulence generated by microscale breaking waves and its influence on air-water gas transfer. *Geophysical Monograph 127, American Geophysical Union*, pages 11–16, 2002.

[152] R. W. Stewart. The air-sea momentum exchange. *Boundary-Layer Meteorology*, 6:151–167, 1974.

[153] G. G. Stokes. On the theory of oscillatory waves. *Trans. Camb. Philos. Soc.*, 8:441, 1847.

[154] G. G. Stokes. On the theories of the internal friction of fluids in motion, and of the equilibrium and motion of elastic solids. *Transactions of the Cambridge Philosophical Society*, 9 (II):8–106, 1849.

[155] S. Stolte. *Modulation des Kurzwelligen Seegands durch langwelligen Seegang und Wind: experimentelle Untersuchung zur Energiebilanz des kurzwelligen Seegangs und seiner Radar - Rückstreueigenschaften*. PhD thesis, Universität Hamburg, 1984.

[156] N. Takagaki and S. Komori. Effects of rainfall on mass transfer across the air-water interface. *Journal of geophysical Research*, 112:C06006, 2007.

[157] B. Tamburic. Measurement of the modulation transfer function through the use of regional circular targets. Master's thesis, Imperial College London, 2006.

[158] M. A. C. Teixeira and S. E. Belcher. On the distortion of turbulence by a progressive surface wave. *Journal of Fluid Mechanics*, 458:229–267, May 2002.

[159] A. Trukenmüller. Einflüsse von Viskosität u. Oberflächenspannung auf winderzeugte Wasseroberflächenwellen. Master's thesis, University of Heidelberg, 1989.

[160] W. Tsai and L. Hung. Three-dimensional modeling of small-scale processes in the upper boundary layer bounded by a dynamic ocean surface. *Journal of Geophysical Research*, 112:C02019, 2007.

[161] B. M. Uz. *Gravity-capillary waves and their influence on air-sea interaction under non-stationary conditions*. PhD thesis, University of Rhode Island, 1999.

[162] B. M. Uz, M. A. Donelan, T. Hara, and E. J. Bock. Laboratory studies of wind stress over surface waves. *Boundary-Layer Meteorology*, 102(2):301–331, 2002.

[163] M. Uz, T. Hara, E. Bock, and M. Donega. Laboratory observations of gravity-capillary waves under transient wind forcing. *Journal of Geophysical Research*, 108(C2):3050, 2003.

[164] K. van Gastel, P. A. E. M. Janssen, and G. J. Komen. On phase velocity and growth rate of wind-induced gravity-capillary waves. *Journal of Fluid Mechanics*, 161:199–216, Dec. 1985.

[165] F. Veron and W. K. Melville. Experiments on the stability and transition of wind-driven water surfaces. *Journal of Fluid Mechanics*, 446:25–65, 2001.

[166] F. Veron, W. K. Melville, and L. Lenain. Infrared techniques for measuring ocean surface processes. *Journal of Atmopheric and Oceanic Technology*, 25:307–326, 2008.

[167] F. Veron, W. K. Melville, and L. Lenain. Wave-coherent air-sea heat flux. *Journal of Physical Oceanography*, 38(4):788–802, 2008.

[168] R. Wanninkhof. Relationship between wind speed and gas exchange over the ocean. *J. Geophys. Res.*, 97:7373–7382, 1992.

[169] R. Wanninkhof and W. R. McGillis. A cubic relationship between gas transfer and wind speed. *Geophysical Research Letters*, 26:1889–1892, 1999.

[170] H. Weiss. Modulation von Windwellen. Diploma thesis, Universität Heidelberg, 1997.

[171] J. W. Wright and W. C. Keller. Dopller spectra in microwave scattering from wind waves. *Phys. Fluids*, 14:466, 1971.

[172] Z. Yang, S. Tang, and J. Wu. An experimental study of rain effects on fine structure of wind wave. *J. Phys. Oceanogr.*, 27:419–430, 1997.

[173] A. Yarin. Drop impact dynamics: Splashing, spreading, receding, bouncing... *Annual Review of Fluid Mechanics*, 38:159–192, January 2006.

[174] I. Young, W. Rosenthal, and F. Ziemer. A three-dimensional analysis of marine radar images for the determination of ocean wave directionally and surface currents. *Journal of Geophysical Research*, 90(C1):0148–0227, 1985. ist gescannt.

[175] C. J. Zappa, W. E. Asher, and A. T. Jessup. Microscale wave breaking and air-water gas transfer. *Journal of Geophysical Research-Oceans*, 106(C5):9385–9391, 2001.

[176] C. J. Zappa, W. E. Asher, A. T. Jessup, J. Klinke, and S. R. Long. Microbreaking and the enhancement of air-water transfer velocity. *Journal of geophysical Research*, 109:C08S16, 2004.

[177] X. Zhang. Capillary-gravity and capillary waves generated in a wind wave tank: Observations and theories. *Journal of Fluid Mechanics*, 189:51–82, 1995.

[178] X. Zhang. An algorithm for calculating water surface elevations from surface gradient. *Experiments in Fluids*, 21:43–48, 1996.

[179] X. Zhang. Surface image velocimetry for measuring short wind wave kinematics. *Exp Fluids*, 35:653–665, 2003.

[180] X. Zhang. Short surface waves on surface shear. *J. Fluid Mech.*, 541:345–370, 2005.

[181] X. Zhang and C. S. Cox. Measuring the two-dimensional structure of a wavy water surface optically: A surface gradient detector. *Experiments in Fluids*, 17:225–237, Aug. 1994.

[182] X. Zhang, J. Klinke, and B. Jähne. Study of advection of short wind wave by long wave from surface slope images. In *Proc. of the Symposium on the Wind-Driven Air-Sea Interface*, pages 93–97, Sydney, Australia, 1999.

A. Appendix

A.1. 2D Saturation Spectra for Wind&Rain&Slick Conditions

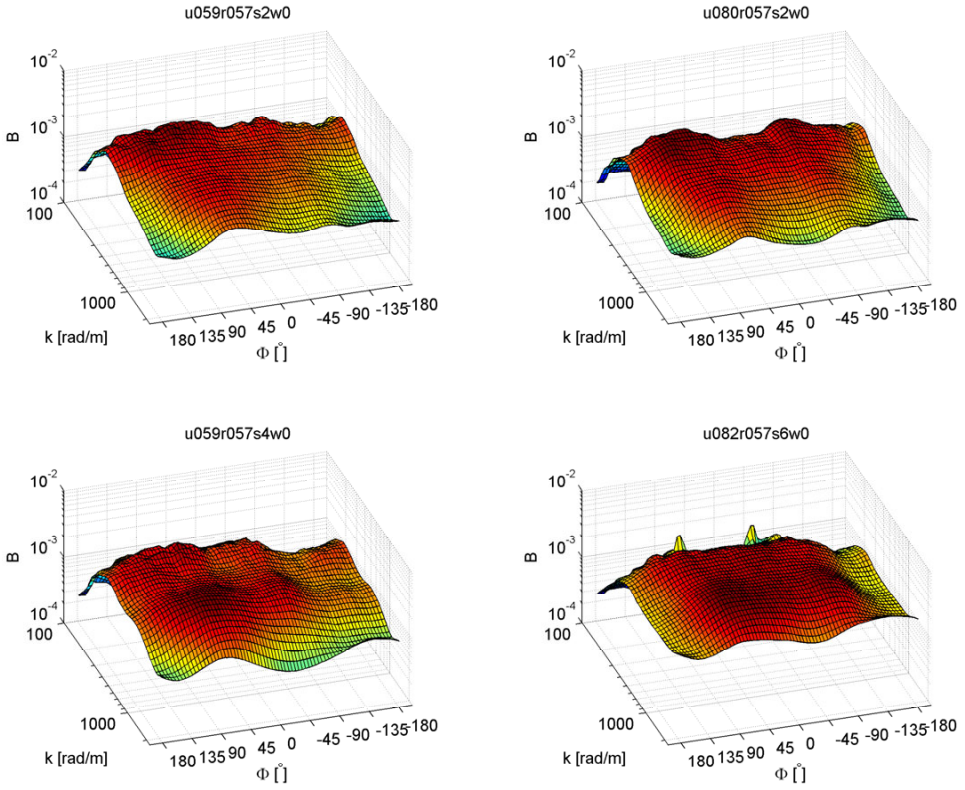

Figure A.1.: Twosided and MTF corrected saturation spectra with surface slicks and rain. Slick type as coded in table A.6.

A.2. Related Wave Measurements

Facility	Image size [m]	resolution [mm]	k range [rad/m]	Reference
Marseille	0.309–0.234	0.61–0.97	98-3225	Klinke 1996
Delft	0.664–0.473	1.30—1.85	52-1701	Jahne and Riemer 1990
Delft	0.165–0.144	0.32–0.56	170—5592	Klinke 1996
Heidelberg	0.180–0.140	0.35–0.58	164–5389	Klinke 1991, 1996
1996 Martha's Vineyard 30m offshore, Nov 92	0.10–0.10 (square scan pattern)	-	31-990	Hara et al. 1994
MBL West Coast, Exp., May 3 1995	0.192-0.151	0.30–0.63	152-4993	Klinke and Jahne 1995; Klinke 1996
MBL West Coast, Exp., May 3 1995	0.10–0.04 eight line scan	2.0—5.0	60—1500	Hwang et al. 1996
Hamburg	0.23-0.114	0.7	28–4500	this paper

Table A.1.: Spatial resolution for wave measurements, modified after [88].

A.3. Frequency Spectra

Frequency spectra have been computed according to equation 6.31 and are presented in section A.3.1 for completeness. Note, we did not incorporate a factor of two in order to compensate the one-sided nature of the frequency domain.

Since we have the combined spatial and temporal information it is also possible to compute frequency spectra for selected wavenumber ranges, e.g. the short gravity wave range and the capillary wave range, as exemplified in the sections A.3.2 and A.3.3. The wavenumber ranges are given in the figure titles.

The wavenumber of the dominant waves can be inferred from the frequency at the dominant peak, given the knowledge of the dispersion relation. For that the frequencies of the dominant peaks have been included in the legend of the figures in section A.3.2

A.3.1. Full Range

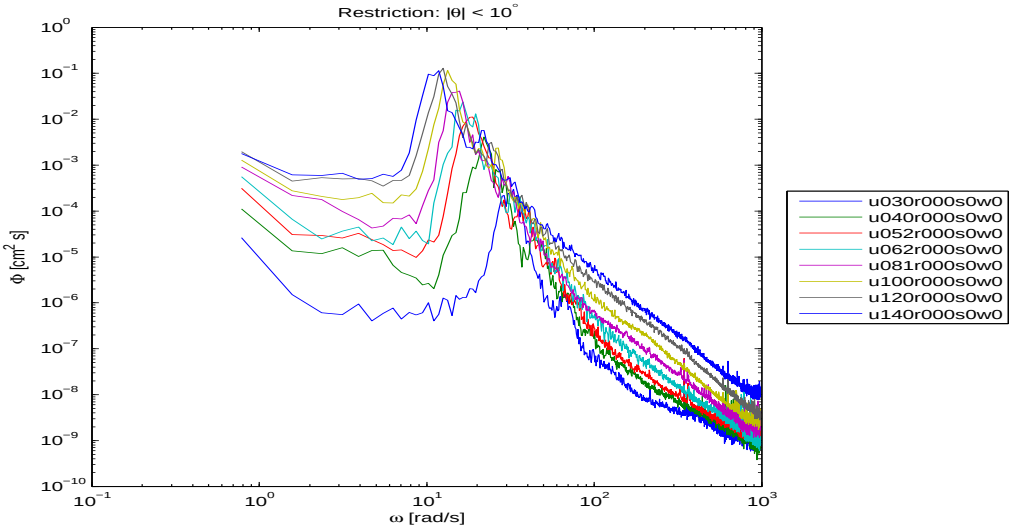

Figure A.2.: Frequency spectra, corresponding to figure 7.1

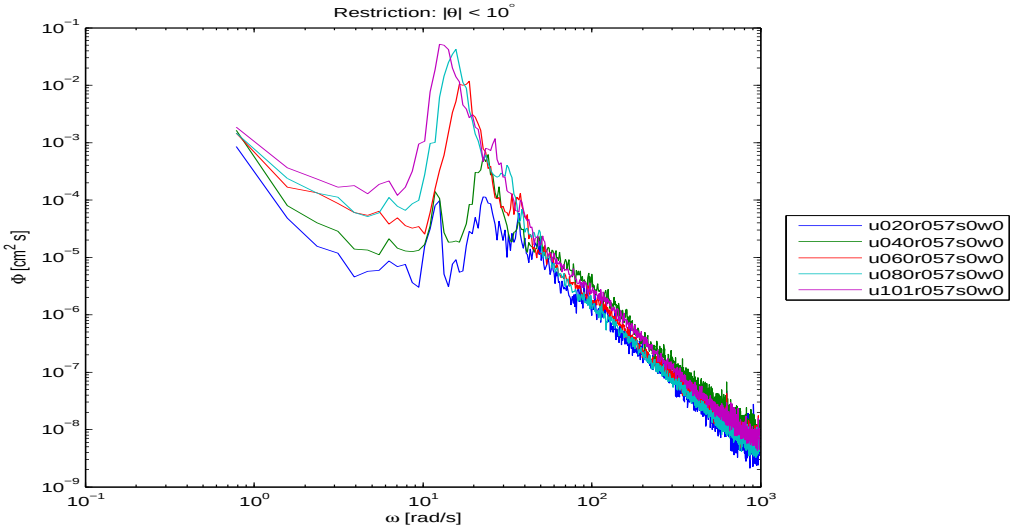

Figure A.3.: Frequency spectra, corresponding to figure 7.8

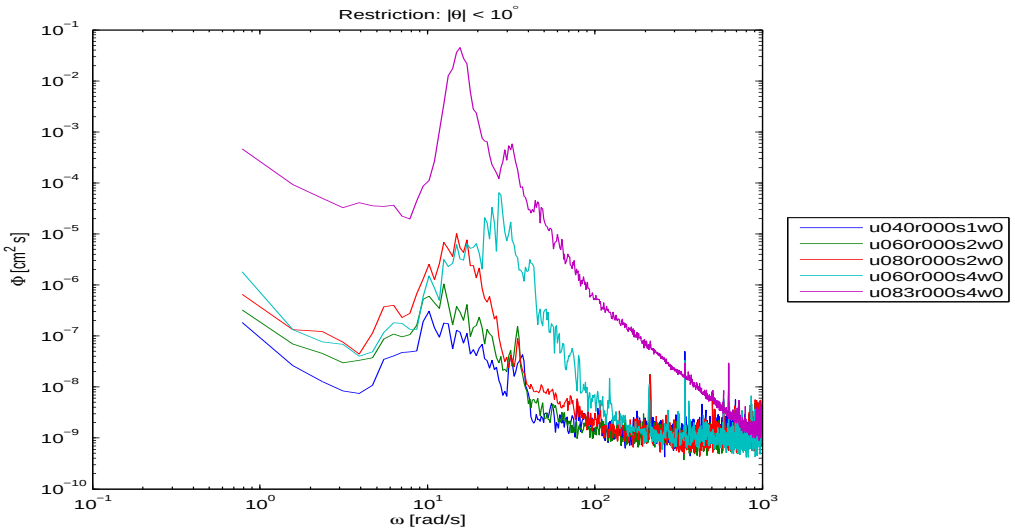

Figure A.4.: Frequency spectra, corresponding to figure 7.10

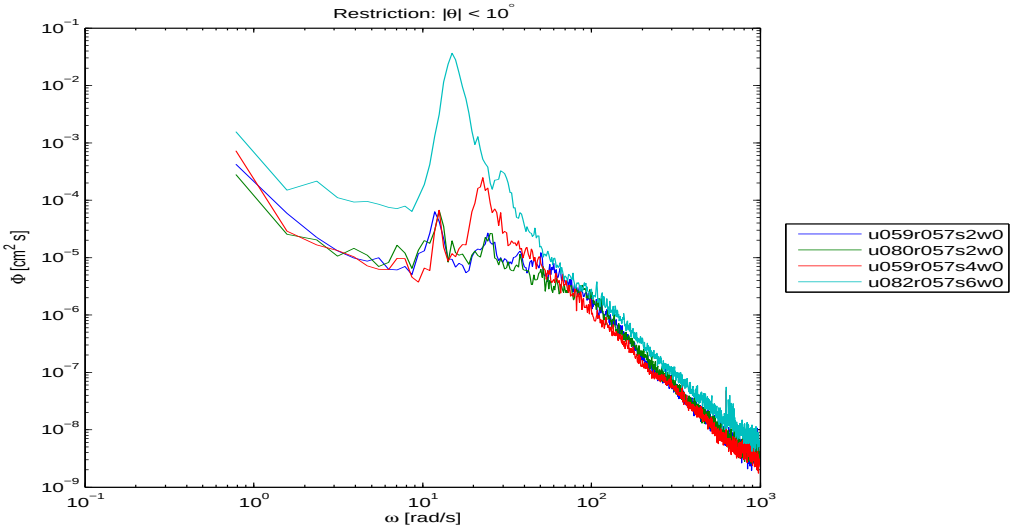

Figure A.5.: Frequency spectra, corresponding to figure A.1

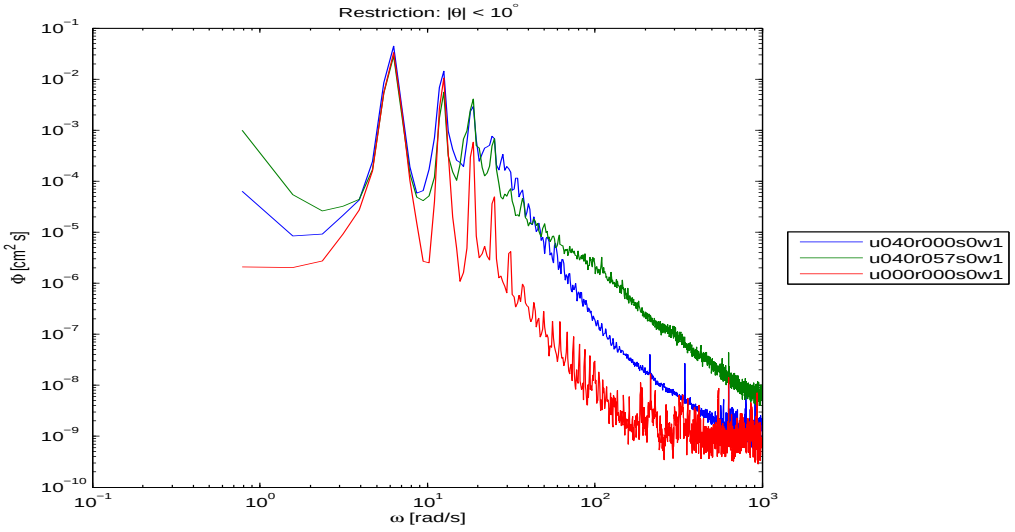

Figure A.6.: Frequency spectra, corresponding to figure 7.13

A.3.2. Short Gravity Wave Range

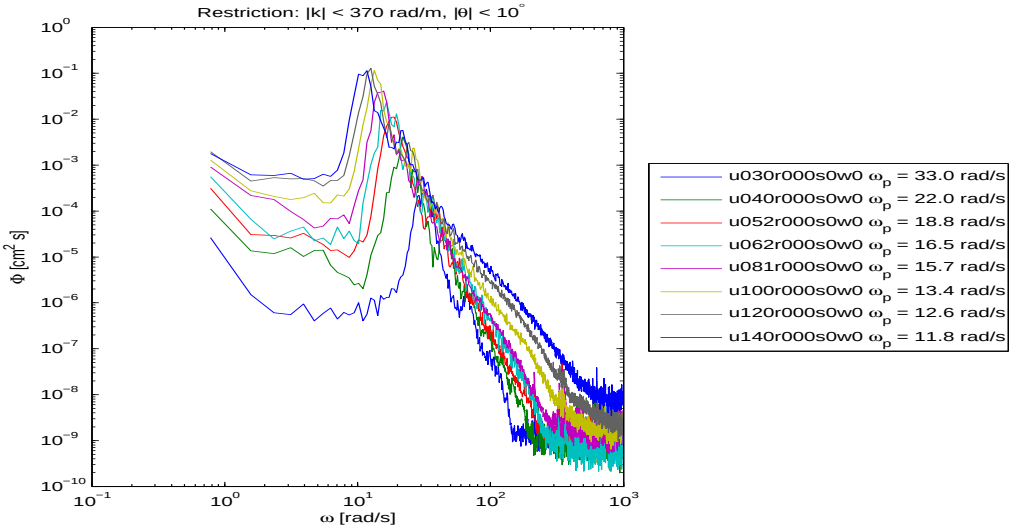

Figure A.7.: Frequency spectra for the short gravity wave range, corresponding to figure 7.1

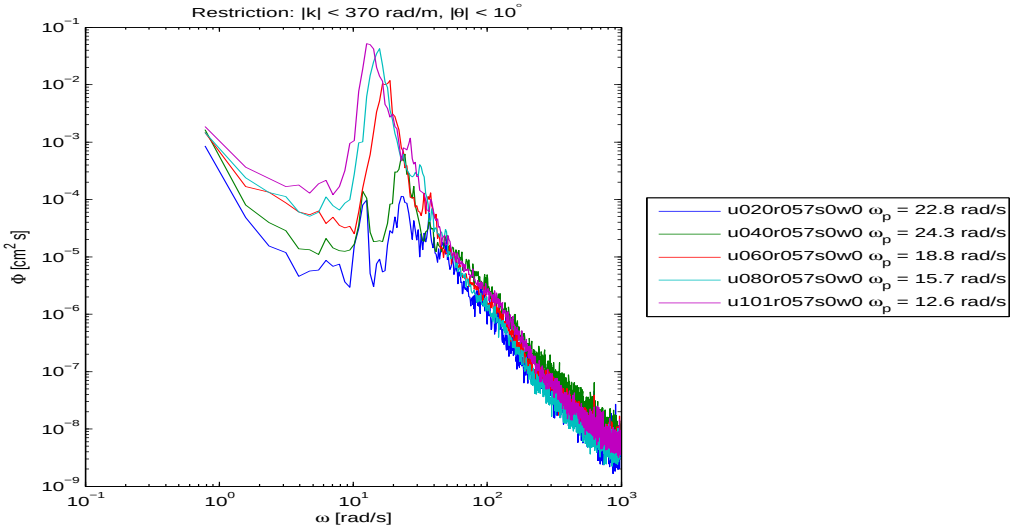

Figure A.8.: Frequency spectra for the short gravity wave range, corresponding to figure 7.8

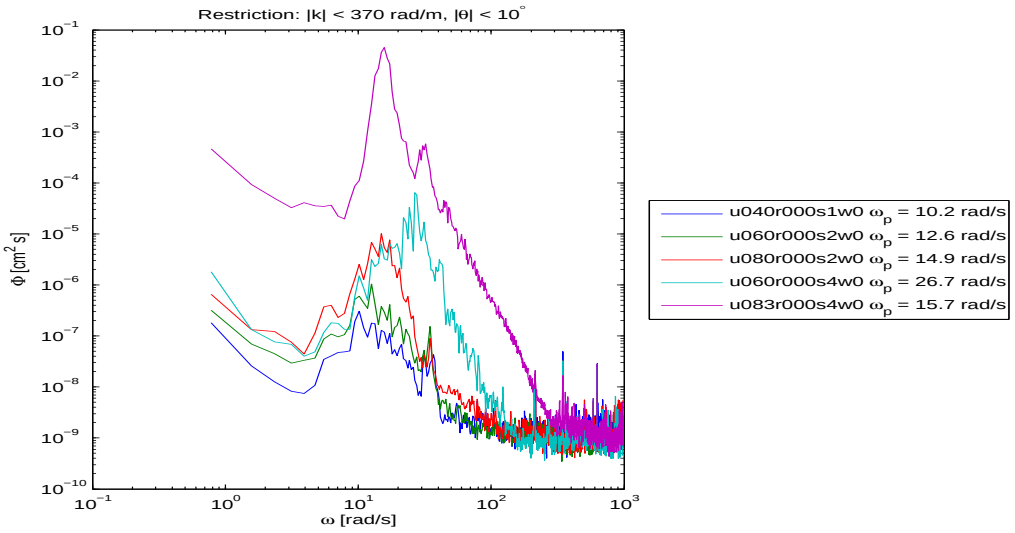

Figure A.9.: Frequency spectra for the short gravity wave range, corresponding to figure 7.10

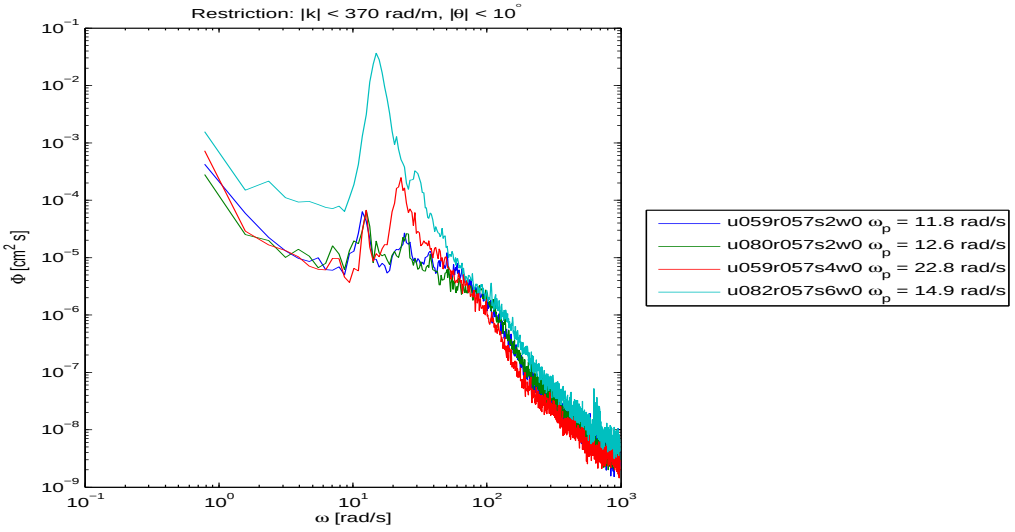

Figure A.10.: Frequency spectra for the short gravity wave range, corresponding to figure A.1

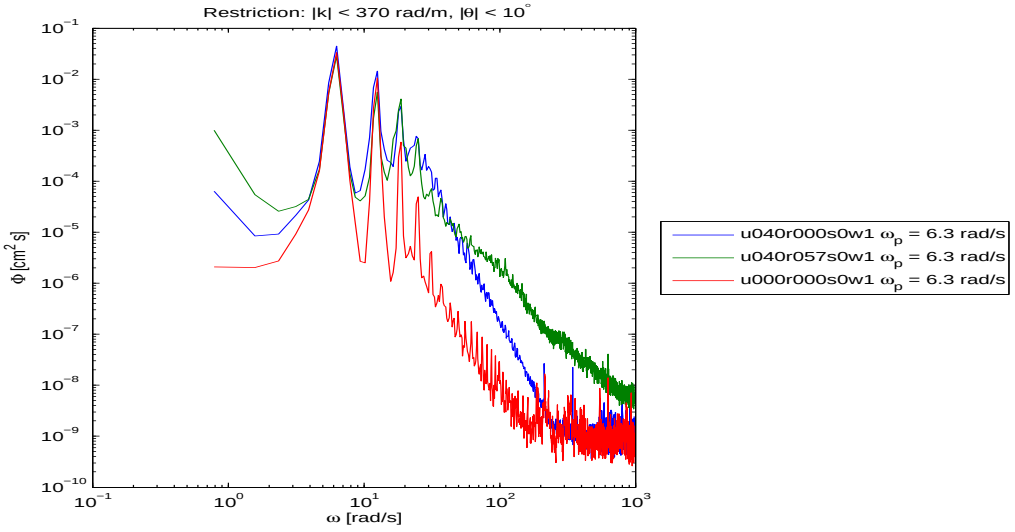

Figure A.11.: Frequency spectra for the short gravity wave range corresponding to figure 7.13

A.3.3. Capillary Wave Range

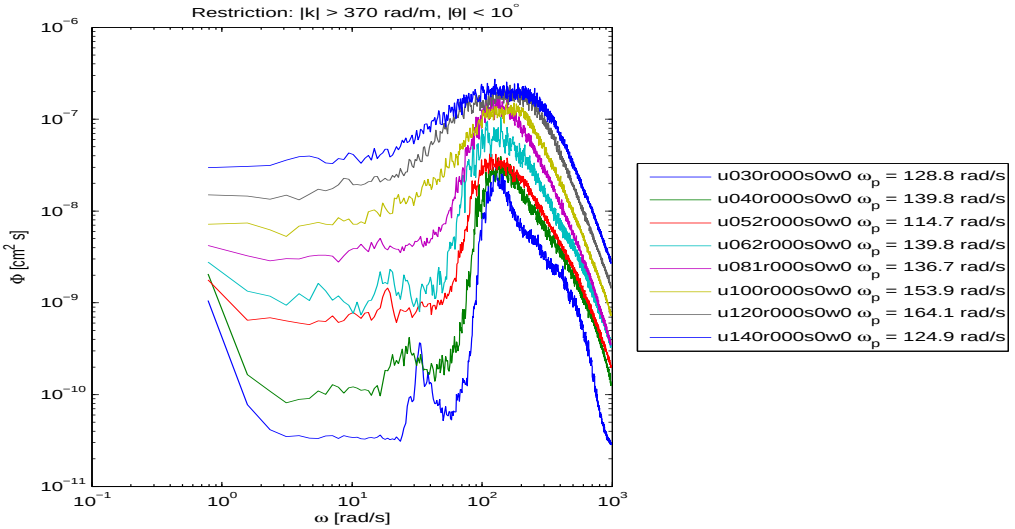

Figure A.12.: Frequency spectra for the capillary wave range, corresponding to figure 7.1

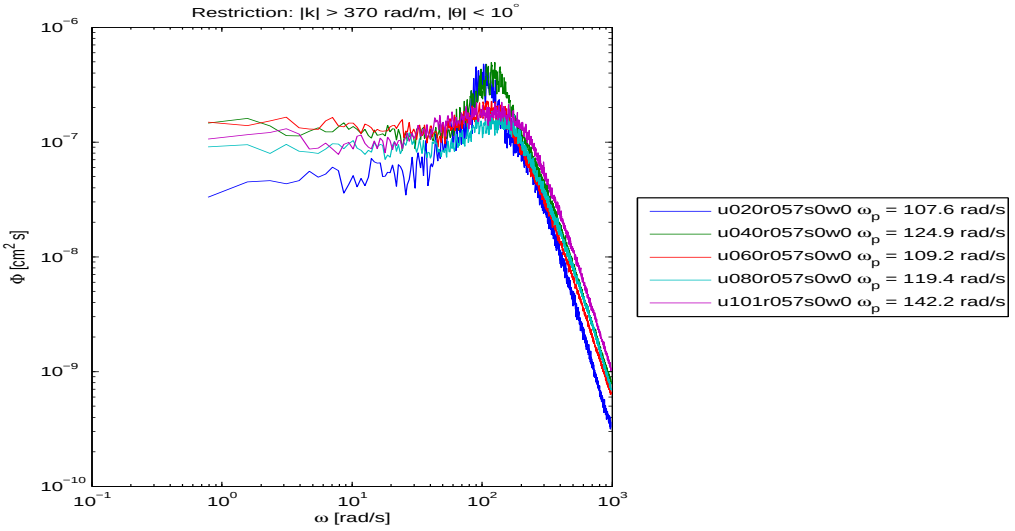

Figure A.13.: Frequency spectra for the capillary wave range corresponding to figure 7.8

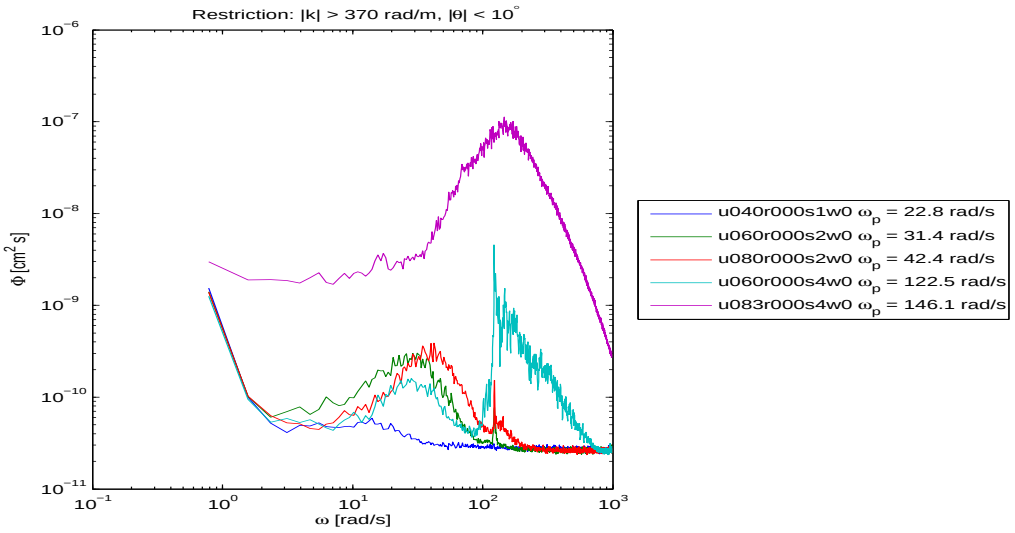

Figure A.14.: Frequency spectra for the capillary wave range corresponding to figure 7.10

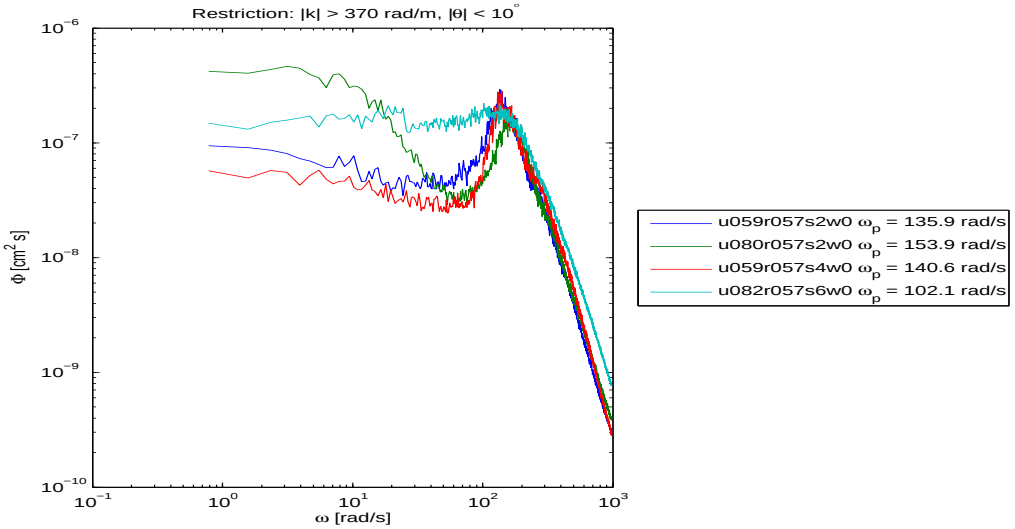

Figure A.15.: Frequency spectra for the capillary wave range corresponding to figure A.1

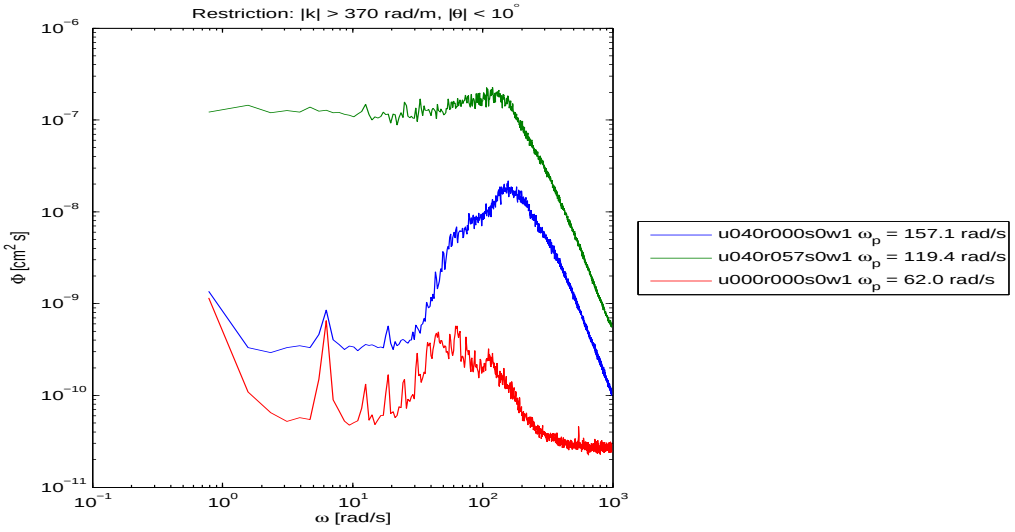

Figure A.16.: Frequency spectra for the capillary wave range corresponding to figure 7.13

A.4. Slices Through the Frequency Wavenumber Spectra

In section 7.3 the interpretation of the 3D spectral distribution was studied for one specific experimental condition. In the figures A.17 though A.42, the ω-k slices through the 3D power spectrum are shown for all other conditions. On page 104 you will find detailed informations for what is displayed. For the discussion please refer to section 7.3.

Each individual plot is accompanied by a title that can be read in terms of the experimental conditions, e.g. u062 stands for a reference windspeed of 6.2 m/s; r057 stands for a rain rate of 57 mm/h; s2 stands for slick type 2 (see table 8.3 for the slick type coding); w1 stands for a mechanical wave with a frequency of 1 Hz.

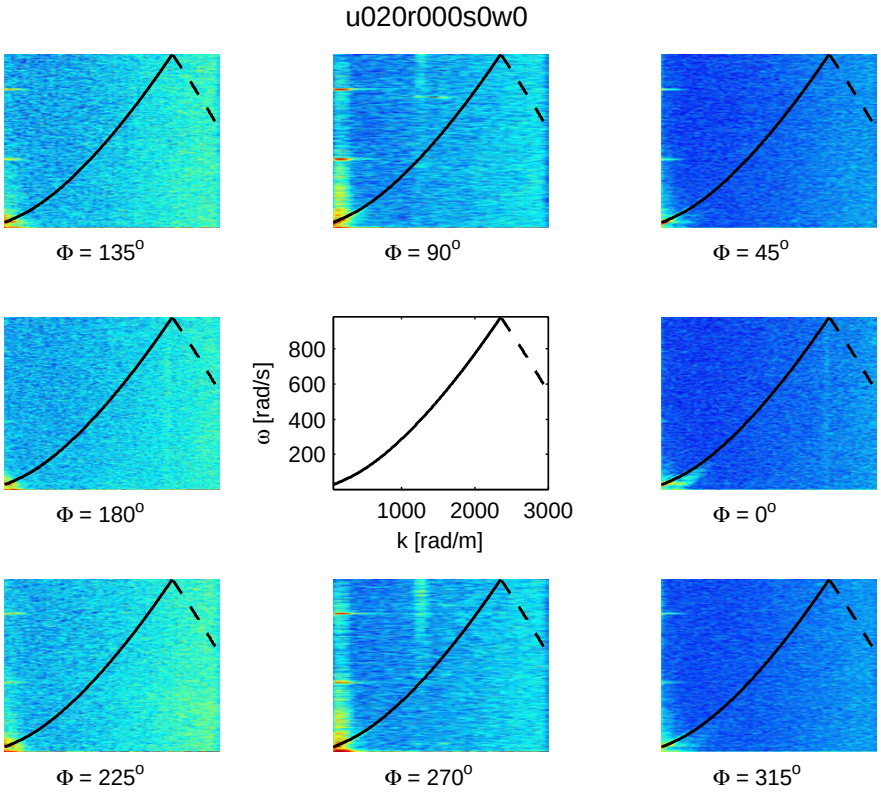

Figure A.17.: ω-k Slices through the 3D power spectrum

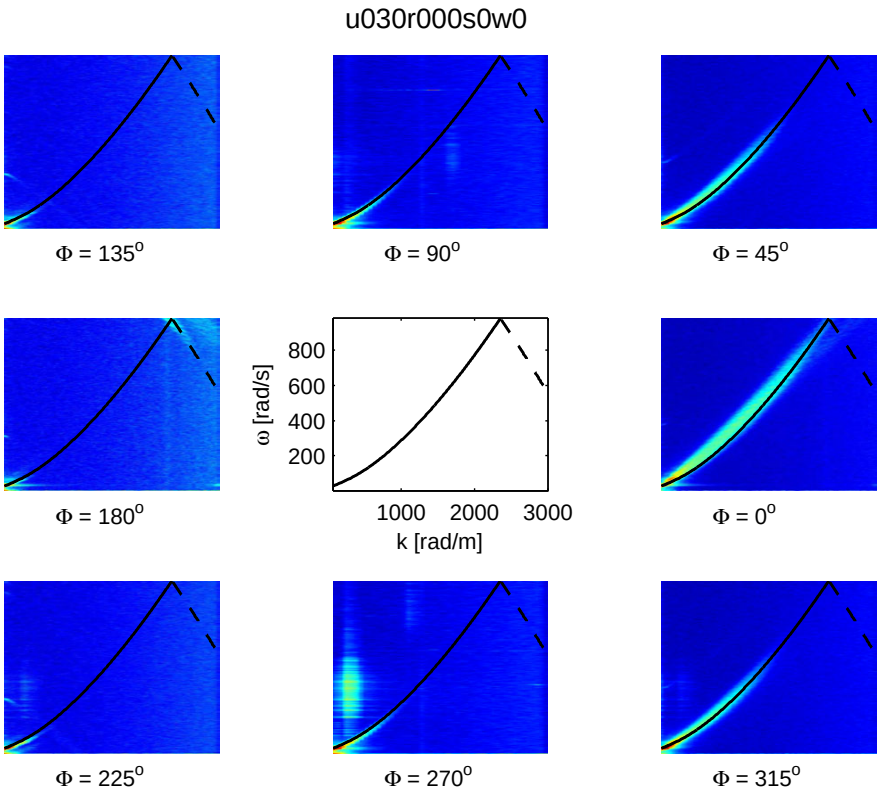

Figure A.18.: ω-k Slices through the 3D power spectrum

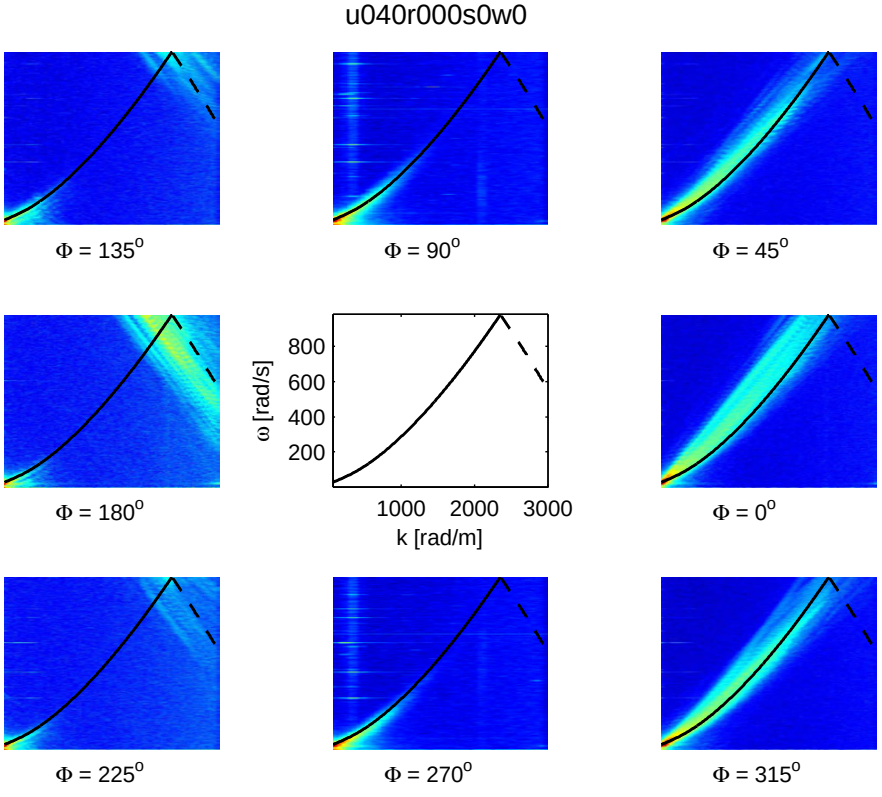

Figure A.19.: ω-k Slices through the 3D power spectrum

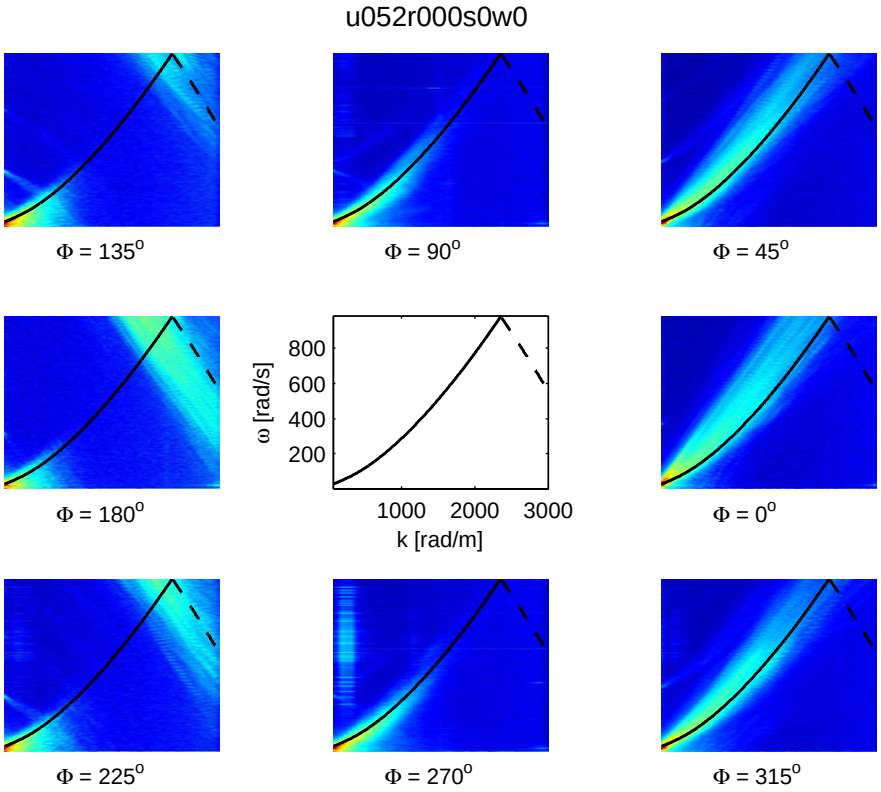

Figure A.20.: ω-k Slices through the 3D power spectrum

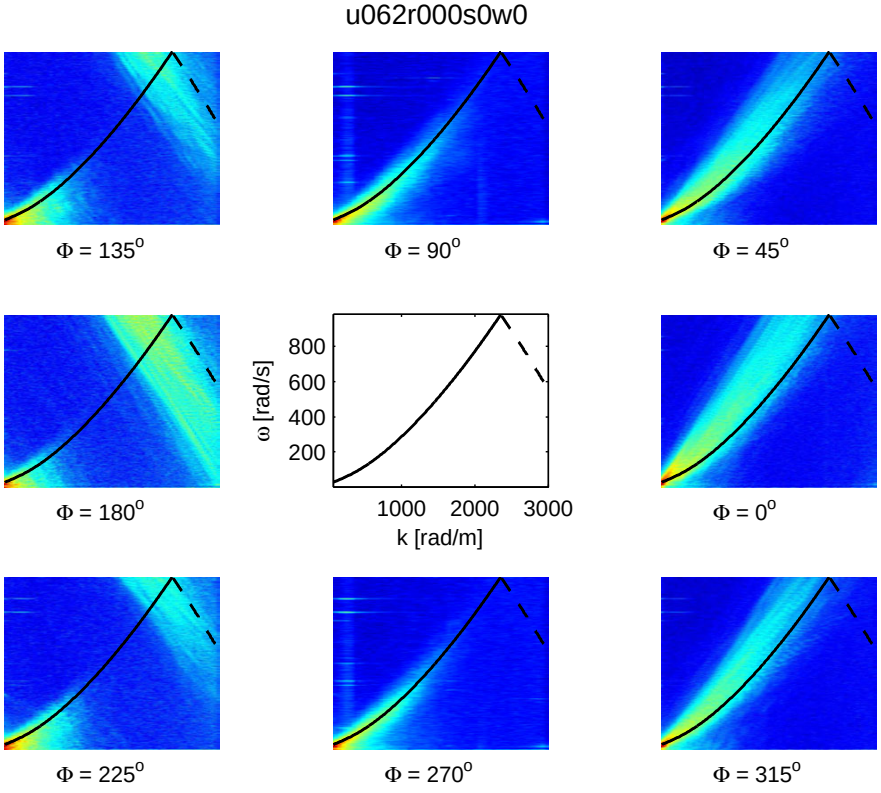

Figure A.21.: ω-k Slices through the 3D power spectrum

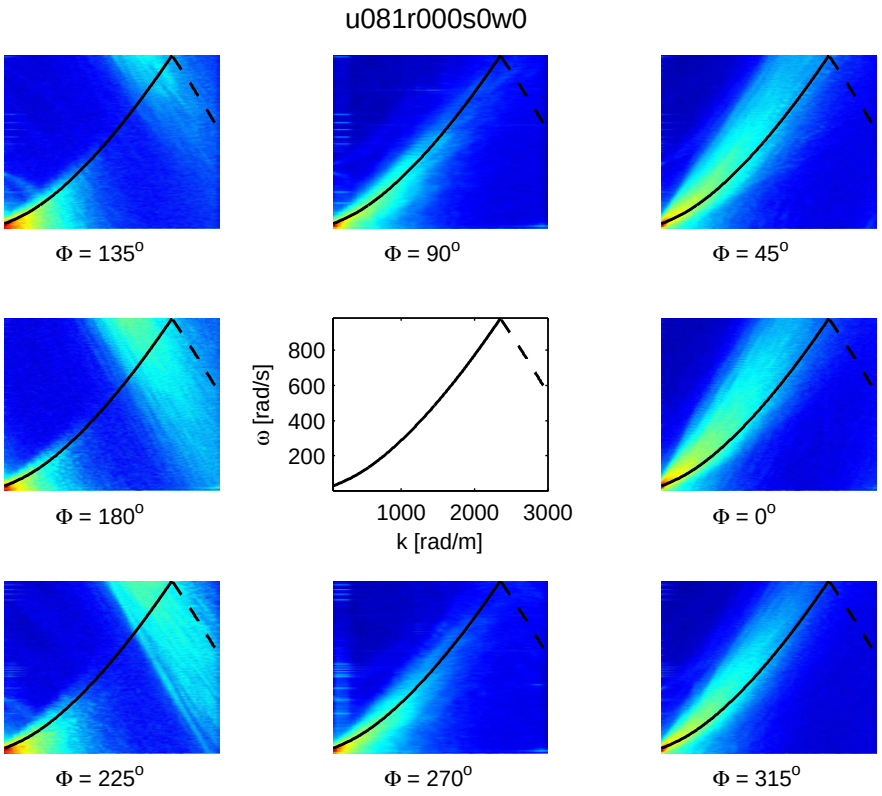

Figure A.22.: ω-k Slices through the 3D power spectrum

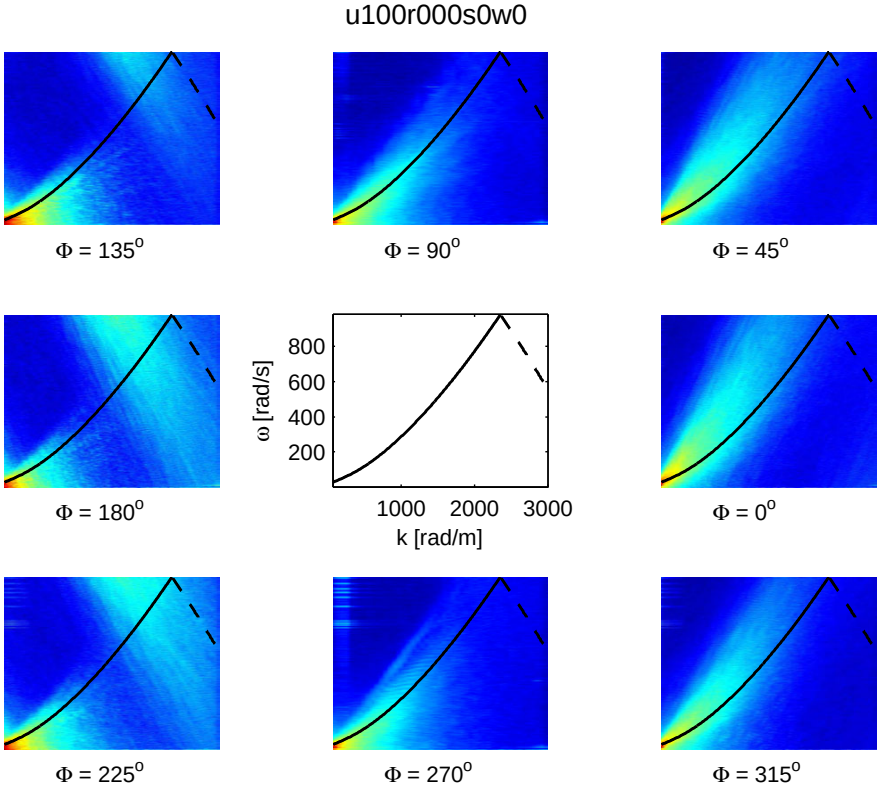

Figure A.23.: ω-k Slices through the 3D power spectrum

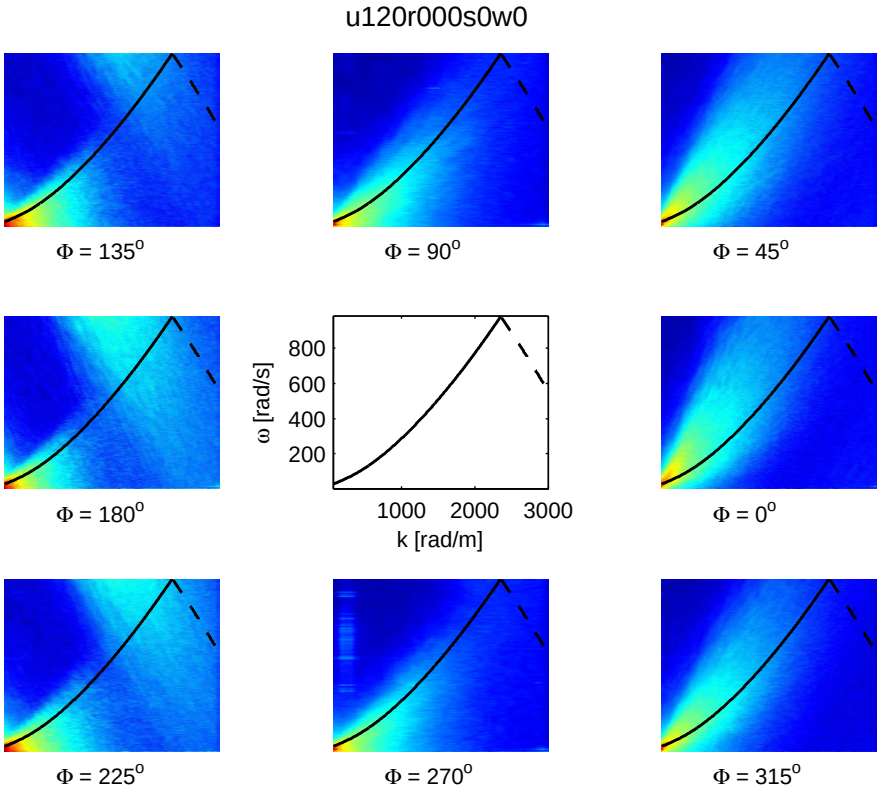

Figure A.24.: ω-k Slices through the 3D power spectrum

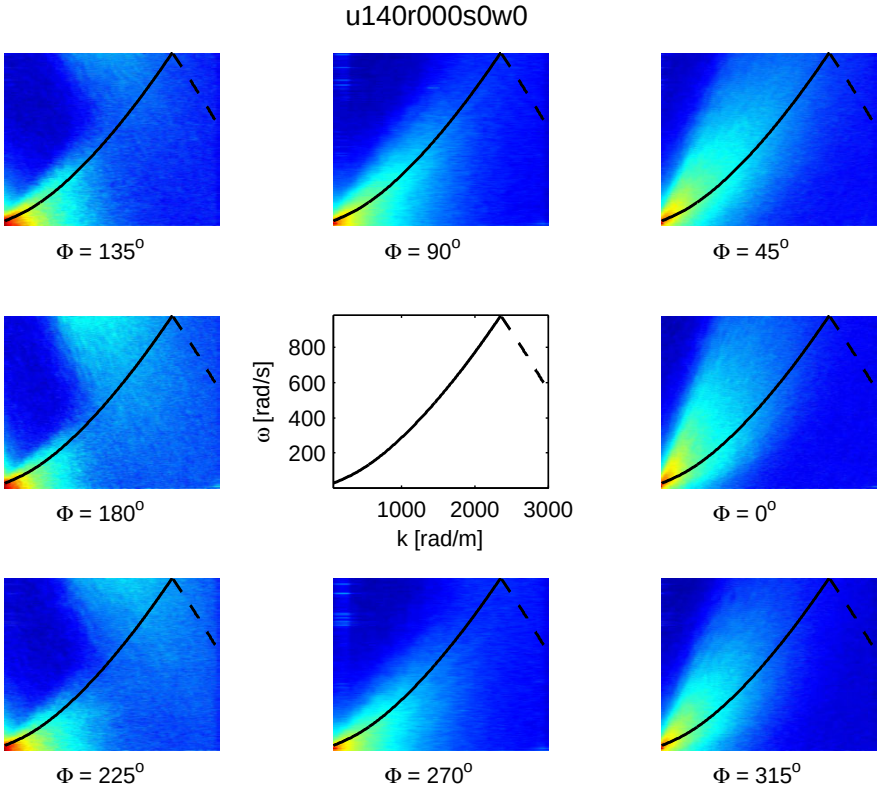

Figure A.25.: ω-k Slices through the 3D power spectrum

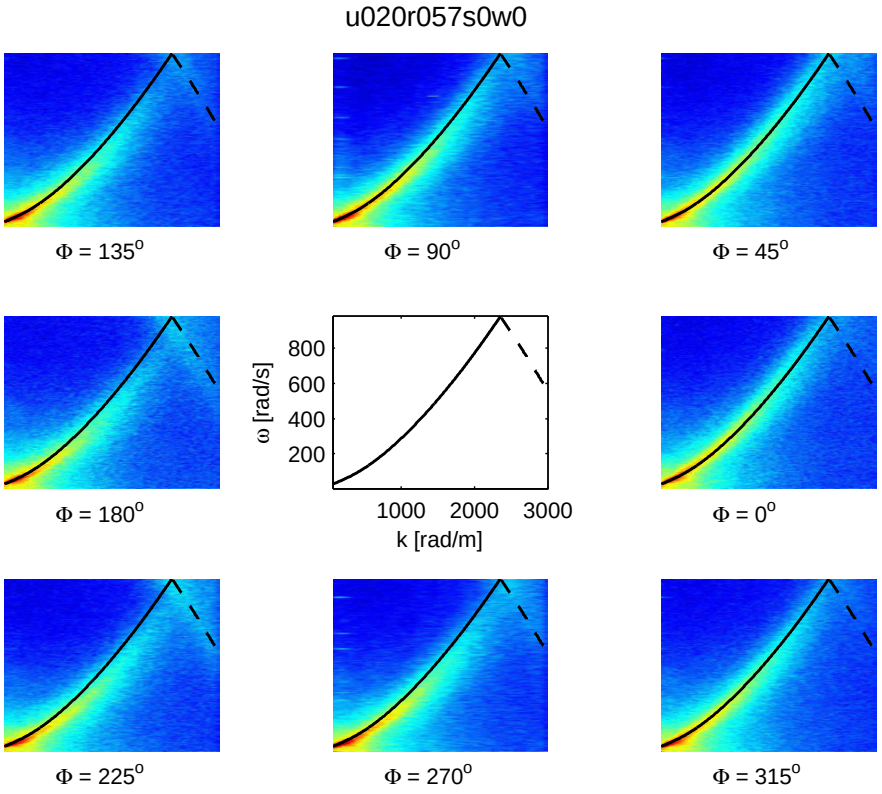

Figure A.26.: ω-k Slices through the 3D power spectrum

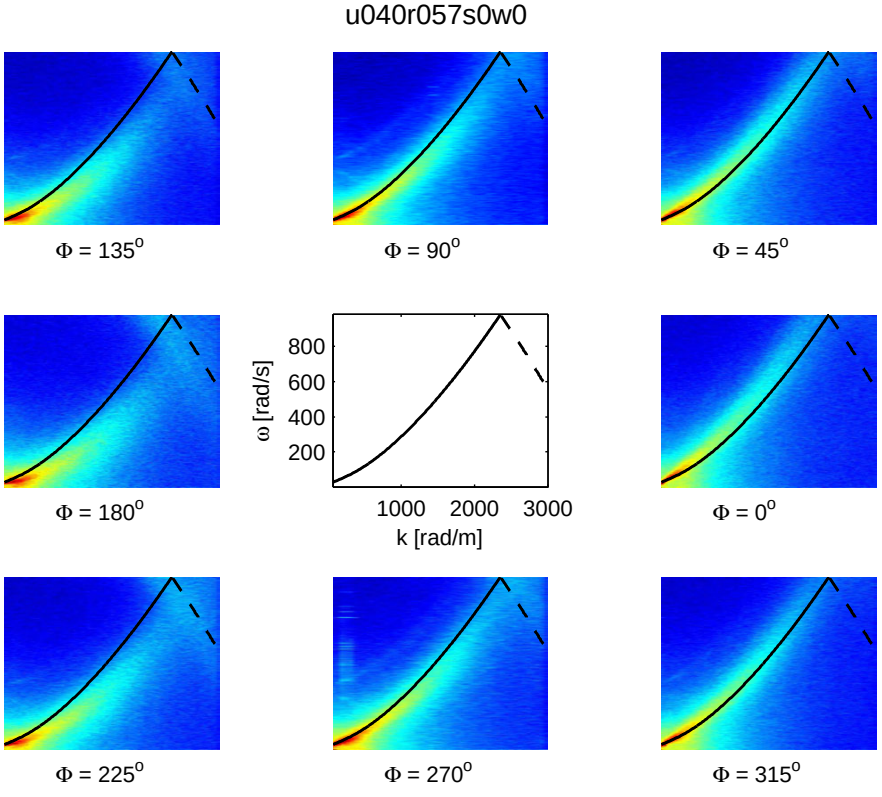

Figure A.27.: ω-k Slices through the 3D power spectrum

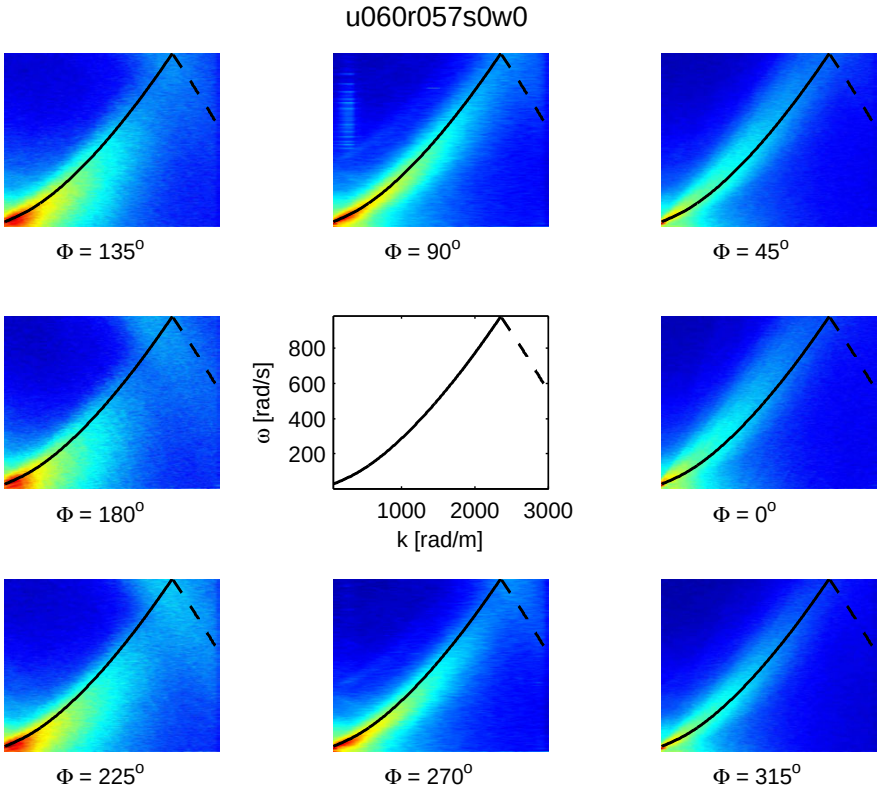

Figure A.28.: ω-k Slices through the 3D power spectrum

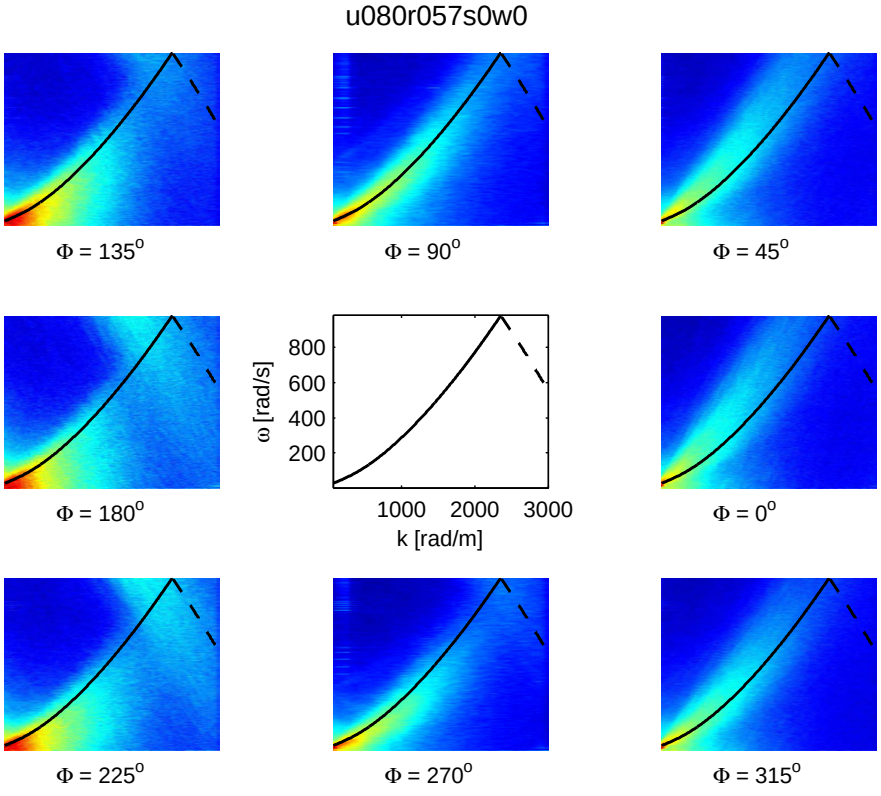

Figure A.29.: ω-k Slices through the 3D power spectrum

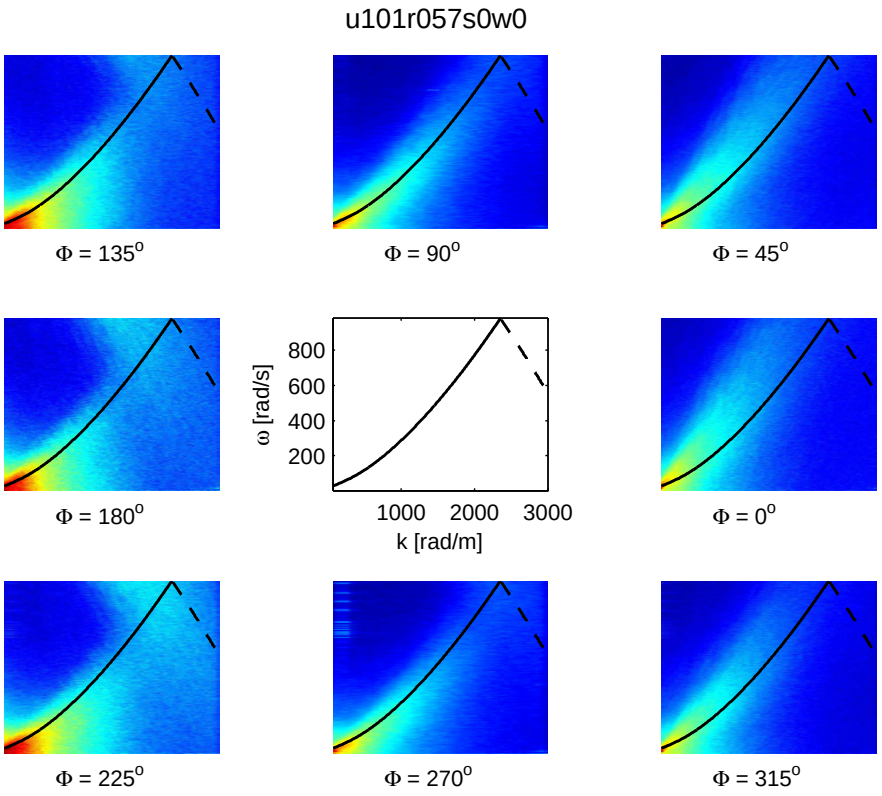

Figure A.30.: ω-k Slices through the 3D power spectrum

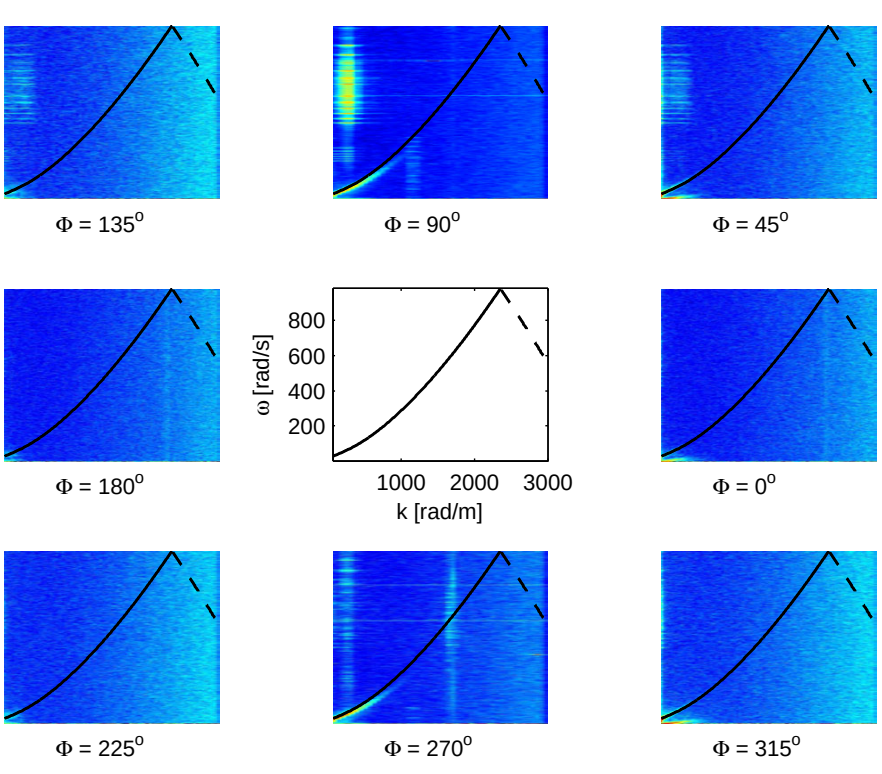

Figure A.31.: ω-k Slices through the 3D power spectrum

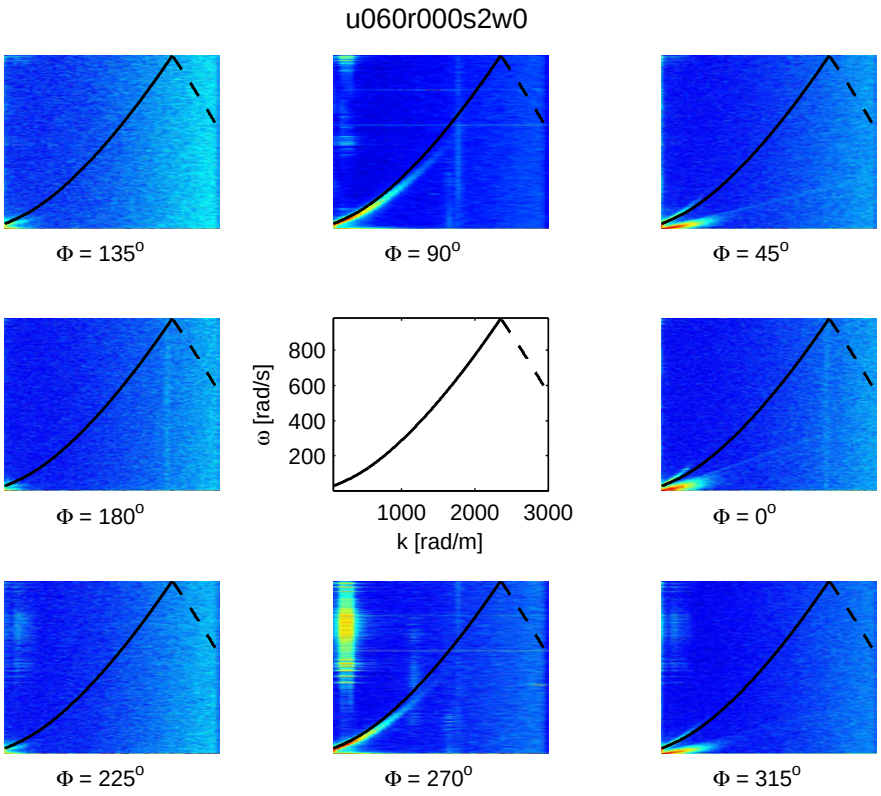

Figure A.32.: ω-k Slices through the 3D power spectrum

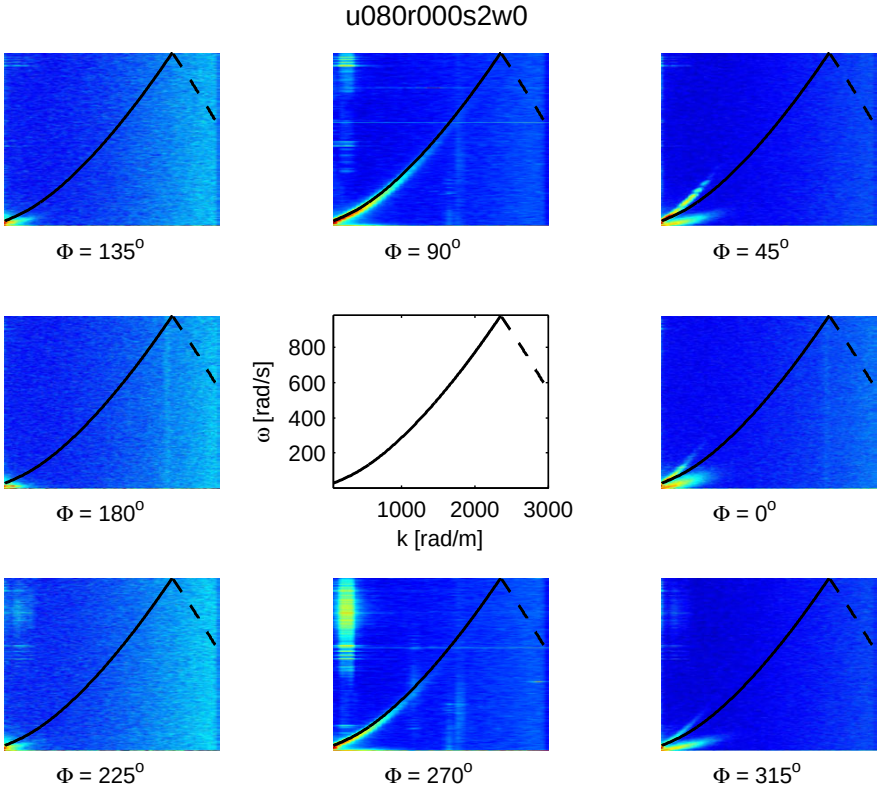

Figure A.33.: ω-k Slices through the 3D power spectrum

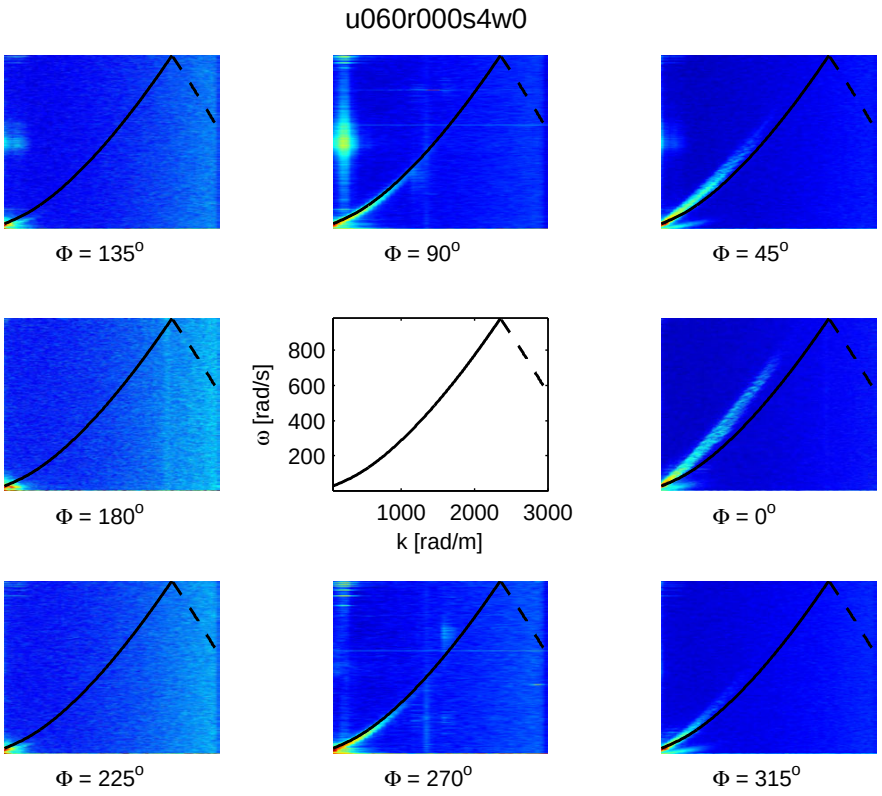

Figure A.34.: ω-k Slices through the 3D power spectrum

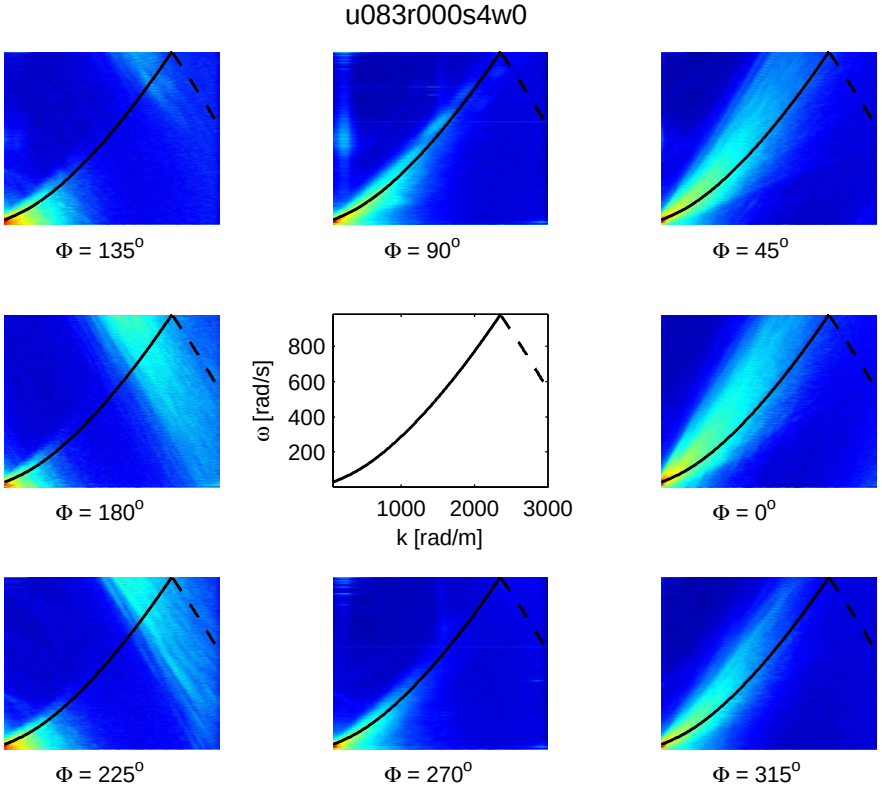

Figure A.35.: ω-k Slices through the 3D power spectrum

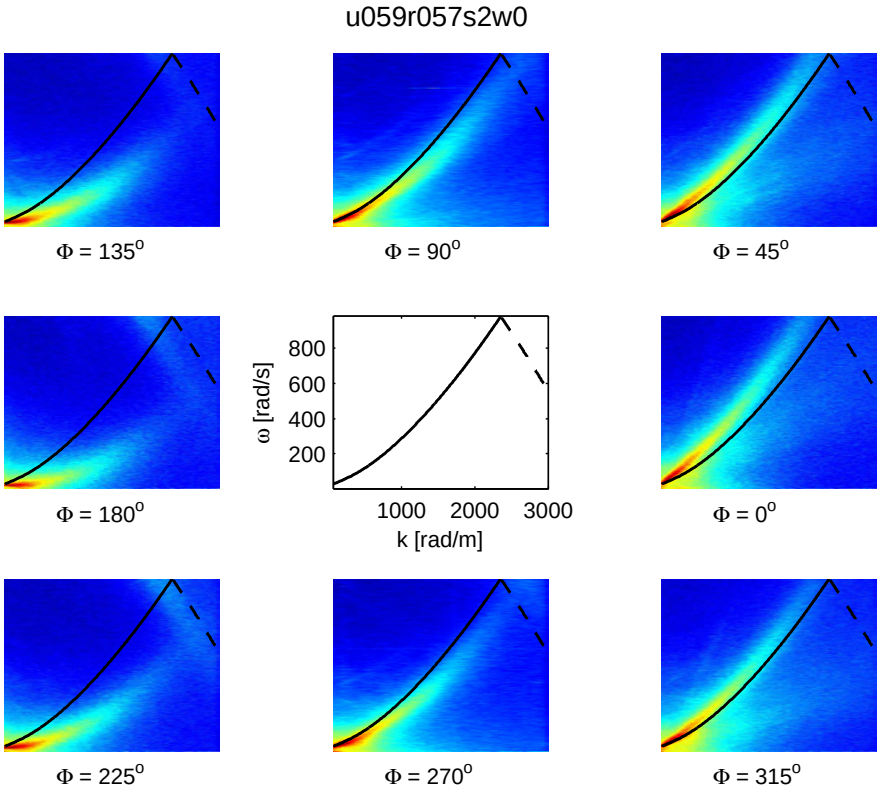

Figure A.36.: ω-k Slices through the 3D power spectrum

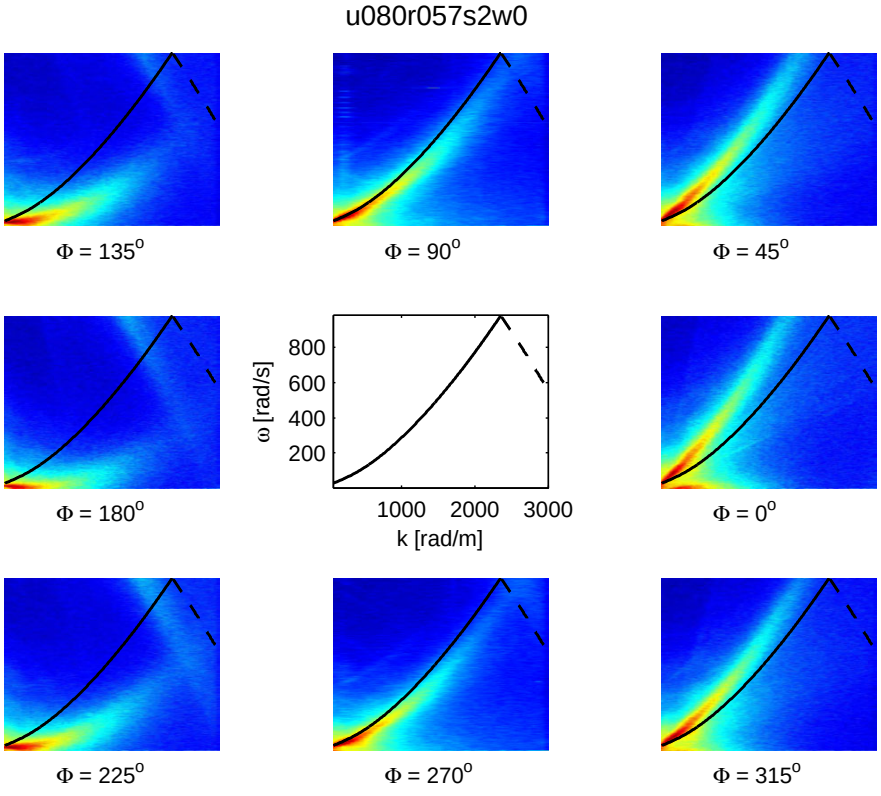

Figure A.37.: ω-k Slices through the 3D power spectrum

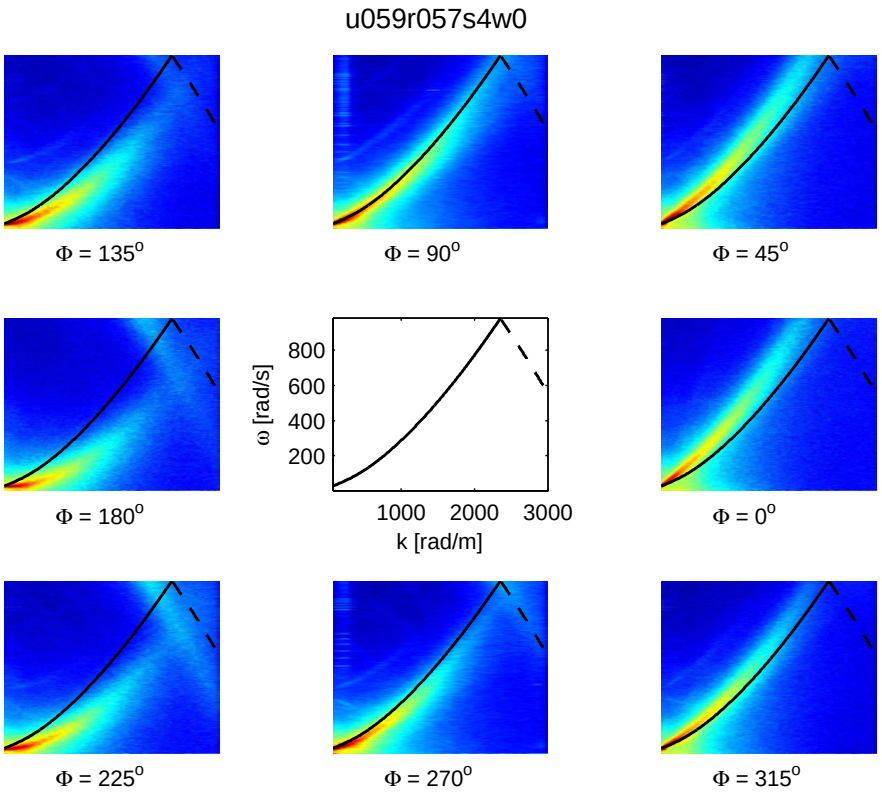

Figure A.38.: ω-k Slices through the 3D power spectrum

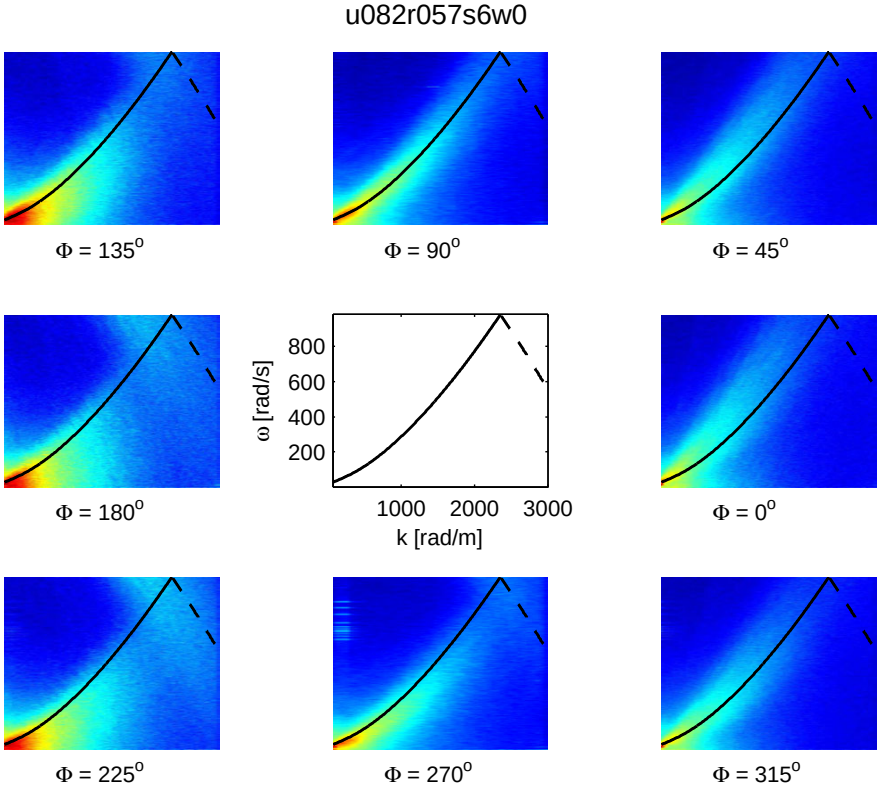

Figure A.39.: ω-k Slices through the 3D power spectrum

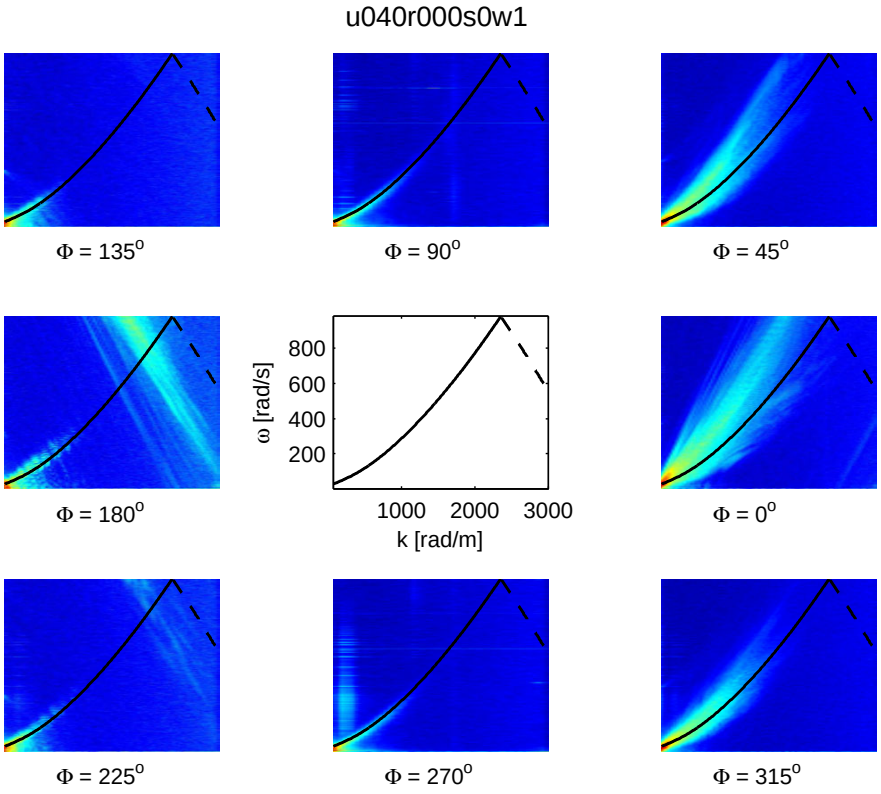

Figure A.40.: ω-k Slices through the 3D power spectrum

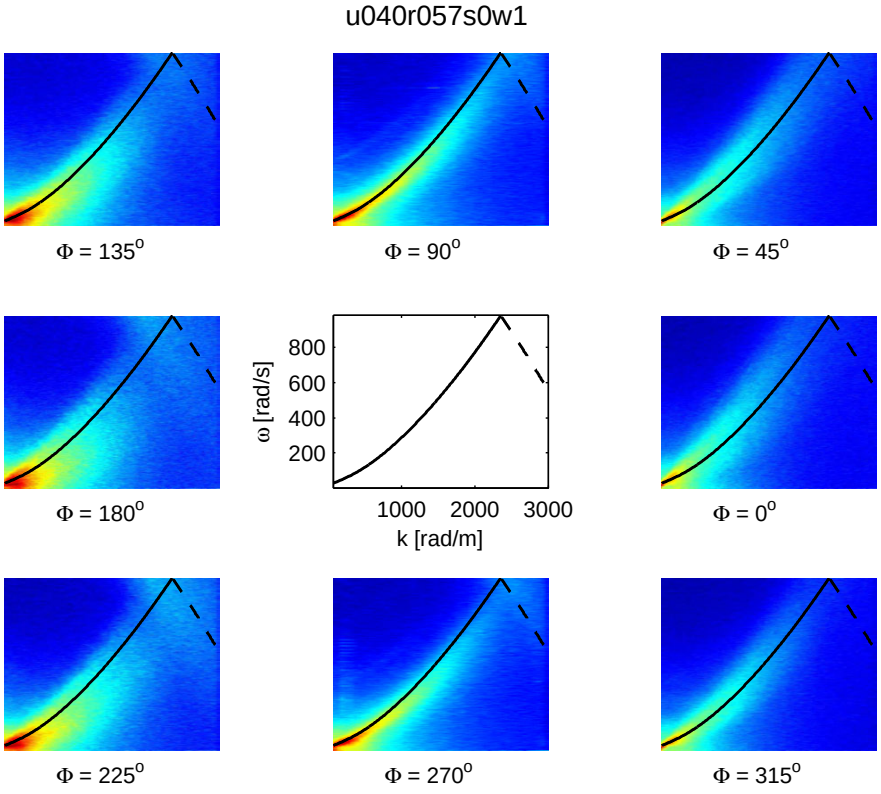

Figure A.41.: ω-k Slices through the 3D power spectrum

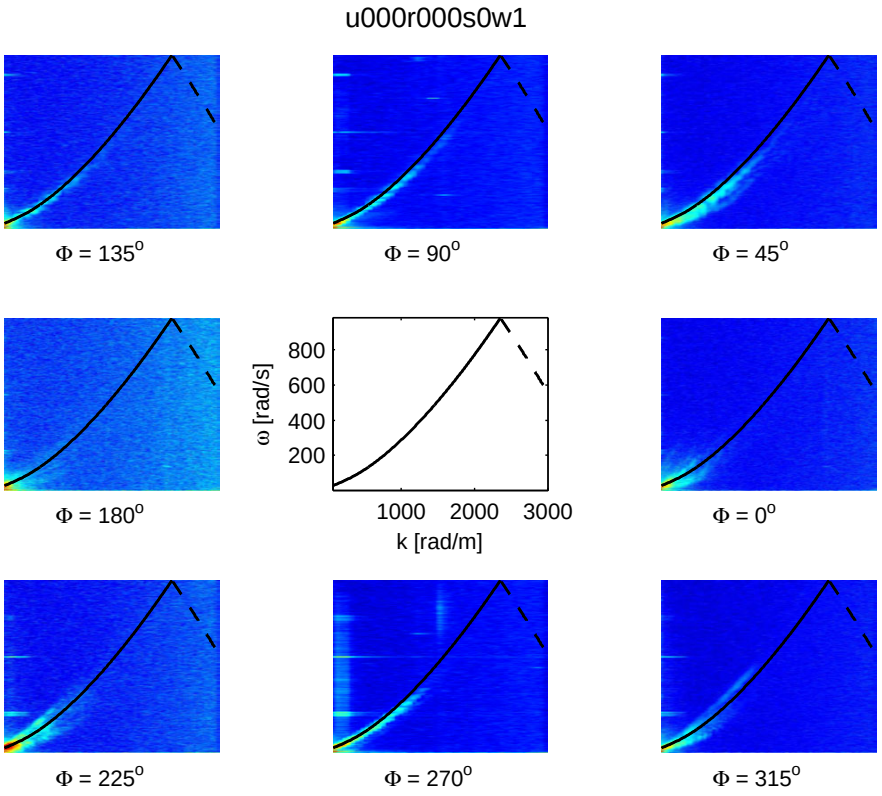

Figure A.42.: ω-k Slices through the 3D power spectrum

A.5. Covariance of Wave Slope and Height

Scatter diagrams for s_x, s_y and h are shown in figure A.43.

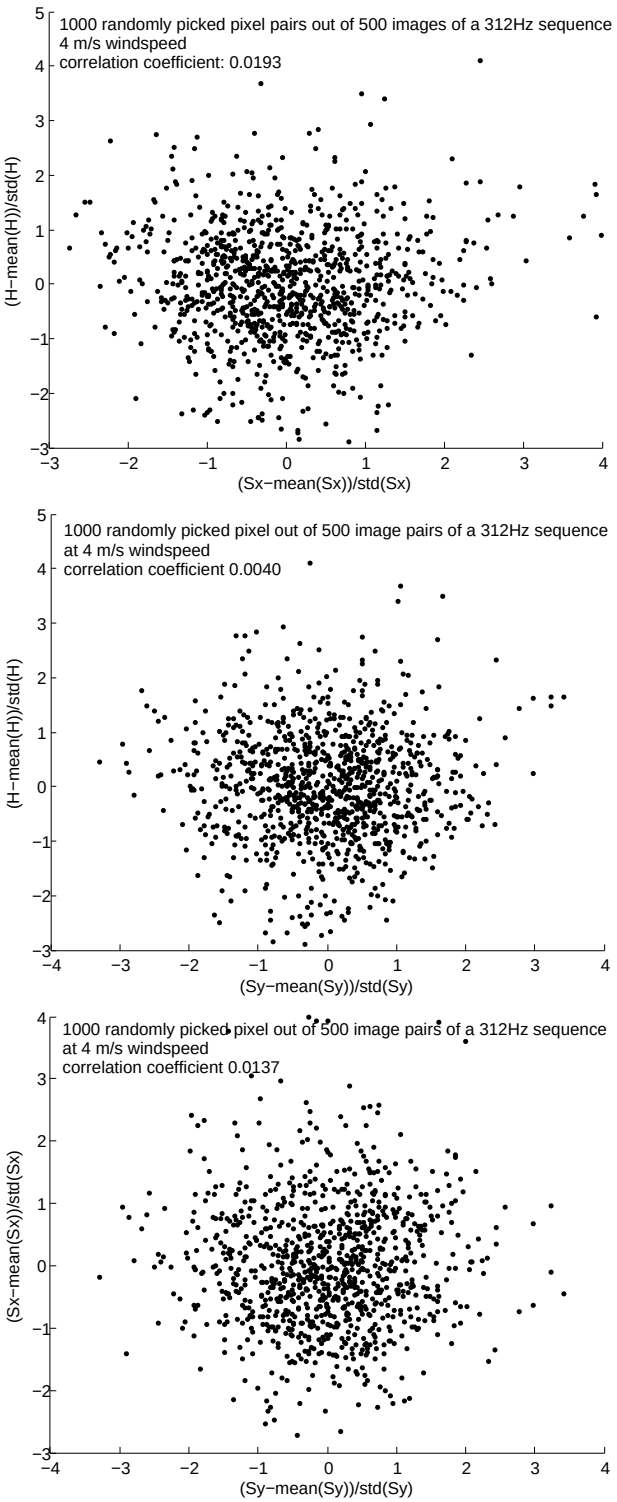

Figure A.43.: Example for scatter diagrams of the slope components s_x and s_y and height H. Correlation coefficients as indicated.

A.6. Monolayer Surface Slicks

For the surface slick conditions, two different monolayer surface slicks have been utilized (OLA = Oleyl Alcohol; PME = Hexadecanoic Acid Methyl Ester). The substances were deployed directly at the wind entrance of the linear wave tank using a little tube that was fixed a few millimeters above the water surface. Over the course of one experiment, the dropping rate of the substances was intended to be constant. However, for some experiments the dropping rate was unsteady, so that for the individual sequences a numeric code is used that allows for an distinction of the surface slick condition, see table A.6. More informations about the wave damping of OLA and PME can also be found in the articles: Gade et al. [51], Lange and Hühnerfuss [105], and Alpers [4]. See Mann [119] and Bock and Mann [19] for further reading about dynamic surface tension and capillary waves.

Code	Substance	Drop Rate
0	no slick	0
1	OLA	?
2	OLA	3
3	PME	?
4	PME	3
5	OLA	<3
6	PME	<3

Table A.2.: Number codes for the monolayer slick conditions. The dropping rate corresponds to the setting of the flexible-tube pump.

TABLE 1. Dependence of the wave induced surface tension variation on time for oleyl alcohol (OLA) and palmitic acid methyl ester (PME) monolayers. Wave height = 2 cm, temperature = 289 K. The data values are estimated to be accurate to $\pm 1.0 \times 10^{-3}$ N m^{-1}.

Time (min)	Surface tension variation (10^{-3} N m^{-1})	
	OLA	PME
1.5–2.0	10.7	—
3.0–3.5	12.3	—
5.0	12.9*	9.2
9.5–10.0	—	10.2
18.5	—	13.8*

* Relaxation approached limiting value.

Figure A.44.: Modified surface tension for the monolayer surface slicks (OLE and PME). Source: Lange and Hühnerfuss [105]

A.7. MTF Target

The hole diameters for the *MTF target* are given in figure A.45. The usage of the target for the MTF measurement is described in section 4.5, and for the geometrical calibration in section 4.2. The thin metal stencil, with a design resolution of 0.5 μm and an accuracy of $\pm 10\,\mu$m, was manufactured by Beta LAYOUT GmbH, 65326 Aarbergen, Germany (`www.schablone.de`).

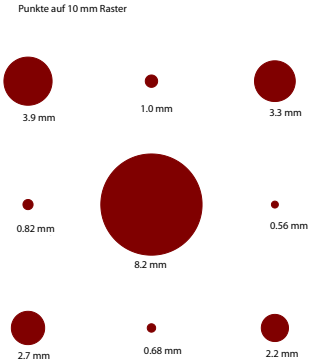

Figure A.45.: Hole diameters for a unit cell of the *MTF target*. The holes are arranged on a 10 mm grid.

A.8. Camera

The camera AVT-Pike032C was used for the CISG measurements, for technical details see figure A.46. The camera lens was manufactured by Ernst Leitz Wetzlar Germany, Model ELMAR 1:4/90, No. 1712906. The lens was augmented by an external transaxle for the focousing.

PIKE F-032C / F-032C fiber

Feature	Specification
Image device	Type 1/3 (diag. 5.92 mm) type progressive scan KODAK IT CCD KAI340
Effective picture elements	648 (H) x 488 (V)
Lens mount	Adjustable C-Mount: 17.526 mm (in air); Ø 25.4 mm (32 tpi) Mechanical Flange Back to filter distance: 12.5 mm (see Figure 31: Pike C-Mount dimensions (VGA size filter for Pike F-032) on page 64)
Picture sizes	320 x 240 pixels (Format_0 Mode_1) 640 x 480 pixels (Format_0 Mode_2 to Mode-5) 640 x 480 pixels (Format_7 Mode_0) 320 x 480 pixels (Format_7 Mode_4, 2 x H-sub-sampling) 640 x 240 pixels (Format_7 Mode_5, 2 x V-sub-sampling) 320 x 240 pixels (Format_7 Mode_6, 2 x full sub-sampling)
Cell size	7.4 µm x 7.4 µm
ADC	14 bit
Color modes	Raw8, Raw16, Mono8, YUV4:2:2, YUV4:1:1, RGB8
Frame rates	1.875 fps; 3.75 fps; 7.5 fps; 15 fps; 30 fps; 60 fps; 120 fps up to 202 fps in Format_7 (Mono8, Raw8) up to 139 fps (YUV 4:1:1) up to 105 fps (YUV 4:2:2, Raw 16) up to 70 fps (RGB8)
Gain control	Manual: 0-20 dB (0.0353 dB/step); auto gain (select. AOI)
Shutter speed	26 ... 67.108.864 µs (~67s); auto shutter (select. AOI), level mode
External trigger shutter	Programmable, trigger level control, single trigger, bulk trigger, programmable trigger delay
Internal FIFO memory	Up to 105 frames
# look-up tables	4 user programmable (14 bit → 14 bit); gamma (0.45 and 0.7)
Smart functions	AGC (auto gain control), AEC (auto exposure control), AWB (auto white balance), color correction, hue, saturation, real-time shading correction, LUT, 64 MByte image memory, mirror, binning, sub-sampling, High SNR, storable user sets Two configurable inputs, four configurable outputs RS-232 Port (serial port, IIDC V1.31)
Transfer rate	100 Mbit/s, 200 Mbit/s, 400 Mbit/s, 800 Mbit/s

Source:
Allied Vision Technologies
AVT-Pike
Technical Manual
V2.0.0 July 2006

Figure A.46.: Technical details for AVT Pike032c, Source: `http://www.alliedvisiontec.com/`

A.9. Normalization Factor in the modified 3d-DFT

Here we give a detailed derivation of the normalization factor for the power spectra that is used in section 2.3. As in section 2.3 we have

$$\Delta k_x = \frac{2\pi}{X}, \quad \Delta k_y = \frac{2\pi}{Y}, \quad \Delta\omega \;=\; \frac{2\pi}{T} \tag{A.1}$$

$$M = \frac{2\pi}{\Delta k_x \Delta x} = \frac{X}{\Delta x}, \quad N = \frac{2\pi}{\Delta k_y \Delta y} = \frac{Y}{\Delta y}, \quad O = \frac{2\pi}{\Delta\omega\Delta t} = \frac{T}{\Delta t}, \tag{A.2}$$

$$\eta_{m,n,o} = \sum_{u=0}^{M-1}\sum_{v=0}^{N-1}\sum_{w=0}^{O-1} \hat{\eta}_{u,v,w}\, \mathrm{w}_M^{mu}\ \mathrm{w}_N^{nv}\ \mathrm{w}_O^{-ow}, \tag{A.3}$$

$$\hat{\eta}_{u,v,w} = \frac{1}{MNO}\sum_{m=0}^{M-1}\sum_{n=0}^{N-1}\sum_{o=0}^{O-1} \eta_{m,n,o}\, \mathrm{w}_M^{-mu}\ \mathrm{w}_N^{-nv}\ \mathrm{w}_O^{ow}. \tag{A.4}$$

We define the modified spectrum $\hat{\eta\prime}_{u,v,w}$ that satisfies

$$\eta_{m,n,o} = \sum_{u=0}^{M-1}\sum_{v=0}^{N-1}\sum_{w=0}^{O-1} \hat{\eta\prime}_{u,v,w}\, \mathrm{w}_M^{mu}\ \mathrm{w}_N^{nv}\ \mathrm{w}_O^{-ow}\Delta k_x\Delta k_y\Delta\omega, \tag{A.5}$$

or in other words we define

$$\hat{\eta\prime}_{u,v,w} \equiv \hat{\eta}_{u,v,w}/(\Delta k_x\Delta k_y\Delta\omega), \tag{A.6}$$

so that $\hat{\eta\prime}_{u,v,w}$ has the same dimensions as the continuous spectrum. We are now searching for the normalization factor F, so that the forward transform

$$\hat{\eta\prime}_{u,v,w} = F\sum_{m=0}^{M-1}\sum_{n=0}^{N-1}\sum_{o=0}^{O-1} \eta_{m,n,o}\, \mathrm{w}_M^{-mu}\ \mathrm{w}_N^{-nv}\ \mathrm{w}_O^{ow}\Delta x\Delta y\Delta t \tag{A.7}$$

is fulfilled. Factoring out the terms $\Delta x\Delta y\Delta t$ gives

$$\hat{\eta\prime}_{u,v,w} = F\Delta x\Delta y\Delta t\sum_{m=0}^{M-1}\sum_{n=0}^{N-1}\sum_{o=0}^{O-1} \eta_{m,n,o}\, \mathrm{w}_M^{-mu}\ \mathrm{w}_N^{-nv}\ \mathrm{w}_O^{ow} \tag{A.8}$$

With (A.4) we get

$$\hat{\eta\prime}_{u,v,w} = FMNO\Delta x\Delta y\Delta t\,\hat{\eta}_{u,v,w} \tag{A.9}$$

Using (A.6) and (A.9) we have the condition for F

$$\frac{1}{\Delta k_x\Delta k_y\Delta\omega} = F(MNO)\Delta x\Delta y\Delta t. \tag{A.10}$$

This is solved using (A.2) with the result

$$F = \frac{1}{(2\pi)^3} \tag{A.11}$$

So that the modified forward transform can be written just like in the continuous case as

$$\hat{\eta\prime}_{u,v,w} = \frac{1}{(2\pi)^3}\sum_{m=0}^{M-1}\sum_{n=0}^{N-1}\sum_{o=0}^{O-1} \eta_{m,n,o}\, \mathrm{w}_M^{-mu}\ \mathrm{w}_N^{-nv}\ \mathrm{w}_O^{ow}\Delta x\Delta y\Delta t, \tag{A.12}$$

which is the same as (6.22).

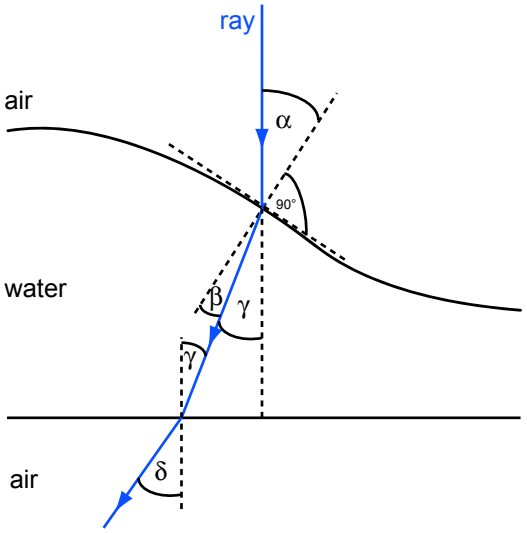

Figure A.47.: The light ray points vertically on the water surface. At the surface it undergoes refraction. A second refraction occurs when the ray leaves the water body at a horizontal interface (e.g. glas bottom of the tank).

A.10. Derivation of the General Expression for the Ray Geometry

Here we give a detailed derivation of equations (3.3) and (3.2) from the sections 3.1.1 and 3.1.2. The relationship between the ray inclination $\tan\delta$ above the fresnel lens of the light box and the water surface inclination $\tan\alpha$ is given by the one dimensional equation

$$\tan\alpha = \frac{\tan\delta}{\sqrt{n_w^2 + \tan^2\delta(n_w^2 - 1)} - \sqrt{1 + \tan^2\delta}}. \tag{A.13}$$

In the first paragraph, we explicitly go through the derivation of (A.13). The second paragraph explains, how the extension for two dimensions is justified, so that we finally get (3.3).

1d-Derivation: Consider the light path that is sketched in figure A.47. The refraction is expressed by snells law, so we are starting with

$$\sin\alpha = n \cdot \sin\beta \tag{A.14}$$
$$n \cdot \sin\gamma = \sin\delta \tag{A.15}$$
$$\beta = \alpha - \gamma, \tag{A.16}$$

where n is the index of refraction for water. Using the trigonometric identity

$$\sin(\alpha - \gamma) = \sin\alpha\ \cos\gamma - \sin\gamma\ \cos\alpha \tag{A.17}$$

we get

$$\sin\alpha = n \cdot (\sin\alpha\ \cos\gamma - \sin\gamma\ \cos\alpha) \tag{A.18}$$

after inserting (A.16) in (A.14). Dividing (A.18) by $\cos\alpha$ gives

$$\tan\alpha = n \cdot (\tan\alpha\ \cos\gamma - \sin\gamma)\,. \tag{A.19}$$

Solving (A.19) for $\tan\alpha$ yields

$$\tan\alpha = \frac{n\cdot\sin\gamma}{n\cdot cos\gamma - 1}. \tag{A.20}$$

With (A.15) and $\cos = \sqrt{1-\sin^2}$ we have

$$\tan\alpha = \frac{\sin\delta}{\sqrt{n^2-\sin^2\delta}-1}. \tag{A.21}$$

Expanding the right side of (A.21) by $\cos^{-1}\delta$ we obtain

$$\tan\alpha = \frac{\tan\delta}{\sqrt{\frac{n^2}{\cos^2\delta}-\tan^2\delta}-\frac{1}{\cos\delta}}. \tag{A.22}$$

Inserting

$$\frac{1}{\cos\delta} = \sqrt{1+\tan^2\delta}$$

to equation (A.22) gives

$$\tan\alpha = \frac{\tan\delta}{\sqrt{n^2\cdot(1+\tan^2\delta)-\tan^2\delta}-\sqrt{1+\tan^2\delta}} \tag{A.23}$$

and finally

$$\tan\alpha = \frac{\tan\delta}{\sqrt{n^2+\tan^2\delta\cdot(n^2-1)}-\sqrt{1+\tan^2\delta}}. \tag{A.24}$$

Figure A.49 a) shows a plot for equation (A.24) and the inverse relation in b).

2d-Extension: The one dimensional expression (A.24) can be easily extended into two 2 dimensions to obtain (3.3), which is rewritten here:

$$\mathbf{s} = \begin{bmatrix} s_x \\ s_y \end{bmatrix} = \begin{bmatrix} \cos\Phi \\ \sin\Phi \end{bmatrix} \cdot \frac{|\tan\delta|}{\sqrt{n_w^2+(n_w^2-1)\tan^2\delta}-\sqrt{1+\tan^2\delta}}. \tag{A.25}$$

Consider the decomposition of the total slope $s = \tan\alpha$ for the along wind and cross wind direction

$$\mathbf{s} = [s_x, s_y]^T = |\tan\alpha|[\cos\Phi, \sin\Phi]^T, \tag{A.26}$$

where the polar angle Φ is given by the orientation of the plane that is spanned from the water surface normal and the vertical, see figure A.48. The ray $\mathbf{k}$ is vertically pointing down on the water surface. After refraction at the water surface the refracted ray $\mathbf{k}'$ always lies in the plane that is spanned by the water surface normal[1] $\mathbf{n}$ and the vertical $\mathbf{e_z}$. A second refraction occurs at the glass window at the bottom of the tank. The glass window is horizontal so that its normal is vertical $\mathbf{n}_{window} = \mathbf{e_z}$. After the second refraction the ray $\mathbf{k}''$ lies in the plane that is spanned by the vertical $\mathbf{e_z}$ and the $\mathbf{k}'$. So the ray does not change the orientation in the x–y–plane again, under the conditions:

1. the surface normal of the glas window is in good horizontal alignment.
2. the camera vector $\mathbf{k}$ has no inclination to the vertical.

[1] note: $\mathbf{n} \propto \left[-\frac{\partial z}{\partial x}, -\frac{\partial z}{\partial y}, 1\right]^T$ also lies in the plane that is given by the 3–d extension of the slope in gradient space $\mathbf{s} = \left[\frac{\partial z}{\partial x}, \frac{\partial z}{\partial y}, 1\right]^T$ and the vertical $\mathbf{e_z} = [0,0,1]^T$

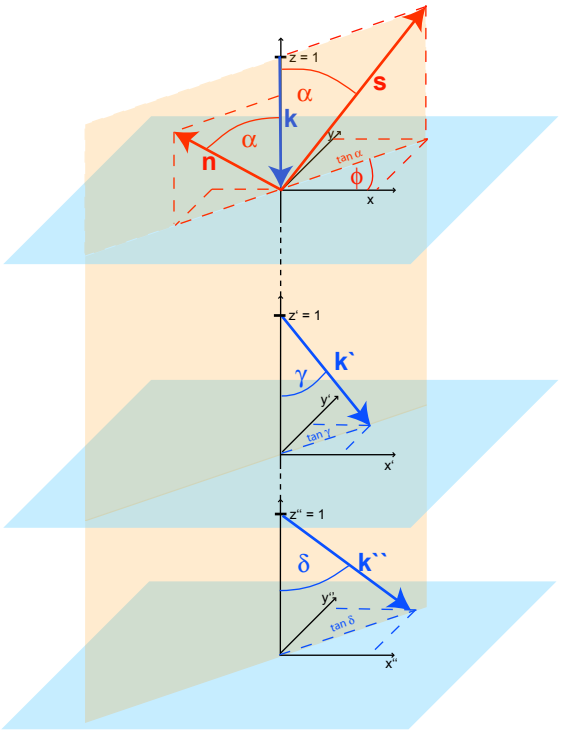

Figure A.48.: Sketch for the orientations of the rays in the plane that is spanned by the water surface normal $\mathbf{n}$ and the incident ray vector $\mathbf{k}$. In the air space above the water surface the ray $\mathbf{k}$ points vertically down to the surface that is inclined by the angle α against the vertical. The ray after the refraction at the water surface is denoted by $\mathbf{k}'$. The ray inclination in the water body γ is linked to the surface inclination α according to snells law ($\gamma = \alpha - \sin^{-1}(\frac{1}{n}\sin\alpha)$). The orientation of $\mathbf{k}'$ in the x–y–plane is defined by the orientation Φ of the surface normal, because the tangential component of the E–field vector does not change and for that $\mathbf{k}$, $\mathbf{n}$ and $\mathbf{k}'$ always lie in the same plane. If the ray undergoes a second refraction at a horizontal interface between water body and air space then the ray vector $\mathbf{k}''$ still lies in this plane (assumption: the glass window with normal $\mathbf{n}'$ at the tank bottom is perfectly horizontal, and thus $\mathbf{n}' = -\mathbf{k}$).

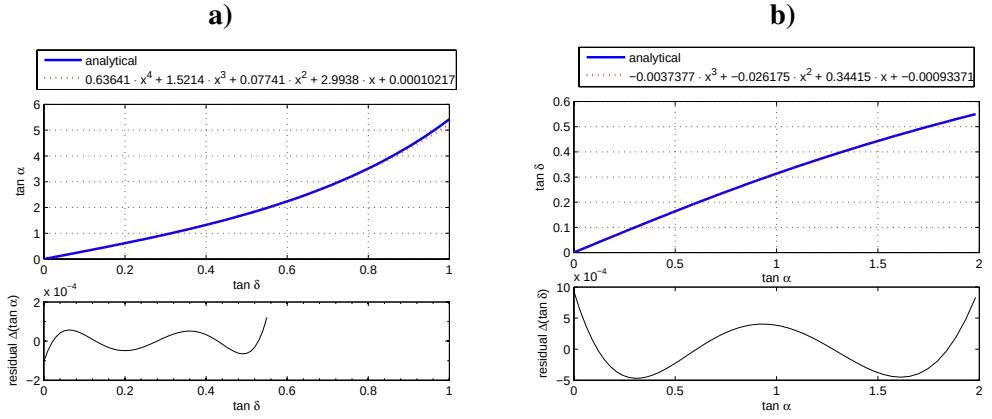

Figure A.49.: a) top: $\tan\alpha$ as function of $\tan\delta$ (blue) and polynomial fit for $\tan\alpha < 2$ (red dashed); bottom: residual of the polynomial fit. **b)** top: $\tan\delta$ as function of $\tan\alpha$ (blue) and polynomial fit for $\tan\alpha < 2$ (red dashed); bottom: residual of the polynomial fit

Danksagung

Ich bedanke mich herzlich bei Prof. Dr. Bernd Jähne für die Ermöglichung und Betreuung dieser Arbeit, sowie bei Prof. Dr. Werner Aeschbach-Hertig für die freundliche Bereitschaft zur Begutachtung.

Die *Windis*-Arbeitsgruppe ist für mich ein Hort der Kreativität, nicht zuletzt aufgrund des freundschaftlichen Umgangs untereinander und der vielen inspirierenden Ideen unseres Chefs. Für die angenehme Arbeitsatmosphäre gilt es allen Kollegen zu Danken.

Besonderen Dank schulde ich Dr. Günther Balschbach für seine stete Diskussionsbereitschaft und für sein Engagement als Mentor in der Gruppe.

Zum Gelingen diese Arbeit haben zudem Dr. Uwe Schimpf, Martin Schmidt, Dr. Kai Degreif, Dr. Achim Falkenroth, PD Dr. Christoph Garbe, Kerstin Richter und Florian Huhn besonders beigetragen - und zwar durch eine gelungene Mischung aus Tatkraft, Expertise und Frohsinn - vielen Dank!

Ich danke den *WiSSCy*-Kooperationspartnern der Forschergruppe um Dr. Martin Gade aus Hamburg, insbesondere Anne-Kristin Anweiler, für die Zusammenarbeit. Die Hilfe der Deutschen Forschungsgemeinschaft (DFG) zur Finanzierung des *WiSSCy-Projekts* wird dankbar anerkannt.

Das IUP schätzt sich glücklich, kompetente und kooperative Leute in der feinmechanischen Werkstatt zu haben - mein Dank für die Unterstützung beim Bau des Roboters und der Lichtquelle gilt insbesondere Ralph Pfeifer, Sebastian Welk, Heribert Sommer und Udo Weller.

Danke an Dr. Helmut Herrmann für die zahlreichen und schnellen Verbesserungen der Bildverarbeitungs-Software Heurisko. Auch danke ich den Machern des Online-Wörterbuchs LEO, welches die Erstellung dieser Arbeit in (d)englischer Sprache erheblich vereinfacht hat.

Meinen lieben Freunden und meiner Familie möchte ich für ihre Geduld und ihre mentale Unterstützung in den vergangenen Monaten danken. Ich freue mich darauf schon bald wieder etwas entspannter mit Euch das Leben zu feiern. Ganz besonders freue ich mich darauf, meine unersetzbare Agnès für ihre Liebe, ihre Geduld und ihr Verständnis zu entlohnen... in unserer baldigen Zukunft als kleine Familie.

B. Erratum

Correction to the Registration Parameters of IR Images on Page 45: The registration parameters on page 45 are incomplete. Due to maintenance of the IR scanner mirror between June the 16th 2007 and June the 20th 2007 another set of parameters is required. Manual tuning of the parameters (using rain drop impacts from Run234 as reference) lead to the set

```
points[0] = {169.6401 , 74.8098};
points[1] = {37.3000  , 80.8252};
points[2] = {40.5682  , 142.7987};
points[3] = {172.5244 , 135.7481};
```

valid after June the 20th 2007.

Concerning section 2.5.2 There is an error in the sentence:

"Then follows that the amplitude damping at the Nyquist wavenumber is $\mathrm{MTF}(\tilde{\mathbf{k}}) = 1/\sqrt{2}$*, see Jähne [77, chapter 9.2.5]."*

Correct is: $\mathrm{MTF}(\tilde{\mathbf{k}}) = \frac{2}{\pi}$.

Explanation: The Transfer Function of the rectangular box function is given by the sinc function $\mathrm{sinc} = \frac{\sin(\pi \check{k})}{\pi \check{k}}$, in terms of normalized wavenumber $\check{k} = \frac{k \Delta x}{2\pi}$. Therefore the value of the Transfer function for the Nyquist wavenumber ($\check{k} = 1/2$) the Transfer Function attains a value of $\frac{\sin(\frac{\pi}{2})}{\frac{\pi}{2}} = \frac{2}{\pi} = 0.6366$.

Mistake in equation (3.1) correct is

$$\Delta x = f \tan \delta. \tag{B.1}$$